FABRICATION OF POROUS CERAMICS AND COMPOSITES BY A NOVEL FREEZE CASTING PROCESS

by

GANG LIU

A thesis submitted to
The University of Birmingham
for the degree of
DOCTOR OF PHILOSOPHY

School of Metallurgy and Materials
College of Engineering and Physical Sciences
The University of Birmingham
March 2011

ABSTRACT

Porous ceramics have been widely used in many fields. Among the fabrication techniques for porous ceramic, freeze casting has recently attracted much attention as being a versatile, low cost and environmental friendly process. In this study, alumina and Al_2O_3-ZrO_2 were utilized as model materials to investigate the preparation technique of freeze casting. Basic factors such as initial solids loading, cooling rate, and sintering temperature that would affect the final morphologies and the effect of additives have been studied. Porous alumina ceramics with lamellar microstructure exhibited compressive strengths up to 123 MPa for 33% porosity and 55 MPa for 42% porosity, making them suitable to be considered for potential load-bearing applications. In a two-phase system (Al_2O_3-ZrO_2), the choice of particle size of the ceramic powder was of great significance, which can lead to engulfment and phase segregation. $BaTiO_3$ and Lead zirconate titanate were employed to demonstrate the application of the freeze casting technique. $BaTiO_3$-epoxy composites exhibited modest piezoelectric constant but the dielectric constant was 1 order of magnitude higher than conventional composites with randomly distributed ceramic particles. For the 2-2 $Pb(Zr,Ti)O_3$-epoxy composites, with an increase of initial solids loading from 11 vol.% to 25 vol.%, the volume of ceramic phase in the composite gradually increased from about 30 vol.% to 50 vol.%, the piezoelectric constant d_{33} increased from about 103 pC/N to 203 pC/N, demonstrating the potential applications of this technique for the fabrication of 2-2 piezocomposites.

ACKNOWLEGEMENTS

I would gratefully like to acknowledge my supervisor Prof. Tim W Button for his excellent supervision and continuing support throughout this research project, and for offering me a pleasant research environment to complete this research work.

I would like to thank the Overseas Research Students Awards Scheme (ORSAS) and School of Metallurgy and Materials for providing financial support for this research project.

I would like to express my gratitude to Prof. Paul Bowen and Prof. Stuart Blackburn for the provision of laboratory equipment in the School of Metallurgy and Materials and the Interdisciplinary Research Centre (IRC), respectively.

I would like to thank Dr. Dou Zhang, who is now a professor in China, for his patient guidance and valuable discussion on my research work, and also for the generous help in and support during my first and second study years.

Special thanks go to members of Functional Materials Group, especially to Mr. Carl Meggs, for assisting in research-related issues and providing comic relief in the office.

I would also like to express great gratitude to my parents, my sister, and my girlfriend's family for love, financial and emotional support, and encouragement to pursue my PhD education.

Finally, I would like to deeply thank my girlfriend, Yan Yan, for all of her love, support, understanding, and patience all throughout my graduate study. For without her support, none of this work has been possible.

CONTENTS

INDEX OF FIGURES

INDEX OF TABLES

NOMENCLATURES AND ACRONYMS

3D: three dimension

BAT: alumina-doped barium titanate

BT: barium titanate

CNC: computer numeric-controlled

DSC: differential scanning calorimetry

dwb: dry weight of the powder basis

EDX: energy dispersive X-ray

HA: hydroxyapatite

HCR: high cooling rate

JCPDS: joint committee on powder diffraction

LCR: low cooling rate

MCR: medium cooling rate

MPB: morphotropic phase boundary

NH_4PAA: ammonium polyacrylate

PDMS: poly(dimethylsiloxane)

PE: poly(ethylene)

PVA: poly(vinyl alcohol)

PVC: poly(chloroethanediyl)

PZT: lead zirconate titanate

RT: room temperature

SEM: scanning electron microscopy

XRD: X-ray diffraction

YSZ: yttria-stabilized zirconia

CHAPTER 1 INTRODUCTION

Porous ceramics and composites (originating from porous ceramics) are of particular interest because of their interesting structural and functional properties. This thesis reports the efforts of fabrication of porous ceramics and composites through a novel freeze casting technique.

In order to take full advantage of the porous structure, it is necessary to be able to control the pore morphology, pore feature size and the amount of porosity. Current fabrication techniques suffer from an inherent limitation of a narrow range of pore characteristics. Moreover, the pore forming agents pose challenges in the removal process, leading to the increased processing cost and environmental hazards. Among many fabrication techniques for porous ceramics, freeze casting has recently attracted much attention as being a cost effective and environmentally friendly process. In this process a ceramic slurry, with generally low solids loading, is first frozen to form vehicle ice crystals, which often connect with each other in dendritic shapes, surrounded by frozen concentrated ceramic slurry. After freeze drying, channels are created replicating the shape of the interconnected ice crystals. Following that, the resultant green compacts are sintered in a muffle furnace to obtain the porous ceramic.

The structure of the thesis is as follows.

The literature review in Chapter 2 consists of four parts. The first section summarizes the current fabrication methods of porous ceramics and describes the merits and disadvantage of each method. The second section presents the history, development, advantages and actuality of freeze casting. The third part summarizes the basic theories in ceramic colloidal suspensions. The fourth section introduces the properties of the ceramic materials used in this thesis and highlights their important properties.

Chapter 3 describes the experimental methods utilized in this investigation, which include the mould, setup, and experimental procedures for freeze casting, traditional electroceramics fabrication method for bulk ceramic, and measurement and analysis methods for related properties at different stages.

Alumina powder has been employed as a model material to demonstrate the freeze casting technique in Chapter 4. A variety of basic processing variables such as solids loading of the slurry, the cooling rate, and the sintering temperature were investigated. Moreover, the influence of additives on the morphology of the porous microstructures was also studied. Finally, an innovative double-side freezing technique was demonstrated as well.

Chapter 5, as a comparative chapter, focuses on the two-phase ceramic system, Al_2O_3-ZrO_2 composite, to make further investigation of freeze casting including fabrication and mechanism explanation.

Chapter 6 and Chapter 7 concentrate on the application of the freeze casting technique utilizing functional materials ($BaTiO_3$ and PZT), especially the functional properties.

The main findings and conclusions of this investigation are summarized in Chapter 8. Suggestions for future work that should be carried out in order to obtain further understanding of the freeze casting technique and its application are also proposed.

It should be noted that, because of the various material systems in this study, though relevant research background is described in the literature review, additional information is also presented at appropriate points in the results and discussion chapters.

CHAPTER 2 LITERATURE REVIEW

2.1 Fabrication Techniques and Applications of Porous Ceramics

Porous materials are usually understood as materials with porosity over 30%. In previous decades, materials with controlled porosity have already exhibited special features and properties which cannot be fulfilled by their conventional dense counterparts[1]. Therefore, porous materials have attracted a great deal of attention as new kinds of materials with a wide range of technical and engineering applications[2].

In general, contrary to polymeric and metallic materials with porous structures, pores are traditionally avoided in ceramics due to their inherently brittle nature[1]. However, because of their irreplaceable and unique merits such as high temperature and environmental stability in comparison to conventional polymers and metals[3], practical implementation of the technology of porous ceramics started in the 1930s and an increasing demand for porous ceramics has appeared in the recent decades.

Due to their structures and unique characteristics, porous ceramics exhibit a rather special combination of properties, such as low thermal conductivity, low thermal mass, low dielectric constant, low density, high thermal shock resistance, high wear resistance, high specific strength, high permeability for gases and liquids, making them indispensable for a wide range of engineering applications[3], as shown below[4]:

(1) Heat insulation of buildings and thermal machines; (2) Heat insulation of aircraft, mainly spacecraft; (3) Filtration of liquids, hot gases, liquid metals and alloys; (4) Refining metals and alloys by inert gas blowing via porous ceramics; (5) Cooling hot surfaces by feeding pressurized gas via porous ceramics; (6) Catalyst carriers in various chemical processes, including high-temperature ones; (7) Electrolyte carriers in fuel elements; (8)

Membranes for separation and purification of gas and liquids; (9) Artificial scaffolds for osseous tissue regeneration.

Generally speaking, there is no unanimous classification criterion for porous ceramics, since each sector of application has its own classification principles and norms. However, porous ceramic products can be classified according to the application attributes described above. They can also be classified according to characteristic attributes, such as the chemical composition of the initial material, porosity and so on.

The final properties of the porous ceramics can be modified for each specific application by controlling the microstructures and volume fraction. In another words, control of open or closed porosity, pore size distribution and pore morphology are normally the critical factors. All of these microstructural features are greatly affected by the fabrication methods utilized to produce cellular ceramics.

The most direct fabrication method for producing porous ceramics is the partial sintering of initially porous powder compacts or sintering of powder mixtures that can form pores through solid state reactions[1,5]. Unfortunately, porous ceramics obtained by this technique usually have low porosity (< 60%).

Besides this direct technique, a lot of novel fabrication methods for porous ceramics with controlled microstructures have been developed in order to satisfy the requirements of different specific applications.

Though there are many different types of processing routes found in the literature, on the whole, they can be generally divided into five main groups: replica method, sacrificial phase technique, direct foaming method, paste extrusion, and the most recently developed rapid prototyping technique. The characterizations, merits and drawbacks of each fabrication processing route will be considered in the following section.

2.1.1 Replica Method

The replica method consists of the impregnation of a porous organic material with a ceramic slurry or ceramic precursor followed by a heat treatment, which leads to the burning out of the organic body (sponge) and the sintering of the ceramic skeleton, to fabricate porous ceramics which will present a similar morphology to the initial porous material. In fact, the replica technique was the first method invented to produce porous ceramic structures[6]. The basic principle for this technique is illustrated schematically in Figure 2.1.

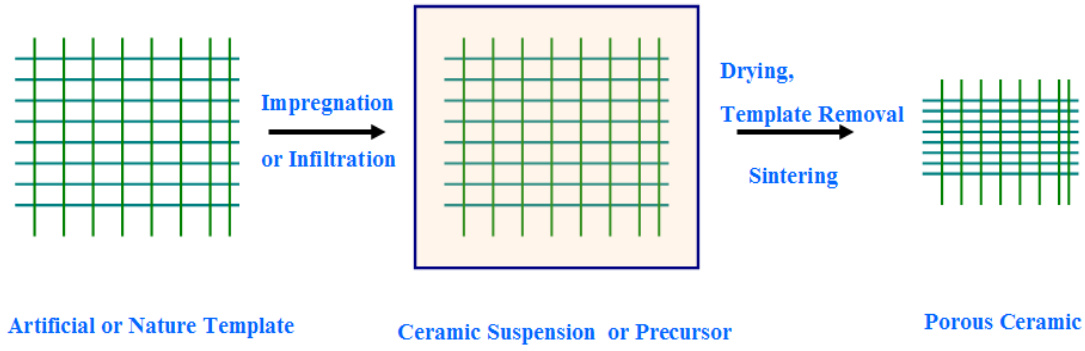

Figure 2.1 Schematic of replica method utilized for the fabrication of porous ceramics (after Studart[1]).

The replica method can be divided into two different groups according to the type of the template used, namely the artificial template (synthetic template) and the natural template.

2.1.1.1 Artificial Template

In 1963, Schwartzwalder and Somers began to use polymeric sponges to produce porous ceramics[6]. It became a cornerstone in the history of fabrication techniques for porous ceramics with various chemical compositions and porosities because, since then the sponge replica method has become one of the most popular techniques to produce porous ceramics and it is still widely utilized today to fabricate porous ceramics such as filters.

In this technique, a polymeric sponge with high porosity (typically polyurethane) is

generally first immersed in a ceramic suspension (or slurry) until the pores of the sponge are completely filled with the slurry. The excess suspension is then removed by passing the sponge through rollers, resulting in the formation of a ceramic coating over the struts of the initial polymeric sponge. At this stage, the ceramic suspension is required to have good fluidity. Therefore, dispersants are usually employed to obtain suspensions showing shear-thinning behaviour. Moreover, binder and plasticizer are also employed in the suspension in order to enhance the strength of the ceramic coating to prevent or avoid cracking the struts. Subsequently, the ceramic-coated polymeric sponge is carefully dried and pyrolysed by heat treatment. After removal of polymeric sponge, the residual ceramic is ultimately sintered under an appropriate temperature and atmosphere. Many porous ceramics with various chemical compositions, including alumina and silicon carbide, have already been prepared using this technique. Table 2.1 lists several literature-reported examples produced by this method.

Table 2.1 Literature-reported examples produced by artificial template

Ceramic Material	Polymeric Materials	Heat Treatment / Sintering Temperature (ºC)	Year	Author (References)
Al_2O_3	polyurethane	400/1600	1999	Paiva[7]
Mullite	polyurethane	300/1550	1999	Tulliani[8]
SiC&SiC-Si_3N_4 precursor	polyurethane	900	2000	Nangerjo[9]
SiC–TiC precursor	polyurethane	900/ 1100~1600	2000	Nangerjo[10]
SiC-Si_3N_4 precursor	polyurethane	900/ 1100~1600	2000	Nangerjo[11]
SiC precursor	polyurethane	900/ 1100~1300	2000	Bao[12]
Mullite	polyurethane	550/1600	2000	Roncari[13]
Hydroxyapatite (HA)	polyurethane	600/ 1350	2003	Ramay[14]
SiC	polyurethane		2004	Pu[15]
Reaction bonded Al_2O_3	polyurethane	500	2005	Luyten[16]
SiC	polyurethane	500/2120	2005	Mouazer[17]

Simplicity and flexibility are the two main advantages of this technique, because it is applicable to any ceramic material which can be easily and properly dispersed into a

suspension. Moreover, the porous ceramics fabricated by this technique generally have a wide range of total open porosity from 40% to 95%[1], and they usually show reticulated architectures with highly interconnected pores between 200 μm and 3 mm, typically shown in Figure 2.2 (a).

However, a distinct type of defect does occur in this fabrication technique, as illustrated in Figure 2.2(b): there are always voids inside the struts and cracks between the ceramic walls as a consequence of burnout of the polymer and different expansion between the polymer and ceramic powder during pyrolysis of the polymer template. Such defects will have an appreciable detrimental effect on the final mechanical properties of the porous ceramic.

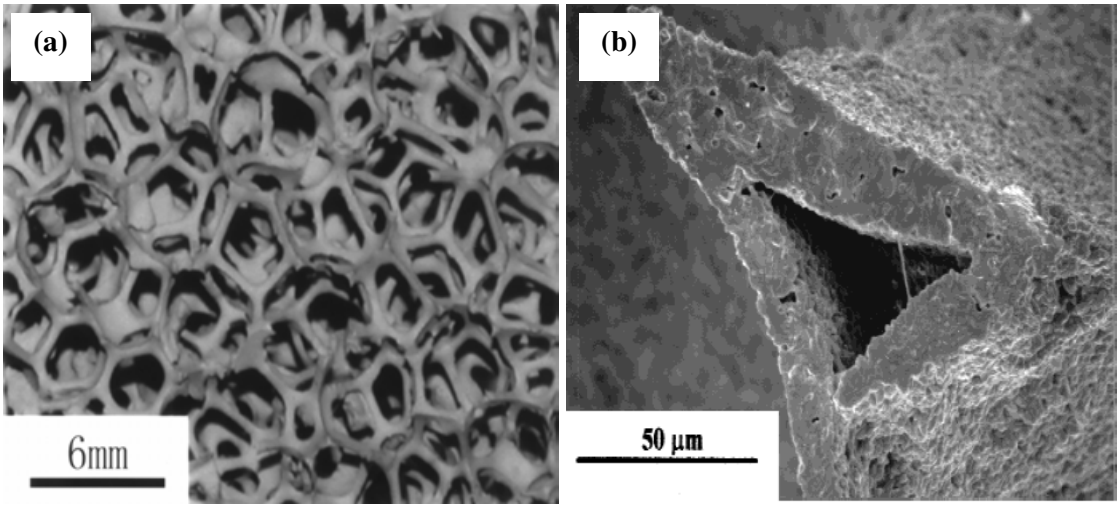

Figure 2.2 SEM Microstructures of porous ceramics fabricated by the artificial template replica method (a) silicon nitride reticulated porous ceramics with regulated structure (after Pu[15]) (b) detail of typical defects (triangular pores inside struts) (after Tulliani[8]).

Many attempts have been made to overcome this disadvantage, for example by adding additives to improve the wetting of the slurries on the polymer sponge[16], using polymeric precursor solutions[9] and introducing fibers[6]. Nangrejo and Bao[9] developed a method to produce silicon carbide (SiC) foams using polymeric precursor solutions and showed that there were no holes at the centre of struts. According to their report, the elimination of the

holes was probably due to the better penetration of the precursor solution into the polyurethane web structure during coating and the inward mobility of the polymeric precursor during pyrolysis, compared with slurry based methods.

Though porous ceramic structures with crack-free struts can be obtained through the use of preceramic polymers, the cost of these materials will be higher.

2.1.1.2 Natural Template

Besides the artificial polymeric sponges, there are many other available cellular materials which could be utilized as templates in the replica technique. The porous structures in nature are of special interest because of their unique pore morphologies and complicated microstructures, which may not be easily obtained artificially.

Corals are early natural templates used to prepare porous ceramics. In 1972, White[18] produced several porous materials using coral as a template. In that investigation, liquid wax was first used to obtain a negative replica of the original coral porous structure under vacuum, following which the $CaCO_3$ of the coralline skeleton was leached out by washing in strong acid. Finally, porous alumina ceramic was achieved by a positive replica of the wax template using an alumina ceramic suspension. Corals have also been used as a template to produce other porous materials such as $Pb(Zr,Ti)O_3$ and hydroxyapatite, as listed in Table 2.2. Following this so called biomimetic method of using coral as a template, wood is another natural template which has attracted a great deal of attention due to an anisotropic, porous morphology with excellent strength at low density, high stiffness, elasticity, and damage tolerance[23]. The unique structures in wood at the micrometer level can not be fabricated easily by technical (foam, extrusion or substitution) processing; therefore, many investigations have been undertaken to transform the cellular wood into porous ceramics.

Examples are also shown in Table 2.2. Coniferous wood and deciduous wood are the two types of wood usually used in this technique, which are easily obtained in nature. The former has a very homogeneous structure and consists of 90 ± 95% tracheids, which are long and slender cells tapered at the ends[23]. However, the later is less homogeneous. Tracheary elements (diameter up to 500 mm, length less than 1 mm) form long tubes of a few centimetres. Tracheids and tracheary elements are oriented in the direction of the trunk axis. The tracheary and tracheid cells in wood form directed pore structures at the micrometer level[23].

Table 2.2 Literature-reported examples produced by natural template

Template	Ceramic material	Method	Year	Author (References)
Coral	Al_2O_3	Impregnation with ceramic slurry	1972	White[18]
	Hydroxyapatite	Hydrothermal exchange	1974	Roy[19]
	PZT	Impregnation with ceramic slurry	1978	Skinner[20]
	Hydroxyapatite	Sol-gel coating	2003	Ben-Nissan[21]
Wood	SiC	Liquid Si infiltration	1998	Greil[22]
	SiC	Liquid or gaseous Si infiltration	2000	Sieber[23]
	SiC	Melt Si infiltration	2002	Feria [24]
	SiC	Si-vapor phase infiltration	2002	Greil[25]
	Zeolites	Liquid precipitation of precursors	2002	Dong[26]
	SiOC/C	preceramic polymer infiltration	2004	Zollfrank[27]
	Al_2O_3,TiO_2, ZrO_2	Sol-gel infiltration	2004	Cao[28]
	SiSiC	Precursor solusion infiltration	2005	Schwieger[29]
	SiC/C,ZrC/C, TiC/C	Sol-gel infiltration	2005	Rambo[30]
	Al_2O_3	Al-vapor infiltration	2005	Rambo[31]
	Fe_2O_3	Precursor solution infiltration	2005	Liu[32]

It is common in this method for the cellular wood to be first heated at elevated temperature (600~1800 ℃) under inert atmosphere to obtain a carbon cellular preforms. Subsequently, the carbon preform can be infiltrated with liquid or gases at higher temperature to prepare porous ceramic through a reaction process. A schematic procedure is illustrated in Figure 2.3.

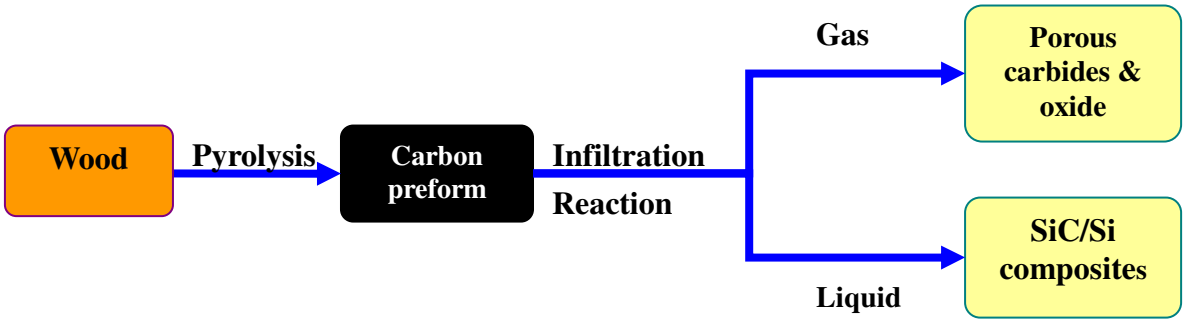

Figure 2.3 Schematic processing routes to transform cellular wood into porous ceramics (after Greil[22,25]).

The final porous architecture is a replica of the wood. Therefore, the pore size distribution, morphology, and porosity of wood-derived cellular ceramics are governed by the microstructure of the original wood template.

The wood templates used in this method generally have small pore sizes, therefore, the cellular ceramics obtained by this approach usually exhibit smaller pore sizes (10~300 μm)[1] compared to those produced by the polymeric sponge method. Furthermore, the most important advantage is that the porous ceramics fabricated by the wood template method possess an anisotropic nature, which will be a great advantage in applications where oriented pores are needed. A typical example of anisotropic nature is shown in Figure 2.4 ((a), (b), (c)). However, as in the case of polymeric sponge replica method, the ceramic walls may contain pits or pores (as shown in Figure 2.4 (d)) originated from the pyrolysis of the residual carbon, which could decrease the mechanical properties. It is very important to

totally convert the carbon preform into the ceramic phase if porous structures are required. Another drawback for the wood replica technique is that the high temperature and time-consuming steps in this technique might lead to high cost and restrict its application.

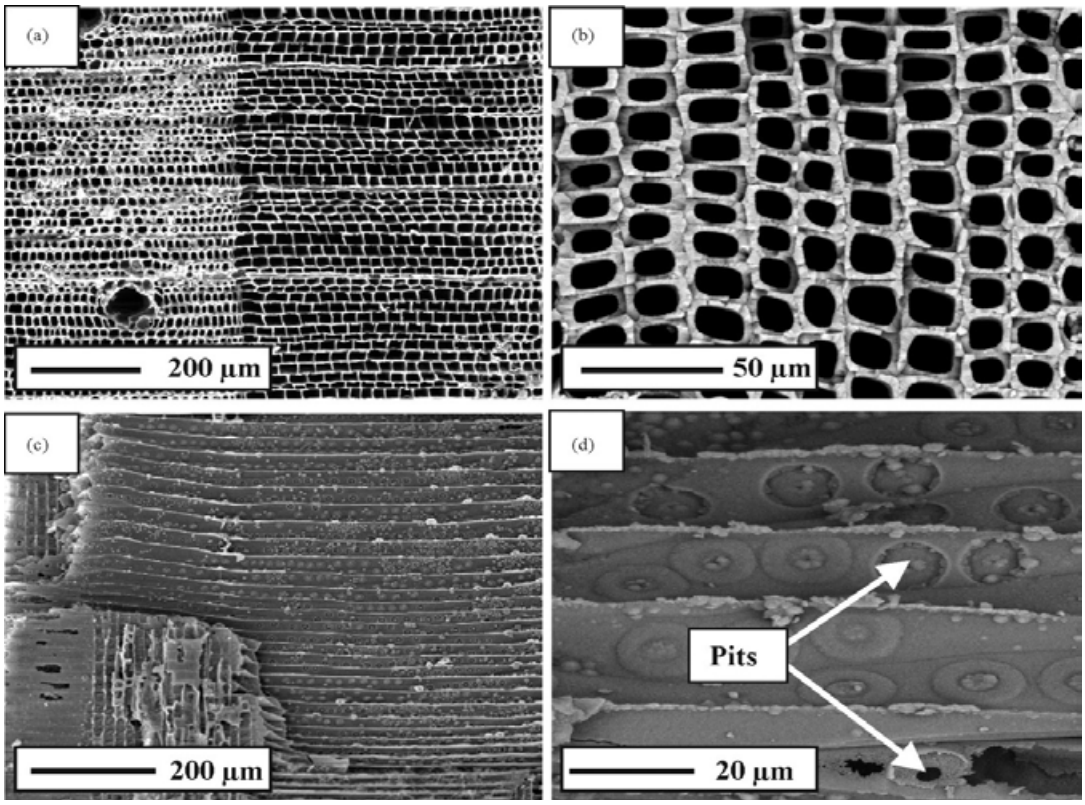

Figure 2.4 Porous β-SiC ceramic manufactured by Si-vapor infiltration of pyrolysed pine-wood at 1600 ºC for 4 h: SiC derived from pine in axial (a) & (b) and tangential direction (c) & (d) (after Greil[25]).

2.1.2 Sacrificial Phase Technique

The sacrificial phase technique is another widely used method for the fabrication of porous ceramics. This method usually involves the preparation of a biphasic composite comprising ceramic and sacrificial phase particles. Therefore, a sacrificial phase is first well dispersed in the initial ceramic powder or its precursors to obtain a biphasic mixture. The homogeneous distribution of the sacrificial phase in the matrix is of significant importance, since this will dominate the final porous structure. Subsequently, the sacrificial phase is removed from the

mixture either by pyrolysis or by another way such as sublimation or evaporation to obtain a cellular structure, and this is then followed by the sintering of the ceramic.

The final porous structure is a negative replica of the initial sacrificial phase, as opposed to the positive cellular structures achieved from the replica method mentioned in Section 2.1.1. The basic principle for this technique is shown schematically in Figure 2.5.

There are two main ways usually employed to prepare the biphasic mixture: one is powder pressing[33], and the other is a colloidal process followed by slip[34], tape[35] or direct casing[36], and other routes[37]. A great numbers of materials have been utilized as the pore former agent, and Table 2.3 lists some examples for those materials reported in the literature.

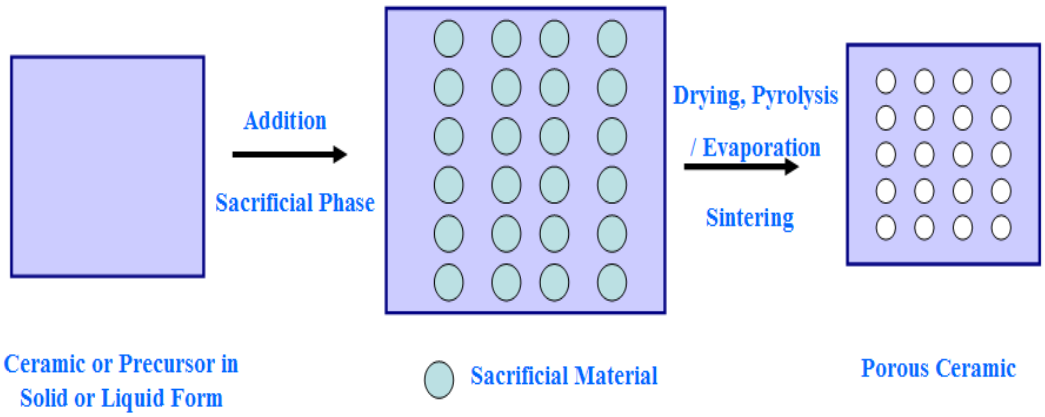

Figure 2.5 Schematic of the sacrificial phase technique utilized for the fabrication of porous ceramics. (after Studart[1]).

The sacrificial phase technique is very flexible, enabling porous ceramic structures with various chemical compositions to be produced. Compared with the polymeric replica techniques described in Section 2.1.1, the main merit for the sacrificial phase method is that it is feasible to modify the pore size, porosity and pore morphology of the final products by appropriate choice of the sacrificial phase. Moreover, due to the negative replica of the initial sacrificial material, shortcomings such as defects in the ceramic walls can be avoided. Some examples obtained by this technique are shown in Figure 2.6.

Table 2.3 Sacrificial materials reported in literatures

Artificial or Natural	**Sacrificial materials**
Man-made materials	PMMA[38-43], PVB[44], PVC[45], PS[46-50], Nylon[51], Cellulose acetate[52], Naphtalene[53]
Natural materials	Starch[54-60], Alginate[61], Cellulose[62], Glucide[63], Dextrin[64],Sucrose[65], Wax[66], Gelatine[67], Water[68-70], Oil[71-72]

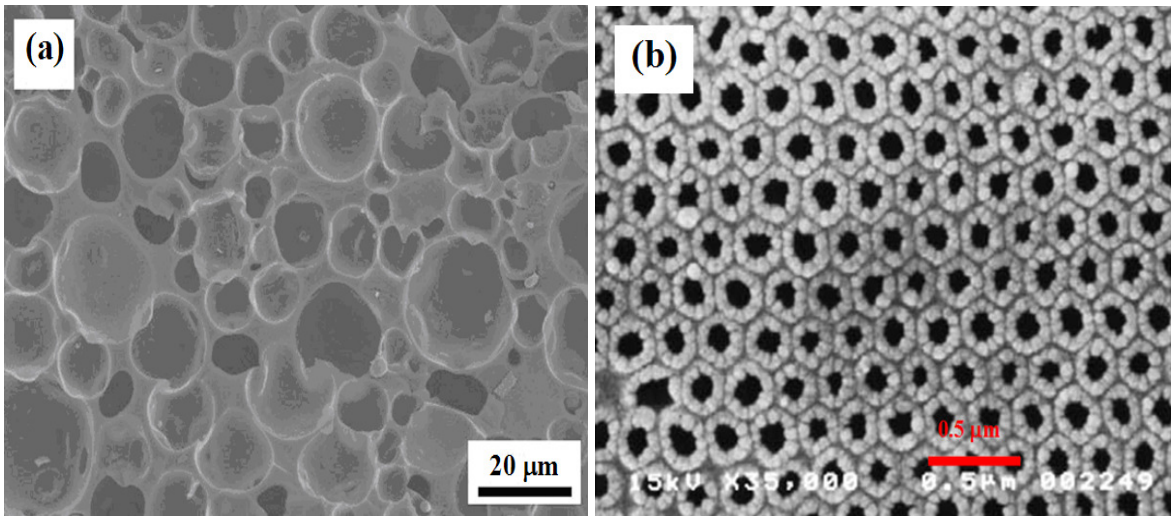

Figure 2.6 Example micrographs of the cellular structure obtained by the sacrificial phase method: (a) closed-cell silicon oxycarbide foams from the mixture prepared by powder pressing (with initial 40 wt.% Polyalkylsiloxane) (after Kim[73]); (b) Porous TiO_2 materials through colloidal process showing a hexagonal close-packed arrangement of pores (after Yoshio Sakka[74]).

However, the introduction of a large quantity of polymer component as the sacrificed phase has become a main shortcoming for this technique. Firstly, it can be very time-consuming to burn out the sacrificial phase completely and, secondly a large amount of exhaust gas may be generated during the process causing environmental problems. Such difficulties could be overcome by employing liquid sacrificial materials such as water or oil. Freeze casting is one technique using water as a sacrificial material, which will be detailed in later sections.

2.1.3 Direct Foaming Techniques

In the direct foaming technique, the ceramics with cellular structure are prepared through incorporating gas bubbles into a liquid media or slurry, followed by setting to keep the porous structures created by the gas bubbles intact. Subsequently, the consolidated foams are fired to obtain porous ceramics with good mechanical properties. The basic principle for the direct foaming technique is illustrated schematically in Figure 2.7. The porosity of the final porous ceramic is determined by the amount of the gas incorporated into the liquid media or the slurry during the foaming process. Moreover, the pore size, on the other hand, is governed by the wet foam stability prior to setting. However, the unstable system of the wet foam undergoes Ostwald ripening and coalescence processes to lower free energy[1]. These destabilization processes will greatly increase the size of gas bubbles and further result in large pores in the final product. So the stabilization of the bubbles in the wet foam is a very important factor in the direct foaming technique.

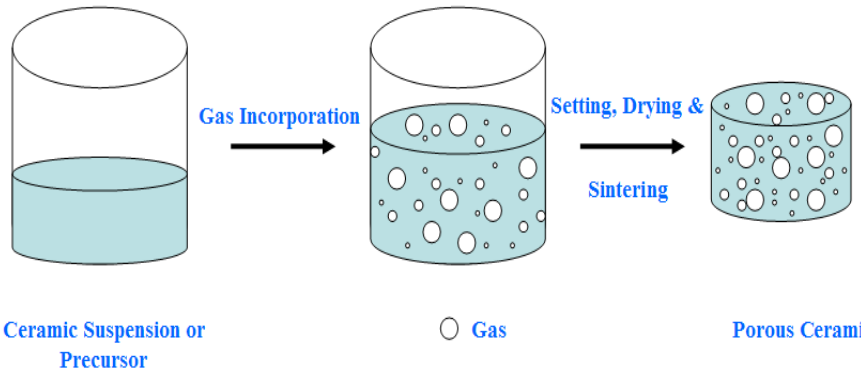

Figure 2.7 Schematic of direct foaming utilized for the fabrication of porous ceramics. (after Studart[1]).

Two different methods are employed for wet foam stabilization. One is using surfactants: amphiphilic molecules with long chains and biomolecules such as lipids and proteins [75-81]. Such materials can adsorb onto the surface of gas bubbles and decrease the interfacial energy

between gas and media, thus retarding coalescence. Figure 2.8 shows several examples produced by this approach. However, because of the low adsorption energy of the surfactant at the gas-liquid interface, the long-term destabilization of foams cannot be achieved by long-chain amphiphilic molecules and biomolecules. Stabilization through long-chain surfactant only lasts several minutes, while the stabilization by proteins can last a few hours. Introducing powders with modified surface chemistry is another effective way to stabilize the gas bubbles in wet foam. In this technique, the wettability of the particles on adsorption of short-chain amphiphilic molecules on the surface is changed, so the attachment of particles at the gas-liquid interface can be improved which can slow down destabilization for several days. Several examples produced by this approach are shown in Figure 2.9.

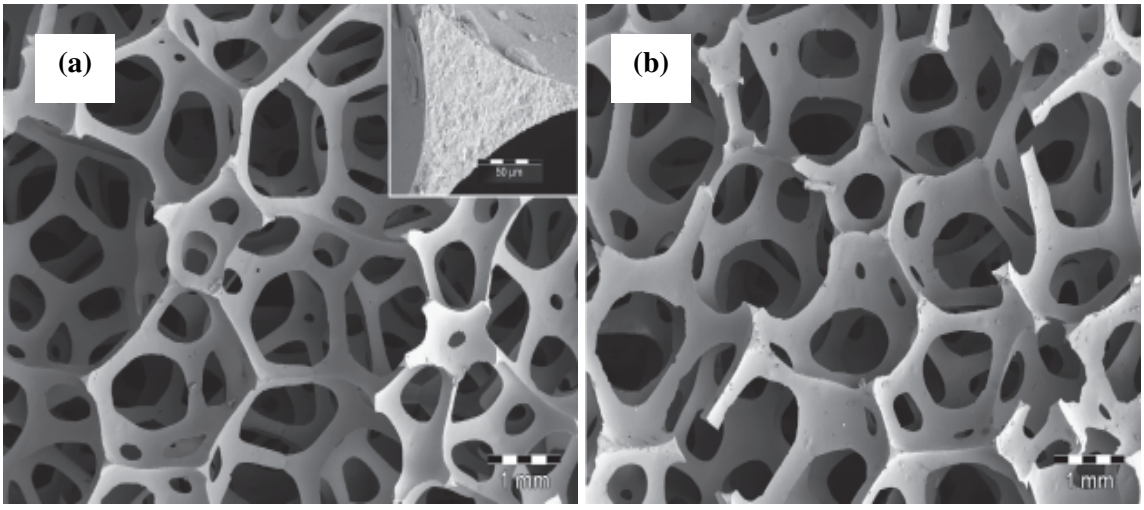

Figure 2.8 Macrostructures of cellular alumina produced from powder suspensions containing 5.5 vol.% heptane with the addition of anionic (a) and cationic (b) long-chain surfactants (Lutensit AS 2230). (after Barg[82]).

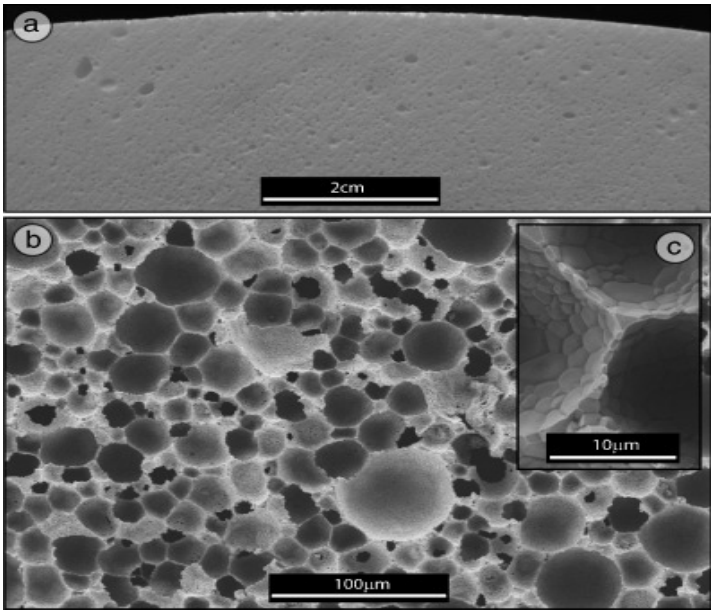

Figure 2.9 Cellular ceramics obtained by particle-stabilized direct foaming, (a) cross section and (b and c) microstructure of foam that was physically gelled before drying. (after Gonzenbach [83]).

The direct foaming technique provides a fast and environmental-friendly way to produce cellular ceramic structures with a wide range of porosity. Due to flaw-free cell struts (Figure 2.9 (c)), the cellular ceramics fabricated by direct foaming show a relatively higher mechanical strength in comparison with the replica method[1]. However, in the absence of a setting system, particle rearrangement within the foam might take place during drying, leading to a shrinkages or cracks. Therefore, unidirectional drying is needed[1].

2.1.4 Paste Extrusion

Paste extrusion is the traditional technique employed to manufacture honeycombs used as catalysts, filters, and so on. In this technique, a paste containing ceramic powders, polymeric or mineral binder additions and lubricating agents is first prepared by high-shear mixing. After mechanical extrusion, the green bodies go though the classic ceramic processing procedures of drying, debinding and sintering to become the final compact. An example of honeycombs fabricated by this method is presented in Figure 2.10.

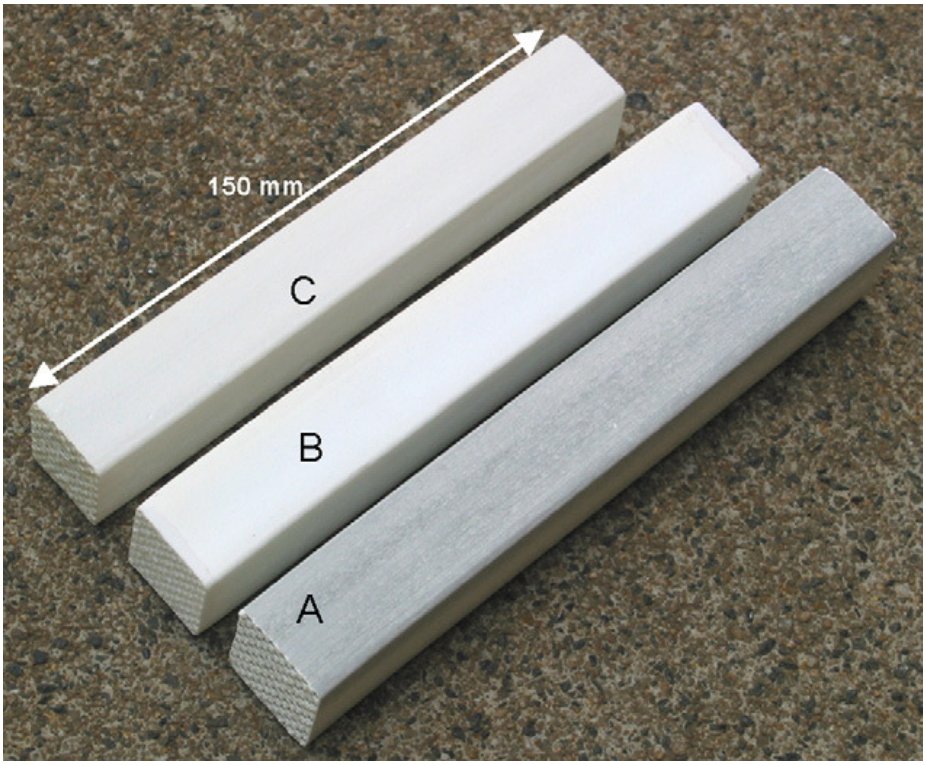

Figure 2.10 Honeycombs: (A) as pressed, (B) material alumina 1600 as fired and (C) material Al_2O_3-ZrO_2-TiO_2 1600 as fired (after Aneziris[84]).

The main advantage of this technique is that the honeycombs can be extruded with well-defined unidirectional channels with many different cross-sectional shapes (square, circular, triangular) for different specific applications. However, the large quantity of polymeric binders and lubricating agents Employed could be a shortcoming for this porous ceramic fabrication method due to environmental concerns.

2.1.5 Rapid Prototyping Technique

The Rapid Prototyping (RP) technique, also called solid free-form fabrication, has recently been developed as one class of the well-established techniques to produce prototypes from complicated three-dimension (3D) datasets in which three-dimensional objects are assembled by point, line or planar addition material. Confining surfaces, such as mould or die walls, are absent. A number of RP techniques are currently commercially available, including Stereolithography (SLA), Selective Laser Sintering (SLS), Laminated Object

Manufacturing (LOM), Fused Deposition Modeling (FDM), Solid Ground Curing (SGC), and Ink Jet printing techniques. Tay[85] has reviewed those techniques recently. All rapid prototyping techniques are based on the same principle of building 3D architectures directly layer by layer[86]. Porous ceramic with cellular and periodic structures can be manufactured by such techniques. An example made by extrusion free forming is shown in Figure 2.11. The processing, controlled by a computer, consists of extruding a continuous filament through a *ca* 50 μm to 1 mm diameter nozzle to build these complicated 3D structures. Compared to other techniques for porous ceramics, a particular advantage of the RP technique is the ability to create more complex shapes and control the character of the pores. However, currently the manufacturing cost is high.

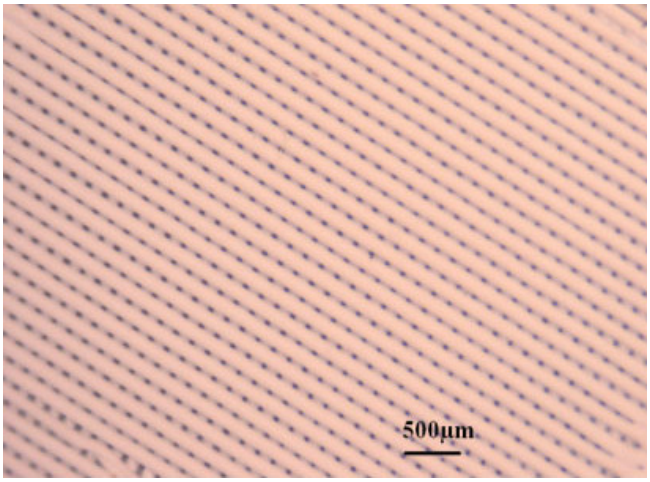

Figure 2.11 Optical micrograph of a hydroxyapatite latticework made by extrusion free forming with 150 μm diameter filaments and 50 μm interstices-unsintered (after Yang [87]).

2.1.6 Summary of Fabrication Techniques for Porous Ceramics

Those fabrication techniques mentioned above are available approaches for the production of porous ceramics. Each technique has its own advantages and drawbacks, so the selection of the processing route should depend primarily on the final application. Those techniques are

quite different in terms of processing features and final architectures, as briefly shown in Table 2.4.

Table 2.4 Summary of characterizations of different techniques

Fabrication Technique	Pore Size	Porosity (%)	Typical Defects
Polymer Replica	200 μm~3 mm	40~90	Voids inside the struts and cracks between the ceramic walls
Wood Replica	10~300 μm	25~95	Pits or pores originated from pyrolysis of residual carbon
Sacrificial Template	1~700 μm	20~90	Time-consuming to burn out the sacrificial phase
Direct Foaming	35 μm~1.2 mm	40~97	Cracks in drying process and directional drying is needed
Paste Extrusion	---	---	Time-consuming to burn out the polymeric binders
Rapid Prototyping	---	up to 97	Manufacturing cost is high

---Lack enough literature data

2.2 Research Progress of Freeze Casting Technique

2.2.1 Historical Perspective of Freeze Casting

In 1954, freeze casting was described as a shaping method for refractories[88]. Until recently, the utilization of ceramics to produce large components has been limited by two major factors: shrinkage and toughness. Shrinkage experienced during the sintering process can be as high as 20%. That can be factored in when fabricating smaller components. However, it is quite difficult to manage on large work pieces especially with complex shapes. And it is known that the low toughness of ceramics prevents the fabrication of large components (difficulties in machining). Under these circumstances, because of its own special advantages, such as using molecular van der Waals forces to hold the green body together during demoulding and drying, freeze casting was developed as a near net shape forming technique to yield dense ceramic parts with complex shapes[89]. However, any ice crystals

formed in the freezing process may lead to porosity and defects in the final product, which is not desired[90]. A lot of effort has been made to control or avoid the formation of ice crystals and it was further discovered that the use of freezing additives such as glycerol, glycols and alcohols in aqueous systems was necessary to achieve high green density and improve particle packing after solidification[91].

It was more recently, however, that researchers realized that the undesired porosity that was first recognized from these freezing processes focused on fabricating dense ceramics, showed pore morphologies that have driven the technology towards the fabrication of porous ceramics which can not be achieved through other routes. Freeze casting could be a potential way to produce porous ceramic with a specific porosity if the formation and growth of ice crystals could be appropriately controlled. Early research work by Fukasawa[92-94] revealed the potential for making porous ceramic utilizing this technique. Since Zhang[95] and Deville[96] published papers sequentially in Nature and Science, respectively, freeze casting, as a novel technique for making porous materials, has attracted a great deal of attention and as a result, many papers involved in this field have appeared in the last three years.

Freeze casting has already shown a promising beginning, and it will herald a bright future for porous ceramics.

2.2.2 Principles of Freeze Casting for Porous Ceramic

Freeze casting involves the preparation of a ceramic suspension (aqueous or nonaqueous), casting and freezing the suspension, followed by sublimating the solvent from solid to gas state under vacuum, and subsequent sintering to consolidate the ceramic walls leading to a porous structure, which is actually a replica of the solvent crystals.

The four basic processing procedures in freeze casting are illustrated schematically in Figure 2.12.

The step of preparing ceramic slurries for freeze casting is very similar to the preparation of slurries for traditional colloidal processes such as slip casting[97]. The ceramic powders should be well dispersed in the liquid solvent; therefore appropriate dispersants are often needed. In order to obtain the desired porosity, the solids loadings of the slurries for freeze casting are usually lower than those used for traditional dense ceramics.

Solidification of the slurry of all freeze casting techniques is the most critical step in the freeze casting process, because the final pore morphology and pore size of the porous ceramic are mainly governed by this stage.

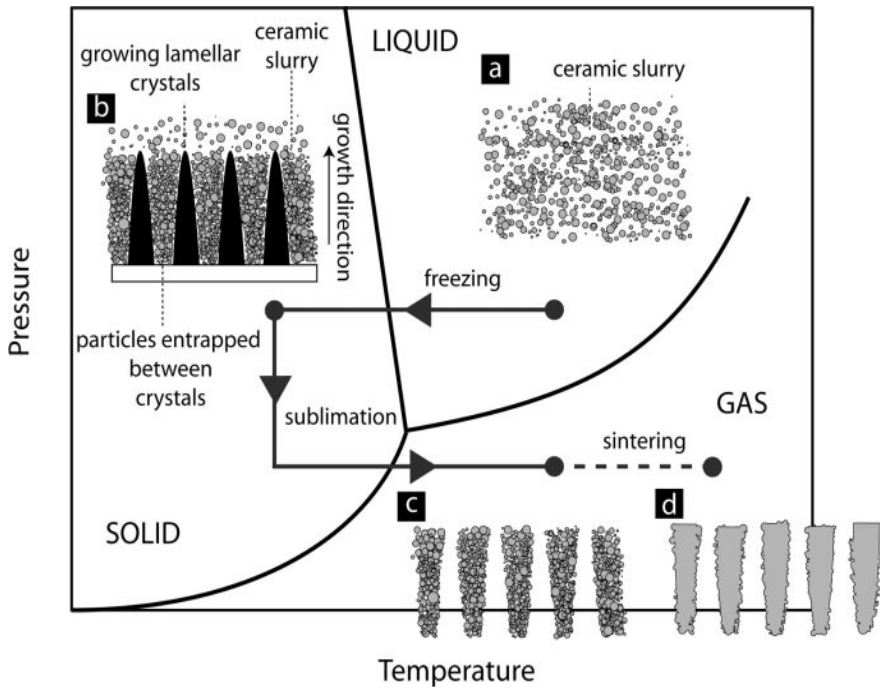

Figure 2.12 Four processing steps of freeze-casting: slurry preparation, solidification, sublimation and sintering (after Deville[97]).

The solidification is mainly based on phase segregation during the physical interaction of the solvent and ceramic particles during the phase transition of the solvent. The solidification conditions are determined by the initial choice of solvent type. Therefore, the physics of ice is the basic theory for the water-based freeze casting technique.

As it is observed in sea ice, pure hexagonal ice platelets with randomly oriented horizontal crystallographic c-axes are formed, and the various impurities originally present in sea water (salt, biological organisms, etc.) are expelled from the forming ice and entrapped within channels between the ice crystals[98].

In the freeze casting technique, during the freezing process, particles in the slurry are ejected from the advancing solidification front and concentrated between the growing solvent crystals. The detailed principle for this technique using water as a vehicle is illustrated schematically in Figure 2.13.

While the ceramic slurry is freezing, the growing ice crystals expel the ceramic particles, creating a lamellar microstructure oriented in a direction parallel to the movement of the freezing front. For highly concentrated slurries, the interaction between particles becomes critical: a small fraction of particles are entrapped within the ice crystals by tip-splitting and subsequent healing, leading to the formation of inorganic arms between adjacent walls. A great number of materials have already been prepared using the freeze casting method, which suggests that the principle of this technique are not strongly dependent on the types of materials, but relies more on physical rather than chemical interactions[97].

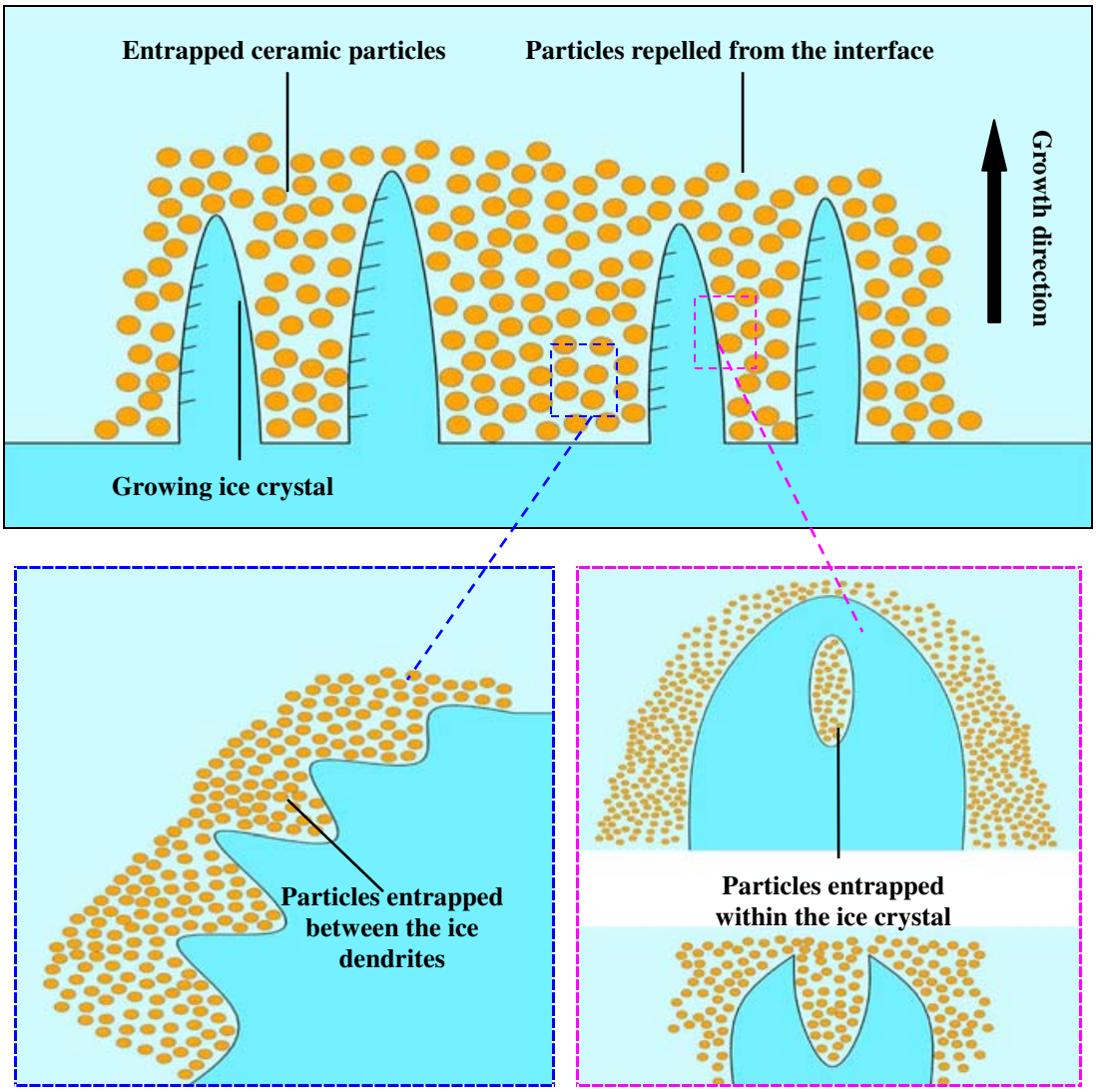

Figure 2.13 Schematic diagram of the basic principle for freeze casting (after Deville[96])

After solidification, the solvent crystal needs to be sublimated at low temperature and reduced pressure. The sublimation conditions are normally determined by the type of the initial solvent. For example, sublimation of water-based freeze casting is below zero. The solidified solvent will convert from solid state into gas state under appropriate conditions. The sublimation of the solvent leaves pores matching the shape and size of the original solvent crystals.

With small amounts of organic binders in the green body, burnout and sintering is not usually a problem, and traditional sintering techniques can be used. After sintering, the ceramic walls

will possess a dense microstructure, but the porosity created by the solvent crystals will be retained.

2.2.3 Current Research Progress

2.2.3.1 Solvent System in Freeze Casting

As outlined in the basic principle described above, the final porosity of the sintered ceramic is a negative replica of the initial solvent crystals. Therefore, the final morphology of the pores is mainly determined by the type of solvent used. Water and camphene are the two most frequently used solvents in the freeze casting technique. In the case of water utilized as a solvent, the microstructure of the final porous ceramics is always lamellar[102]. By analysing the basic crystallography (Figure 2.14 (a)) of ice and its crystal growth behaviour (Figure 2.14 (b), the special microstructure can be readily understood.

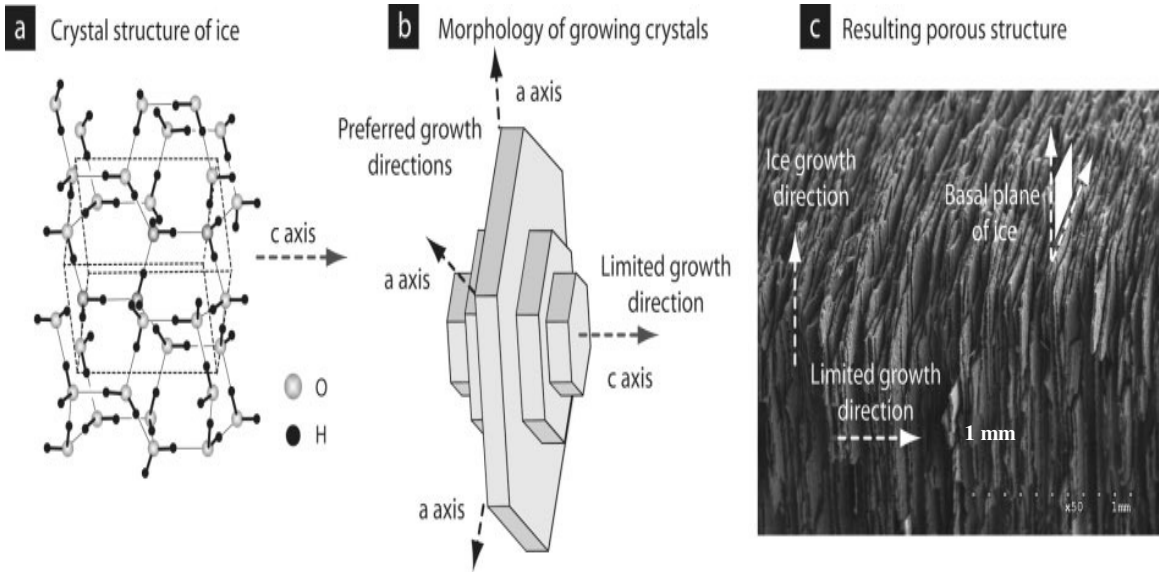

Figure 2.14 Water used as a solvent (a) ice crystal structure, (b) anisotropy of ice crystal growth, (c) porous structure obtained after sublimation and sintering. (after Deville[97]).

Because of the anisotropy of the ice crystal structure, the ice crystal grows quickly along the direction perpendicular to the *c* axis, while, it grows very slowly along the *c* axis and the

thickness of the ice crystal remains small[97]. This results in the lamellar ice crystals, and finally in lamellar ceramic structures (Figure 2.14 (c)).

In the case of camphene used as a solvent, a similar explanation can be introduced. The solidification process of liquid camphene is shown in Figure 2.15 (a). It shows very clearly defined dendrites, which of course will be reflected in the final microstructure of the porous ceramic (Figure 2.15 (b)).

In summary, different solvents will lead to different microstructures.

In this research work, we will only focus on water based systems, because aqueous media is desirable nowadays due to economic and environmental considerations; moreover, water based system can lead to lamellar microstructure, witch is useful for the fabrication of 2-2 ceramic-epoxy composite.

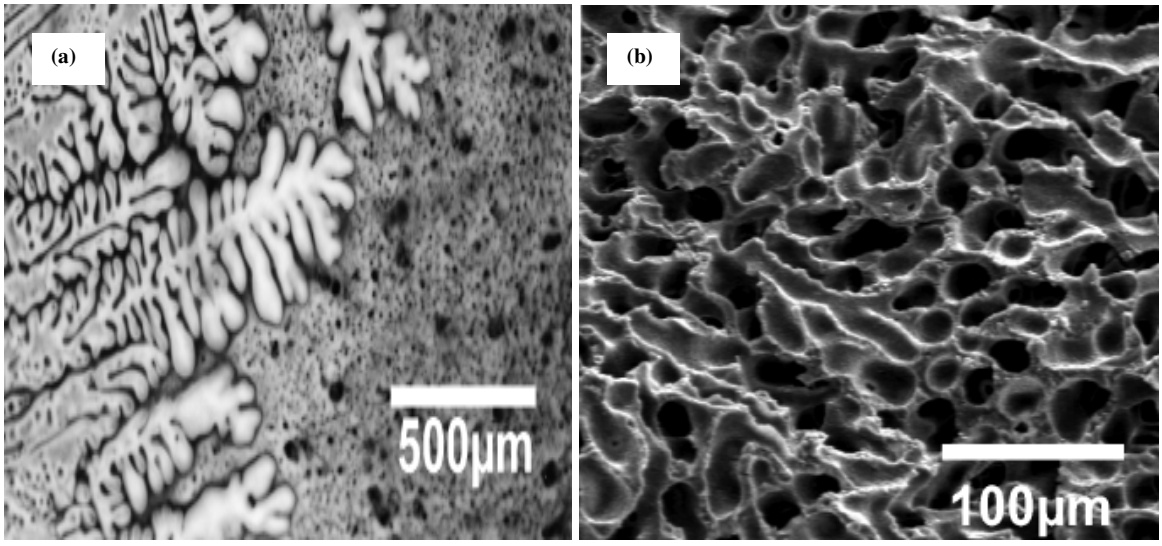

Figure 2.15 Camphene used as a solvent (a) solidified camphene dentrides, (b) porous alumina using camphene as a solvent (after Araki[99]).

2.2.3.2 Advantages of Porous Ceramic by Freeze Casting

As mentioned in Section 2.1.2, freeze casting is actually one kind of sacrificial phase technique using solvent (water or camphene) as a sacrificial material. Freeze casting has

recently attracted much attention as being a cost effective and environmental friendly process, because the solvent can temporarily act as binder to keep the part together for demoulding, which can minimize the additive concentration for enhanced solid purity and faster binder burnout cycles compared with other polymeric-based sacrificial template methods and the replica technique. Moreover, removal of the solvent by sublimation can also eliminate drying stresses and shrinkage which may lead to cracks during normal drying of the solvent-saturated body[89]. The most important benefit is that porous ceramics fabricated by freeze casting demonstrate better mechanical properties compared with those obtained from other methods, and one example concerning porous hydroxyapatite (HA) is shown in Figure 2.16.

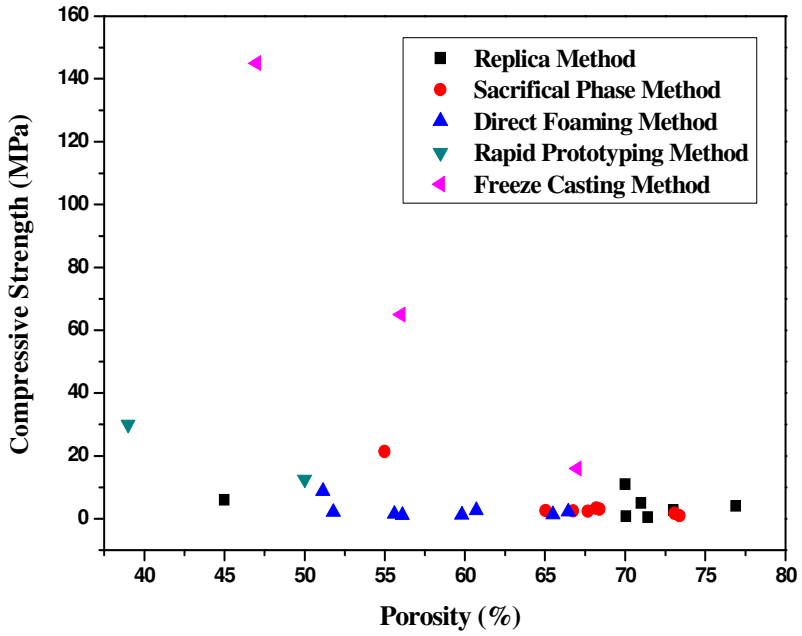

Figure 2.16 Comparison of compressive strength for porous hydroxyapatite obtained by different techniques according to literature data[100, 149-152].

2.2.3.3 Ceramics Materials and Current Problem in Freeze Casting

Up to now, a large variety of ceramic materials have already been investigated using freeze casting, including alumina, zirconia, hydroxyapatite, silicon nitride, and NiO-yttria-stabilized zirconia (YSZ). Detailed information of materials used in the freeze casting, freeze conditions and pore sizes of the final porous ceramics are displayed in Table 2.5 and 2.6.

In the investigations of water-based freeze casting, the particle size of the ceramic powders used varies from about 60 nm to 6.5 μm. Many different freezing conditions and moulds are employed. The pore size of the final porous ceramics varies in a wide range from 0.5 μm to 200 μm. In the investigations of camphene-based freeze casting, the freeze condition is often from 60 ºC (higher than the melting point of camphene, 45 ºC). The pore size of the final porous ceramic varies in a relatively narrow range compared with water-based system.

As mentioned above, reports of many research investigations have appeared in the last three years. Great developments have been made using the freeze casting technique, porous HA, alumina and zirconia exhibiting high porosity and high compressive strength[100,133,142], but those investigations are mainly focused on the fabrication of the porous ceramics and the evaluation of the mechanical properties. The understanding of the relationships between the rheological properties of the initial suspension and the final characteristic of the porous structures, and corresponding mechanisms in freezing process, is lacking and still at an early stage, so further investigation involving those aspects is urgently required.

Table 2.5 Summary of ceramic materials, experimental conditions and morphology in water-based freeze casting

Materials	Particle Size	Freezing Condition & Mould	Directional or Not	Pore Size	Sintering Temperature	Reference
Alumina		-20~-80 ℃	Yes	40μm	1400~1600 ℃	Fukasawa, 2001[94]
Alumina		-50 ℃	Yes	30μm	1400-1550 ℃	Fukasawa, 2001[92]
Alumina	300 nm	-20 ℃		2~200 μm	1500 ℃	Nakata, 2005[100]
Alumina	400 nm	RT~-100 ℃	Yes	2~200 μm	1500 ℃	Deville, 2007[102]
Alumina	400 nm	Rubber Mould	Yes	16~55 μm	1400 ℃	Pekor, 2008[103]
Alumina	2.5 μm	-10~-30 ℃			1550 ℃	Roy, 2008[104]
Alumina	200 nm	Gradient Temperatue	Yes			Deville, 2009[105]
Alumina	400 nm	Gradient Temperatue, PE mould	Yes	15~103μm	1550 ℃	Han, 2009[106]
Alumina	400 nm	Gradient Temperatue, PE mould	Yes		1500 ℃	Zhang 2009[107]
Alumina	350 nm	-20 ℃	Yes	10~100 μm	1200 ℃	Tallón 2009[108]
Alumina	1μm	Gradient Temperature, Glass Mould	Yes			Waschkies 2009[109]
Si_3N_4	550 nm	-25 and -80 ℃	Yes	50 μm	1700~1850 ℃	Fukasawa,2002[110]
Si_3N_4	550 nm	-50 and -80 ℃	Yes	30 μm	1700~1850 ℃	Fukasawa,2002[111]
SiC	16 μm	-40 ℃	Yes	~300 μm		Tang 2005[112]
Clay		-70 ℃	Yes	~20 μm	800 ℃	Hwang 2006[113]
Clay	5 μm	-35 ℃				McKee 2009[114]
TiO_2	150 nm	-18 ℃	Yes	~15 μm	1000 ℃	Ren 2007[115]
TiO_2	100~200 nm	-18 ℃	Yes	0.5~2.64μm	1000 ℃	Ren 2009[116]
NiO-YSZ		-30 ℃	Yes	10 μm	1400 ℃	Moon, 2003[117]
YSZ		-40 ℃	Yes	15~30 μm		Bettge 2005[118]
YSZ	550 nm	-10~60 ℃	Yes	<100 μm	1400 ℃	Sofie 2007[119]
YSZ	60 nm	-18 ℃, Silicon Mould	Yes	1~80μm	1300~1400 ℃	Zuo 2008[120]
Glass	6.5 μm	-55 ℃	Yes	100~150 μm	620 ℃	Deng2007[121]
HA	2 μm	RT~	Yes	15~40 μm	1250~1350 ℃	Deville 2006[100]
HA	2 μm	-19 ℃, Ice Mould	No	20~100 μm	1350 ℃	Moritz 2007[122]
HA	<500 nm	-20 ℃, PVC Mould	Yes	5~110 μm	1350 ℃	Rahaman 2008[123]
HA	150 μm	-10 ℃, Plastic Mould			1300 ℃	Landi 2008[124]
HA	<1 μm	-20~-196 ℃, PVC Mould	Yes	5~110 μm	1250~1375 ℃	Fu 2008[125]
HA	<500 nm	-20~-196 ℃, PV C Mould	Yes	5~60 μm	1250~1375 ℃	Fu, 2008[126]
HA	600 nm	-18 ℃, Silicon Rubber Mould	Yes		1300 ℃	Zhang, 2009[127]

$BaTiO_3$		-60 ºC, 5 ºC/min, Teflon Mould	Yes	1300 ºC	Gorzkowski, 2009[128]
CPC		-30 ºC, Glass Mould			Qi, 2009[129]
Bilglass	3 μm			1100 ºC	Mallick, 2009[130]

Table 2.6 Summary of ceramic materials, experimental conditions and morphology in camphene-based freeze casting

Materials	Particle Size	Freezing Condition & Mould	Directional or Not	Pore Size	Sintering Temperature	Reference
Alumina	400 nm	From 60 ºC to RT,		<10μm	1600 ºC	Arakie, 2004[131]
Alumina	400 nm	From 55ºC to RT, Mould Partly in Freezing Bath.	Yes	5~20 μm	1600 ºC	Araki, 2005[132]
Alumina	300 nm	From 60 ºC to 20 ºC	No	5~40 μm	1400 ºC	Koh, 2006[133]
Alumina	300 nm	PE Mould	Yes	> 100μm	1600 ºC	Yoon, 2008[134]
PZT-PZN		From 60 ºC	No	10~50μm	1200 ºC	Lee, 2007[135]
PZT-PZN		To RT	No		1200	Lee, 2008[136]
Ni-YSZ	300 nm	From 60 ºC to 20 ºC	No	30μm	1100~1600 ºC	Koh, 2007[137]
8YSZ		From 60 ºC to RT	Yes		1400 ºC	Koh, 2006[138]
8YSZ	300nm	From 55 ºC	Yes	2~25μm	1400 ºC	Sofie, 2007[139]
YSZ	400 nm	To 5 ºC, PE Mould			1500	Hong, 2010[140]
YSZ	400 nm	PE Mould			1400~1550 ºC	Han, 2010[141]
YSZ	800 nm	To 35 ºC PE Mould			1450	Hong, 2010[142]
SiC	300 nm Precursor	From 20 ºC to -40 ºC, PE Mould,	Yes	2~30μm	1400 ºC	Yoon, 2007[143]
Bioglass		From 60 ºC	No	20~40μm	700~1100 ºC	Song, 2006[144]
HA		From 60 ºC, PE Mould,	No	20~40μm	1250 ºC	Lee, 2007[145]
HA		From 60 ºC, PE Mould,	No	80~220μm	1250 ºC	Yoon, 2007[146]
HA		From 35 ºC, PE Mould			1250 ºC	Yoon, 2008[147]
HA	6 μm	To RT			1280 ºC	Macchetta, 2009[148]

2.3 Colloidal Processing and Theoretical Background

Ceramics have been processed through colloidal routes for several thousand years[153]. Most of the traditional forming techniques available today such as slip casing, extrusion, and filter pressing, originated in the 17th century. It was not until recently that colloidal forming techniques for ceramics have emerged as a scientific field of research and attracted a lot of interest from scientists and engineers for the shaping of defect-free ceramic components.

As mentioned in Section 2.1, many of the fabrication techniques used for porous ceramics start from ceramic colloidal suspensions. Generally, a well-dispersed and stable ceramic suspension is always required in these fabrication techniques.

The term "colloid" is utilized to represent particles which possess at least one dimension in the size range of 10^{-3}~1μm. Colloidal processing routes for the preparation of ceramic components usually consist of five basic procedures[153]: (1) powder synthesis, (2) suspension preparation, (3) consolidation into the desired component shape, (4) removal of the solvent phase, and (5) densification.

A colloidal route can provide a potential way to reliably prepare ceramics through both the accurate control of "structure" of the initial colloidal suspension and its evolution in fabrication[153]. Therefore, there is a continual driving force to have a good understanding of desired stability and phase distribution in colloidal systems.

Generally, a distinct characterization of all colloidal systems is that the contact area between particles and the dispersing medium is quite large. Consequently, the suspension behaviour or the "structure" of the suspension is strongly affected by interparticle (or surface) forces[153].

2.3.1 The Electrical Double Layer

Most substances will obtain surface electrical charge when put in contact with a polar medium (e.g. water). It is now well understood that the development of electrical charge on colloids dispersed in water is due to[159]: (1) surface group ionisation (dominated by the pH of the dispersed medium); (2) differential solubility of ions; (3) isomorphous replacement/lattice substitution. As a result, the distribution of nearby ions in the medium will be affected by this surface electrical charge.

The ions, which already have established surface charges, are termed potential determining ions. These ions include the ions of which the solid is composed, hydrogen and hydoxyl ions, and ions capable of forming complicated or insoluble salts with the solid surface species. Ions with opposite charge are attracted and ions with like charge are repelled away from the surface. Finally, at the interface, one layer, the surface charge (either positive or negative), comprises ions adsorbed directly onto the object, and the other layer, loosely associated with the object, is composed of ions attracted to the surface charge. This leads to the so-called electrical double layer.

The theoretical and practical aspects of the electrical double layer have been recognised and thoroughly understood in the literature. The idea of the electrical double layer was firstly proposed by Helmholtz[155]. A widely accepted model for electrical double layer was developed by Stern[156] and later modified by Graham[157]. A typical schematic is displayed in Figure 2.17.

The part of the counter-ion charge is located close to the particle surface (Stern layer) and the remainder is distributed more broadly in the diffuse double layer. The Stern layer is actually a hypothetical plane representing the closest distance of approach of hydrated counter ions to

the surface. A schematic diagram of the distribution of charge species and the potential drop across the double layer in accordance with the Stern model is also shown in Figure 2.17.

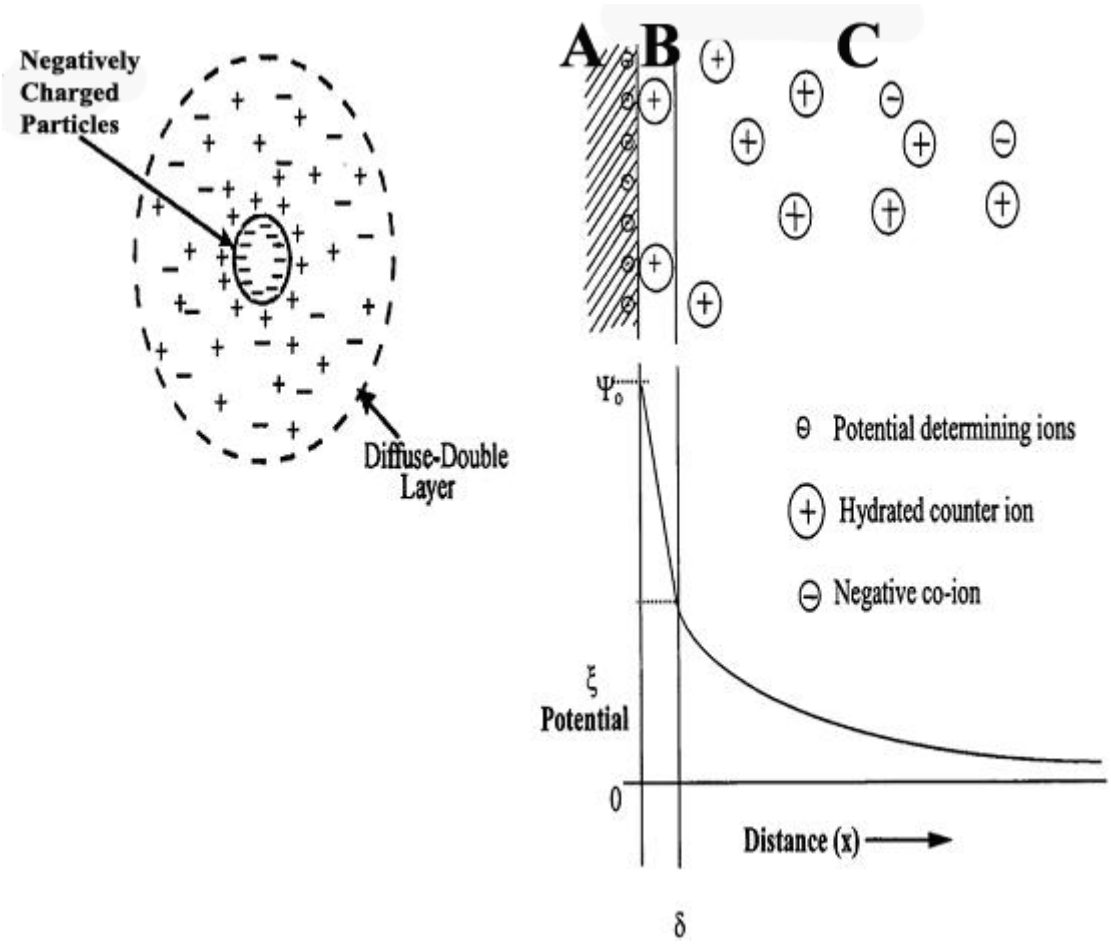

Figure 2.17 Schematic illustration of the double layer and potential drop across the double layer (A) Surface charge, (B) Stern layer, (C) diffuse layers of counter-ions.(after Weise[158,159]).

The interaction between charged particles is controlled predominantly by the overlap of the diffused layer, and accordingly the potential most relevant to the interaction is the one developed at the boundary between the Stern and diffuse layer rather than the potential at the particle surface[159]. This potential difference between the Stern plane and the diffuse layer is named the zeta potential (ζ). Zeta potential is of great importance because it reflects the variation in surface potential for a specific substance in a polar medium and the adsorption

of ions into the inner part of the double layer. Many factors can affect the zeta potential value, the most important of which is the pH value of the medium. The point where zeta potential becomes zero is named the isoelectric point (pH_{iep}), as shown schematically in Figure 2.18. Colloidal suspension systems are normally stable when the zeta potential (absolute value) is large; therefore, it is necessary to adjust the pH value sufficiently away from the pH_{iep} in order to generate a stable colloidal system. The areas besides brace brackets show the stable areas, as shown in Figure 2.18.

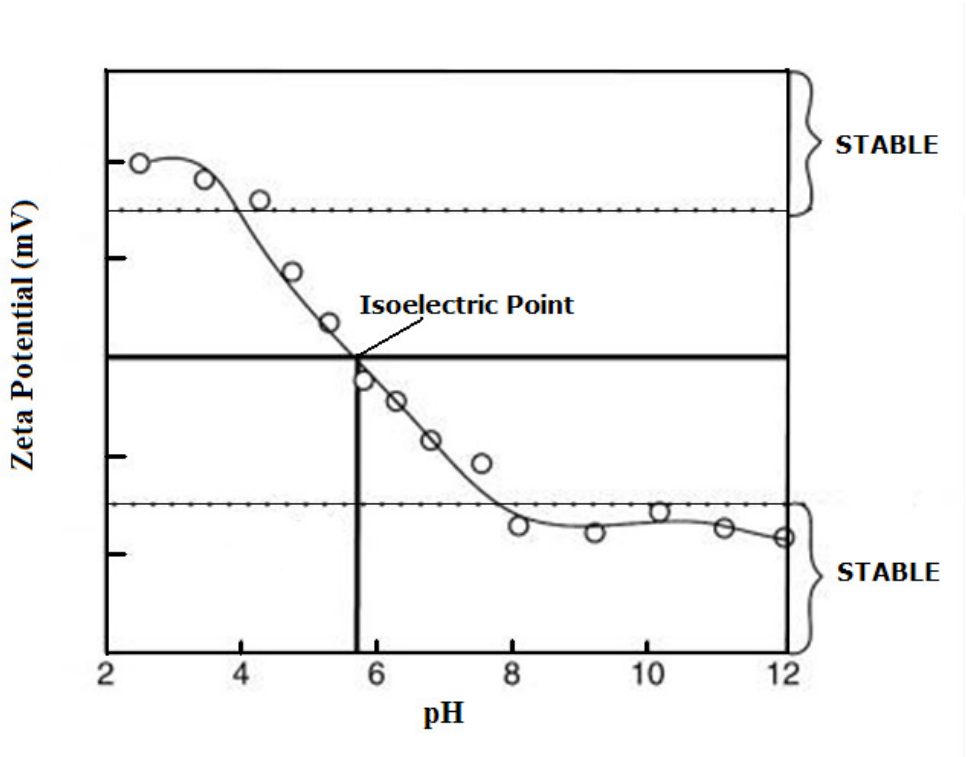

Figure 2.18 Schematic illustration of isoelectric point

2.3.2 Interparticle Forces

Ceramic colloidal suspensions can be produced with various states such as dispersed, weakly flocculated, or strongly flocculated by control of the interparticle forces. The stability of a colloidal system is dominated by the total interparticle potential energy, V_{total}, which can be expressed as[153]:

$$V_{total} = V_{vdW} + V_{elect} + V_{steric} + V_{structural} \quad (2\text{-}1)$$

where V_{vdW} is the attractive potential energy due to long range van der Waals interactions between particles, V_{elect} is the repulsive potential energy resulting from electrostatic interactions between like-charged particles surfaces, V_{steric} is the repulsive potential energy resulting from steric interactions between particles surfaces coated with adsorbed polymeric species, and $V_{structural}$ is the potential energy resulting from the presence of non-adsorbed species in solution that may either increase or decrease suspension stability.

A quantitative estimate of the relationship between the stability of a suspension in terms of interparticle forces and the energies of interactions that exist between colloidal particles and other surfaces in a liquid medium has been represented by the well-known DLVO theory established by Derjaguin and Landau[160] and Verwey and Overbeek[161].

In the DLVO theory, the colloidal stability is dependent on the perikinetic phenomenon i.e., the liquid is assumed to be stationary and collisions occur due to Brownian translational motion. It assumes that the effect of two forces is additive by combining the effect of electrostatic repulsion and van der Waals attraction between two particles[159]. This theory is based on the simple addition of colloidal dispersion and electrostatic interactions, and describes the van der Waals attractive energy of two particles as a function of the distance. The total interaction energy is calculated by superposing a corresponding term for the repulsive coulombic energy of equally-charged particles, as shown schematically in Figure 2.19.

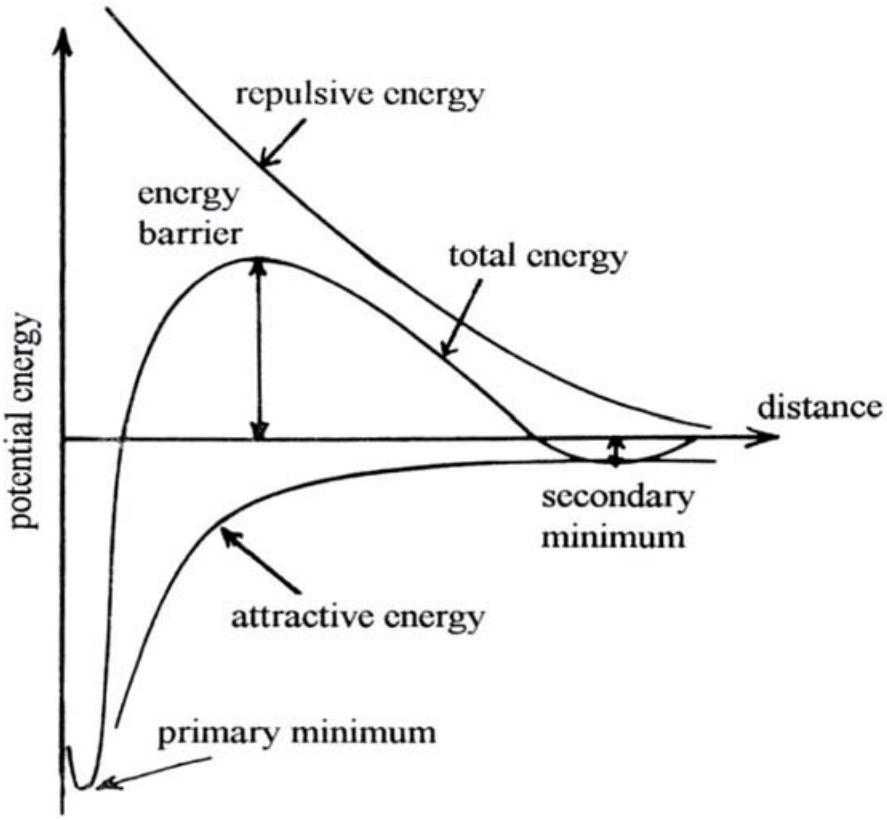

Figure 2.19 Potential energy curve for two charged particles as consequence of superposition of attractive and repulsive forces. (after Tadros[162]).

2.3.2.1 Van der Waals Forces

Long-range forces generated from van der Waals interactions are ubiquitous and usually attractive between like particles. The V_{vdW} shows a power-law distance dependence whose strength is dependent on the dielectric properties of the interacting colloidal particles and intervening medium[148]. If the particles are spherical and of equal size, the V_{vdW} can be expressed by the Hamaker expression, as shown in equation 2-2:

$$V_{\mathrm{vdw}} = -\frac{A}{6}\left(\frac{2}{S^2-4}+\frac{2}{S^2}+\ln\frac{S^2-4}{S^2}\right) \qquad (2\text{-}2)$$

where *s* is

$$s = \frac{2a+h}{a} \qquad (2\text{-}3)$$

and where h is the minimum separation between the particle surfaces, a the particle radius, and A the Hamaker constant[153,154].

In order to obtain a proper degree of colloidal stability, the long-range attractive van der Waals forces must be mitigated during colloidal processing, which must rely on some type of interparticle repulsion. Usually, electrostatic, steric and depletion forces are incorporated to surmount the attractions caused by van der Waals forces to achieve the desired stability.

2.3.2.2 Electrostatic Forces

The stability of an aqueous colloidal system can be governed by generating like-charges of sufficient magnitude on the surfaces of suspended ceramic particles. The resulting repulsive V_{elect} shows an exponential distance dependence whose strength depends on the surface potential induced on the interacting colloidal particles and the dielectric properties of the intervening medium[153].

Because the exact analytical expressions for the electrostatic forces in the system cannot be properly and easily given, numerical solution or analytical approximations are generally used instead.

According to DLVO theory, dispersions can be rendered unstable by either changing ionic strength or modifying pH toward pH_{iep}. For multicomponent ceramic systems, it may be desirable to work in a pH range where opposite charges are induced on different colloidal phases. This method, termed heteroflocculation, prevents unwanted phase segregation from occurring during processing. Electrostatically stabilized colloidal systems are kinetically stable systems.

2.3.2.3 Steric Forces

Steric stabilization offers an alternate way to govern the stability of colloidal systems which can be utilized in both aqueous and nonaqueous colloidal systems. In this method, organic molecules are introduced to generate steric repulsion. In order to work effectively, the organic molecules must be strongly anchored to avoid desorption during particle collisions, and the adsorbed layers should be of sufficient thickness and density to surmount the van der Waals forces between particles and to impede bridging flocculation.

The conformation of the adsorbed layer can be influenced by many factors including molecular structure, solvent quality, quantity of anchoring groups, active surface site density, and colloidal and organic concentration in solution[160]. Some typical conformations of absorbed layers on ideal ceramic surfaces are illustrated schematically in Figure 2.20 for various structures, including homopolymers, dibock copolymers, comblike copolymers, and functionalized short-chain dispersants.

2.3.2.4 Electrosteric Forces

Electrosteric stabilization is the most widely used approach to achieve a stable dispersed colloidal system[164]. Polyelectrolyte species are the most common additives utilized in this approach, because they can impart both electrostatic and steric stabilization to a colloidal suspension simultaneously, which is then referred to as electrosterically stabilized[153]. Usually at least one kind of ionisable group (e.g. sulfonic acid or carboxylic groups) is in the polyelectrolyte. The molecular structures of the ionisable group can change from homopolymers, such as poly(acrylic acid), to block copolymers with one or more ionisable segments. Both the chemical and physical properties of the solid surfaces and solvent medium can markedly affect the adsorption of polyelectrolytes[165].

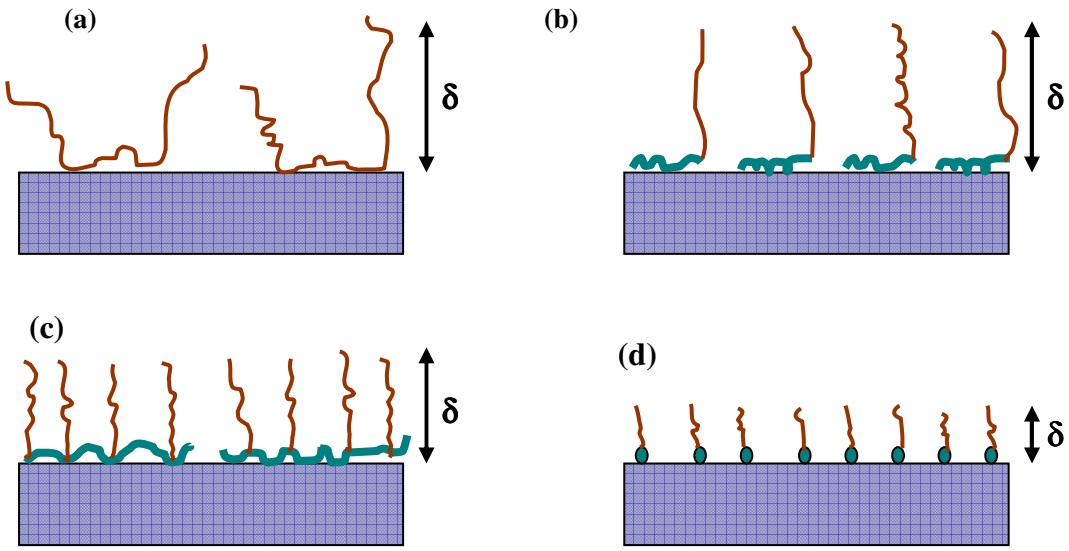

Figure 2.20 Schematic illustrations of molecular structures and adlayer conformation on an ideal ceramic surface: (a) Homopolymer, consisting of tails, loops, and train configuration; (b) Diblock copolymer, consisting of short anchor block and extended chain block; (c) Comblike copolymer, consisting of extended segments attached to anchored backbone; and (d) Functional, short-chain dispersant, consisting of anchoring head group and extended tail. (δ is the adlayer thickness). (after Lewis[153]).

Opposite charges on the particle surfaces and polyelectrolyte species can strongly favour adsorption[166]. At low adsorbed concentrations, the polyelectrolyte can favour flocculation either through surface charge neutralization or bridging mechanisms. At higher adsorbed concentrations, the long-range repulsive forces from the electrosteric interactions are very useful in increasing the colloid stability[167]. In some colloidal systems, the adsorption behaviour and conformation of polyelectrolytes can be modified through altering the solvent conditions (e.g., pH and ionic strength). For anionic polyelectrolytes, the level of ionization increases with increasing pH. At low pH, such species adopt a compact coil configuration with a dense layer of large mass and low adlayer thickness, which is illustrated schematically in Figure 2.21[153]. At high pH, anionic polyelectrolytes form an open coil configuration due to inter-segment repulsion[163]. However, at high ionic strength, screening effects can weaken inter-segment repulsion, leading to the variation of the adlayer architectures[166,167].

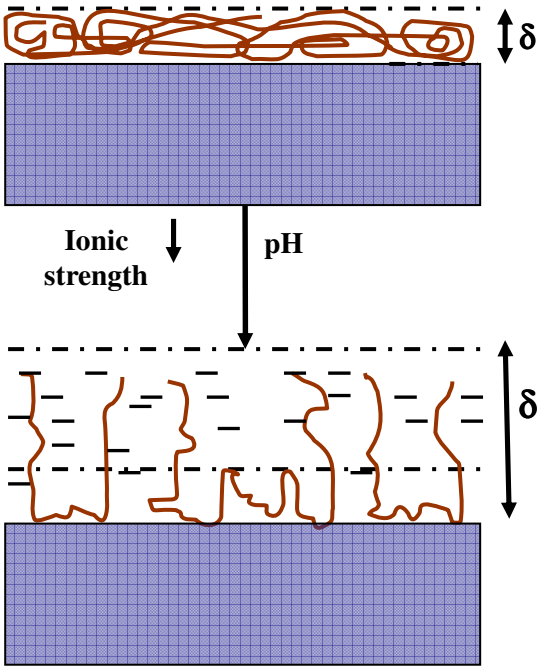

Figure 2.21 Schematic illustration of adsorbed anionic polyelectrolyte species on an ideal ceramic surface as a function of pH and ionic strength (δ is the adlayer thickness). (after Lewis[153]).

2.3.2.5 Depletion Forces

Depletion forces appear between large colloidal particles which are suspended in a suspension of non-adsorbing smaller species (e.g., polyelectrolytes, polymers, or fine colloidal particles). Such species, named as depletants, may cause flocculation or improve stabilization of primary colloidal particles. Depletion means the existence of a negative depletant concentration gradient close to primary particle surfaces. The concentration of rigid depletant species decreases at bare particle surfaces and increases to its bulk solution value at some distance away from these surfaces[153]. This distance, known as the depletion layer thickness, is of the order of the depletant diameter. Recent experimental and theoretical evidence has revealed that the depletion force has the same origin and form as structural

forces[153]. Despite their low concentration in suspension relative to solvent species, depletant influences on suspension stability can be rather dramatic[153].

2.3.3 Rheological Behaviour of Colloidal Suspension

One of the most important properties of colloidal suspensions is the rheological behaviour which describes the variation in flow behaviour in response to an applied stress or strain. Therefore, the degree of suspension structure and stabilization can be inferred from the observed behaviour[153]. The apparent viscosity (η), the yield stress under shear (τ_y) and compression (P_y), and the viscoelastic properties (shear modulus, denoted by G, is defined as the ratio of shear stress to the shear strain, i.e., the loss (G'') and elastic (G') moduli) are the critical parameters of rheological measurements. For the specific forming technique, those parameters should be modified appropriately.

The apparent viscosity (η) is related to the applied shear stress (τ) and shear rate (γ) by the following equation:

$$\tau = \eta \times \gamma \qquad (2\text{-}4)$$

Diverse kinds of flow behaviour can be obtained under steady shear based on the suspension composition and stability, as presented in Figure 2.22. Newtonian behaviour is the simplest flow response, where the viscosity is independent of shear rate (curve (a) in Figure 2.22).

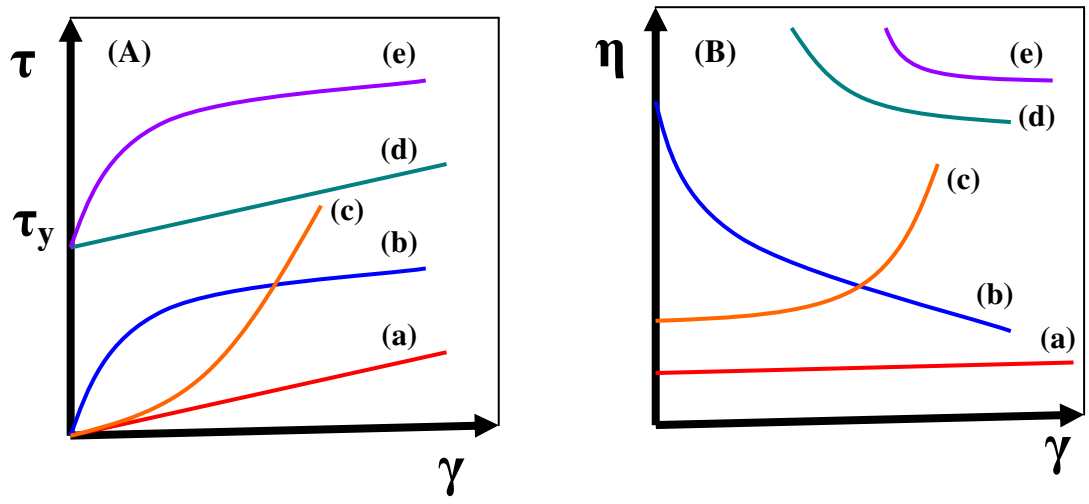

Figure 2.22 Schematic diagram of rheological behaviour of colloidal suspensions under shear stress-shear rate mode (A) and viscosity-shear rate mode (B): (a) Newtonian flow; (b) shear thinning; (c) shear thickening; (d) Bingham plastic; and (e) pseudoplastic with a yield stress. (after Lewis[153]).

Pseudoplastic or shear-thinning behavior happen when the viscosity decreases with the increasing shear rate (curve (b) in Figure 2.22), showing a minimal resistance to the breakdown of primary structures and aligning particles in the colloidal system. Such a response can be accompanied by a yield stress whose magnitude is dependent on the strength of the particle network (curves (d) and (e) in Figure 2.22). If the flow curve is linear above τ_y, the system is referred to as Bingham plastic (curve (d) in Figure 2.22). When the viscosity increases with increasing shear rate, dilatant or shear-thickening occurs (see curve (c)).

In summary, the colloidal processing of ceramics and some basic theories have been introduced briefly in the above section. As described, one must tailor interparticle forces, suspension rheology, etc. to achieve the optimal suspension for a given application.

2.4 Properties and Applications of Ceramic Materials

Because of the broad nature throughout this work, different kinds of commercial ceramic powders were utilized. Alumina (Al_2O_3) and alumina-zirconia (Al_2O_3-ZrO_2) are utilized as

model materials to investigate the factors involved in freeze casting. Barium titanate ($BaTiO_3$) and Lead Zirconate Titanate (PZT) are utilized to demonstrate the versatility of the freeze casting technique. Therefore, there is a need to introduce the basic properties and applications of these materials, which are briefly summarized as below.

2.4.1 Alumina

Alumina is a widespread component of siliceous minerals. It often occurs as single crystal in the form of sapphire and ruby and in large deposits as the hydrated oxide bauxite ($Al_2O_3 \cdot H_2O$) [168].

The Bayer process is the main technique used for the industrial production of α-alumina. Bauxite, naturally contaminated with other oxides, is used as a starting material in the Bayer process[169]. This involves raw material preparation, digestion, clarification, precipitation and calcination. Practically all the powder for the fabrication of alumina ceramics is prepared using this technique. A purer alumina product can be made by preparing ammonium alum ($NH_4Al(SO_4)_2) \cdot 12H_2O$).

Among the aluminium oxide, α-alumina is thermally the most stable phase. For example, γ-alumina will convert to α-alumina above 1000 ºC. α-alumina has a hexagonal structure and two alumina molecules per unit, as shown schematically in Figure 2.23. Three oxygens form an equilateral triangle with aluminiums above and below the centre of the triangle. One of these groups is placed at each corner of a cube while another is placed at the centre of the cube.

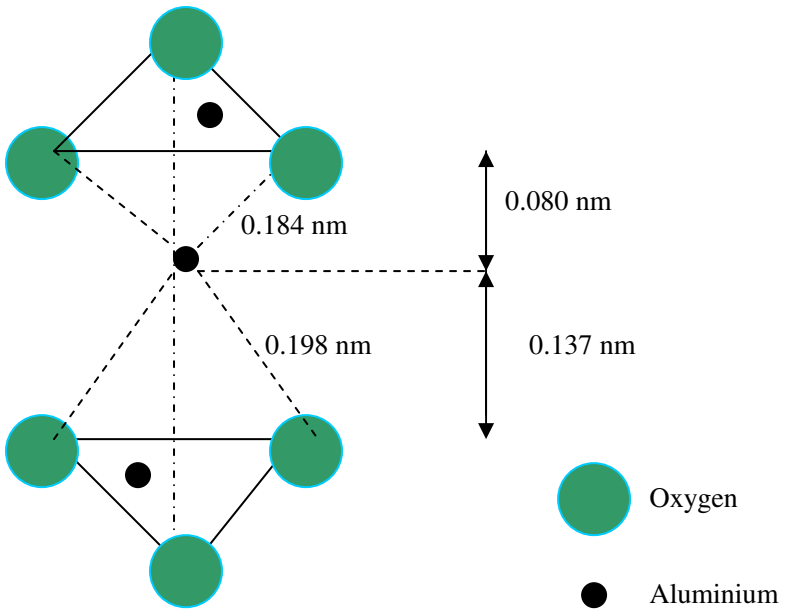

Figure 2.23 Schematic illustration of oxygen arrangement around Al^{3+} ion in alumina. (after McColm[168])

Alumina ceramic is one of the most widely studied and used advanced ceramic materials. Some selected properties of α-alumina are shown in Table 2.7. (The purity of listed α-alumina is at least 99.5% and the density is at least 98% of the theoretical density. The nominal grain size is normally 5 μm.)

Table 2.7 Some properties of sintered α–alumina[170]

Property	Temperature ºC					
	20	500	1000	1200	1400	1500
Bulk density (g/cm^3)	3.984	3.943	3.891	3.868	3.845	3.834
Compressive strength (GPa)	3.0	1.6	0.7	0.4	0.3	0.28
Flexural strength (MPa)	380	375	345	300	210	130

The relative abundance and low cost of the materials resource is an additional benefit for commercial application. Alumina ceramics share with other advanced ceramics the

characteristics of high-temperature stability and the retention of strength at high temperatures. Alumina ceramics can be utilized wherever exceptionally good dielectric properties, high mechanical strength, and high thermal conductivity are needed, such as for microwave windows, cutting tools, and spark plug insulation. Moreover, high-density, high-purity (>99.5%) Al_2O_3 (α-alumina) was the first bioceramic widely used clinically[171].

2.4.2 Alumina-Zirconia Composite

Pure ZrO_2 is polymorphic at ambient pressure. As illustrated schematically in Figure 2.24, it exhibits cubic structure at very high temperatures (more than 2370 ºC), tetragonal structure at medium temperatures (1200~2370 ºC), and monoclinic symmetry at low temperatures (lower than 950 ºC).

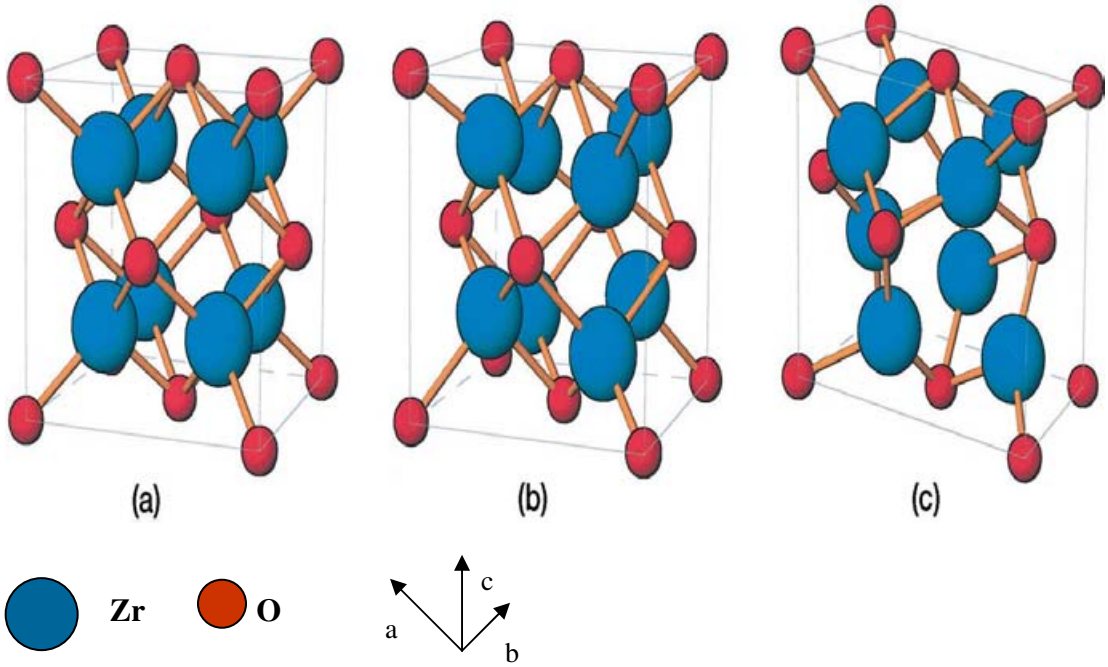

Figure 2.24 Schematic representation of the three polymorphs of ZrO_2 and the corresponding space groups: (a) cubic, (b) tetragonal, and (c) monoclinic. (after Howard[172,173]).

There was very limited interest in using pure zirconia as an engineering or structure ceramic prior to 1975, and the utilization of it was limited to refractory applications[172]. The limitations were predominately due to the displacive tetragonal to monoclinic phase

transformation, which takes place around 950 ºC when cooling pure ZrO_2 and is accompanied by a shear strain of ~ 0.16 and a volume expansion about ~ 4% leading to a unreliability of products.

Though the undesired shape change exists in pure ZrO_2, the intrinsic chemical and physical properties such as wear resistance, hardness, and high melting temperature, make it an attractive and potential engineering material candidate.

The discovery that the phase transformation can be controlled by proper material processing (transformation toughening in tailored, diphase microstructure) brought about a dramatic increase of ZrO_2 application. The volume expansion (from tetragonal to monoclinic) generates both dilatational and shear stresses, and these stresses prohibit the opening of an advancing crack or the microcrack formation, so the toughness of ZrO_2 at room temperature is high compared with other ceramics[172]. Among the transformation of toughening ceramics (based primarily on the transformation in ZrO_2), Al_2O_3-ZrO_2 composites have received much attention because of their excellent properties such as high mechanical strength, wear resistance, good thermal shock resistance and low thermal conductivity[174,176]. Based on these properties, Al_2O_3-ZrO_2 composites have been utilized in a variety of fields including dental screws, cutting blades, and insulators[175-177]. Moreover, porous Al_2O_3-ZrO_2 composites have attracted much attention as well and have been investigated as potential candidates for biomaterials applications[178,179].

2.4.3 Barium Titanate

Since the discovery of ferroelectricity in single-crystal materials (Rochelle salt) in 1921, there has been a continuous succession of new materials and technological developments which have already led to a significant number of industrial and commercial applications[180]. Among these new materials, $BaTiO_3$ is one of the most important ferroelectric materials.

$BaTiO_3$ is the first polycrystalline material in which ferroelectric behaviour was observed[169]. It is widely used in the fabrication of high-dielectric-constant capacitors, particularly multi-layer capacitors[181-183]. $BaTiO_3$ is also the first material to be developed as a piezoelectriceramic. Although for most commercial purposes it has been superseded by PZT, $BaTiO_3$ has attracted interest in medical applications as a piezoelectric material, and this is because bone is piezoelectric[184] and develops a charge under the application of a mechanical stress. It has been hypothesized that stress induced potentials in bone influence the activity of osseous bone cells[185].

Some basic information about crystal structure and properties of $BaTiO_3$ is shown below.

$BaTiO_3$ is isostructural with the mineral perovskite ($CaTiO_3$) and so is referred to having a perovskite structure. Above its Curie temperature (approximately 120 ^oC), the unit cell of $BaTiO_3$ is cubic (known as the paraelectric phase) with ions arranged as illustrated in Figure 2.25 (a). Below the Curie temperature, the structure of $BaTiO_3$ is slightly distorted to the tetragonal (known as ferroelectric phase) form with a dipole moment along the *c* direction resulting in the lattice parameter *c* becoming larger and lattice parameter *a* becoming smaller, as shown in Figure 2.25 (b).

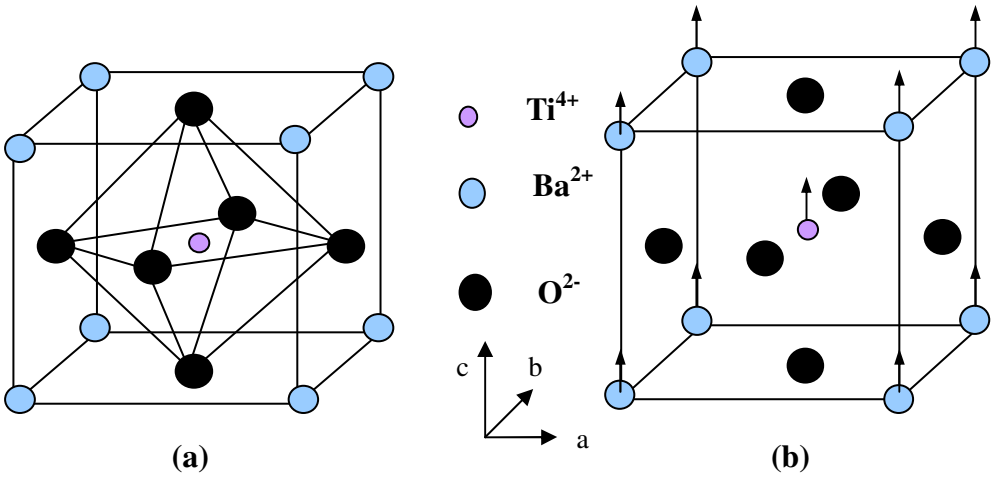

Figure 2.25 The crystal structure of $BaTiO_3$ (perovskite-type structrue): (a) Above the Curie temperature; (b) below the Curie temperature.

The dielectric constant of $BaTiO_3$ also changes with the temperature or phase transition. As shown in Figure 2.26, the dielectric constant has a very large (abnormal) value near phase transition temperature (-90, 0, and 120 ^{o}C). Moreover, the dielectric constant in the *a* axis direction is larger than that in the *c* axis direction. The temperature dependence of the dielectric constant above Curie temperature can be described fairly accurately by the Curie-Weiss law:

$$\varepsilon = \varepsilon_0 + \frac{C}{\theta - \theta_0} \tag{2-5}$$

where C is the Curie-Weiss constant and θ_0 is the Curie-Weiss temperature.

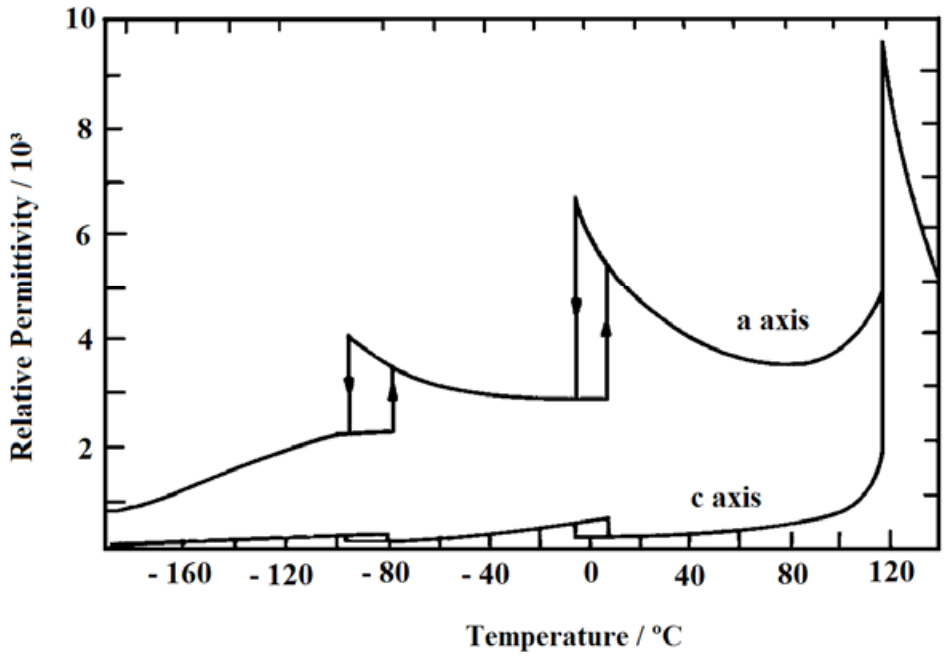

Figure 2.26 Temperature dependence of the dielectric constants in $BaTiO_3$ (after Merz[186]).

Those properties described in the above section are the basic properties of pure barium titanate. Moreover, doping of $BaTiO_3$ based ceramics is of great significance in the production of electric and electronic devices, e.g. multilayer capacitors, heaters and sensors

with positive temperature coefficient of resistivity, piezoelectric transducers, ferroelectric thin film memories[169,187]. One of the main advantages of doping in $BaTiO_3$ is that properties of $BaTiO_3$ such as dielectric property, piezoelectric property, mechanical property, could be modified by introducing aliovalent transition-metal or rare-earth ions on a percentage level. There is a large number of different dopants can be accommodated in the $BaTiO_3$ lattice due to the intrinsic capability of the perovskite structure to host ions of different size.

Principally, the site of incorporation for dopant ions in the $BaTiO_3$ perovskite structure may be predicted by considering the corresponding ionic radii, and the Goldschmidt tolerance factor, as shown in equation 2-6.

$$t = \frac{r_A + r_O}{\sqrt{2}(r_B + r_O)} \qquad (2\text{-}6)$$

where r_A is the ionic radii of A-site in perovskite structure, r_B is the ionic radii of B-site in perovskite structure, r_O is the oxygen ionic radii.

Owing to equation above, dopants will reside on a specific lattice site if a dopant ion's radius is within about 15% of the replaced ion. As a rule-of-thumb, the smaller transition metal ions are incorporated on the perovskite B-site, whereas the larger rare-earth ions will substitute on the A-site. For intermediate ionic radii values, exceptions from this rule were suggested proposing a shared site occupancy. A certain kind of dopant ion is incorporated simultaneously on the A- and B-site[188].

2.4.4 Lead Zirconate Titanate

In 1954, very good piezoelectric performance was found in ceramics with a composition near $Pb(Zr_{0.55}Ti_{0.45})O_3$ by Jaffe[189]. This discovery marked a turning point in the history of piezoelectric ceramics. Since then, due to their superior piezoelectric properties, the solid solution system $Pb(Zr,Ti)O_3$ (PZT) have been widely used in the fabrication of piezeceramics.

The $PbZrO_3$-$PbTiO_3$ phase diagram is shown in Figure 2.27.

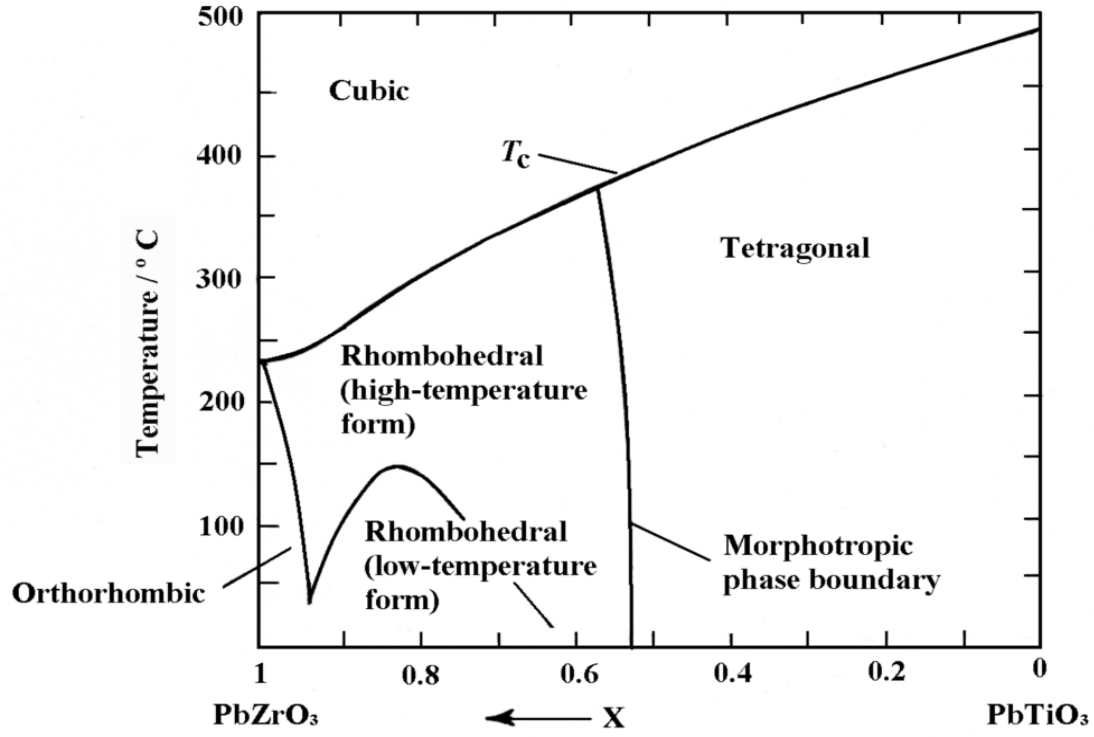

Figure 2.27 Phase stabilities in the system $Pb(Ti_{1-x}Zr_x)O_3$ (after Jaffe[190]).

The solid solution above T_c has the perovskite structure. The crystalline symmetry of this solid solution is governed by the Zr content. It can be seen that the morphotropic phase boundary (MPB) is a significant feature. An MPB denotes an abrupt structural change with composition at constant temperature in a solid solution range. In the PZT system it occurs close to the composition where $PbZrO_3$: $PbTiO_3$ is 1:1.

In piezoceramics, the convention is to define the poling direction as the 3-axis, as illustrated in Figure 2.28. The shear planes are indicated by the subscripts 4, 5, and 6 and are perpendicular to directions 1, 2 and 3 respectively. For example, d_{31} is the coefficient relating to the field along the polar axis to the strain perpendicular to it, whilst d_{33} is the corresponding coefficient for both strain and field along the polar axis. Shear can only occur when a field is applied at right angles to the polar axis so that there is only one coefficient,

d_{15}.

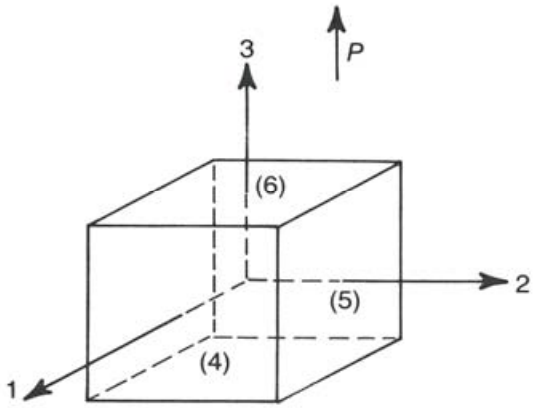

Figure 2.28 Labelling of reference axes and planes for piezoceramics (after Moulson[169])

Figure 2.29 illustrates several piezoelectric *d* constants as a function of composition close to MPB. Each constant obtains the highest value near the MPB, which is attributed to the increased ease of reorientation of the polarization under an applied electric field.

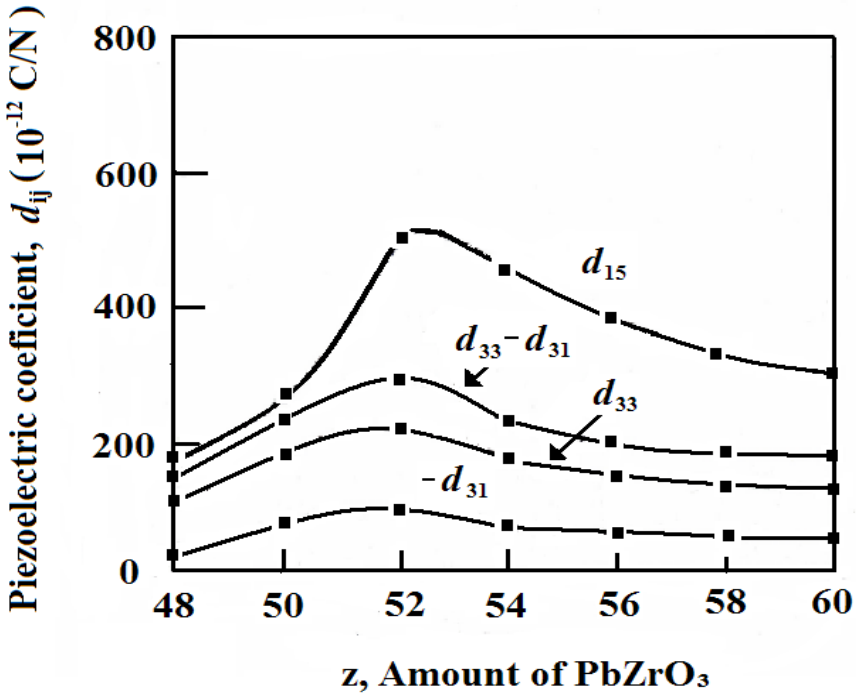

Figure 2.29 Dependence of several *d* constants on composition near the morphotropic phase boundary in PZT system. (after Jaffe[190]).

2.4.5 Piezocomposites

The perovskite family comprises the largest class of piezoelectric ceramics which are currently widely utilized in the transducers fabrication technology. Besides the monolithic ceramics, composites made of piezoelectric ceramics and polymers are also produced.

Ceramics are cheaper and easier to fabricate than single crystals or polymers. Moreover, ceramics possess relatively high dielectric constants compared with polymers and demonstrate good electromechanical coupling coefficients. However, ceramics are limited by their high acoustic impedance, which leads to poor acoustic matching with media such as human tissue and water—the media through which it is typically transmitting or receiving a signal[191]. Furthermore, ceramics show brittleness and high stiffness, therefore, they cannot be formed easily onto curved surfaces, which results in the very limited design flexibility for a desired transducer. Finally, the electromechanical resonances of piezoelectric ceramics cause a high degree of noise, which is not desirable in the context of transducer engineering. The best compromise in properties can be achieved by the combination of piezoelectric ceramics and polymers. Piezoelectric ceramic/polymer composites have exhibited superior properties when compared to single phase materials (monolithic ceramic or polymer)[192]. They combine high coupling, low acoustic impedance, few spurious modes, and an intermediate dielectric constant. In addition, they are flexible and moderately priced[193]. Therefore, piezoelectric ceramic/polymer composites have been widely utilized in the fabrication of sensors and actuators.

The patterns inside the composite, which dominate electromechanical properties, are determined by the arrangement of the phases comprising the composite. The concept of connectivity in composites, put forward by Newnham[194], is a very simple and convenient method to depict the manner in which the individual phase is continuously self-connected.

Each phase in a composite may be self-connected in zero, one, two, or three dimensions. There are 10 connectivity patterns if we limit the discussion to a diphasic composite, which are illustrated schematically in Figure 2.30.

The internationally accepted nomenclature to describe such composites is (0-0), (0-1), (0-2), (0-3), (1-1), (1-2), (2-2), (1-3), (2-3), and (3-3). The first digit refers to the number of connectivity dimensions of the piezelectrical active phase, and the second one refers to the electromechanically inactive polymer phase. In past decades, a variety of piezocomposites with different connectivity patterns have been successfully produced based on the connectivity concept[186].

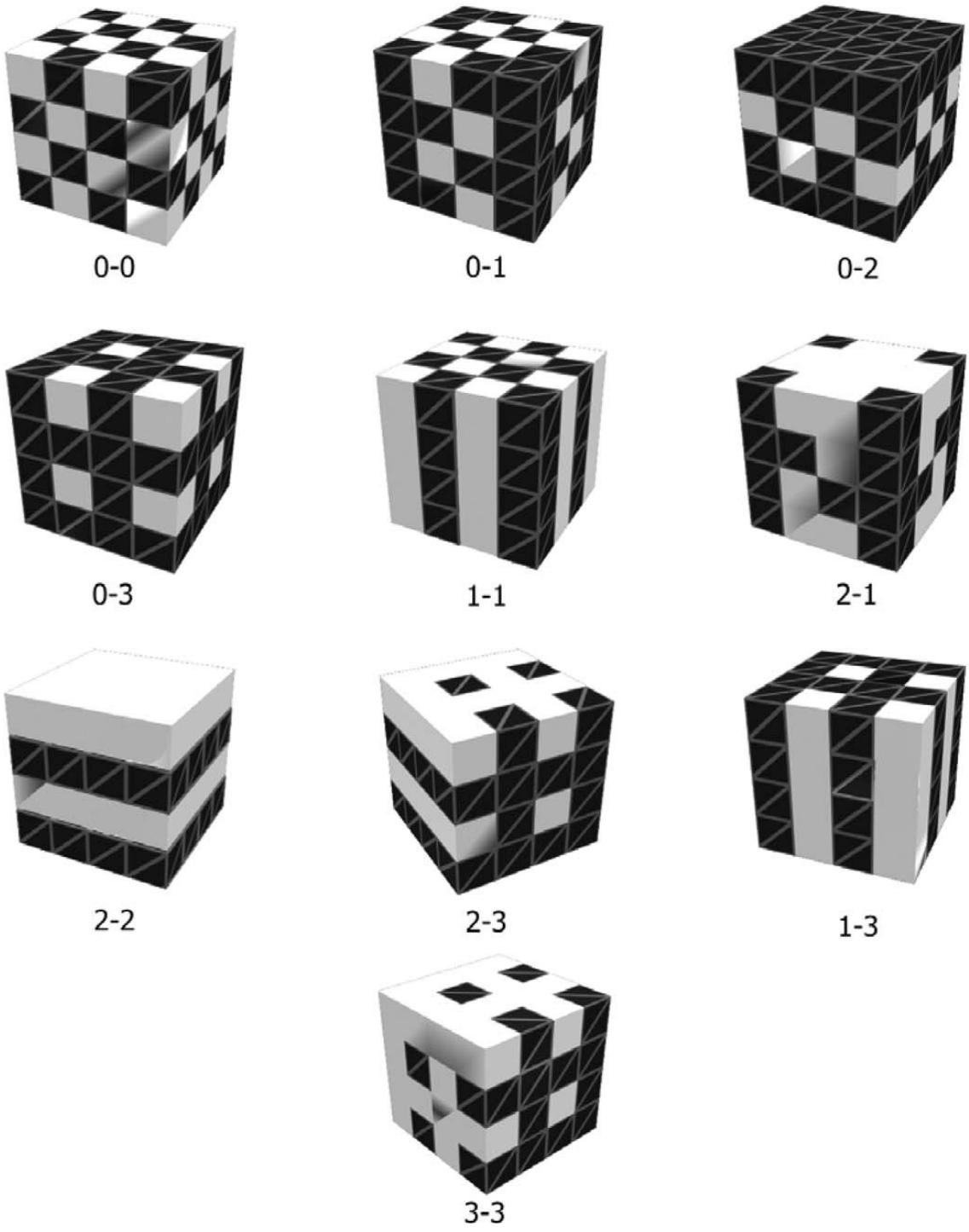

Figure 2.30 Different connectivity patterns for a diphasic solid. Each phase has zero, one, two or three dimensional connectivity to itself. Note that the total number of connectivity patterns arising from the 10 families depicted is 16 due to permutations involved in families (1-0) (0-2) (0-3) (2-1) (2-3) (1-3). (after Newsham[188] and Akdogan[193]).

2.5 Objectives of this Research Project

As mentioned in Section 2.1 and 2.2, freeze casting is a new and very promising fabrication technique for porous materials compared with other preparation methods. However, it is still at an early stage and there is a lack of systematic research. Therefore, the overall aim of this research program is to undertake a thorough investigation of the freeze casting technique.

The objectives of the research project are as follows:

- To carry out a systematic study of the freeze casting technique starting from ceramic slurries. Alumina will be used as a model material to demonstrate the basic factors affecting this technique and also the influences of processing additives.
- To explore the mechanisms, such as engulfment and size effect involved in the freeze casting technique for the fabrication of porous materials. This includes introducing a two-phase colloidal system (alumina and zirconia) into this investigation.
- To explore the versatility of the freeze casting technique for different applications. This involves the preparation of $BaTiO_3$-epoxy composite through the freeze casting technique for application of dielectric composites and also includes the fabrication of 2-2 PZT-epoxy piezocomposites for transducer applications.

References

1. A.R. Studart, U.T. Gonzenbach, E. Tervoort, et al. Processing routes to macroporous ceramics : a review. Journal of the American Ceramic Society, 2006, 89(6), 1771-1789.

2. P. Sepulveda and J.G.P. Binner. Processing of cellular ceramics by foaming and in situ polymerisation of organic monomers. Journal of the European Ceramic Society, 1999, 19, 2059-2066.

3. P. Colombo. Conventional and novel processing methods for cellular ceramics. Philosophical Transaxtions of the Royal Society A, 2006, 364, 109-124.

4 I.Y. Guzman. Certain principles of formation of porous ceramic structures. Properties and applications (a review). Glass and ceramics, 2003, 60(9-10), 280-283.

5 S.Y. Shan, J.F. Yang, J.Q. Gao, et al. Porous silicon nitride ceramics prepared by reduction–nitridation of silica. Journal of the American Ceramic Society, 2005, 88(9), 2594-2596.

6 K. Schwartzwalder and A.V. Somers. Methods of making porous ceramic articles. US patent, No.3090094, May 21 1963.

7. A.E.M. Paiva, P.Sepulveda, and V.C. Pandolfelli. Processing and thermomechanical evaluation of fibre-reinforced alumina filters. Journal of Materials Science, 1999, 34, 2641-2649.

8. J.M. Tulliani, L. Montanaro, and T. J. Bell. Semiclosed-cell mullite foams: preparation and macro- and micromechanical characterization. Journal of the American Ceramic Society, 1999, 82(4), 961-968.

9. M.R. Nangrejo, X. BAO, and M.J. Edirisinghe. The structure of ceramic foams produced using polymeric precursors. Journal of Materials Science Letters, 2000, 19, 787-789.

10. M.R. Nangrejo, X. BAO, and M.J. Edirisinghe. Silicon carbide–titanium carbide composite foams produced using a polymeric precursor. International Journal of Inorganic Materials, 2001, 3, 37-45.

11. M.R. Nangrejo, X. BAO, and M.J. Edirisinghe. Preparation of silicon carbide silicon nitride composite foams from pre-ceramic polymers. Journal of the European Ceramic Society, 2000, 20, 1777-1785.

12. X. Bao, M.R. Nangrejo, and M.J. Edirisinghe. Preparation of silicon carbide foams using polymeric precursor solutions. Journal of Materials Science, 2000, 35, 4356-4372.

13. E. Roncari, C. Galassi, and C. Bassarello. Mullite suspensions for reticulate ceramic preparation. Journal of the American Ceramic Society, 2000, 83(12), 2993-2998.

14. H.R. Ramay and M.Q. Zhang. Preparation of porous hydroxyapatite scaffolds by combination of the gel-casting and polymer sponge methods. Biomaterials, 2003, 24, 3293-3302.

15. X.P. Pu, X.J. Liu, F.G. Qiu, et al. Novel method to optimize the structure of reticulated porous ceramics. Journal of the American Ceramic Society, 2004, 87(7), 1392-1394.

16. J. Luyten, I. Thijs, W. Vandermeulen, et al. Strong ceramic foams from polyurethane templates. Advences in Applied Ceramics, 2005, 104, 4-8.

17. R. Mouazer, S. Mullens, I. Thijs, et al. Silicon carbide foams by polyurethane replica technique. Advenced Engineering Materials, 2005, 7(12), 1124-1128.

18. R.A. White, J.N. Weber, E.W. White. Replamineform: a new process for preparing porous ceramic, metal, and polymer prosthetic materials. Science, 1972, 176, 922-924.

19. D.M. Roy and S.K. Linnehan. Hydroxyapatite formed from coral skeletal carbonate by hydrothermal exchange. Nature, 1974, 247, 220-222.

20. D.P. Skinner, R.E. Newnham and L.E.Cross. Flexible composite transducers. Materials Research Bulletin, 1978, 13, 599-607.

21. Z.T. Liu, T.X. Fan, and W. Zhang. The synthesis of hierarchical porous iron oxide with wood templates. Microporous and Mesoporous Materials, 2005, 85, 82-88.

22. P. Greil, T. Lifka, and A. Kaindl. Biomorphic cellular silicon carbide ceramics from wood: processing and microstructure. Journal of the European Ceramic Society, 1998, 18, 1961-1973.

23. H. Sieber, C. Hoffmann, A. Kaindl, et al. Biomorphic cellular ceramics. Advanced Engineering Materials, 2000, 2(3), 105-109.

24. F.M. Varela-Feria, J. Martínez-Fernández, A.R. de Arellano-López, et al. Low density biomorphic silicon carbide: microstructure and mechanical properties. Journal of the European Ceramic Society, 2002, 22, 2719-2725.

25. E. Vogli, H. Sieber, and P. Greil. Biomorphic SiC-ceramic prepared by Si-vapor phase infiltration of wood. Journal of the European Ceramic Society, 2002, 22, 2663-2668.

26. A.G. Dong, Y.J. Wang, Y. Tang, et al. Zeolitic tissue through wood cell templating. Advanced Materials, 2002, 14(12), 926-929.

27. C. Zollfrank, R. Kladny, H. Sieber, et al. Biomorphous SiOC/C-ceramic composites from chemically modified wood templates. Journal of the European Ceramic Society, 2004, 24, 479-487.

28. J. Cao, C.R. Rambo, and H. Sieber. Manufacturing of microcellular, biomorphous oxide ceramics from native pine wood. Ceramic International, 2004, 30, 1967-1970.

29. A. Zampieri, H. Sieber, T. Selvam, et al. Biomorphic cellular SiSiC/Zeolite ceramic composites: from rattan palm to bioinspired structured monoliths for catalysis and sorption. Advanced Materials, 2005, 17(3), 344-349.

30. C.R. Rambo, J. Cao, O. Rusina, et al. Manufacturing of biomorphic (Si, Ti,Zr)-carbide ceramics by sol-gel processing. Carbon, 2005, 43, 1174-1183.

31. C.R. Rambo and H. Sieber. Novel synthetic route to biomorphic Al_2O_3 ceramics. Advanced Materials, 2005, 17(8), 1088-1091.

32. Z.T. Liu, T.X Fan, W. Zhang, et al. The synthesis of hierarchical porous iron oxide with wood templates. Microporous and Mesoporous Materials, 2005, 85, 82-88.

33. P. Colombo, E. Bernardo, and L. Biasetto. Novel microcellular ceramics from a silicone resin. Journal of American Ceramic Society, 2004, 87 (1), 152-154.

34. D.M. Liu. Preparation and characterization of porous hydroxyapatite bioceramic via a slip-casing route. Ceramic International, 1998, 24, 441-446.

35. M. Boaro, J.M. Vohs, and R.J. Gorte. Synthesis of highly porous yttria-stabilized zirconia by tape-casting methods. Journal of American Ceramic Society**,** 2003, 86(3), 395-400.

36. S. Dhara and P. Bhargava . A simple direct casting route to ceramic foams. Journal of American Ceramic Society, 2003, 86(10), 1645-1650.

37. P.Sepulveda. Gelcasting foams for porous ceramics. Amecrican Ceramic Society Bulletin, 1997, 76 (10), 61-65.

38. S.H. Li, J.R. De Wijn, and P. Layrolle. Synthesis of macroporous hydroxyapatite scaffolds for bone tissue engineering. Journal of Biomedical Materials Research**,** 2002, 61(1), 109-120.

39. P. Colombo and E. Bernardo. Macro- and micro-cellular porous ceramics from preceramic polymers. Composites Science and Technology, 2003, 63, 2353-2359.

40. S.H. Li, J.R. de Wijn, and P. Layrolle. Novel method to manufacture porous hydroxyapatite by dual-phase mixing. Journal of the American Ceramic Society, 2003, 86(1), 65-72.

41. P. Colombo, E. Bernardo, and L. Biasettot. Novel microcellular ceramics from a silicone resin. Journal of the American Ceramic Society, 2004, 87(1), 152-154.

42. N. Koc, M. Timucn, and F. Korkusuz. Fabrication and characterization of porous tricalcium phosphate ceramics. Ceramics international, 2004, 30, 205-211.

43. Y.W. Kim, Y.J. Jin , and Y.S. Chun. A simple pressing route to closed-cell microcellular ceramics. Scripta Materialia, 2005, 53, 921-925.

44. D.M. Liu. Influence of porosity and pore size on the compressive strength of porous hydroxyapatite cermic. Ceramic International, 1997, 23, 135-139.

45. R.A. Lopes and A.M. Segadães. Microstructure, permeability and mechanical behaviour of ceramic foams. Materials Science and Engineering A, 1996, 209, 149-155.

46. D.Y. Wang, R.A. Caruso, and F. Caruso. Synthesis of macroporous titania and inorganic composite materials from coated colloidal spheres: A novel route to tune pore morphology. Chemistry of Materials, 2001, 13(2), 364-371.

47. D.B Kuang, A.W. Xu, J.Y Zhu, et al. Fabrication of ordered macroporous rutile titania at low temperature. New Journal of Chemistry, 2002, 26, 819-821.

48. P.G. Ni, B.Y. Cheng, P. Dong, et al. A novel titania membrane with uniform macropores. Chinese Physics Letters, 2005, 18(12), 1610-1612.

49. S.A. Davis, M, Breulmann, K.H. Rhodes, et al. Template-directed assembly using nanoparticle building blocks: a nanotectonic approach to organized materials. Chemistry of Materials, 2001, 13(10), 3218-3226.

50. I. Thijs, J. Luyten, and S. Mullen. Producing ceramic foams with hollow spheres. Journal of the American Ceramic Society, 2003, 87(1), 170-172.

51. H. Wang, I.Y. Sung, and X.D. Li. Fabrication of porous SiC ceramics with special morphologies by sacrificing template method. Journal of Porous Materials, 2004, 11(4), 265-271.

52. N.W. Androff, L.F.Francis, and B.V.Velamakanni. Macroporous ceramics from ceramic – polymer dispersion methods. AICHE Journal, 1997, 43 (11), 2878-2888.

53. J.M. Bouler, M. Trecant, J. Delecrin, et al. Macroporous biphasic calcium phosphate ceramics: influence of five synthesis parameters on compressive strength Journal of Biomedical Materials Research, 1996, 32(4), 603-609.

54. A. Díaz and S. Hampshire. Characterisation of porous silicon nitride materials produced with starch. Journal of the European Ceramic Society, 2004, 24, 413-419.

55. E. Gregorová, W. Pabst, and I. Bohačenko. Characterization of different starch types for their application in ceramic processing. Journal of the European Ceramic Society, 2006, 26, 1301-1309.

56. G.C.C. Yang and C.M. Tsai. Effects of starch addition on characteristics of tubular porous ceramic membrane substrates. Desalination, 2008, 233, 129-136.

57. C.V. Brovarone, E. Vernè, and M. Bosetti. Microstructural and in vitro characterization of SiO_2-Na_2O-CaO-MgO glass-ceramic bioactive scaffolds for bone substitutes. Journal of Materials Science: Materials in Medicine, 2005, 16, 909-917.

58. L. Yin , H.X. Peng, S. Dhara, et al. Natural additives in protein coagulation casting process for improved microstructural controllability of cellular ceramics. Composites: Part B, 2009, 40, 638-644.

59. S. Marselli, V. Pavia, and C. Galassi. Porous piezoelectric ceramic hydrophone. Journal of Acoustical Society American, August 1999, 106(2), 733-738.

60. E. Gregorová, Z. Živcová, and W. Pabst**.** Starch as a pore-forming and body-forming agent in ceramic technology. Starch, 2009, 61**,** 495–502.

61. H. Katsuki, A.Kawahara, and H. Ichinose. Preparation and some properties of porous alumina ceramics obtained by the gelatination of ammonium alginate. Journal of Materials Science. 1992, 27(22), 6067-6070.

62. G.J. Zhang, J.F Yang, and T. Ohji. Fabrication of porous ceramics with unidirectionally aligned continuous pores. Journal of American Ceramic Society, 2001, 84(6), 1395-1397.

63. L. Montanaro, Y. Jorand, G. Fantozzi, et.al. Ceramic foams by powder processing. Journal of European Ceramic Society, 1998, 18(9), 1339-1350.

64. C.Wang, T. Kasuga, and M.Nogami. Macroporous calcium phosphate glass-ceramic prepared by two-step pressing technique and using sucrose as a pore former. Journal of Materials Science-Materials in Medicine, 2005, 16(8), 739-44.

65. M.H. P. da Silva, A.F. Lemos, I.R. Gibson, et.al. Porous glass reinforced hydroxyapatite materials produced with different organic additives. Journal of Non Crystal Solids, 2002, 304(1-3), 286-292.

66. Y. Sun, S.H. Tan, and D.L. Jiang. Synthesis of porous silicon carbide and its catalysis. Journal of Inorganic Materials, 2005, 18(4), 739-733.

67. J. Luyten, S. Mullens, J. Cooymans, et,al. New processing techniques of ceramic foams. Advanced Engineering Materials, 2003, 5 (10), 715-718.

68. T. Fukasawa, Z.Y. Deng, M. Ando, et.al. Pore structure of porous ceramics synthesized from water-based slurry by freeze-dry process. Journal of Materials Science, 2001, 36(10), 2523-2527.

69. T. Fukasawa, M. Ando, T. Ohji, et al. Synthesis of porous ceramics with complex pore structure by freeze-dry processing. Journal of American Ceramic Society, 2001, 84(1), 230-232.

70. K. Araki and J.W. Halloran. Porous ceramic bodies with interconnected pore channels by a novel freeze casting technique. Journal of American Ceramic Society, 2005, 88 (5), 1108-1114.

71. A. Imhof and D.J. Pine. Ordered macroporous materials by emulsion templating. Nature, 1997, 389 6654, 948-951.

72. A. Imhof and D.J. Pine. Preparation of titania foams. Advanced Materials, 1999, 11(4), 311-314.

73. Y.W. Kim and S.H KIM. Processing of closed-cell silicon oxycarbide foams from a preceramic polymer. Journal of Materials Science, 2004, 39, 5647-5652.

74. Y. Sakka, F.Q Tang, and H. Fudouzi. Fabrication of porous ceramics with controlled pore size by colloidal processing. Science and Technology of Advanced Materials, 2005, 6, 915-920.

75. B.P. Binks. Macroporous silicafrom solid-stabilized emulsion templates. Advanced Materials. 2002, 14 (24), 1824-1827.

76. P. Colombo and M. Modesti. Silicon oxycarbide foams from a silicon preceramic polymer polyurethane. Journal of Sol-Gel Science and Technology, 1999, (14), 103-111.

77. P. Sepulveda and J. G. P. Binner. Processing of cellular ceramics by foaming and in situ polymerisation of organic monomers. Journal of European Ceramic Society, 1999, 19, 2059-2066.

78. E. Dickinson, R. Ettelaie, T. Kostakis. Factors controlling the formation and stability of air bubbles stabilized by partially hydrophobic silica nanoparticles. Langmuir, 2004, 20, 8517-8525.

79. U. T. Gonzenbach, A. R. Studart, E. Tervoort, et. al. Macroporous ceramics from particles-stabilized wet foams. Journal of American Ceramic Society, 2007, 90(1),16-22.

80. U.T. Gonzenbach, A. R. Studart, E. Tervoort, et. al. Materials from foams and emulsions stabilized by colloidal particles. Journal of Materials Chemistry, 2007, 17, 3283-3289.

81. Z.P. Du, M. P. B. Montoya, B. P. Binks, et.al. Outstanding stability of particle-stabilized bubbles. Langmuir, 2003, 19, 3106-3108.

82. S. Barg, C. Soltmann, M. Andrade, et al. Cellular ceramics by direct foaming of emulsified ceramic powder suspensions. Journal of the American Ceramic Society, 2008, 91(9), 2823-2829.

83. U.T. Gonzenbach, A.R. Studart, D. Steinlin, et al. Processing of particle-stabilized wet foams into porous ceramics. Journal of the American Ceramic Society, 2007, 90(11), 3407-3414.

84. C.G. Aneziris , W. Schärfl, and B. Ullrich. Microstructure evaluation of Al_2O_3 ceramics with Mg-PSZ- and TiO_2-additions. Journal of the European Ceramic Society, 2007, 27, 3191-3199.

85. B.Y.Tay, J.R.G. Evans, and M.J.Edirsinghe. Solid free form fabrication of ceramics. International Materials Reviews. 2003, 48(6), 341-370.

86. H. Seitz, W. Rieder, and S. Irsen. Three-dimensional printing of porous ceramic scaffolds for bone tissue engineering. Journal of Biomedical Materials Research Part B: Applied Biomaterials, 2005, 74B(2),782-788.

87. H.Y. Yang, S.F Yang, and X.P. Chi. Fine ceramic lattices prepared by extrusion free forming. Journal of Biomedical Materials Research, 2006, 79B(1), 116-121.

88. T. Moritz and H. J. Richter. Ceramic bodies with complex geometries and ceramic shells by freeze casting using ice as mold material. Journal of the American Ceramic Society, 2006, 89(8), 2394-2398.

89. S.W. Sofie and F. Dogan. Freeze casting of aqueous alumina slurries with glycerol. Journal of the American Ceramic Society, 2001, 84(7), 1459-1464.

90. M.J.Statham, F. Hammett, B. Harris, et al. Net-shape manufacture of low-cost ceramic shapes by freeze-gelation. Journal of Sol-Gel Science and Technology, 1998, 13, 171-175.

91. E.J.W. Verwey and J.T.G. Overbeek. Theory of stability of lyophobic colloids. Elsevier: Amsterdam, The Netherland, 1948.

92. T. Fukasawa, M. Ando, T. Ohji, et al. Synthesis of porous ceramics with complex pore structure by freeze-dry processing. Journal of the American Ceramic Society, 2001, 84(1), 230-232.

93. T. Fukasawa, Z.Y. Deng, T. Ohji, et al. High-surface-area alumina ceramics with aligned macroscopic pores. Journal of the Ceramic Society of Japan, 2001, 109(12), 1035-1038.

94. T. Fukasawa, Z.Y. Deng, T. Ohji, et al Pore structure of porous ceramics synthesized from water-based slurry by freeze-dry process. Journal of Materials Science, 2001, 36(10), 2523-2527.

95. H.F. Zhang, I. Hussain, M. Brust, et al. Nature Materials, 2005, 4, 787-793.

96. S. Deville, E. Saiz, R.K.Nalla, et al. Freezing as a path to build complex composites. Science, 2006, 311, 515-518.

97. S. Deville. Freeze-casting of porous ceramics: a review of current achievements and issues. Advanced Engineering Materials. 2008, 10(3), 155-169.

98. M.G. Worster and J.S. Wettlaufer. Natural convection, solute trapping, and channel formation during solidification of saltwater. The Journal of Physical Chemistry, 1997, 101(32), 6132 -6136.

99. K. Araki and J.W. Halloran. Porous ceramic bodies with interconnected pore channels by a novel freeze casting technique. Journal of the American Ceramic Society. 2005, 88(5), 1108-1114.

100. S. Deville, E. Saiz, and A. P. Tomsia. Freeze casting of hydroxyapatite scaffolds for bone tissue engineering. Biomaterials, 2006, 27, 5480-5489.

101. M. Nakata, K. Tanihata, S. Yamaguchi, et al. Fabrication of porous alumina sintered bodies by a gelate-freezing method. Journal of the Ceramic Society of Japan, 2005, 113(11), 712-715.

102. S. Deville, E. Saiz, and A.P. Tomsia. Ice-templated porous alumina structures. Acta Materialia,

2007, 55, 1965-1974.

103. C.M. Pekor, P. Kisa, and I. Nettleship. Effect of polyethylene glycol on the microstructure of freeze-cast alumina. Journal of the American Ceramic Society, 2008, 91(10), 3185-3190.

104. S. Roy and A. Wann. Metal/ceramic composites from freeze-cast ceramic preforms: domain structure and elastic properties. Composites Science and Technology, 2008, 68, 1136-1143.

105. S. Deville, E. Maire, and Lasalle. In situ X-Ray radiography and tomography observations of the solidification of aqueous alumina particle suspensions-part I: initial instants. Journal of the American Ceramic Society, 2009, 92 (11), 2489-2496.

106. J.C. Han, L.Y. Hu, and Y.M. Zhang. Fabrication of ceramics with complex porous structures by the impregnate freeze-casting process. Journal of the American Ceramic Society, 2009, 92(9), 2165-2167.

107. Y.M. Zhang, L.Y. Hu, and J.C. Han. Preparation of a dense/porous Bi-layered ceramic by applying an electric field during freeze casting. Journal of the American Ceramic Society, 2009, 92 (8), 1874-1876.

108. C. Tallón, R. Moreno, and M.I. Nieto. Shaping of porous alumina bodies by freeze casting. Advancs in Applied Ceramics, 2009, 108(5), 307-313.

109. T. Waschkies, R. Oberacker, and M.J. Hoffmann. Control of lamellae spacing during freeze casting of ceramics using double-side cooling as a novel processing route. Journal of the American Ceramic Society, 2009, 92(1), S79-S84.

110. T. Fukasawa, M. Ando, and T. Ohji. Filtering properties of porous ceramics with unidirectionally aligned pores. Journal of the Ceramic Society of Japan, 2002, 110(7), 627-631.

111. T. Fukasawa, Z.Y Deng, and M. Ando. Synthesis of porous silicon nitride with unidirectionally aligned channels using freeze-drying process. Journal of the American Ceramic Society, 2002, 85(9), 2151-55.

112. J. Tang, Y. F. Chen, H. Wang, et al. Preparation of oriented porous silicon carbide bodies by freeze-casting process. High Performance Ceramics III, PTS, 1 and 2 III**,** 2005, 280-283, 1287-1290.

113. H.J. Hwang, D.Y. Kim, and J.W. Moon. Fabrication of porous clay materials with aligned pore structures by freeze-drying. Materials Science Forum, 2006, 510-511, 906-909.

114. C.T. McKee and J.Y. Walz. Effects of added clay on the properties of freeze-casted composites of silica nanoparticles. Journal of the American Ceramic Society, 2009, 92 (4), 916-921.

115. L.L. Ren, Y.P. Zeng, and D.L Jiang. Fabrication of gradient pore TiO_2 sheets by a novel freeze-tape-casting process. Journal of the American Ceramic Society, 2007, 90(9), 3001-3004.

116. L.L. Ren, Y.P. Zeng, and D.L Jiang. Preparation of porous TiO_2 by a novel freeze casting. Ceramics International, 2009, 35, 1267-1270.

117. J.W. Moon, H.J. Hwang, M. Awano, et al. Preparation of NiO–YSZ tubular support with radially aligned pore channels. Materials Letters, 2003, 57, 1428-1434.

118. M. Bettge, H. Niculescu, and P.J. Gielisse. Engineered porous ceramics using a directional freeze-drying process. 2005 28th International Spring Seminar on Electronics Technology Bettge. 2005, 12-18.

119. S.W. Sofie. Fabrication of functionally graded and aligned porosity in thin ceramic substrates with the novel freeze–tape-casting process Journal of the American Ceramic Society, 2007, 90(7), 2024-2031.

120. K.H. Zuo, Y.P. Zeng, and D.L. Jiang. Properties of microstructure-controllable porous yttria-stabilized ziroconia ceramics fabricated by freeze casting. International Journal of Applied Ceramic Technology, 2008, 5(2), 198-203.

121. Z.Y. Deng, H. R. Fernandes, J. M. Ventura, et al. Nano-TiO_2-coated unidirectional porous glass structure prepared by freeze drying and solution infiltration. Journal of the American Ceramic Society, 2007, 90(4), 1265-1268.

122. T. Moritz and H.J. Richter. Ice-mould freeze casting of porous ceramic components. Journal of the European Ceramic Society, 2007, 27(16), 4595-4601.

123. M.N. Rahaman and Q. Fu. Manipulation of porous bioceramic microstructures by freezing of suspensions containing binary mixtures of solvents Journal of the American Ceramic Society, 2008, 91(12), 4137-4140.

124. E. Landi, F. Valentini, A.T.E. Landi, et al. Porous hydroxyapatite/gelatine scaffolds with ice-designed channel-like porosity for biomedical applications Acta Biomaterialia, 2008, 4, 1620-1626.

125. Q. Fu, M.N. Rahaman, F. Dogan, et al. Freeze-cast hydroxyapatite scaffolds for bone tissue engineering applications. Biomedical Materials, 2007, 3(2) 025005.

126. Q. Fu, M.N Rahaman, F. Dogan, et al. Freeze Casting of Porous Hydroxyapatite Scaffolds. I. Processing and General Microstructure Journal of Biomedical Materials Research Part B: Applied Biomaterials, 2008, 86B (1), 125-135.

127. Y Zhang, K Zuo, Y.P. Zeng. Effects of gelatin addition on the microstructure of freeze-cast porous hydroxyapatite cerarmics. Ceramics international. 2009,35(6), 2151 -2154.

128. E.P. Gorzkowski and M.J. Pan. Barium titanate polymer composites produced via directional freezing. IEEE Transactions on Ultrasonics, Ferroelectrics, and Frequency Control. August 2009, 56 (8), 1613-1616.

129. X.P. Qi, J.D. Ye, and Y.J Wang. Alginate/poly (lactic-co-glycolic acid)/calcium phosphate cement scaffold with oriented pore structure for bone tissue engineering. Journal of Biomedical Materials Research Part A, 2009, 89A (4), 980-987.

130. K.K. Mallick. Freeze Casting of Porous Bioactive Glass and Bioceramics Journal of the American Ceramic Society, 2009, 92, S85–S94.

131. K. Araki and J. W. Halloran. New freeze-casting technique for ceramics with sublimable vehicles. Journal of the American Ceramic Society, 2004, 87(10), 1859-1863.

132. K. Araki and J. W. Halloran. Porous ceramic bodies with interconnected pore channels by a novel freeze casting technique Journal of the American Ceramic Society, 2005, 88(5), 1108-1114.

133. Y.H. Koh, J.H. Song, E.J. Lee, et al. Effect of polystyrene addition on freeze casting of ceramic/camphene slurry for ultra-high porosity ceramics with aligned pore channels. Journal of the American Ceramic Society. 2006, 89(12), 3646-3653.

134. B.H. Yoon, W.Y. Choi, H.E. Kim,et al. Aligned porous alumina ceramics with high compressive strengths for bone tissue engineering. Script Materialia, 2008, 58 (7), 537-540.

135. S.H. Lee, S.H. Jun, H.E. Kim. Fabrication of porous PZT-PZN piezoelectric ceramics with high hydrostatic figure of merits using camphene-based freeze casting. Journal of the American Ceramic Society, 2007, 90 (9), 280-2813.

136. S.H. Lee, S.H. Jun, H.E. Kim, et al. Piezoelectric properties of PZT-based ceramic with highly aligned pores. Journal of the American Ceramic Society, 2008, 91(6), 1912-1915.

137. Y.H. Koh, J.J. Sun, and H.E. Kim. Freeze casting of porous Ni-YSZ cermets. Materials Letters. 2007, 61(6), 1283-1287.

138. Y.H. Koh, E.J.Lee, B.H. Yoon, et al. Effect of polystyrene addition on freeze casting of ceramic/camphene slurry for ultra-high porosity ceramics with aligned pore channels. Journal of the American Ceramic Society, 2006, 89(12), 3646-3653.

139. S.W. Sofie. Fabrication of functionally graded and aligned porosity in thin ceramic substrates with the novel freeze-tape-casting process. Journal of the American Ceramic Society, 2007, 90 (7), 2024-2031.

140. C.Q. Hong, X.H. Zhang, J.C. Han, et al. Camphene-based freeze-cast ZrO_2 foam with high compressive strength. Materials Chemistry and Physics, 2010, 119(3), 359-362.

141. J.C. Han, C.Q. Hong, X.H. Zhang, et al. Highly porous ZrO_2 ceramics fabricated by a camphene-based freeze-casting route: Microstructure and properties Journal of the European Ceramic Society, 2010, 30(1), 53-60.

142. C.Q. Hong, X.H. Zhang, J.C. Han, et al. Ultra-high-porosity zirconia ceramics fabricated by novel room-temperature freeze-casting. Scripta Materialia, 2009, 60(7), 563-566.

143. B.H. Yoon, C.S. Park, H.E. Kim, et al. In situ synthesis of porous silicon carbide (SiC) ceramics decorated with SiC nanowires. Journal of the American ceramic society. 2007, 90(12), 3759-3766.

144. J.H. Song, Y.H. Koh, and H.E. Kim. Fabrication of a porous bioactive glass-ceramic using room temperature freeze casting. Journal of the American Ceramic Society, 2006, 89(8), 2469-2453.

145. E.J. Lee, Y.H. Koh, B.H. Yoon, et al. Highly porous hydroxyapatite bioceramics with interconnected pore channels using camphene-based freeze casting. Materials Letters, 2007, 61(11-12), 2270-2273.

146. B.H. Yoon, Y.H. Koh and H.E. Kim. Generation of large pore channels for bone tissue engineering using camphene-based freeze casting. Journal of the American Ceramic Society, 2007, 90(6), 1744-1752.

147. B.H. Yoon, C.S. Park, H.E. Kim, et al. In-situ fabrication of porous hydroxyapatite (HA) scaffolds with dense shells by freezing HA/camphene slurry. Materials Letters, 2008, 62(10-11), 1700-1703.

148. A. Macchetta, I.G. Turner, and C.R.Bowen. Fabrication of HA/TCP scaffolds with a graded and porous structure using a camphene-based freeze-casting method Acta Biomaterialia, 2009, 5(4), 1319 -1327.

149. H.R. Ramay, M.Q. Zhang. Preparation of porous hydroxyapatite scaffolds by combination of the gel-casting and polymer sponge methods. Biomaterials, 2003(24), 3293–3302.

150. D.M. Liu. Influence of porosity and pore size on the compressive strength of porous hydroxyapatite ceramic. Ceramics International, 1997(23), 135-139.

151. R.P. del Reala, J.G.C. Wolkeb, M. Vallet-Regí, et al. A new method to produce macropores in calcium phosphate cements. Biomaterials, 2002(23), 3673-3680.

152. T.M.G. Chu, D.G. Ortone, S.J. Hollisterb, et al. Mechanical and in vivo performance of hydroxyapatite implants with controlled architectures. Biomaterials, 2002(23), 1283-1293.

153. J.A. Lewis. Colloidal processing of ceramics. Journal of the American Ceramic Society, 2000, 83(10), 2341-2359.

154. R.J. Hunter. Foundations of colloid science. Vol 1 and 2 Oxford University press. Oxford, UK, 1987 and 1989, 168-224.

155. A.W. Adamson. Physical chemistry of surfaces. 3rd Edition,Wiley-Interscience: New York, 1984.

156. M.J. Jaycock. In dispersion of powders in liquids, 3rd Edition; Elsevier Applied Science: London, 1986, 51-98.

157. R.J. Hunter. Zeta potential in colloid science. London: Academic Press; 1981.

158. N.L. Weise SME Mineral processing handbook, vol. 1. New York: Society of Mining Engineers, 1985. 5.42.

159. L. Besra and M.L. Liu. A review on fundamentals and applications of electrophoretic deposition (EPD). Progress in Materials Science, 2007, 52, 1-61.

160. B.V. Derjaguin and L.D. Landau. Theory of stability of highly charged lyophobi sols and adhesion of highly charged particles in solutions of electrolytes. Acta Physicochim, 1941, 14, 633-52.

161. E.J.W. Verwey and J.T.G. Overbeek. Theory of stability of lyophobic colloids. Elsevier: Amsterdam, the Netherlands, 1948.

162. T.F. Tadros. Chap. 9. In Surfactants, Tadros, T. F., Ed. Academic Press: London, 1984, 197-220.

163. D.H. Napper. Polymeric stabilization of colloidal dispersions. Academic Press: London, 1983, 4-13.

164. J. Cesarano, I. A. Aksay, and A. Bleier. Stability of aqueous alpha-Al_2O_3 suspensions with poly(methacrylic acid) poly-electrolyte. Journal of the American Ceramic Society, 1988, 71(4), 250-255.

165. S. Biggs and T.W. Healy. Electrosteric stabilization of colloidal zirconia with lowmolecular-weight polyacrylic-acid - an atomic-force microscopy study. Journal of the Chemical Society-Faraday Transactions, 1994, 90(22), 3415-3421.

166. O.J. Rojas, P.M. Claesson, D. Muller, et al. The effect of salt concentration on adsorption of low-charge-density polyelectrolytes and interactions between polyelectrolyte-coated surfaces. Journal of Colloid and Interface Science, 1998, 205(1), 77-88.

167. J. Marra and M.L. Hair. Forces between two poly(2-vinylpyridine)-covered surfaces as a function of ionic-strength and polymer charge. Journal of Physical Chemistry. 1988, 92(21), 6044-6051.

168. I.J. McColm. Ceramic science for materials technologists. Leonard Hill: New York, 1983, 257-272.

169. A.J. Moulson and J.M. Herbert. Electroceramics materials, properties, applications. Chapman and Hall. 1990, 68-76.

170. N. Claussen. Fracture toughness of Al_2O_3 with a sustabilized ZrO_2 dispersed phase. Journal of the American Ceramic Society, 1976, 59 (1-2), 49-51.

171. L.L. Hench. Bioceramics. Journal of the American Ceramic Society, 1998, 81 (7), 1705-1728.

172. R.H.J. Hannink, P.M. Kelly, and B.C.Muddle. Transformation toughening in zirconia-containing ceramics. Journal of the American Ceramic Society, 2000, 83(3), 461-487.

173. C.J. Howard, B.A. Hunter, and D.J. Kim. Oxygen position and bond lengths from lattice parameters in tetragonal zirconias. Journal of the American Ceramic Society, 1998, 81(1), 241-243.

174. S.M. Olhero, I. Ganesh, and P.M.C. Torres. Aqueous colloidal processing of ZTA composites. Journal of the American Ceramic Society, 2009, 92(1), 9-16.

175. Y.S. Shin, Y.W. Rhee, and S.J. Kang. Experimental evaluation of toughening mechanisms in alumina-zirconia composites. Journal of the American Ceramic Society, 1999, 82(5), 1229-1232.

176. R.H.J. Hannink, P.M. Kelly, B.C. Muddle. Transformation toughening in zirconia-containing ceramics. Journal of the American Ceramic Society, 2000, 83 (3), 461-487.

177. W.H. Tuan, R.Z. Chen, T.C. Wang, et al. Mechanical properties of Al_2O_3/ZrO_2 composites. Journal of the European Ceramic Society, 2002, 22 (16), 2827-2833.

178. J.Y. Yu, X.D. Sun, Q. Li, et al. Preparation of Al_2O_3 and Al_2O_3–ZrO_2 ceramic foams with adjustable cell structure by centrifugal slip casting. Materials Science and Engineering: A, 2008, 476 (1-2), 274-280.

179. X. He, Y.Z. Zhang, B. Su, et al. Zirconia toughened alumina ceramic foams for potential bone graft applications: fabrication, bioactivation, and cellular responses. Journal of Materials Science. Materials in Medicine, 2008, 19(7), 2743-2749.

180. G.H. Haertling. Ferroelectric ceramics: history and technology. Journal of the American Ceramic society, 1999, 82(4), 797-818.

181. H. Kishi, Y. Mizuno, and H. Chazono. Base-metal electrode-multilayer ceramic capacitors: Past, present, and future perspectives. Janpanese Journal of Applied Physics Part 1(regular papers short note& review papers), 2003, 42(1), 1-15.

182. D.E. Kotechi, J.D. Baniecki, H. Shen, et.al. (Ba,Sr)TiO_3 dielectrics for future stacked-capacitor DRAM. IBM Journal of Research and Development, 1999, 43(3), 367-382.

183. A.R. West, T. B. Adams, and F.D. Morrison. Novel high capacitance materials: $BaTiO_3$: La and $CaCu_3Ti_4O_{12}$. Journal of the European Ceramic Society, 2004, 24, 1439-1448.

184. E. Fukada and I. J. Yasuda. On the piezoelectric effect of bone. Journal of the Physical Society of Japan, 1957, 12(10), 1158-1162.

185. C.A.L. Bassett and R.O. Becker. Generation of electric petentials by bone in response to mechanical stress. Science, 1962, 137, 1063-1064.

186. W.J. Merz. The dielectric beharior of $BaTiO_3$ single domain crystals. Physical Review, 1949, 75, 687-687.

187. Y.H. Xu. Ferroelectric materials and their applications. North-Holland: Amsterdam, 1991.

188. R.A. Eichel. Defect structure of oxide ferroelectrics—valence state, site of incorporation, mechanisms of charge compensation and internal bias fields. Journal of Electroceramics, 2007, 19, 9-21.

189. B. Jaffe, W.R. Cook, and H. Jaffe. Piezoelectric Ceramics, Academic Press, London, 1971.

190. B. Jaffe, R.S. Roth, and S. Marzullo. Properties of piezoelectric ceramics in the solid solution series lead titanate-lead zirconate –lead oxide- tin oxide and lead titanate –lead hafnate. Journal of Research of the National Bureau of Standards, 1955, 55(5), 239-254.

191. A.Safari, M.Allahverdi, E.K. Akdogan. Solid free form fabrication of piezoelectric sensors and actuators. Journal of Materials Science. 2006 (41), 177-198.

192. T.R. Gururaja. Piezoelectrics transducers for medical ultrasonic imaging. American Ceramic Society Bulletin, 1994, 73, 50-54.

193. E.K. Akdogan, M. Allahverdi, A. Safari. Piezoeletric composites for sensor and actuator applications. IEEE Transactions, Terroelectrics and Trequency Control, 2005, 52 (5), 746-775.

194. R.E. Newnham, D.P. Skinner, L.E. Cross. Connectivity and piezoelectric-pyroelectric composite. Materials Research Bulletin, 1978, 13, 525-536.

CHAPTER 3 EXPEIMENTAL PROCEDURES

This chapter details the experimental work in relation to the fabrication methods of polydimethylsiloxane (PDMS) soft moulds, porous ceramics and composites (through freeze casting), bulk ceramics (by centrifugal casting and die pressing), ceramic-epoxy composites, and also presents characterization methods including property measurements at different stages and relevant analysis methods.

The fabrication process of PDMS soft moulds is described in Section 3.1.1. The detailed information about the freeze casting technique including the home-made setup and the detailed process procedures are described in Section 3.1.2. The fabrication processes (centrifugal casting and die pressing) which were used in Chapter 6 to prepare the bulk ceramics are shown in Section 3.1.3 and 3.1.4. The method employed for producing ceramic-epoxy composite in Chapter 6 and 7 are described in Section 3.1.5. The characterization methods are shown in Section 3.2. Due to the broad nature of this study, some specific details about the experimental will be described in relevant chapters.

3.1 Process Procedures

3.1.1 Fabrication of Soft Mould and Setup for Freeze Casting

The elastomeric molds used in this investigation are made from polydimethylsiloxane prepolymer according to the procedures shown in Figure 3.1.

First, a master (alumina ceramic cylinder, diameter: 12 mm, height: 13.5 mm) was placed in a weighing boat. A 10:1 (weight ratio) mixture of PDMS-Sylgard Silicone Elastomer 184 and Sylgard Curing Agent 184 (Dow Corning Corp.) was mixed manually in a beaker and left in the air for about half an hour to release the air bubbles. When there were no visible air

bubbles, the mixture was then poured into the master template and the whole assembly was moved into a vacuum desiccator to remove the residual air bubbles for another half an hour. After that, the PDMS was cured at 40 ºC in an oven for 24 hours. Finally, the rigid PDMS was carefully peeled off the master template. Typical PDMS moulds fabricated by this method are shown in Figure 3.2.

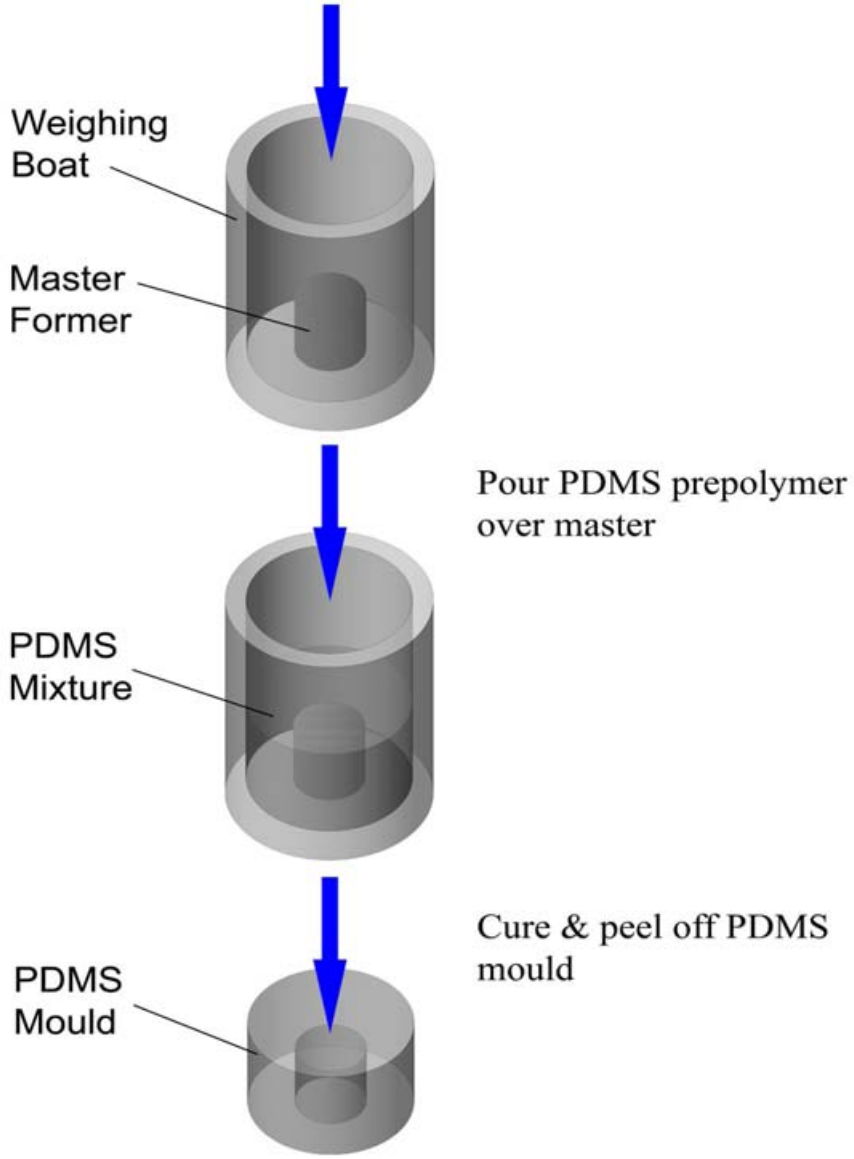

Figure 3.1 Schematic illustration of the procedure for casting PDMS replicas from a ceramic master

Moreover, these moulds are transparent, which is very helpful for the observation of the freezing process and estimation of the solidification rate.

.

Figure 3.2 Typical PDMS moulds used in this study

The freezing apparatus is one of the most important elements used in the freeze casting technique[1,2]. The apparatus used in this investigation was a custom built design comprised of a thermally insulated dewar and a mechanism for controlling the distance between the sample and the surface of liquid nitrogen contained within the dewar. A schematic diagram of this experimental setup for freeze casting is shown in Figure 3.3. Liquid nitrogen was employed as the freezing media, so that low temperatures could be easily obtained. A simple and manually operated elevator (plastic handle with copper wire) was made and added to the setup. By rotating the handle, different levels where the freezing started could be achieved. A stainless steel ruler was fixed along the cylinder edge in order to help in determining the distance between the samples relative to the liquid nitrogen surface and controlling the amount of liquid nitrogen inside the cylinder. Moreover, the freezing plate used in this study

was a very thin plate (less than 1 mm) made from stainless steel, which was connected to a thermocouple and timer. The solidification rate in the axial direction of the cylindrical sample can be estimated by observing the time for the slurry at the top of the mould to freeze.

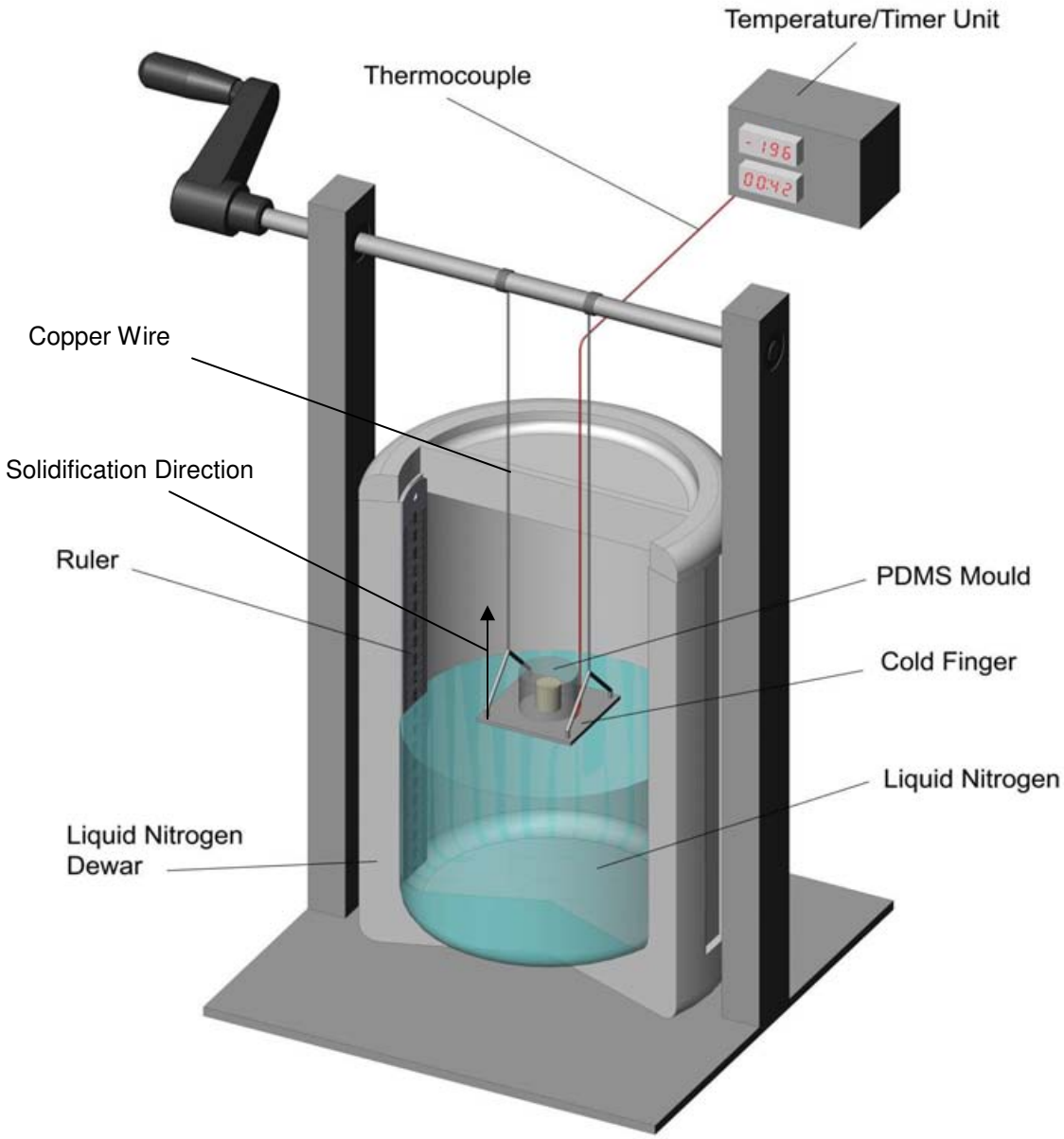

Figure 3.3 Schematic diagram of the experimental apparatus for freeze casing process

With those designs described above, a wide range of different freeze conditions (cooling

rates) could be obtained using the elevator to adjust the distance between stainless steel (cold finger) and the surface of liquid nitrogen.

3.1.2 Fabrication Process of Porous Ceramics by Freeze Casting

3.1.2.1 Preparation of Different Aqueous Ceramic Colloidal Suspensions

Five different commercial ceramic powders were utilized in this thesis: alumina (CT300SG, Caldic)[3] for the work described in Chapter 4; 3% mol. yttria-stabilized zirconia (Tosoh-zirconia, Japan)[3] for the work described in Chapter 5; barium titanate (BT) (HPB-1000,TPL Inc., USA)[4] and nano-sized alumina (α–phase, 99%, Alfa Aesar) for the work described in Chapter 6; and PZT (TRS610,TRS Ceramics, USA) for the work described in Chapter 7.

This investigation concentrates only on freeze casting based on water. Therefore, distilled water (17 MΩ·cm) was employed as a vehicle.

In order to obtain stable suspensions, various amounts of ammonium polyacrylate (NH_4PAA) solution (D3021, Allied Colloids, Bradford, UK, a 40% concentrated solution of average molecular weight 2500 $g \cdot mol^{-1}$) were used for ceramic slurries with different solids loadings. NH_4PAA was chosen in this study to disperse ceramic powders because this dispersant is one of the most often used in aqueous solutions and its temperature of thermal decomposition by depolymerization is below 400 ^oC, allowing clean burnout with little residual carbon[4].

In order to improve the strength of the green bodies, 3 wt.% B-1000 and 2 wt.% B-1007 (acrylic polymer emulsion, Duramax, Chesham Chemicals Ltd, Middlesex, UK) were added to the suspension as binder according to the recommendation of the supplier[5]. In order to characterize their effects on the final morphology of porous ceramic during the freeze casting process, several additives were utilized including polyvinyl alcohol (Nippo Gohsei, Osaka, Japan) and glycerol (Laboratory reagent, Fisher scientific UK limited, Loughborough,

UK). The detailed information will be illustrated in the corresponding chapters. Please note that the amount of any additive used in this study is expressed on a dry weight of the powder basis (dwb), equivalent to the wt./wt. basis of the ceramic powder.

Moreover, any pH adjustment needed was achieved by using 1 M hydrochloric acid (HCl) and concentrated (35%) ammonia hydroxide (NH_4OH).

The preparation process of the ceramic colloidal suspension is detailed below. Calculation of the amount of each reagent (water, dispersant, binder, powder) was carefully done before any operation. Typical batch size for each sample was 50 g according to previous work[6]. All the suspensions used in this thesis were all prepared under room temperature.

Firstly, distilled water was weighed and poured into a 60 ml plastic bottle (Azlon, UK). An appropriate amount of dispersant was then added to the distilled water and the bottle was sealed and placed on a magnet stirrer for mixing for about 5 minutes.

The required amount of ceramic powder was then gradually added to the plastic bottle (the mixture, water and dispersant), whilst still under the constant magnet stirring. In order to achieve better dispersion of the ceramic powder and reduce the agglomeration, this process was normally very time-consuming and it varied much depending on the nature of the ceramic powder such as particle size. In different chapters, suspensions with various solids loadings were all prepared according to this method as described above.

Following that, slurries were ball-milled overnight (24 hours) with ball-milling media (alumina, 5 mm in diameter and zirconia balls, 4.8 mm in diameter) to achieve better dispersion and mixing. Before casting or rheological measurement, appropriate amounts of binders were added to the suspensions, followed by ball milling at very low speed for about 20 minutes and then de-airing in a vacuum desiccator for 2 hours. Finally, the ceramic colloidal suspensions were ready for casting and measurement.

3.1.2.2 Casting, Freezing, Demoulding and Sublimation

The resultant ceramic suspensions were poured into the transparent PDMS mould (15 samples can be made from each slurry batch) and the very thin stainless steel disc was glued over the top to form a seal. When the glue (Araldite Rapid, Bostik limited, UK) became dry (it usually takes about 10 minutes), the resultant mould was turned over and transferred onto the stainless steel cold finger of the setup shown in Figure 3.3.

The sample was quickly placed at the proper location using the manual elevator. Unless there was a need for the observation of freezing and adding liquid nitrogen, the dewar was then covered by a thermal insulating top. Freezing of the slurry occurred quickly, which was from the bottom to the top. The solidification rate in the axial direction of the cylindrical samples could be estimated by observing and recording the time for the suspension at the top of the mould to freeze. Then the solidification rate could be obtained by calculation (distance and time). In reality, the freezing time was mainly dependant on the cooling rate employed on the sample. The frozen samples were then carefully and slowly demoulded from the PDMS moulds by hand to avoid cracking or breaking. This process was carried out inside a freezer, so the melting of the frozen sample could be avoided. The demoulded frozen sample was stored in a freezer where the temperature was kept at -40 ºC until all the samples were finished. The completed samples were then quickly transferred into a freeze dryer (Labconco Corp., Kansas City, MO, USA). The sublimation of the ice was under a low temperature (-40 ^{o}C) and pressure for 24 h to make sure the ice was sublimated completely. Finally, the green bodies were obtained and they were ready to be sintered in a muffle furnace in an air atmosphere.

3.1.2.3 Sintering

For the green bodies obtained from freeze casting or other processing, all the sintering was

carried out in a muffle furnace (Lenton furnace, Leicestershire, UK) in air. All the samples except the PZT samples were placed in an alumina or zirconia ceramic crucible, on the bottom of which was a thin layer of the original ceramic powder, and put in the furnace for sintering. A schematic diagram of the sintering regime is presented in Figure 3.4. In order to burn out the binder, the samples were heated at very small and constant ramp speed of 60 ºC/h going up to 325 ºC and dwelled for one hour; then they were heated to 500 ºC under the same ramp speed and dwelled for one and half hours. If the green bodies did not contain any binder, a high ramp speed of 300 ºC/h was used directly going up to 500 ºC. The samples were then heated at 300 ºC/h to the target sintering temperatures and dwelled for 1 to 2 hours. The target sintering temperature will be described in each chapter. The sintering cycle was completed with a cooling rate of 300 ºC/h down to room temperature.

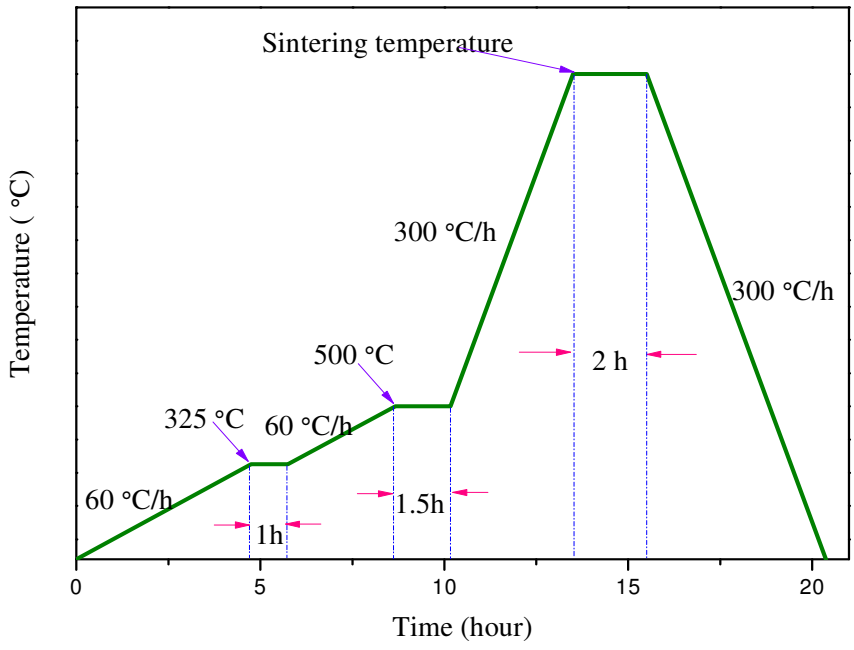

Figure 3.4 Schematic diagram of sintering regime for all green samples

Special procedures were adopted for sintering the PZT samples to avoid the volatilization of lead oxide during sintering. This procedure is shown schematically in Figure 3.5. First, the

porous PZT green samples were carefully placed into an alumina crucible which already had a flat bed of PbO-doped ZrO_2 sand. As shown in the picture, the ZrO_2 sand bed had two layers: one layer was coarse sand, and the other was a thin layer of fine sand which was on top of the coarse layer sand. The cylindrical PZT samples were then covered by a small alumina crucible, on top of which was covered by two additional layers of zirconia sand in order to reduce the volatilization of lead oxide. Finally, the crucible was covered by another alumina plate and was then ready for sintering. All the ZrO_2 sand used was mixed with extra PbO in advance to offer an atmosphere with excess lead. The porous PZT samples could not be buried in sand during sintering to avoid the sand significantly changing the morphology of the pores.

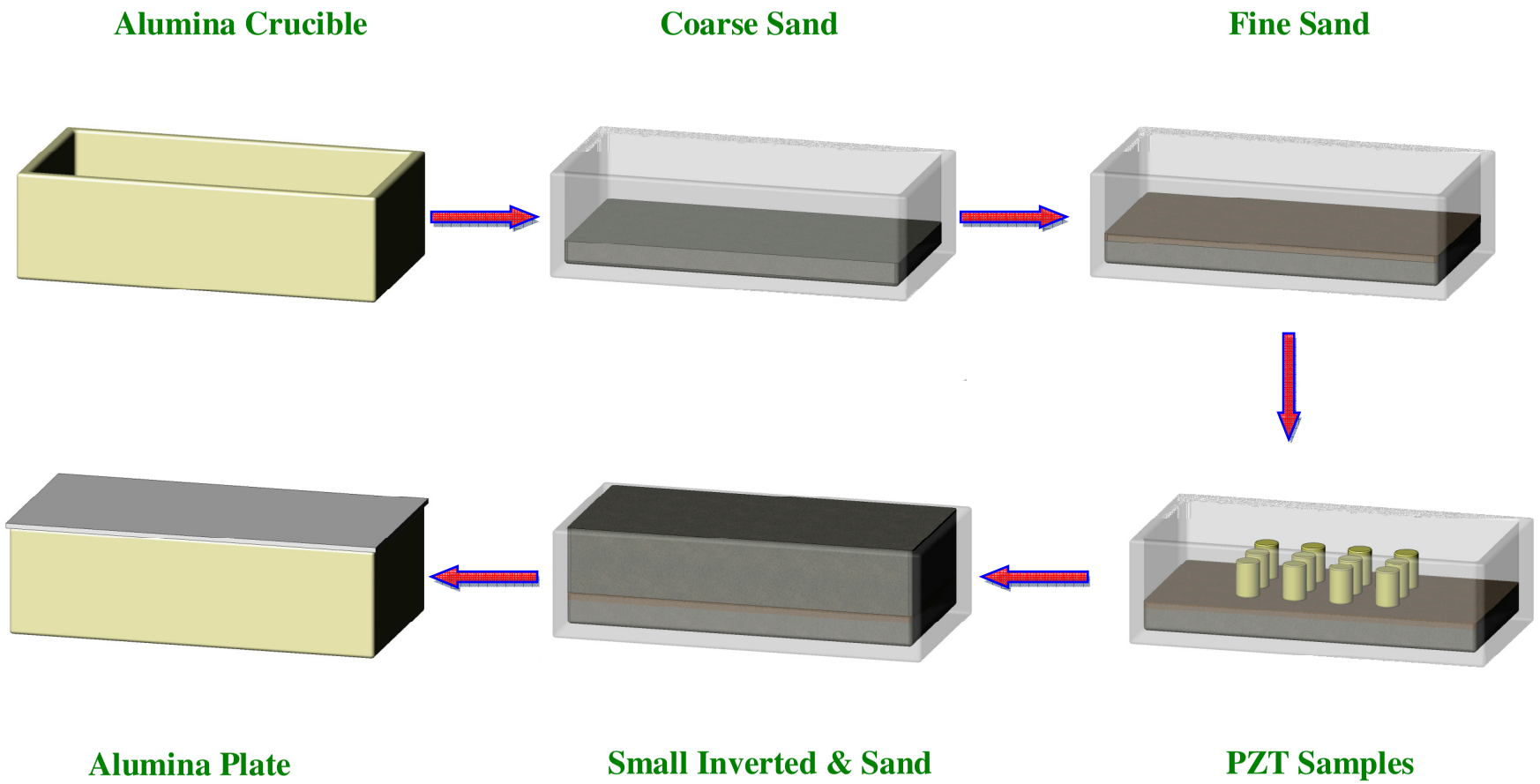

Figure 3.5 Schematic diagrams of special procedure to sinter PZT samples.

3.1.2.4 Summary: Flow Chart of Freeze Casting Process

Suspension, freezing, sublimation and sintering are the four main procedures in freeze casing, which have already been described in the above section. As a summary, a flow chart in Figure 3.6 presents schematically the process procedure of freeze casting.

3.1.3 Fabrication Process for Centrifugal Aided Slip Casting

As mentioned in Chapter 2, colloidal processing offers the potential to reliably produce ceramic components through careful control of initial suspension "structure" and its evolution during fabrication[7]. Moreover, colloidal processing is a very versatile route[4], because following on the suspension preparation, many ceramic forming techniques can be utilized to fabricate ceramic products, such as slip casting[8], tape casting[9], and gel casting[10]. Therefore, as described in Chapter 6, an easy forming technique, centrifugal aided slip casting, was employed to characterize the dispersion of nano-sized Barium Titanate (BT) powder and sintering of BT ceramics. Centrifugal aided slip casting from a suspension of particles is done by the removal of liquid as in filtration or by the movement of particles through the liquid because of the force acting on the particles. This mechanism[11] is called sedimentation and is the basis of cast formation in centrifugal casting. The BT slurries were obtained through the method illustrated in section 3.1.2.1. The amount of the dispersant (NH_4PAA), hydrochloric acid (HCl) and concentrated (35%) ammonia hydroxide (NH_4OH) will be detailed in Chapter 6. In this process, BT aqueous suspensions with high solids loadings were poured into cylindrical PDMS soft moulds, which were then placed in a Clandon T-52 bench top centrifuge for half an hour at 3000 rpm. Subsequently, ceramic particles started to move toward the base of the mould due to the centrifugal force and formed a cast with increasing thickness. After this, the water was decanted away and the

mould and the green body was left at room temperature for 24 hours, and then were put in an oven at 40 ℃ for another 24 hours to completely dry out the water.

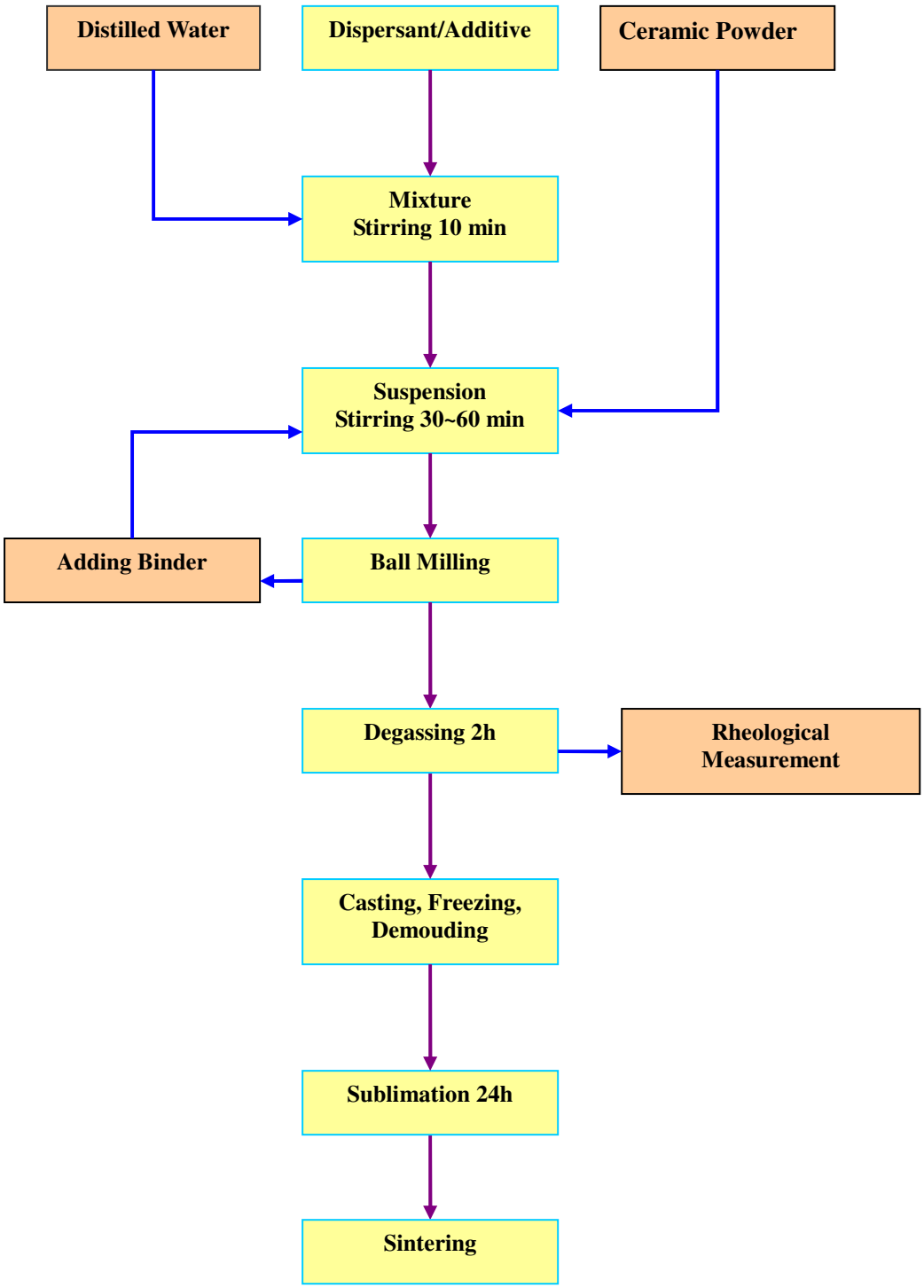

Figure 3.6 Flow chart of the whole process of freeze casting.

Finally, the dried green bodies were carefully peeled off from the mould prior to sintering. The procedure is shown schematically in Figure 3.7. The resulting cylindrical samples were then sintered and cut into discs for further measurement.

3.1.4 Process for the Fabrication of the Alumina-Doped BT Ceramics by Traditional Electroceramics Fabrication Method

In order to improve the mechanical properties of the BT ceramics, nano-sized α–alumina was incorporated into BT as described in Chapter 6. The traditional electroceramics fabrication method was utilized to make bulk samples for the comparison with the porous samples. Nano-sized alumina and BT were first dispersed in the distilled water according to the method described in 3.1.2.1. After ball milling and addition of binder, freeze-drying was employed to dry the mixed powders. A 250 micron sieve was used to sieve the powder. As-prepared powder was then pressed into pellets (13 mm diameter × 2 mm thick) using a 13 mm diameter steel die under a pressure of 150 MPa. Green compacts were fired in air for 2 hours. After polishing, gold electrodes were sputtered on both sides of the sample by a sputter coater (EMITECH, K575X, UK) for 4 minutes. In summary, a flow chart for the preparation procedure is shown in Figure 3.8.

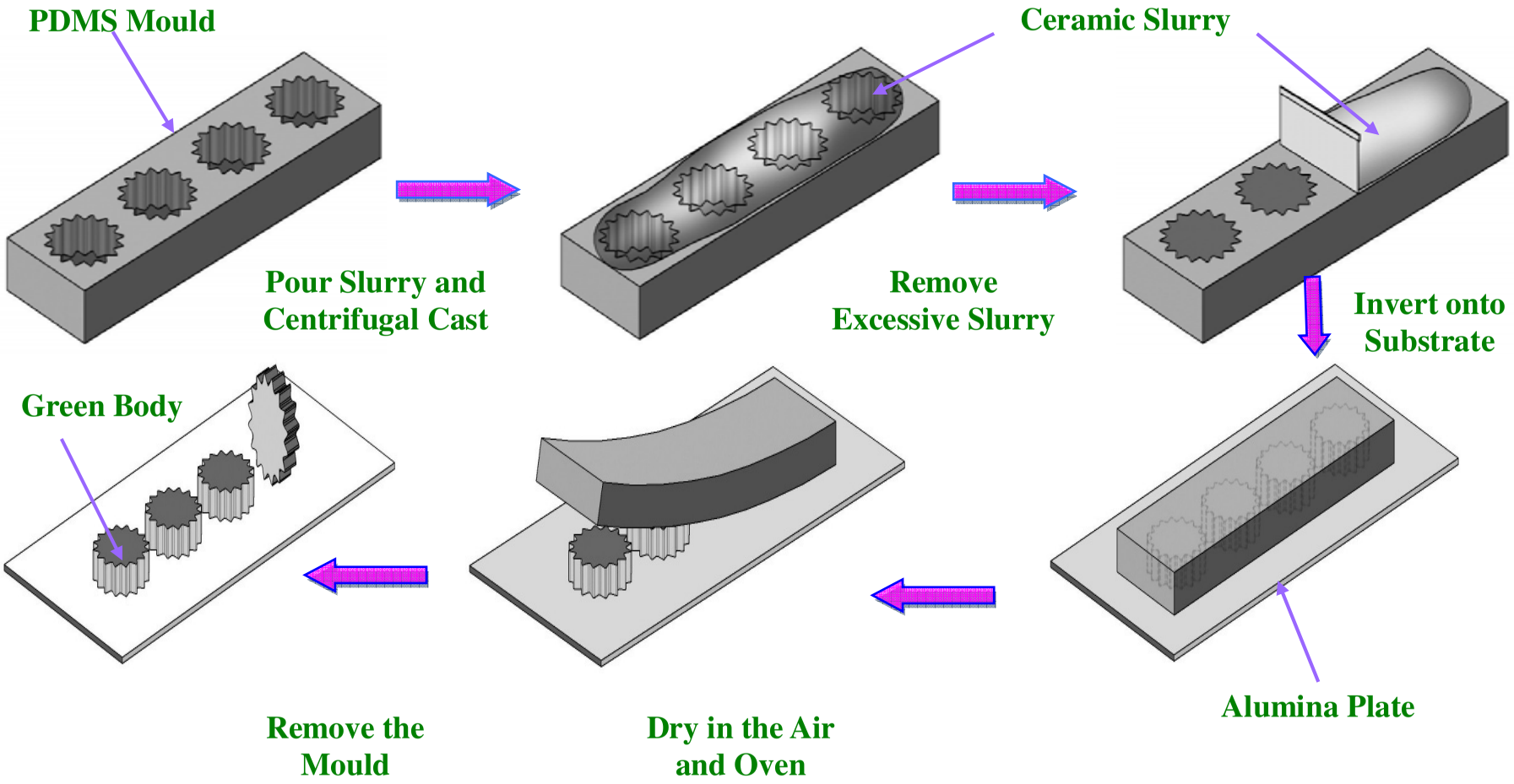

Figure 3.7 Schematic procedures for centrifugal aided slip casting (after Zhang[12]). Though the schematic moulds shown are in gear shape, the actual moulds used in experiment are cylindrical moulds.

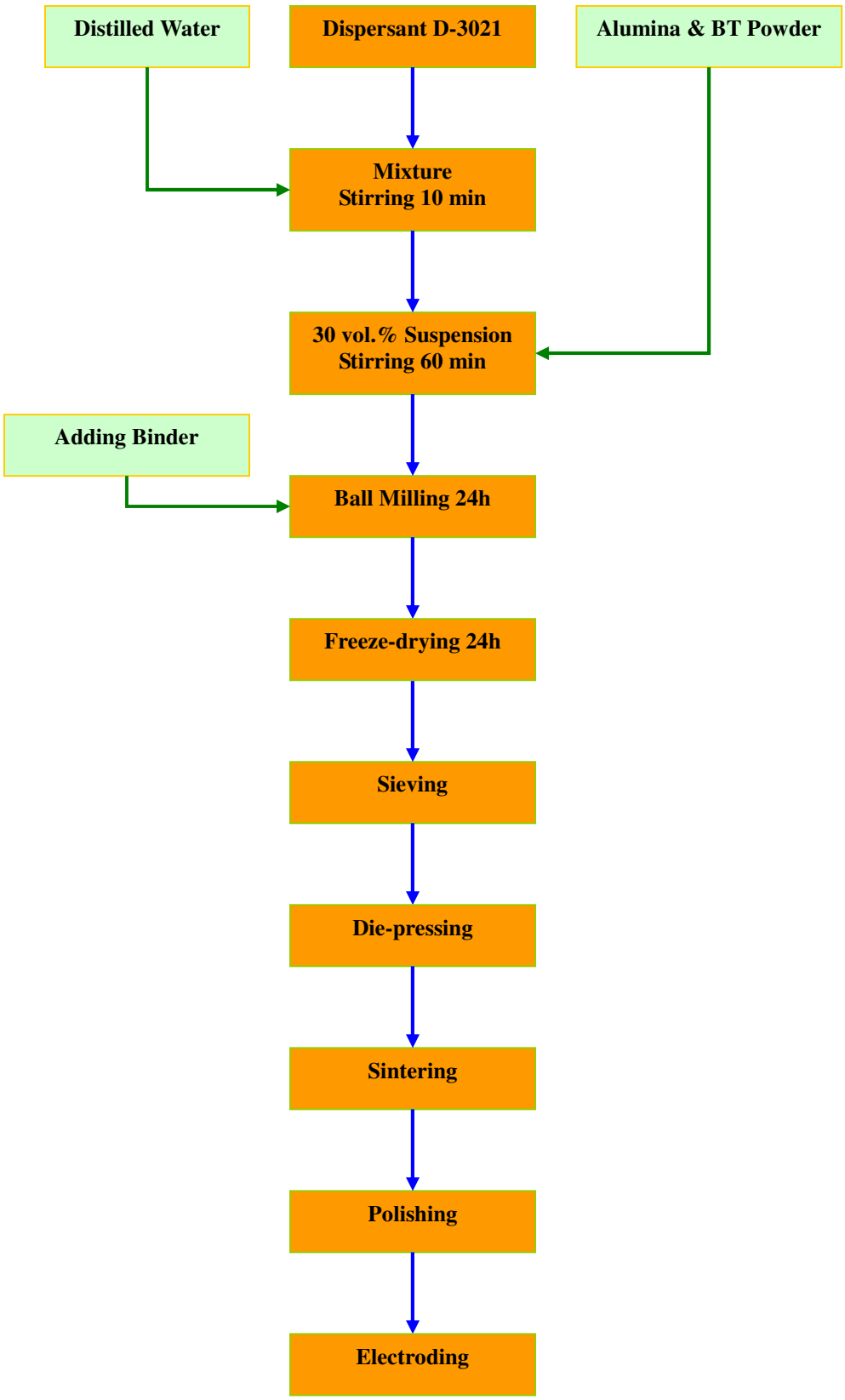

Figure 3.8 Flow chart of the fabrication process for the alumina-doped BT ceramics.

3.1.5 Fabrication of BT-Epoxy and PZT-Epoxy Composites

The sintered porous BT (or Alumina doped Barium Titanate (BAT)) and PZT ceramics were backfilled with an epoxy resin (Cat.No: 4020029, Struers, DK-2750 Ballerup, Denmark) in a vacuum container for 1~2 hours. Curing was done in a 40-degree oven for 24 h. After curing, composites were cut into discs (1~2 mm thick) along the direction perpendicular to the ice front using a precision diamond saw. After polishing, gold electrodes were sputtered on both sides of the sample by a sputter coater (Cr target, at 100 mA current strength for 2 mins, then Au target, at 80 mA current strength for 2 mins). Poling was done in a custom built corona poling machine under a voltage of 28 kV. The poling temperature and time for the BT based samples were 130 ℃ and 30 min according to Bowen's work[13]. For the PZT based samples, they were 90 ℃ and 10 mins, respectively according to our previous work[6]. The procedure for producing ceramic-epoxy composite is shown schematically in Figure 3.9.

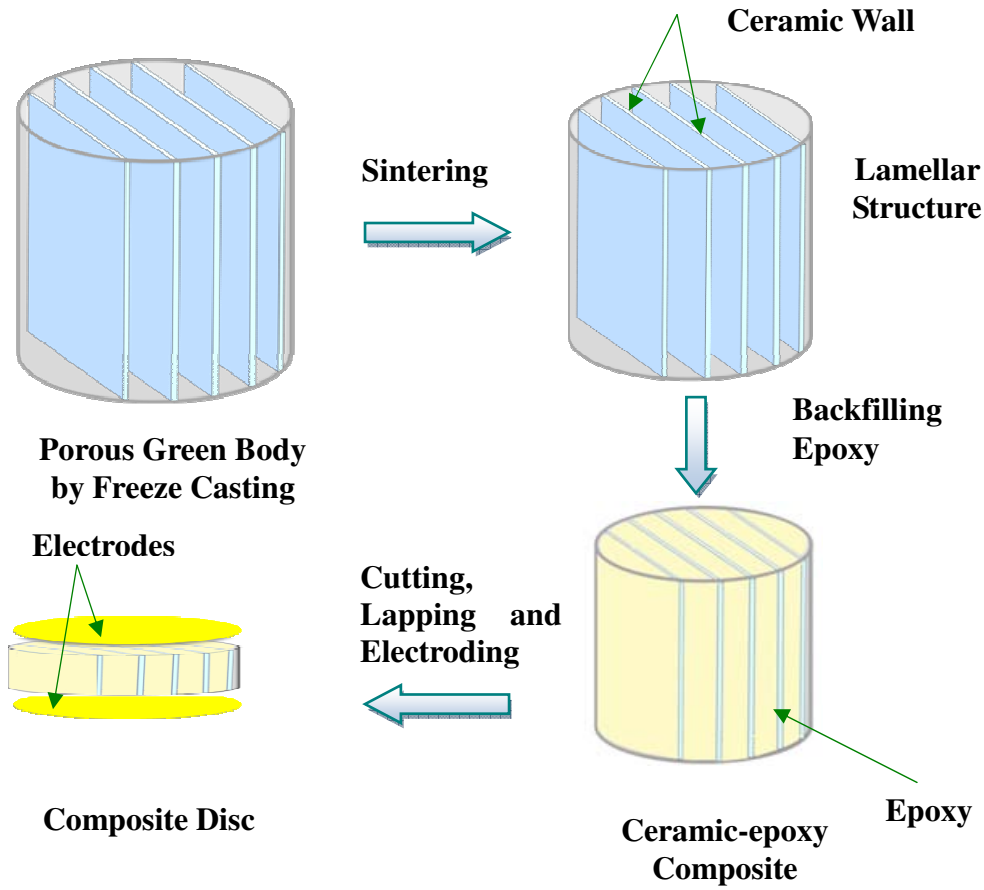

Figure 3.9 Schematic procedure for the fabrication of BT (or BAT) & PZT-epoxy composites.

3.1.6 Preparation of PVA Solution

The PVA aqueous solutions (5 wt.% and 20 wt.%) used in Chapter 4 were made by the conventional method. A beaker was filled with appropriate amounts of distilled water. The distilled water was heated to 90 °C using a hot plate. Polyvinyl alcohol (Nippon Gohsei, Osaka, Japan) was then lightly sprinkled into the water while stirring continuously using a magnetic stirrer. The addition of PVA into water was done lightly and slowly until a clear PVA solution was obtained.

3.2 Property Characterization

3.2.1 Particle Size Analysis

A laser diffraction particle size analyzer (Sympatec GmbH System-Partikel-Technik) was employed to measure the particle size of the ceramic powders. Distilled water and $Na_4P_2O_7$ were utilized as the solvent and dispersant, respectively. One drop of $Na_4P_2O_7$ and ~ 0.5 g ceramic powder were first added to a vial, and then the distilled water was added to the vial (5 ml) to prepare the suspension. The vial with the prepared suspension was then sonicated for about 30 seconds in the Sympatecs integral ultrasonic bath. After sonication, a reference was taken immediately. The sample would then be measured. The measurement range in this study was from 0.25 μm to 87.5μm.

3.2.2 Viscosity Measurement

The rheological properties of the suspensions were investigated by using the CSL Rheometer (Carri-med 115/A) with the cone and plane system (Truncation: 59 microns; Core: 4 cm, 20º) at the temperature of 20 ºC. 4~6 drops of the suspension were added onto the measuring plate, which were then pre-sheared for 10 seconds before measuring. The measurement range of the shear rate was from 1 to 600 (1/sec) and the duration was 3 minutes.

3.2.3 Porosity and Volume Fraction Measurement

3.2.3.1 Mercury Method

The porosity was measured by mercury porosimetry (Autopore Ш 9400, Micromeritics, US). 0.6 ~ 0.8 g sample was utilized for each measurement. After weighing the sample, it was placed in the penetrometer for low pressure measurement and then for high pressure measurement. Data was recorded by the computer. Due to a breakdown of the equipment,

only the porosities of porous alumina with PVA addition two-phase porous alumina-zirconia were measured in this way. Porosities of other porous ceramics were measured by the method described below.

3.2.3.2 Archimedes's Method

The densities of the porous ceramic and ceramic-epoxy composites were obtained by Archimedes' method. The total porosity of the porous ceramics was derived from the density. The calculation of the porosity was based on the theoretical densities of different ceramic materials (Al_2O_3: 3.96 g/cm^3, BT: 6.02 g/cm^3, PZT: 8.02 g/cm^3). The formulas are shown below:

$$\rho_A = \frac{W_d}{W_d - W_w} \text{ (g/cm}^3\text{)} \qquad (3\text{-}1)$$

$$p = \frac{\rho_A}{\rho_T} \times 100\% \qquad (3\text{-}2)$$

where ρ_A means the apparent density, ρ_T means the theoretical density, W_d means the dry weight, W_w means the wet weight, and p means the total porosity.

The volume fraction of ceramic in the composites was calculated using the mixing rule and the following equation:

$$\text{BT(PZT)vol.\%} = \frac{\rho_{\text{composite}} - \rho_{\text{polymer}}}{\rho_{\text{BT(PZT)}} - \rho_{\text{polymer}}} \qquad (3\text{-}3)$$

where $\rho_{\text{composite}}$, ρ_{polymer}, $\rho_{\text{BT(PZT)}}$ are the densities of composites, polymer and pure BT (PZT), respectively. The densities of bulk BT (PZT) ceramic and polymer were referred as 5.67 (7.77) g/cm^3 and 1.1 g/cm^3, respectively.

3.2.4 Linear Shrinkage Measurement

The linear shrinkage of the samples was obtained using measurements of sample diameters

before and after sintering, and calculated by the following equation:

$$L = \frac{\varphi_b - \varphi_a}{\varphi_b} \times 100\% \qquad (3\text{-}4)$$

where L is the linear shrinkage, φ_b is the diameter of the sample before sintering, and φ_a is the diameter after sintering.

3.2.5 Mechanical Property Measurement

Compressive strength was measured to evaluate the mechanical properties of the porous ceramics or composites. Cubes 4×5×5 mm[14] were cut off from the sintered porous ceramic or composite by using a precision diamond saw (Struers Accuton-50). Compression tests were carried out parallel to the freezing direction of the samples using an Instron testing machine (Series IX, Instron limited, UK), with a crosshead speed of 0.2 mm/min. Six samples were tested to obtain the average value.

The mechanical properties (surface hardness) of bulk BT and alumina doped BT ceramics were measured using a Leitz Miniload 2 Microhardness Tester with a Vickers indenter under an applied load of 25 gf (~0.25 N). In view of the scatter of the microhardness data, the hardness value reported was a mean of at least three measurements made under the same conditions[15].

3.2.6 Frequency Dependence Dielectric Property

The room temperature frequency dependence of capacitance and dielectric loss of the BT-based ceramic and composites reported in Chapter 6 were measured by using an impedance /gain-phase analyzer (Hewlett Packard 4194A). Samples are in the form of disc with gold electrodes on both sides. The dielectric constant ε_r was calculated by using the following formula:

$$\varepsilon_r = \frac{4C_S d}{\pi \varepsilon_0 D^2} \tag{3-5}$$

where C_S is the capacitance, d is the thickness of disc, D is the diameter of the disc, ε_0 is the permittivity of free space (= 8.8542×10^{-12} F/m).

3.2.7 Piezoelectric Parameters Measurement

The longitudinal piezoelectric coefficient d_{33} of the ceramic and composites reported in Chapter 6 and 7 was directly recorded from a d_{33} meter (YE2730A, Sinoceramics Piezo d_{33} test system, Shanghai, China). Samples are in the form of disc with electrodes. Six readings from each surface of the sample were done to obtain the average value.

3.2.8 Impedance Analysis

A Hewlett Packard 4194A impedance analyzer was also employed to characterize the electrical impedance of 2-2 PZT piezocomposites described in Chapter 7. The measurement frequency range was from 100 kHz to 300 kHz. The planar coupling factor k_p is obtained from the fundamental mode parallel resonance frequency (f_p) and the series resonance frequency (f_s) of a thin disc using the following curve in Figure 3.10:

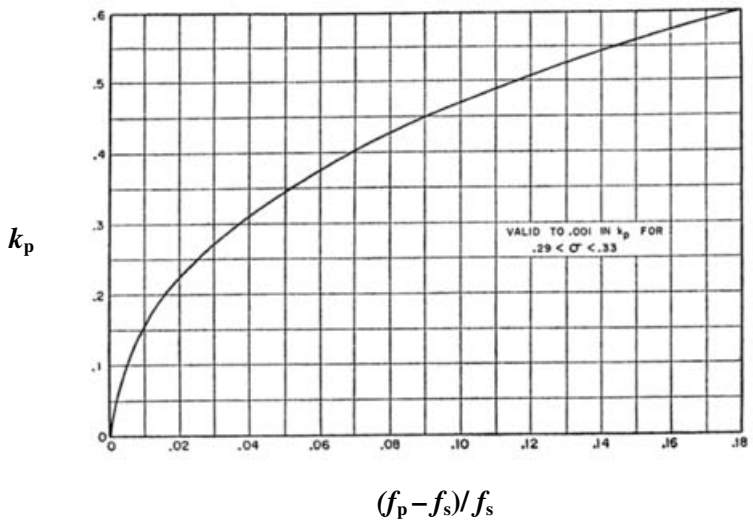

Figure 3.10 Planar coupling factor of thin disc (after Jaffe)[16].

3.2.9 Thermal Analysis

Differential scanning calorimetry (DSC) (Perkin Elmer DSC7, UK) was employed to detect the phase transition temperature of the bulk alumina doped BT ceramics. DSC was conducted in a flowing argon atmosphere under a heating rate of 10 ℃/min. The typical amount of sample was 15 mg. Samples are in the bulk form.

3.2.10 X-ray Diffraction

Any phase analysis was done by using an X-ray diffractometer (Philips X'pert) with monochromatic CuKα radiation. The detection is normally from 10 ° to 80 ° with a step size of 0.02 ° and a speed of 1.2 °/min. Comparison of XRD patterns with JCPDS standards was carried out to identify the crystalline phases.

3.2.11 Microstructure Characterization

The microstructure of the samples was analyzed by both optical microscopy (Techno RZ Series) and scanning electron microscopy (SEM) (JSM6060 and JSM 7000, Jeol, Tokyo, Japan). Energy dispersive X-ray (EDX) was done using an Oxford Inca EDX system to evaluate the chemical composition of the samples. Sample preparation was shown below: samples were first stuck to SEM stubs (stainless steel) through carbon adhesive tape, and a thin layer of gold was coated on the surfaces by sputter coating at 80 mA for 2 min. EDX spectra were acquired using an accelerating voltage 20 kV, a working distance of 10 mm, an acquisition time of 60 s and zero sample tilt. Any size obtained from the SEM photos, such as ceramic wall thickness and particle size, is the average value of 30 measurements.

References

1. S. Deville, E. Saiz, and A.P. Tomsia. Ice-templated porous alumina structures. Acta Materialia, 2007, 55, 1965-1974.

2. T. Waschkies, R. Oberacker, and M.J. Hoffmann. Control of lamellae spacing during freeze casting of ceramics using double-side cooling as a novel processing route. Journal of the American Ceramic Society, 2009, 92(1), S79-S84.

3. G. Liu, D. Zhang, and T.W. Button. Porous Al_2O_3-ZrO_2 composites fabricated by an Ice template method. Scripta Materialia, 2010, 62, 466-468.

4. G. Liu, D. Zhang, and T.W. Button. Preparation of concentrated barium titanate suspensions incorporating nano-sized powders. Journal of the European Ceramic Society, 2010, 30, 171-176.

5. D. Zhang, B. Su, and T.W. Button. Preparation of concentrated aqueous alumina suspensions for soft-moulding microfabrication. Journal of the European Ceramic Society, 2004, 24, 231-237.

6. D. Zhang. Fabrication of ceramic micro-components. PhD thesis, University of Birmingham, October, 2005.

7. J.A. Lewis. Colloidal processing of ceramics. Journal of the American Ceramic Society, 2000, 83(10), 2341-2359.

8. D.M. Liu. Preparation and characterisation of porous hydroxyapatite bioceramic via a slip-casting route. Ceramics International, 1998, 24(6), 441-446.

9. D.H. Yoon and B.I. Lee. Processing of barium titanate tapes with different binders for MLCC applications-Part I: Optimization using design of experiments. Journal of the European Ceramic Society, 2004, 24(5), 739-752.

10. O.O. Omatete, M.A. Janney, and S.D. Nunn. Gel casting: from laboratory development toward industrial production. Journal of the European Ceramic Society, 1997, 17(2-3), 407-413.

11. P.M. Biesheuvel, A. Nijmeijer, and H. Verweij. Theory of batchwise centrifugal casting. Amrican institute of chemical engineers. AIChE Journal, 1998, 44(8), 1914-1922.

12. D. Zhang, B. Su, and T.W. Button. Microfabrication of three-dimensional, free-standing ceramic MEMS components by soft moulding. Advanced Engineering Materials, 2003, 5 (12), 924-927.

13. C.R. Bowen, J.P. Gittings, and I.G. Turner. Dielectric and piezoelectric properties of hydroxyapatite-$BaTiO_3$ composites. Applied Physics Letters, 2006, 89, 132906.

14. S. Deville, E. Saiz, and A. P. Tomsia. Freeze casting of dydroxyapatite scaffolds for bone tissue engineering. Biomaterials, 2006, 27, 5480-5489.

15. J. Chen, X.Y. Li, T. Bell, et al. Improving the wear properties of Stellite 21 alloy by plasma surface alloying with carbon and nitrogen. Wear, 2008, 264, 157-165.

16. B. Jaffe, W.R. Cook, and H. Jaffe. Piezoelectric Ceramics, Academic Press, London, 1971.

CHAPTER 4 POROUS ALUMINA CERAMICS

4.1 Introduction

As described in Chapter 2, freeze casting is in its early stages of development; therefore, this chapter focuses on the freeze casting preparation technique. A single phase (ceramic phase) colloidal system was utilized and micro-sized alumina powder was employed as a model material. A variety of processing factors involved in the freeze casting process such as the rheological properties of the slurries, solids loadings of the slurries, cooling rate, sintering temperature, and their effects on the morphology and properties of the final sintered samples were investigated, and the results are presented and discussed in the first part of this chapter. The influence of additives (PVA, commercial binder, and glycerol) on the morphology of the porous microstructures was also investigated and is presented in the part of this chapter. Finally, an innovative technique of freezing (double-sided freezing) is presented and discussed.

4.2 Characterization of Alumina Powder

A SEM micrograph of the alumina powder (CT300SG, Caldic) used in this study is shown in Figure 4.1(a). It can be seen that the powders show an irregular morphology with a primary particle size of around 0.7μm, which is consistent with the result obtained from particle size distribution analysis as shown in Figure 4.1 (b) (d_{50} ~ 0.71 μm). Figure 4.1(c) shows the results of XRD analysis of this micro-sized alumina powder. By comparing the XRD pattern with JCPDS standards (No.10-173), the diffraction peaks from the particles can be indexed as alpha alumina.

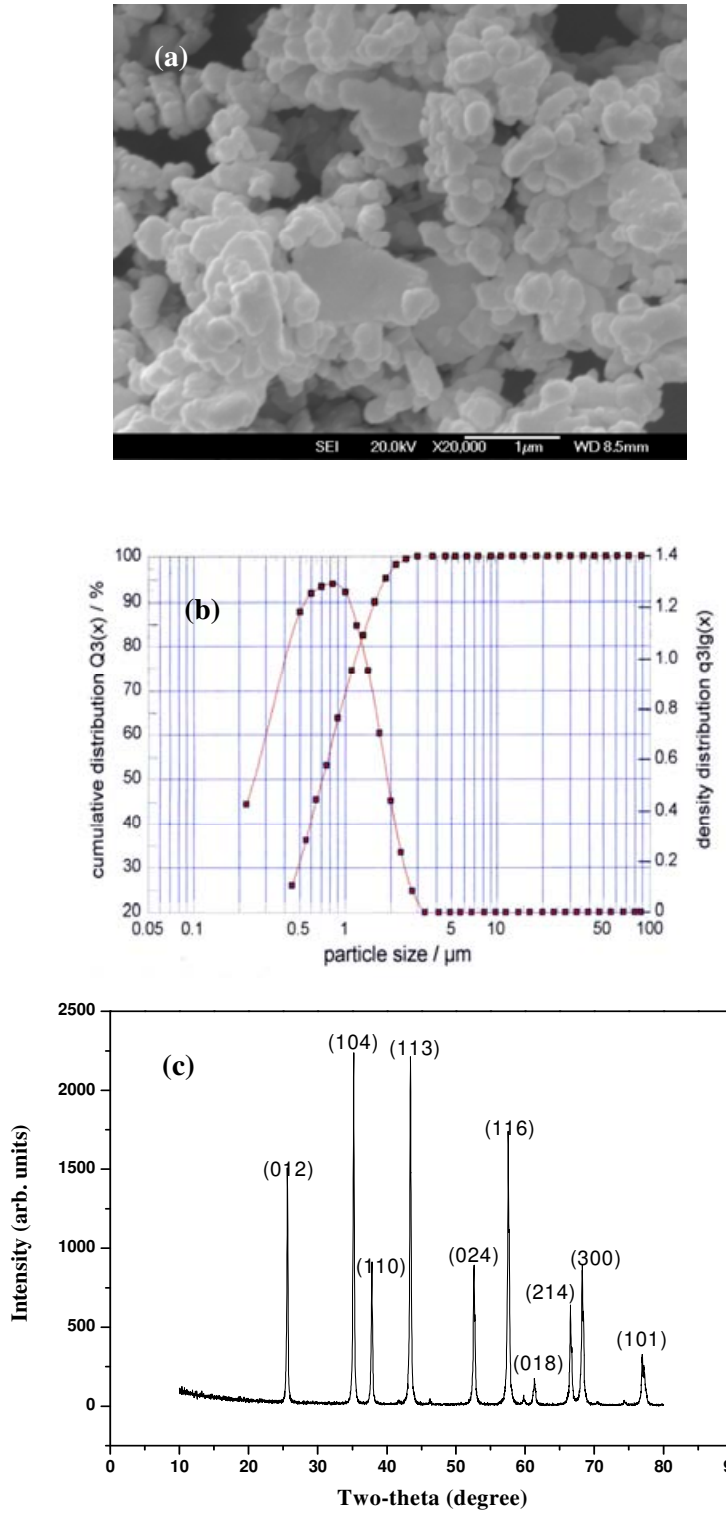

Figure 4.1 SEM photograph, particle size distribution analysis, and XRD pattern of the as-received alumina powders used in this study: (a) SEM photograph of the powder; (b) particle size distribution; (c) XRD pattern of the powder.

4.3 Rheological Properties of the Alumina Slurries

It is well known that the rheological properties of the colloidal suspensions are among their most important properties and play a very significant role in controlling the shape forming behaviour and optimizing the properties of the green body in all kinds of colloidal shape forming methods for ceramics[1], ranging from injection moulding[2] to slip casting[3]. Therefore, it was very necessary to measure the rheological properties of the slurries used in the current study.

Dispersant is widely used in the preparation of stable colloidal suspensions. The amount of dispersant used in a suspension can significantly affect the final properties of the slurries. Here, the amount of the dispersant used is based on Zhang's work[4] as discussed in Chapter 3.1.2.1 and will be detailed for each slurry.

Figure 4.2 shows the relationships between the shear stress and the shear rate, as well as between the viscosity and the shear rate for a 27 vol.% solids loading alumina slurry. The viscosity-shear rate curve shows that the viscosity decreased with increasing shear rate: at low shear rates, the viscosity was high to delay sedimentation, whilst at high shear rate the viscosity was low to produce a castable state, which represents a typical shear thinning behaviour. This behaviour is very common for all the colloidally stable ceramic powder slurries. At low shear rates the slurry structure is very close to the equilibrium structure at rest because thermal motion dominates over viscous forces. At higher shear rates the viscous forces affect the slurry structure more, and shear thinning occurs.

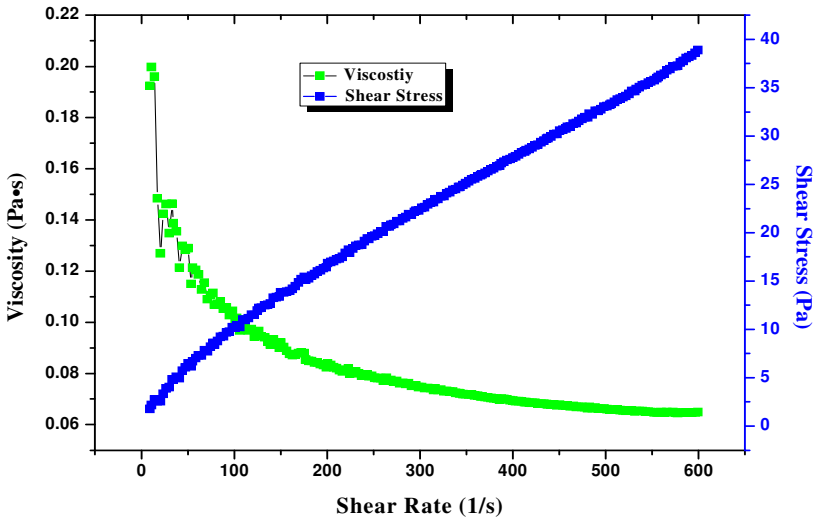

Figure 4.2 Typical rheological flow behaviour for the 27 vol.% solids loading alumina slurry with 0.14 wt.% NH_4PAA and 3 wt.% B1000 and 2 wt.% B1007 binders.

Figure 4.3 shows the effects of initial solids loadings on the rheological properties of the slurries. All the slurries showed shear thinning behaviour. Viscosities increased steadily with the increase of initial solids loadings. The viscosity of 20 vol.% solids loading slurry increased almost three times compared to that of 14 vol.% solids loading slurry under a shear rate of 100 s^{-1}. However, the change slowed down with further increases of initial solids loadings.

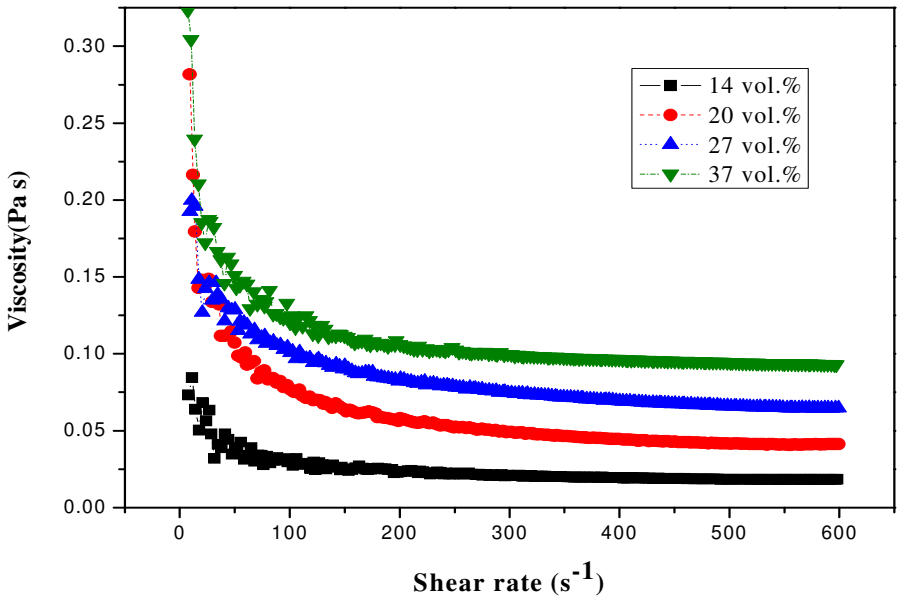

Figure 4.3 Viscosities of alumina slurries in dependence on the initial solids loading (vol.%) vs. shear rate. All slurries contain 0.14 wt.% NH_4PAA and 3 wt.% B1000 and 2 wt.% B1007 binders.

4.4 Comparison of Quench and Directional Freezing Techniques

As mentioned in Chapter 2, the solidification of the suspension is very important in the whole process of freeze casting. Therefore, two different ways were adopted to freeze the alumina slurry. The first method involved a partially quenched technique, in which the alumina slurry was poured over a cold finger that was maintained at a reduced and constant temperature. Figure 4.4 (a) presents the cross-sectional SEM micrograph of the sample obtained by this technique. Small areas of aligned channels (around 70~100 μm wide) can be observed in Figure 4.4 (a), but their orientations are almost random and no long-range order is found. The other technique was a directional freezing method using the equipment shown in Chapter 3 (Figure 3.3). Figure 4.4 (b) shows the cross-sectional micrograph for the sample obtained by the directional freezing technique. Lamellae and channels (around 10~25 μm wide) with relatively long-range order in the freezing direction can be found in this sample.

For the quenched sample, a steady initial freezing regime can not be achieved. Although channels and lamellar structures are obtained, their orientation over the cross section is random even in small area. However, by using the directional freezing technique, a relatively homogeneous freezing regime can be obtained easily, which leads to a much more homogeneous ice nucleation resulting in a lamellar porous structure and channels running continuously from nearly the bottom to the top of the sample perpendicular to the page. Unless explicitly stated otherwise, this study will focus on the directional freezing technique in order to obtain relatively homogeneous microstructures.

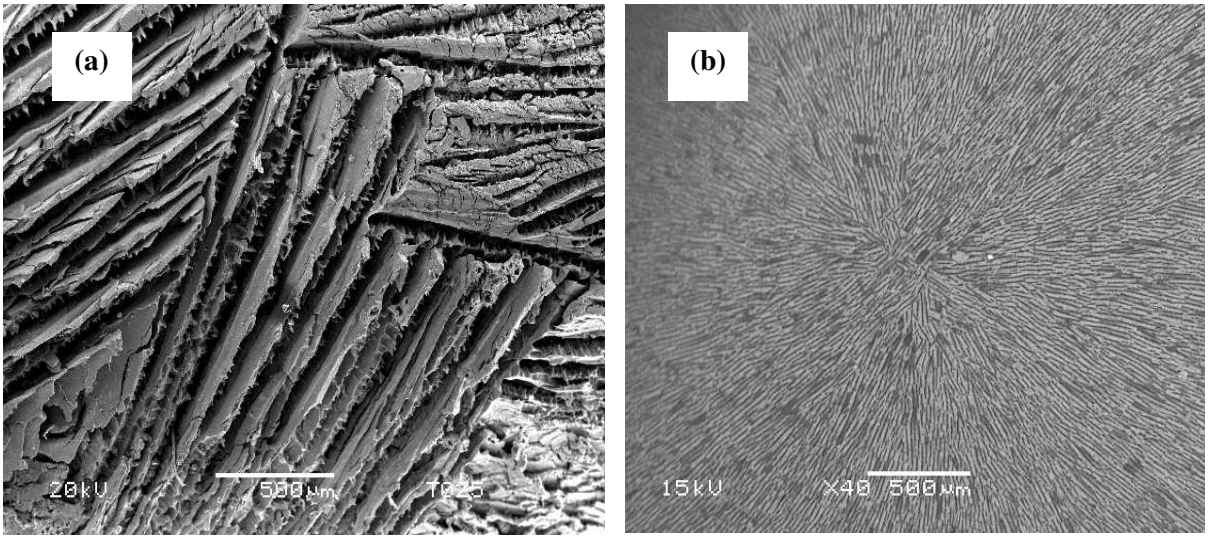

Figure 4.4 SEM micrographs of cross-sectional porous structures after sintering obtained from 27 vol.% solids loading alumina slurry with 0.14 wt.% NH_4PAA and 3 wt.% B1000 and 2 wt.% B1007 binders: (a) obtained by the quench technique (from the surface of the sample), (b) obtained by the directional freezing technique (from 1mm below the top of the sample), ice growth direction is perpendicular to the page.

4.5 General Characteristics of Samples Produced by Directional Freeze Casting

Figure 4.5 shows typical sintered samples (~10 mm in diameter and ~11 mm in height) obtained through directional freezing of alumina suspensions. There is no visible crack or distortion. Figure 4.6 shows the results of XRD analysis of the sintered sample. By

comparing XRD patterns with JCPDS standards (No. 10-173), the diffraction peaks from the sintered sample can be indexed as α-Al_2O_3, the only phase present. No secondary phases were found in the sintered samples.

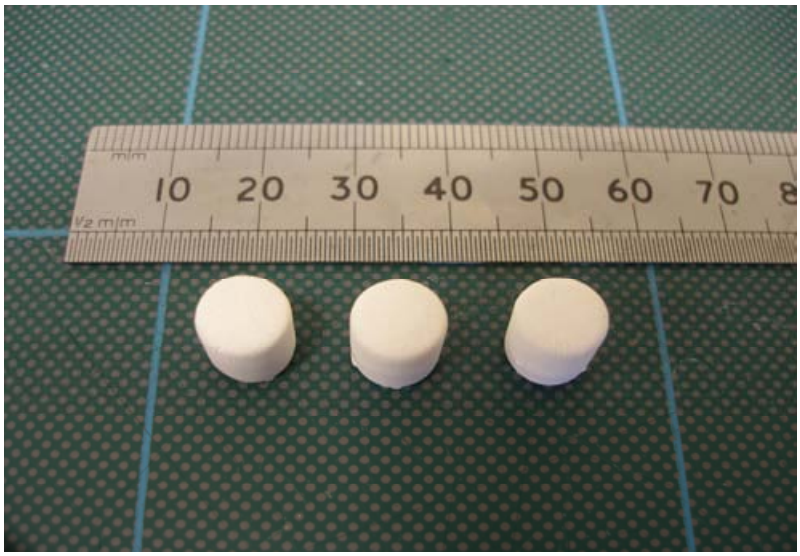

Figure 4.5 Typical sintered samples (at 1500 ºC, 2h) obtained from 20 vol.% solids loading alumina slurry with 0.14 wt.% NH_4PAA and 3 wt.% B1000 and 2 wt.% B1007 binders through directional freezing casting under a cooling rate of 0.5 ºC/sec.

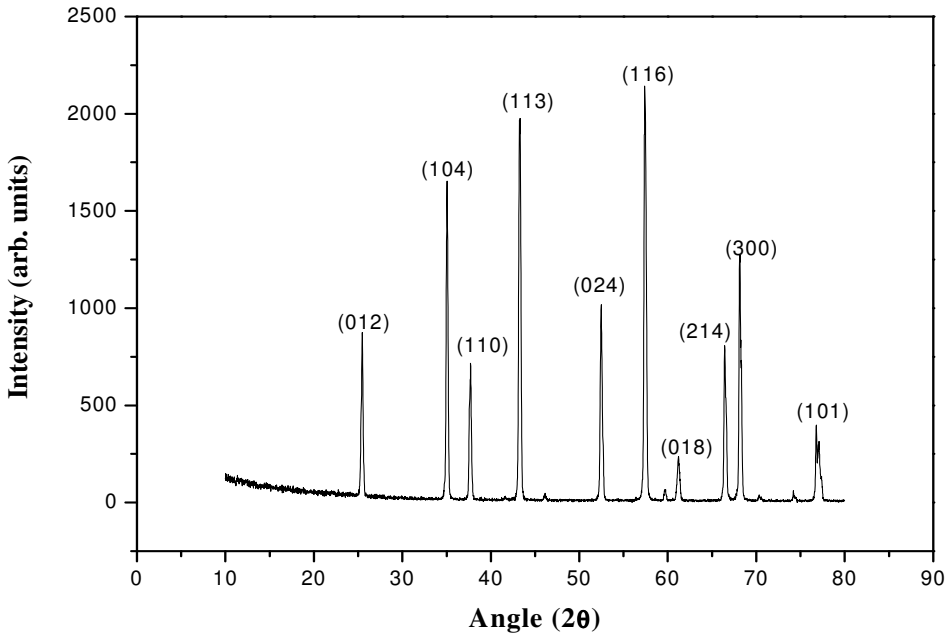

Figure 4.6 XRD spectrum of the typical sintered alumina sample (at 1500 ºC, 2h) obtained from 27 vol.% solids loading alumina slurry with 0.14 wt.% NH_4PAA and 3 wt.% B1000 and 2 wt.% B1007 binders through directional freezing casting under a cooling rate of 0.5 ºC/sec.

When freezing the slurries, the ceramic particles in the suspensions can be ejected from the advancing ice front and concentrate between the growing columnar ice crystals. After sublimation of the ice, a porous ceramic architecture will be produced whose microstructure is actually a negative replica of the ice crystals.

Figure 4.7 shows the microstructure of the samples shown in Figure 4.5. Because the samples were obtained through directional freeze casting, a homogeneous freezing regime could be obtained, which resulted in a much more homogeneous ice nucleation and ice growth leading to a lamellar porous architecture (Figure 4.7), with relative long-range order, both in the perpendicular (Figure 4.7(a)) and parallel (Figure 4.7 (b)) directions of the ice front.

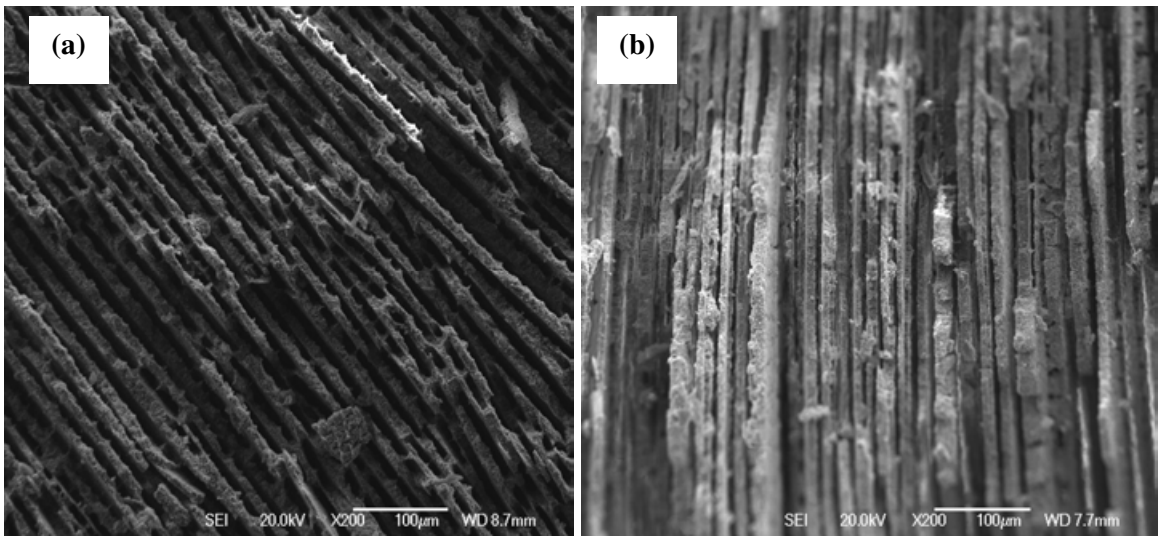

Figure 4.7 SEM micrographs of homogeneous sintered lamellar alumina cross-sections obtained from 20 vol.% solids loading alumina slurry with 0.14 wt.% NH_4PAA and 3 wt.% B1000 and 2 wt.% B1007 binders through the directional freezing casting under a cooling rate of 0.5 ºC/sec: (a) perpendicular to the ice front (ice growth direction coming out of the picture); (b) parallel to the ice front (ice grows from bottom to top).

The SEM microstructure of the lamellae ceramic walls are shown in Figure 4.8. After sintering, the ceramic walls become very dense. The surface exhibited a special morphology: one side remained smooth (red circle zone), and the other side had small ceramic arms (the

blue arrow zone).

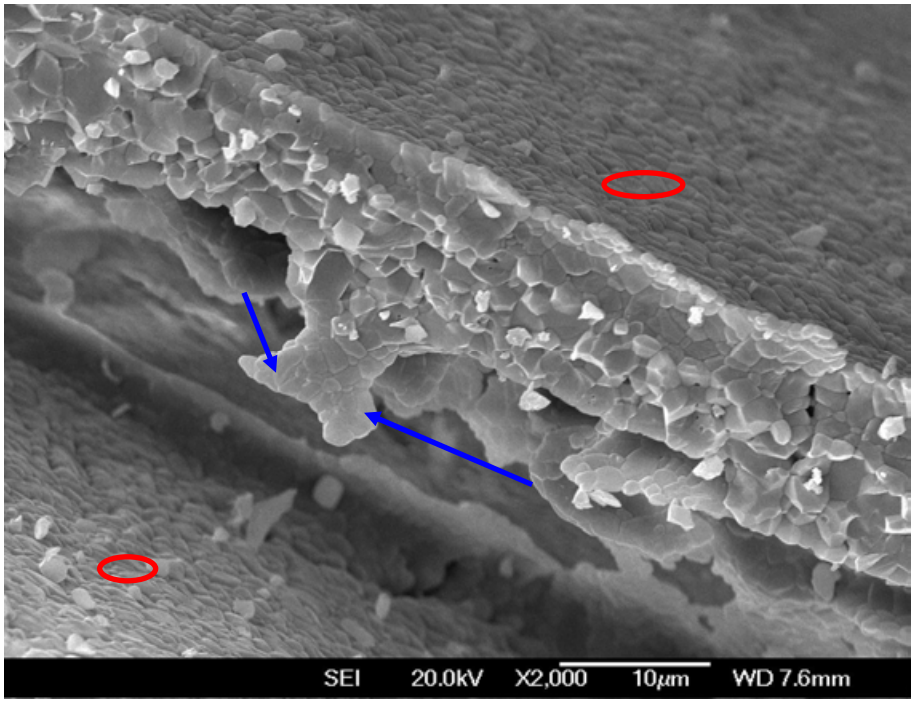

Figure 4.8 SEM micrograph of lamellae surface features: rough side and smooth side, sample was obtained from 20 vol.% solids loading alumina slurry with 0.14 wt.% NH_4PAA and 3 wt.% B1000 and 2 wt.% B1007 binders through directional freezing casting under a cooling rate of 0.5 ºC/sec

A schematic diagram of the microstructure of the samples obtained through the directional freeze casting technique is shown in Figure 4.9, which is very consistent with Deville's[5] work on hydroxyapatite.

Due to the characteristics of their architecture, the sample can be divided in sequence into three distinctive zones along the solidification direction (dense, cellular, and lamellar zone), each of them demonstrated by different morphologies. SEM photos of the different zones in one sintered sample are shown in Figure 4.10. As shown in Figure 4.10 (a), it's the closest part to the cold finger, and the morphology of it was much less porous compared with the other two zones, this is defined as the dense zone (Zone 1, corresponding part shown in Figure 4.9). A cellular microstructure was observed in Figure 4.10(b), therefore, this is

defined as the cellular zone (Zone 2). Finally, as presented in Figure 4.10(c), the architecture of the ceramic was lamellar (Zone 3), with long-range parallel pores. We define this as the lamellar zone.

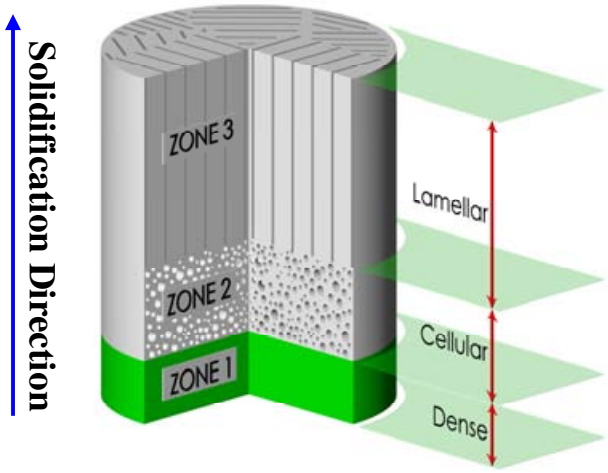

Figure 4.9 Schematic diagram of the microstructure for the samples obtained through directional the freeze casting technique (after Deville[5]).

The existence of three zones in the sample shown above is basically dominated by the fundamentals of the physics of freezing. The sequence leading to a steady ice front is widely known[6] and includes a gradual evolution of the ice front morphology (from planar to cellular and cellular to lamellar)[5], because of the gradual set up of supercooling ahead of the ice front induced by the ceramic particles. This transition is reproduced in the microstucture close to the initial freezing front. The transition zone is shown in the middle of Figure 4.11. Once the transition has happened, a steady condition is obtained, and the ice front keeps its morphology. Therefore, two different structures are achieved in the ceramic samples shown in Figure 4.11. The bottom part in Figure 4.11, obtained under the cellular regime, displayed a cellular structure. However, zone 3 exhibited lamellar morphology, with open and interconnected porosity. This study will only focus on the third zone (zone 3, lamellar zone) if there is no special declaration made.

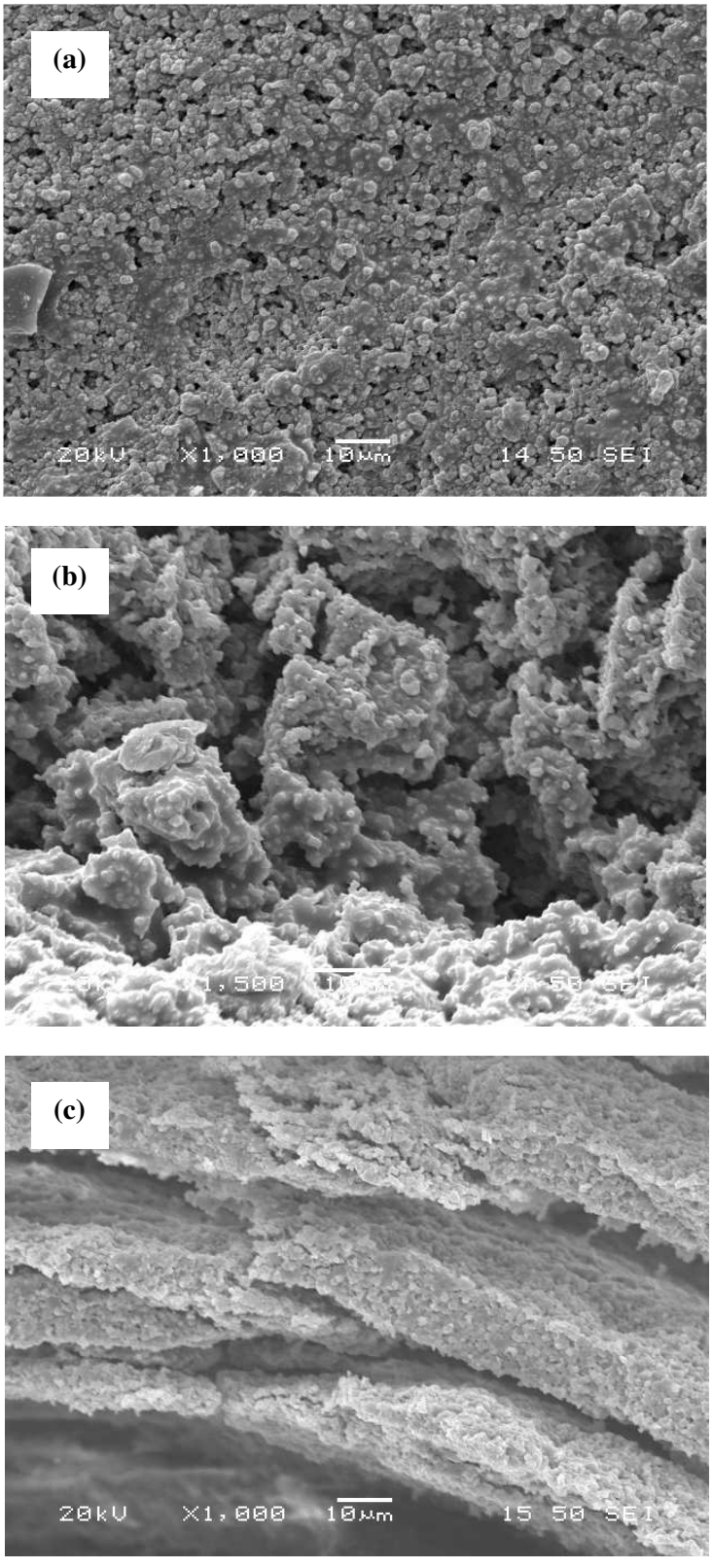

Figure 4.10 SEM photos of different zones in one sintered alumina sample: (a) dense, (b) cellular, (c) lamellar (sample was obtained from an 23 vol.% initial solids loading slurry with 0.14 wt.% NH_4PAA and 3 wt.% B1000 and 2 wt.% B1007 binders and the cooling rate was 0.5 ºC/sec).

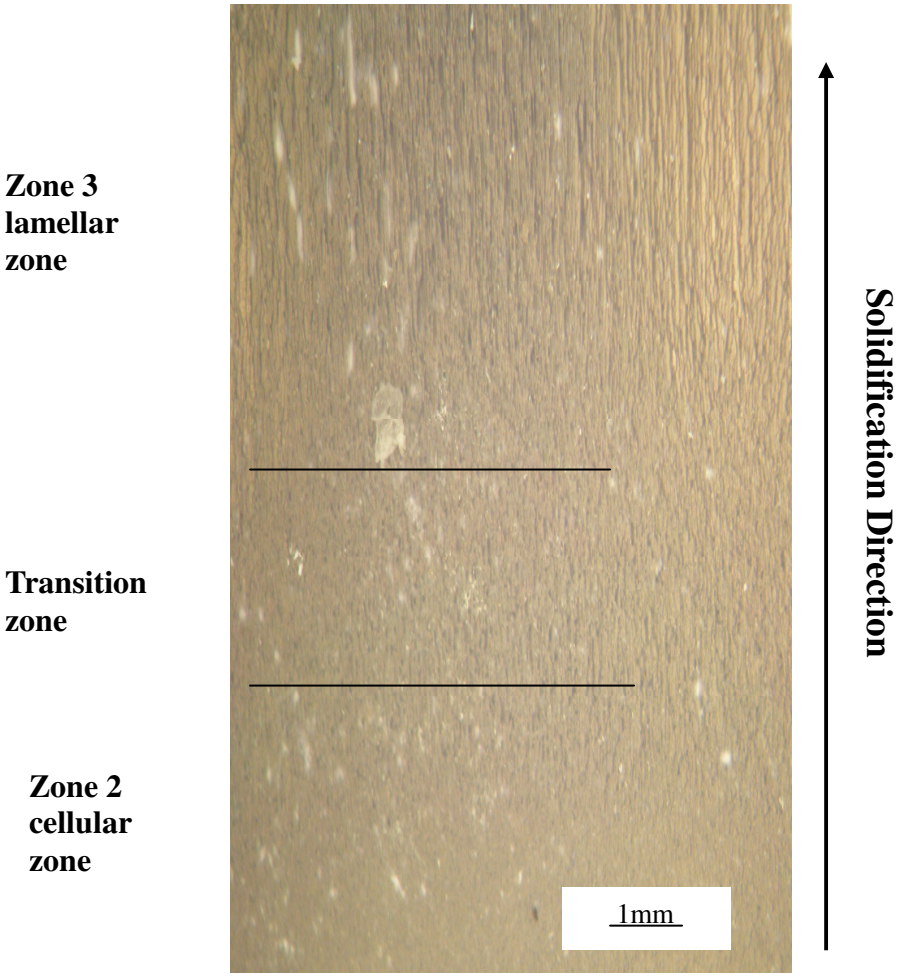

Figure 4.11 Microstructure of sintered alumina sample, obtained from 23 vol.% initial solids loading slurry with 0.14 wt.% NH_4PAA and 3 wt.% B1000 and 2 wt.% B1007 binders, cooling rate of 0.5 ºC/s, sintered at 1525 ºC for 2h.

4.6 Effect of Initial Solids Loading

In order to characterize the effects of initial solids loadings in the freeze casting process, four suspensions with different initial solids loadings (14, 20, 27, 37 vol.%) were prepared and used to fabricate porous alumina ceramics.

4.6.1 Porosity

Figure 4.12 presents the relationship between the total porosity of the sintered sample and the initial solids loadings. All the samples produced for total porosity measurement (by

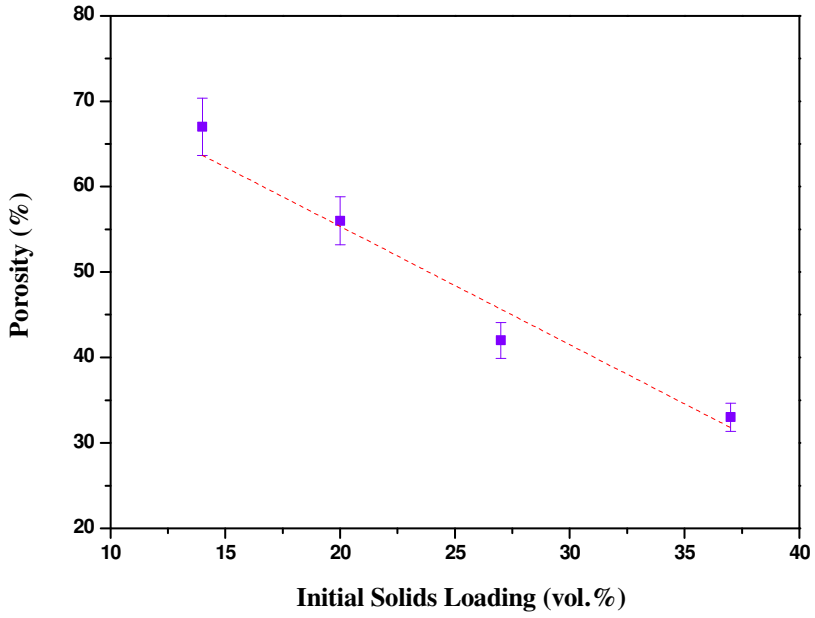

Figure 4.12 Total porosity of sintered alumina samples versus initial solids loading. The samples are obtained from different initial solids loading slurries with 0.14 wt.% NH_4PAA and 3 wt.% B1000 and 2 wt.% B1007 binders, under a cooling rate of 0.5 ºC/s, and sintered at 1525 ºC for 2h

Archimedes's Method) were sintered at 1525 ºC for 2 hours. As the solid loading is increased, the porosity was found to decrease proportionately. With increasing initial slurry concentration from 14 vol.% to 37 vol.%, the total porosity decreased from about 67% to 33%. The linear relationship between the porosity and the initial solid loading can be expressed as follows:

$$P = 83 - 1.4X \qquad (4\text{-}1)$$

Where P is the porosity, and X the solid loading. Therefore, the lower the initial slurry concentration, the higher the final porosity. This is to be expected as the volume of water controls much of the final porosity during the freeze casting of an aqueous system.

4.6.2 Ceramic Wall (Lamellae)

Figure 4.13 shows SEM micrographs of samples obtained from the different initial slurry

concentrations mentioned above. The cooling rate for these samples was 0.5 ^{o}C/sec and they are cross-section micrographs perpendicular to the ice front. As mentioned in Section 4.5, the ceramic walls of all the samples became dense after sintering. One marked phenomenon was that the wall thickness of the sintered samples increased distinctly from about 10 μm to 60 μm as the solids loading increased from 14 vol.% to 37 vol.%.

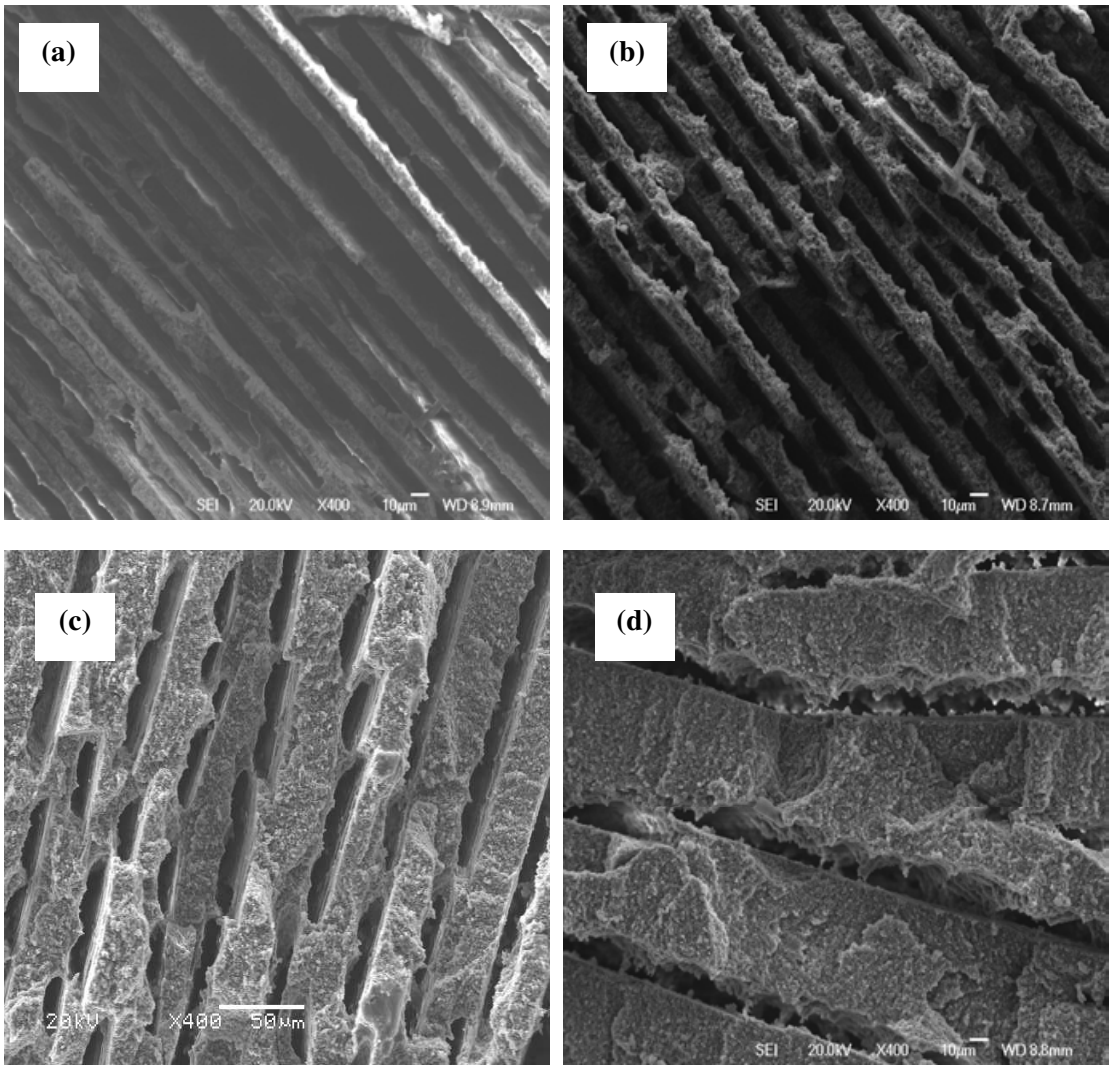

Figure 4.13 Cross-section microstructure of sintered samples (1525 ºC for 2h) (perpendicular to the ice front). Samples were obtained from different initial slurry concentrations ((a) 14 vol.%, (b) 20 vol.%, (c) 27 vol.%, (d) 37 vol.%.) with 0.14 wt.% NH_4PAA and 3 wt.% B1000 and 2 wt.% B1007 binders, and under a cooling rate of 0.5 ºC/sec.

Furthermore, the ratio (wall thickness/gap between walls) also increased markedly from

about to 0.5 to 6 with increasing the initial slurry solids loadings. This is because the increase of initial solids loading means the reduction of water content in the corresponding suspensions, resulting in smaller empty channels after sublimation of the ice.

4.6.3 Compressive Strength

Figure 4.14 shows the maximum compressive strength as a function of the initial solids loading and the curve shows nonlinear relationship.

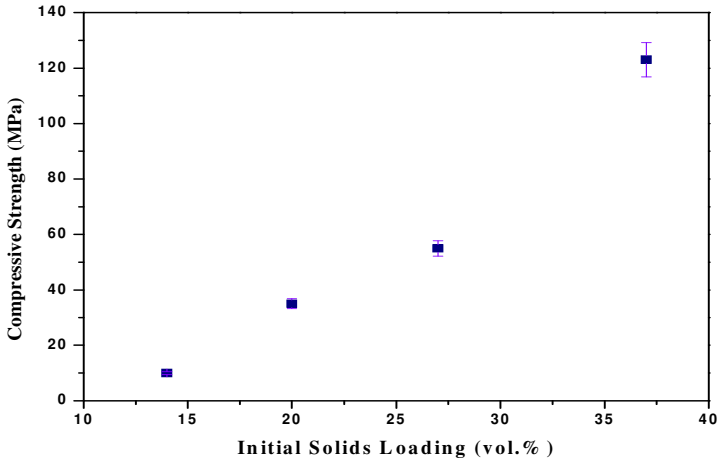

Figure 4.14 Maximum compressive strength versus slurry initial solids loading, samples (sintered at 1525 ºC for 2h) were obtained from different slurries with 0.14 wt.% NH_4PAA and 3 wt.% B1000 and 2 wt.% B1007 binders and under a cooling rate of 0.5 ºC/sec.

All the samples here were sintered at 1525 ºC for 2 hours. Although the compressive strength of the samples obtained from low solid loadings was low, it increased rapidly when the slurry concentration increased, reaching 55 MPa at 42% porosity for the 27 vol.% slurry and 123 MPa at 33% porosity for the 37 vol.% slurry. Usually there are many expressions which can be used to describe the porosity-strength behaviour of porous ceramics. One of the simplest expressions was developed by Rice[7] based on the minimum solid area approach and the resulting porosity-strength dependence can be approximated by an exponential function,

$$\sigma = \sigma_0 \exp(-bP) \qquad (4\text{-}2)$$

where σ_0 is zero-porosity strength, σ is the strength at pore volume fraction P, and the constant b is related directly to the pore characteristics.

The expected compressive strength according to equation (4-2) decreases with the increase of the porosity. The measured compressive strength shown in Figure 4.14 shows a same trend. Moreover, some investigation[8] showed that the mechanical behaviour of porous ceramic is determined mainly by the bending behaviour of the cell struts. The wall thickness shown in Figure 4.13 increased with the increase of the initial solid loading. Larger wall thickness results in larger compressive strength. Therefore, a higher slurry solid loading means larger wall thickness and finally leads to a higher compressive strength.

Particularly, the compressive strength values were higher compared with those with similar porosities reported in the literature, e.g. 23 MPa at 33% porosity and 13 MPa at 44% porosity) by fused deposition modeling[9], and 5.9 MPa at 67% porosity by sacrificial phase technique[10]. The porous aluminas reported in literatures[9,10] showed three-dimension interconnected structures. Thus the lamellae microstructure of the porous alumina ceramics in this study contributes much to the higher compressive strength.

In summary, it is clear that the final porous microstructure of the ceramic sample is a negative replica of the ice structure. The smooth freezing regime results in a more homogeneous ice nucleation[11] and ice crystal growth, and the ice crystals present a homogenous morphology throughout the whole sample, which leads to relatively homogenous wall thickness shown in Figure 4.13. All the changes caused by the initial slurry concentration shown in Figure 4.12, Figure 4.13 and Figure 4.14 indicate that the initial solids loading contributes much to the porosity , the wall thickness or the ratio of layer thickness/ gap thickness and the final mechanical property of the ceramic. Therefore,

modifying the ratio of the water in the slurry will alter the final properties of the porous ceramic.

Moreover, the range in which the porosity can be modified is physically limited by two phenomena. For a slurry with low solids content (lower than 14 vol.%, such as 5 vol.%, 10 vol.% has been tried), even with binder added, collapse of the green body occurs when sublimating the ice. On the other hand, when the solids loading is too high (≥ 50 vol.%, equals to 80 wt.%), the interaction between ceramic particles in suspensions becomes more important and particles cannot be ejected from the ice front, which finally results in loss of the porous architecture. This will be discussed later in Chapter 5.

4.7 Effect of Cooling Rate

It is well known that the freeze casting technique is based on the physics of ice, therefore, the control of the transition from water to ice (in other words, control of the freezing process) could be a very important factor. In order to characterize the effect of cooling rate in the freeze casting technique, different cooling rates were employed through changing the distance between the cold finger and the surface of liquid nitrogen, which was already shown schematically in Chapter 3 (Figure 3.3). Here, the value of the cooling rate was expressed through the time dependent temperature variation of the cold finger. Moreover, the slurry used here had a solids loading of 27 vol.% (with 0.14 wt.% NH_4PAA and 3 wt.% B1000 and 2 wt.% B1007 binders). Three different cooling rates were obtained through the method described above, respectively named as high cooling rate (HCR), medium cooling rate (MCR), and low cooling rate (LCR), which are shown in Figure 4.15.

The HCR showed a linear relationship, while the MCR and LCR almost showed a linear relationship but with some deviations. That is because the lower cooling rate means larger distance (between the cold finger and the surface of liquid nitrogen) compared with that of

HCR, finally resulting in the inhomogeneous distribution of the temperature gradient in the cylinder. The value of each cooling rate (the slope of the each line shown in Figure 4.15) was about 1.1 ºC/sec, 0.4 ºC/sec, 0.25 ºC/sec, respectively.

It should be noted that these values were not the actual cooling rates in the slurries during freezing because of the limitations of the equipment shown in Chapter 3 (Figure 3.3), i.e. temperature measurement of cold finger.

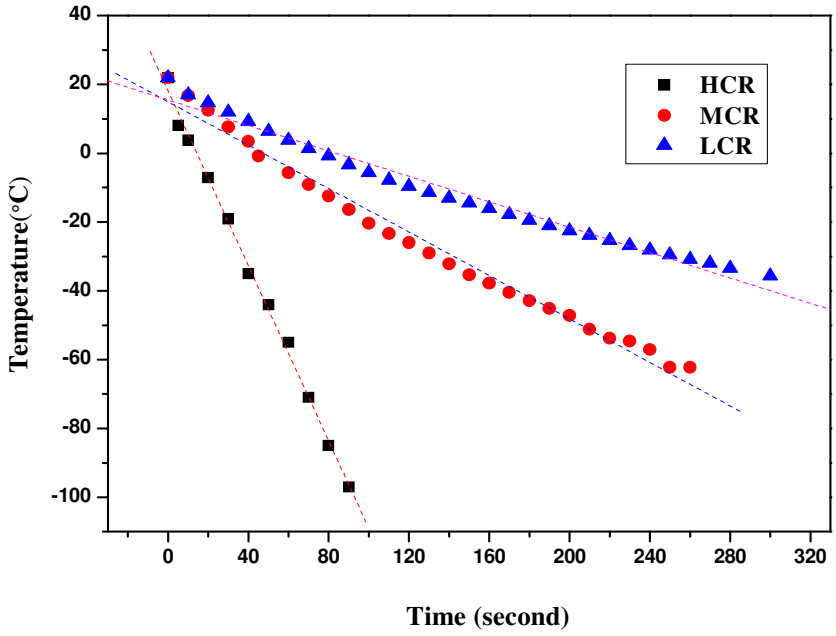

Figure 4.15 Different cooling rates used in this work from the measurement of the cold finger.

During the process of freezing, the ceramic particles in the suspension are ejected by the advancing ice solidification front and concentrate between the growing columnar or lamellar ice (as shown schematically in Figure 4.16), which is very similar to the way that salt and biological organisms are entrapped in the brine channels in sea ice[12,13]. The ice platelets grow in the direction perpendicular to the *c*-axis of hexagonal ice. In order to make a better description of the lamellar structure created by the ice, here, the wavelength of the structure is defined as λ, which is displayed schematically in Figure 4.16.

Figure 4.17 presents the SEM micrographs of the sintered samples (at 1525 ºC, 2h), which were obtained under the different cooling rates. It can be seen from Figure 4.17, the thickness of the ceramic wall varied over a wide range, from about 125 μm to 17 μm and it decreased dramatically as the cooling rate increased from 0.25 to 1.1 ºC/sec. Meanwhile, starting from the same initial solids loading, the wavelength λ (the gap between the walls) decreased from about 285 μm to 17 μm as the cooling rate increased.

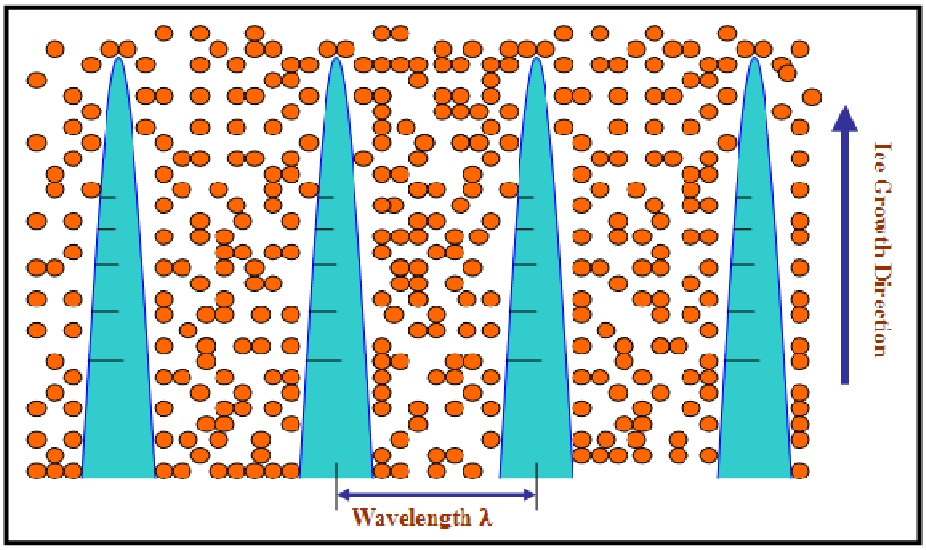

Figure 4.16 Pattern formation and particle segregation during freeze casting of ceramic slurries. Definition of wavelength (λ).

The relationship of the ceramic wall thickness and wavelength λ versus cooling rate (also expressed by the solidification rates which are described in Chapter 3.1.1) is summarized in Table 4.1.

Moreover, the microstructures of the samples shown in Figure 4.17 (b) and (c) were not very uniform compared with those shown in Figure 4.17 (a). That is mainly because the distribution of the temperature gradient was not very homogenous.

Table 4.1 Ceramic wall thickness and wavelength under different cooling rates

Cooling rate (ºC/sec)	Solidification rate (μm/s)	Ceramic wall thickness (μm)	Wavelength λ (μm)
1.1	110	17	17
0.4	45	89	179
0.25	20	125	285

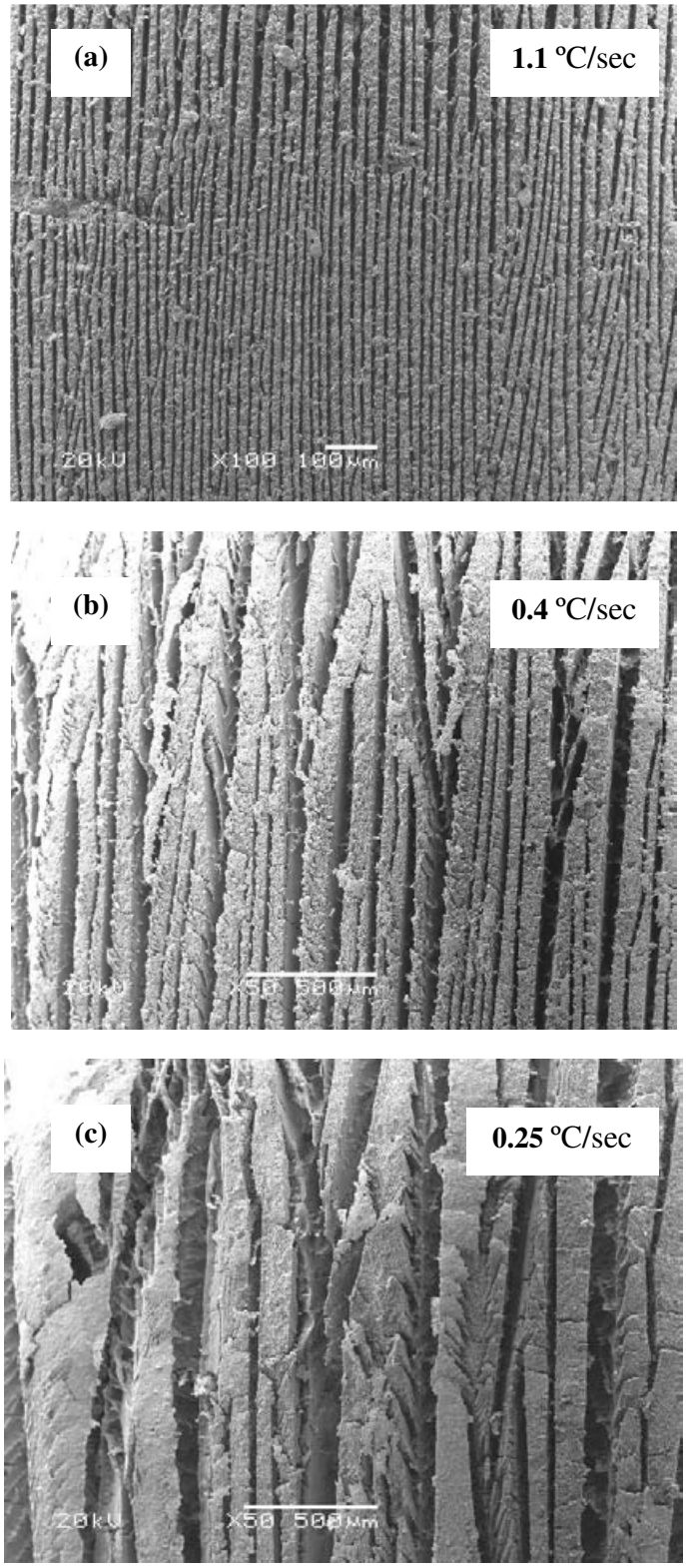

Figure 4.17 Surface of the sintered alumina samples (1525 ºC, 2h, parallel to the ice front). Samples were obtained from the same solids loading of 27 vol.% (with 0.14 wt.% NH_4PAA and 3 wt.% B1000 and 2 wt.% B1007 binders) but under different cooling rates: (a) 1.1, (b) 0.4, (c) 0.25 ºC/sec.

In summary, when the freezing kinetics is increased, in another word, the cooling rates (solidification front speed) increases, the supercooling becomes larger and the final microstructure (ice crystal and corresponding ceramic wall) is scaled down. Otherwise, under a low cooling rate (very slow solidification rate), the scale of the microstructure can be dramatically increased. Particularly, the wavelength of the ice crystals (λ), which is physically dominated by the magnitude of supercooling ahead of the ice front[14], can be accurately controlled by increasing or decreasing the cooling rate during the freezing process.

4.8 Effect of Sintering Temperature

It is known that sintering is the method for making ceramic from powder, by heating the material in a sintering furnace below its melting point (solid state sintering) until its particles adhere to each other and it is part of the firing process used in the manufacture of ceramic components. Sintering can convert a compacted powder into a denser structure of crystallites joined to one another by grain boundaries[15]. Therefore, the sintering conditions are of great significance for optimizing the physical and mechanical properties of the final ceramic components.

In this section, five different sintering temperatures were employed in order to characterize its effects on the properties of the final porous alumina ceramics.

Figure 4.18 presents the XRD results of the porous alumina ceramics with various sintering temperatures. There was little difference between the peaks for different sintering temperatures. By comparing XRD pattern with JCPDS standards, the diffraction peaks from all the sintered aluminas can be mainly indexed as α-alumina, although some variations in peak intensities were observed.

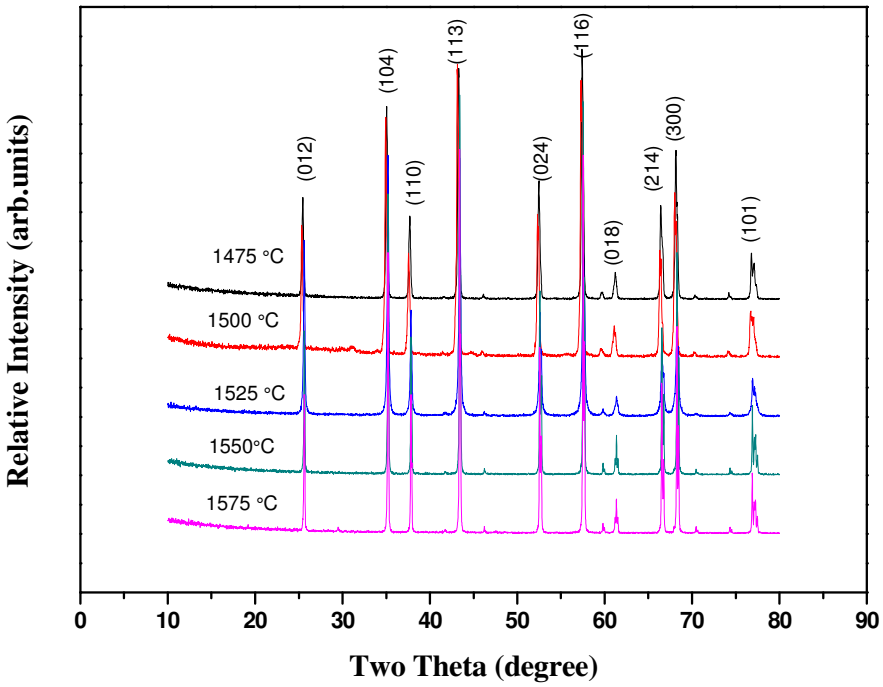

Figure 4.18 XRD patterns for porous alumina ceramics sintered at different temperatures. Samples were obtained from the same slurry with a solids loading of 27 vol.% (with 0.14 wt.% NH_4PAA and 3 wt.% B1000 and 2 wt.% B1007 binders) and under a cooling rate of 0.5 ºC/sec.

The porosity, compressive strength, and the grain size of the final porous alumina ceramics as a function of the sintering temperature are shown in Figure 4.19. Figure 4.19(a) presents the total porosity versus sintering temperature. When the sintering temperature increased from 1475 ºC to 1575 ºC, the final porosity of the samples decreased from about 48.0% to 40.0%. Higher sintering temperature leads to lower porosity. That is because higher sintering temperature always results in a larger shrinkage during the densification process.

The shrinkage is shown in Table 4.2. Shrinkages parallel and perpendicular to the ice front were measured. With an increase in the sintering temperature, the shrinkages in both directions increased, from 17.7% to 23.8% in the direction parallel to the ice front; and from 19.6% to 26.8% in the direction perpendicular to the ice front, respectively.

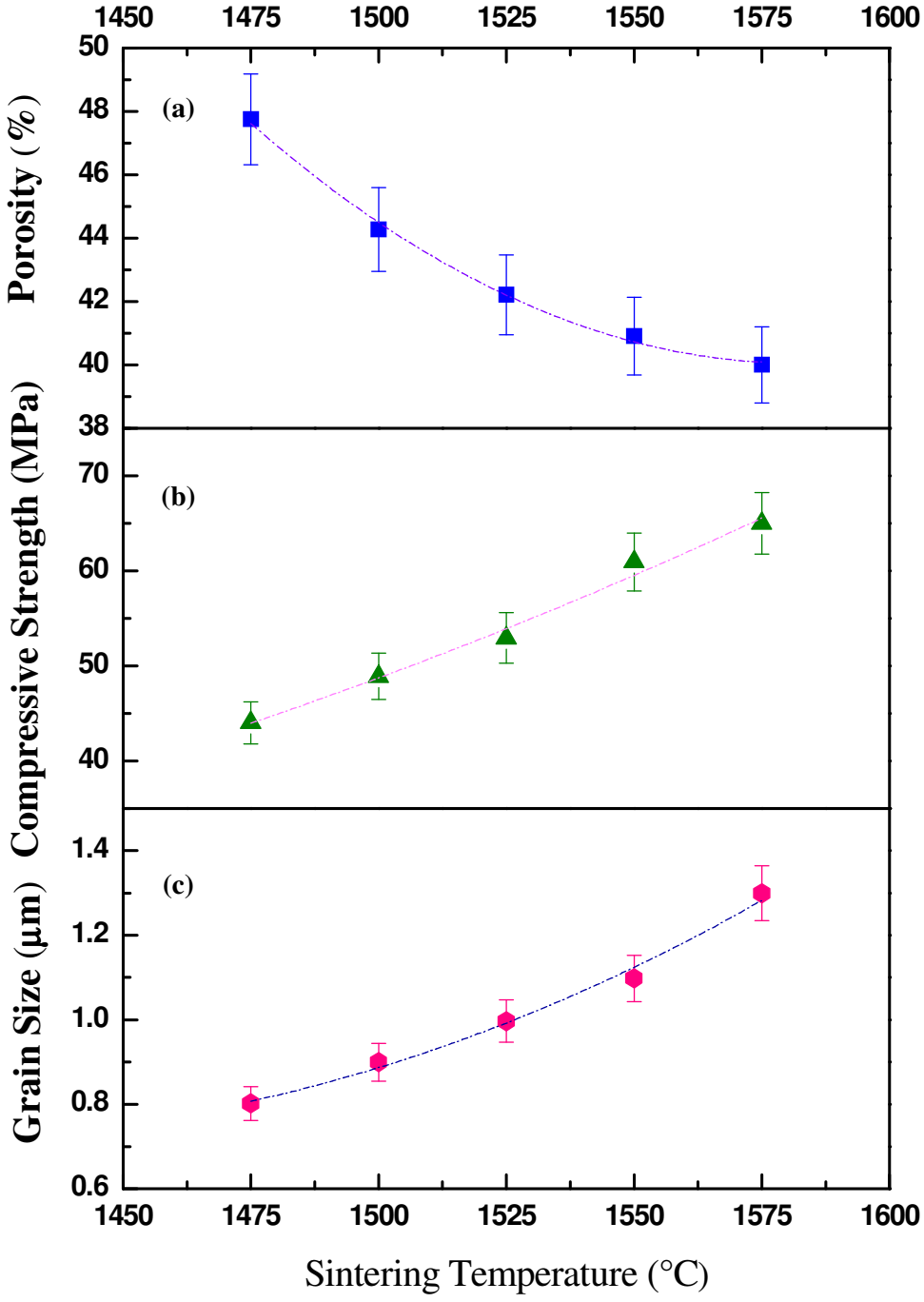

Figure 4.19 Influence of sintering temperature on total porosity, compressive strength and grain size for porous alumina samples fabricated by directional freeze casting. Samples were obtained from the same slurry with a solids loading of 27 vol.% (with 0.14 wt.% NH_4PAA and 3 wt.% B1000 and 2 wt.% B1007 binders) and under a cooling rate of 0.5 ºC/sec.

Table 4.2 Linear shrinkages for porous aluminas sintered at different temperatures

Temperature (ºC)	1475	1500	1525	1550	1575
S_1 (%)	17.7	20.5	22.5	23.3	23.8
S_2 (%)	19.6	22.9	23.7	24.3	24.8

Note: S_1, parallel to the ice front; S_2, perpendicular to the ice front (as shown in Figure 4.20)

Moreover, one interesting phenomenon was that the shrinkage in the direction perpendicular to the ice front was larger than that parallel to the ice growth direction. One possible explanation for this is that the direction parallel to the ice front is the direction where the alumina grain mainly grows, while, the direction perpendicular to the ice growth direction has large areas of porosity between the lamellae, so the shrinkage in the direction parallel to the ice front could be easily hampered by the growth of the grain. Therefore, the shrinkage perpendicular to the ice front was a little larger than that parallel to the ice growth direction and contributed more to the final porosity.

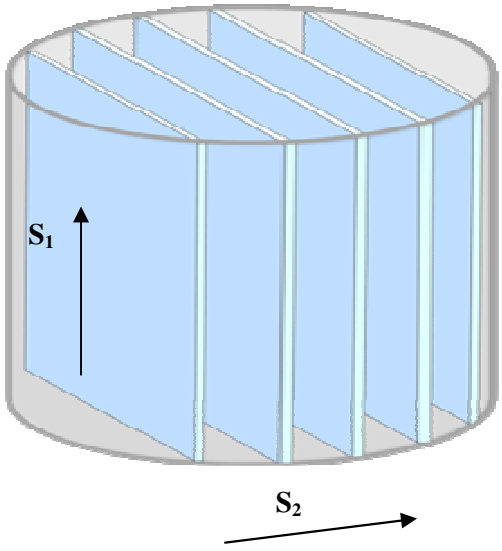

Figure 4.20 Schematic diagram of shrinkages for the sintered lamellae structure.

Figure 4.19 (b) presents the compressive strength of the sintered porous ceramics as a function of the sintering temperature. In the range of this study, the compressive strength was inversely proportional to the porosity, increasing with increasing sintering temperature. So,

in the range of our study, high sintering temperature led to higher compressive strength (of course with lower porosity).

Figure 4.21 displays the SEM photos of the sintered porous ceramics. With the increase of the sintering temperature, the ceramic walls became denser. Furthermore, the grain size increased slightly with increasing the sintering temperature, which is also shown in Figure 4.19 (c).

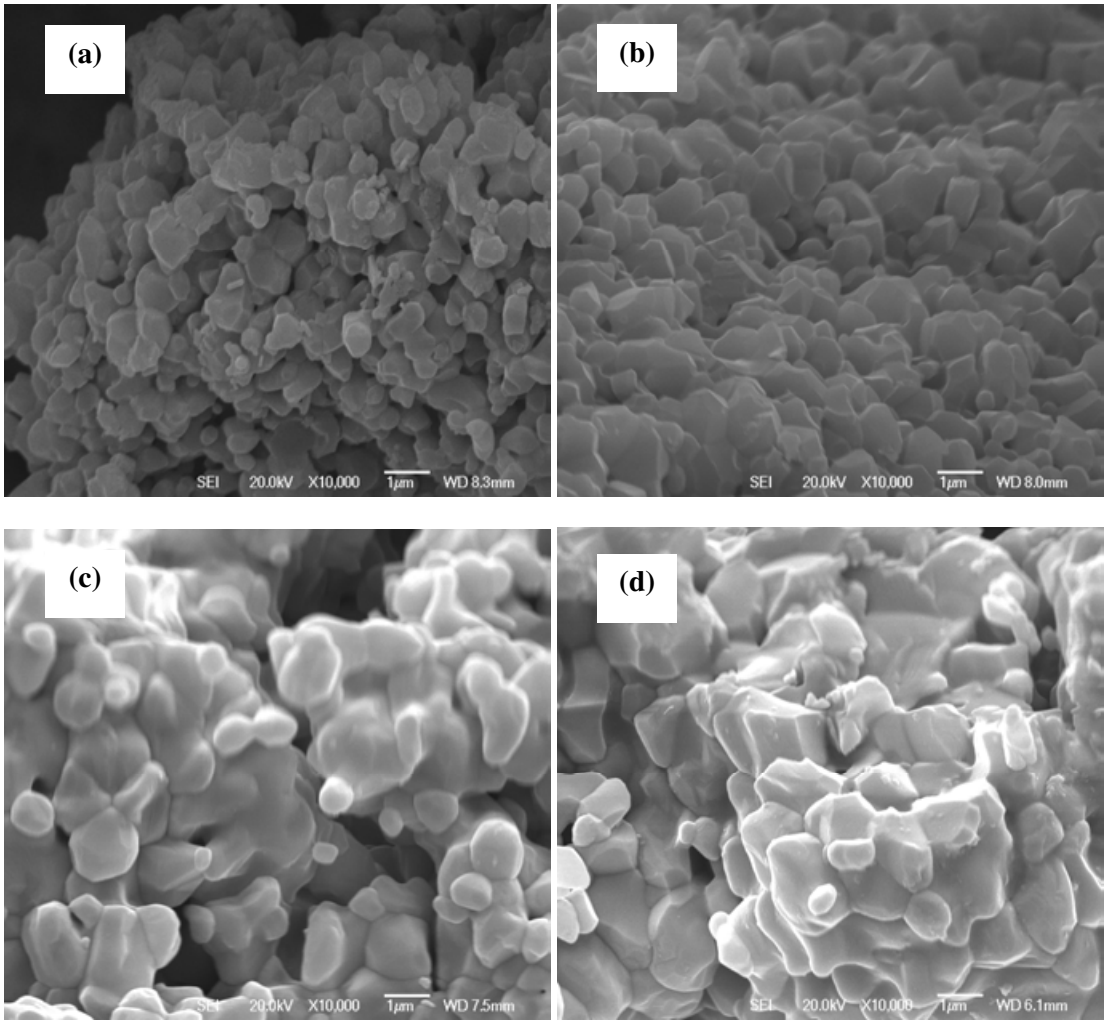

Figure 4.21 Porous alumina samples were sintered at: (a) 1475 (b) 1500 (c) 1550 (d) 1575 ºC for 2 h. Samples were fabricated by directional freeze casting, obtained from the same slurry with a solids loading of 27 vol.% (with 0.14 wt.% NH_4PAA and 3 wt.% B1000 and 2 wt.% B1007 binders) and under a cooling rate of 0.5 ºC/sec.

In summary, changing the sintering temperature will affect the final porosity and compressive strength of the porous alumina. Therefore, optimization of the sintering

temperature is needed to obtain appropriate compressive strength and porosities values for specific applications.

4.9 Effects of Binders in the Freeze Casting Technique

It is known that the ceramic powders are inherently difficult to handle and shape into desired components because of their discreet nature and lack of cohesiveness and plasticity[16].

Organic processing aids, such as polymers (or binders), are an essential component for the effective processing of many commercial high performance ceramics, and they are often required to enhance the ceramic forming capabilities.

Binder systems offer a variety of very useful functions in ceramics processing techniques. Ceramic forming methods depend on organic additions to various extents; among the most common methods are dry (die) pressing, slip casting, tape casting, isostatic pressing, extrusion, and injection moulding. The selection of a given forming method, dominated by a lot of factors such as product geometry and complexity, the dimensional tolerances required, the quantity to be produced, and cost, has a strong effect on the choice of binder system formulation and loading. Typically such systems contain between approximately 5 and 40 vol.% of a given ceramic green body, depending on the chosen forming method[16].

In the freeze casing technique, binders are also needed in order to enhance the strength of the green body. However, up to now, there are few reports of investigations concerning the influence of the addition of binders in the freeze casting technique. Therefore, it is very necessary to carry out some research on this aspect.

In this section, poly(vinyl) alcohol (PVA) and a commercial binder were chosen as the binders to characterize their effects on the final properties of the porous ceramics produced in the freeze casting technique. The alumina solids loadings used in this section were all fixed at 20 vol.%. The PVA was introduced to the suspensions through self-made PVA

solution (20 wt.%) as described in Chapter 3.1.6.

4.9.1 Effect of PVA in the Freeze Casting Technique

Polyvinyl alcohol (PVA) is an obvious choice as a binder in that it has low toxicity, and also has the advantage that it is already widely used as a low cost binder in the commercial production of ceramics[17].

4.9.1.1 Effect of PVA Content on Rheological Properties of the Alumina Slurries

In this section, 0.14 wt.% NH_4PAA was added into all slurries as the dispersant since this concentration had shown the best performance in a previous study[4]. It indicated that at higher concentration (> 0.14 wt.%), the NH_4PAA will remain unabsorbed in the suspension and the functions as an electrolyte, which reduces the range and extent of the electrostatic repulsion[4].

Figure 4.22 shows the relationship between the viscosity and the shear rate of 20 vol.% alumina slurries with different PVA contents.

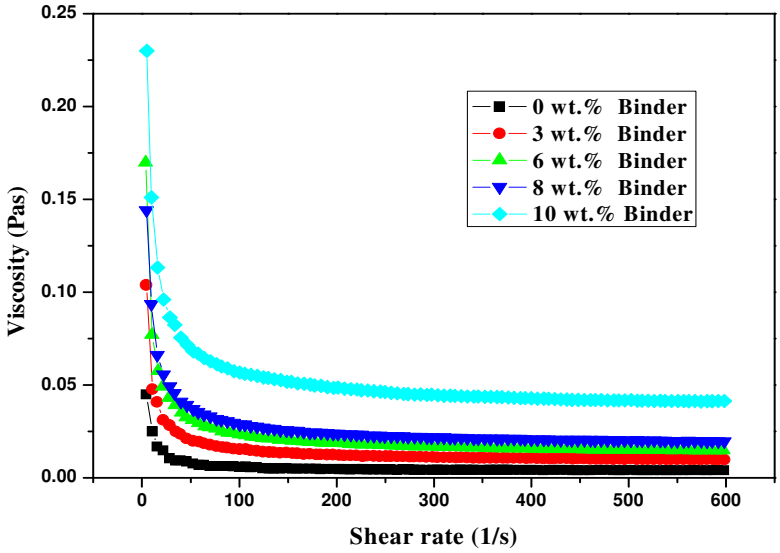

Figure 4.22 Viscosity of 20 vol.% solids loading alumina slurries with and without PVA binder (with 0.14 wt.% NH_4PAA dispersant).

It can be seen from Figure 4.22, that the behaviour of each slurry was similar: when the shear rate was low, the viscosity was high, while at higher shear rates, the viscosity became relatively low, and the viscosity decreased with the increase of the shear rate, which represented a typical shear thinning behaviour.

The addition of PVA to dispersant-stabilized alumina slurry could change the viscosity of the slurry significantly. Figure 4.23 shows the viscosity at four different shear rates as a function of the PVA content. The viscosity increased monotonically as the PVA content increased. As the PVA content increased from 0 wt.% to 8 wt.%, the viscosity went up almost linearly, while over 8 wt.%, the viscosity increased abruptly.

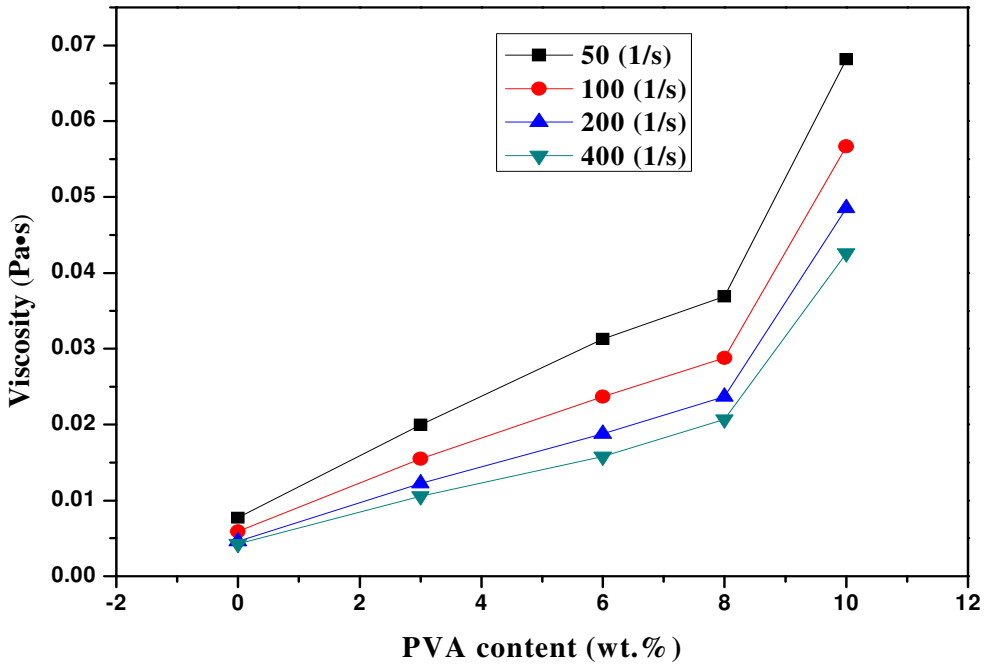

Figure 4.23 Viscosity of 20 vol.% solids loading alumina slurries as a function of PVA content (with 0.14 wt.% NH_4PAA dispersant).

The increase of the viscosity of the NH_4PAA stabilized slurries at different shear rates with increasing of the PVA content indicated that the addition of the PVA had probably caused a flocculation of the alumina stabilized particles with the 0.14 wt.% dispersant. The degree of

the flocculation increased as the PVA content went up, and this effect of flocculation became more pronounced when the PVA content was more than 8 wt.%.

It has been discussed in the literature review (Chapter 2, section 2.3) that when particles are dispersed in a medium (aqueous or nonaqueous), there are normally four different kinds of interactions between the different compositions in the slurries. Among them, van der Waals attractive forces are the most important. Particularly for particulate materials with high surface area, it usually causes agglomeration of the particles. If the particles have an electrical charge, caused by the adsorption of a charged dispersant, the agglomeration of the particles in a colloidal suspension can be restrained by the formation of the so-called electrical double layer[18]. Adsorption (or grafting) of polymer molecules can impede the agglomeration of the particles through the steric stabilization mechanism as well. The addition of a non-adsorbing polymer to a stabilized colloidal suspension may result in depletion flocculation, whereby the concentration of the non-adsorbing free polymer is effectively reduced between the particles, and the higher concentration outside the particle–particle approach zone, exerts an osmotic pressure causing the particles to flocculate[18]. Figure 4.24 illustrates schematically different influence factors that could cause instability in a stabilized suspension.

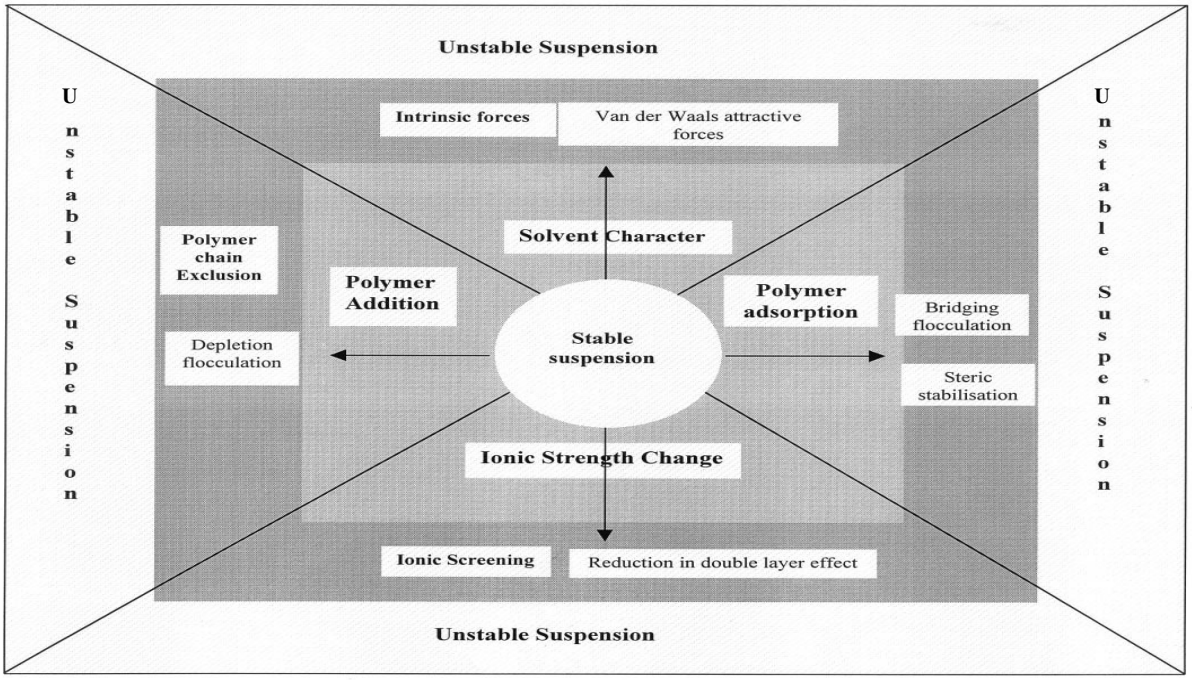

Figure 4.24 Different factors that cause instability in a stabilized suspension. The arrow direction indicates the increasing of the effect (After Khan[18]).

According to the agglomeration theories described above, the agglomeration in the PVA added stabilized alumina suspension in this section (Figure 4.22) can be explained as follows.

It has been shown by Pasi[19] that PVA has a rather low adsorption ability on an Al_2O_3 surface. Pasi and his colleagues showed that an acidic condition was better for the adsorption of PVA. Only 5% of PVA (from the 0.5 wt.% PVA solution) was adsorbed on an alumina surface at pH 4.3 and 95% remained in the solution; however, with the increase of PVA concentration (from 2.15 wt.% PVA solution), the adsorbed fraction was even lower, 2.1%. Meanwhile, in Khan's study, it had been found that PVA did not adsorb in their measurable extent (40 vol.% alumina with 1.5 wt.% PVA). Therefore, the possibility that the flocculation of this alumina (stabilized by NH_4PAA) and PVA system was caused by a bridging mechanism can be reasonably excluded.

The alumina particles, in the presence of aqueous NH_4PAA solutions, are surface charged,

which can be confirmed by a former study[4]. This study also indicated that alumina particles were stabilized largely by a classical electrostatic repulsion mechanism. However, in the case of stabilized particles in the presence of non-adsorbing PVA, the flocculation is unlikely to be due to van der Waals forces because the particles are stable in the absence of the PVA (Figure 4.23, 0 wt.% Binder). It is therefore highly probable that the flocculation of the NH_4PAA stabilized alumina slurries was induced by a depletion flocculation mechanism when PVA was introduced to these slurries. A schematic explanation is given in Figure 4.25. In the absence of PVA, the alumina particles were in a well dispersed state (Figure 4.25 (a)). When PVA was added to the dispersed colloidal system, a depletion flocculation was caused and some particles agglomerated forming "large" particles as shown in Figure 4.25 (b). With the increase of PVA content, the degree of flocculation increased and the amount of the "large" particles increased as well.

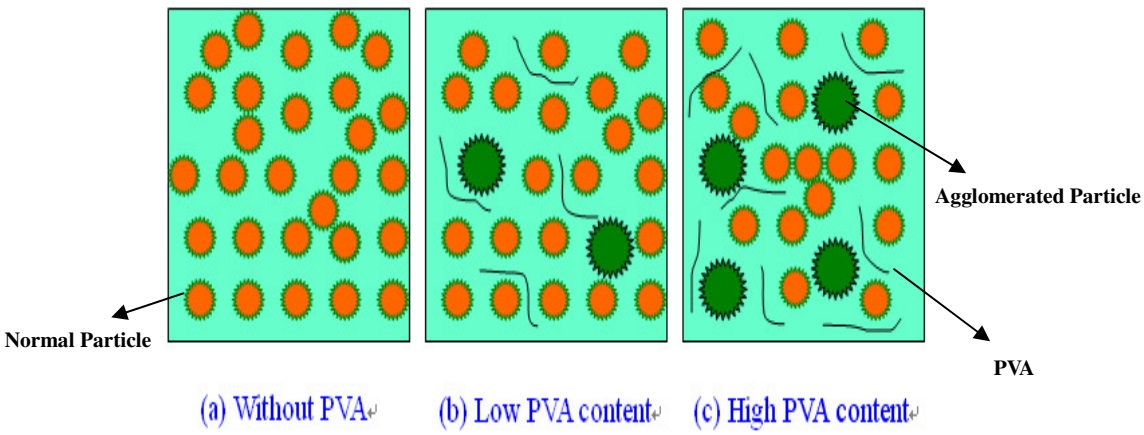

Figure 4.25 Schematic illustration of depletion flocculation.

4.9.1.2 Morphology of Porous PVA Monoliths

Two concentrations of PVA solutions were prepared for this study: 5 wt.%, and 20 wt.%, as described in Chapter 3.1.6. In order to understand the effect of PVA binder during the freeze casting process, porous PVA monoliths were obtained through directional freeze casting of

those PVA solutions mentioned above under a cooling rate of 1.1 ºC/sec.

Figure 4.26 shows the SEM photo of the porous PVA which was obtained from the 20 wt.% PVA solution. It shows a channel morphology as shown in Figure 4.26 (a)). The direction of the channels was parallel to the ice growth direction. Figure 4.26 (b) and (c) show the detailed information for Figure 4.26 (a). Figure 4.26 (b) shows the details of the morphology of the PVA wall. The surface of the wall was rather rough and contained lots of small pores. The region between two adjacent walls was not empty. Detailed information is shown in Figure 4.26 (c). The two walls were connected by many PVA 'belts'.

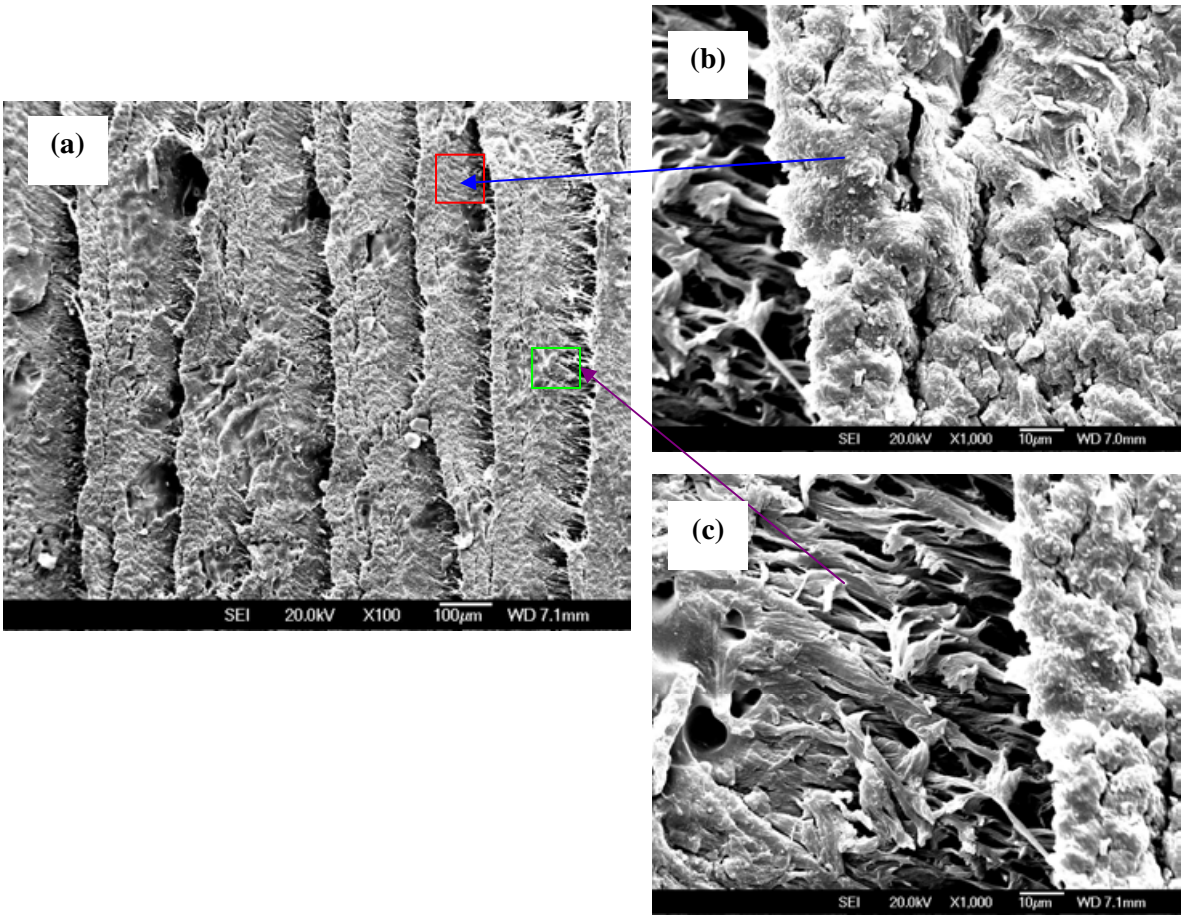

Figure 4.26 SEM photographs of porous PVA monolith obtained from 20 wt.% PVA water solution under a cooling rate of 1.1 ºC/sec.

Figure 4.27 (a) presents the microstructure of the PVA monolith from the 5 wt.% PVA solution. Compared with Figure 4.26 (a), this PVA monolith was more porous. Figure 4.27 (b)

shows the detailed information for the porous monolith from the 5 wt.% PVA solution.

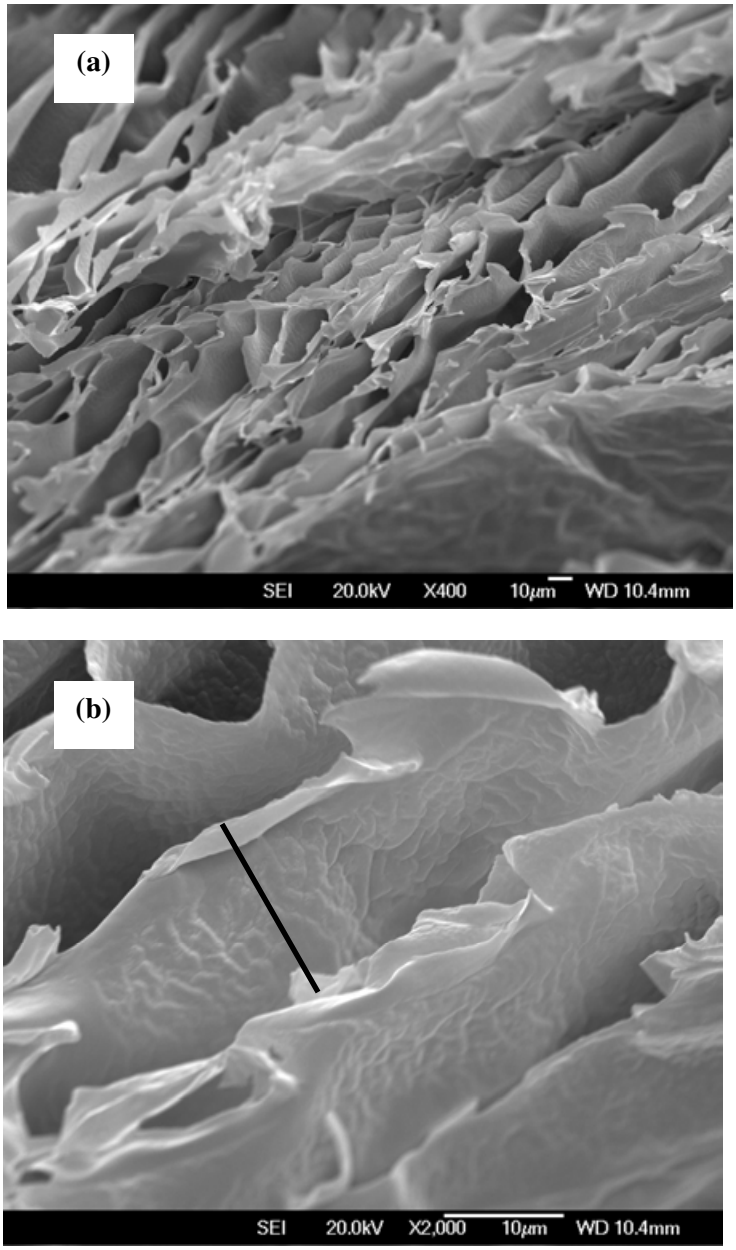

Figure 4.27 SEM photographs of porous PVA monolith obtained from 5 wt.% PVA water solution under a cooling rate of 1.1 ºC/sec.

The PVA wall was much denser compared to that of the porous monolith from the 20 wt.% PVA solution, meanwhile, the walls were much thinner than that of the porous monolith from the 20 wt.% PVA solution, which is consistent with the result in Section 4.6.2 that lower suspension concentrations resulted in thinner walls in the freeze casting technique.

The region between the walls in this porous PVA monolith was empty compared with those of the porous monolith from the 20 wt.% PVA solution. Moreover, the wall thickness was nano-sized scale (~100 nm), which offered a potential way to produce architectures with nano-sized dimensions for biomedical applications through freezing a solution with low concentration.

The two aligned porous PVA monoliths shown above can also be interpreted by incorporating the phase separation (water and PVA) during the directional freeze casting process, which is very similar to the freezing of alumina suspension.

It is well known that an initially planar interface will develop a morphological instability under certain conditions. During freezing, the increased PVA concentration could cause constitutional supercooling at the interface, where a small protrusion of ice would form and grow rapidly[20,21], meanwhile, the PVA became concentrated and was trapped between the ice cells. After removing the ice crystals by sublimation, the PVA monolith showed porous architecture (channels), which was actually a negative replica of the structure of the ice crystal.

A mathematical expression for the amplification rate of a perturbation has been developed by Mullins and Sekerka which can be used to determine the length scale of the instability[22,23] . The wavelength of this instability defines the primary periodicity of the porous structure in Figure 4.27 (b) (black line), as well as the wavelength shown in Figure 4.16.

If the relevant parameters (such as the equilibrium melting point, the latent heat of fusion, etc.) can be obtained, it is feasible to predict the wavelength at certain growth velocities by utilizing the mathematical expression developed by Mullins and Sekerka. Actually, obtaining these parameters is not easy even at low growth velocity. For a higher growth velocity[18], the

interfacial attachment kinetics becomes more important making it more difficult to obtain reasonable parameters. Therefore, an accurate estimate is rather difficult to achieve.

4.9.1.3 Effect of PVA Content on Morphology of Porous Alumina

Figure 4.28 shows the microstructures of the porous alumina ceramics obtained by the directional freeze casting technique from the 20 vol.% solids loading slurries with different PVA contents (under a cooling rate of 1.1 ℃/sec and sintered at 1525 ℃, 2h). Images were taken from the same position on all samples, 8 mm above the bottom (cold side), which was definitely in the lamellar zone mentioned in Section 4.5.

Figure 4.28 (a) shows the architecture of the sample without any PVA addition. It shows typical lamellae microstructure with dendritic-like features on one surface of the ceramic wall. The morphology of the sample with 3 wt.% PVA is shown in Figure 4.28 (b). It presents a similar lamellae structure compared with the sample without PVA addition. However, in some parts of this sample, the regions between the ceramic walls were not as empty as those in Figure 4.28 (a) and they were filled with alumina particles, which indicated that engulfment had happened in this sample during the freeze casting process. As shown in Figure 4.28 (c), (d), (e), with increasing PVA content in the slurries, more engulfment could be found in the final samples. The regions between the ceramic walls in the samples (d) and (e) were almost fully filled with alumina particles.

The relevant pore size distribution is shown in Figure 4.29. With the increase of the PVA content, the pore size became smaller (from about 10 μm to 0.3 μm) and the distribution became narrow, which is consistent with the microstructure photographs shown in Figure 4.28.

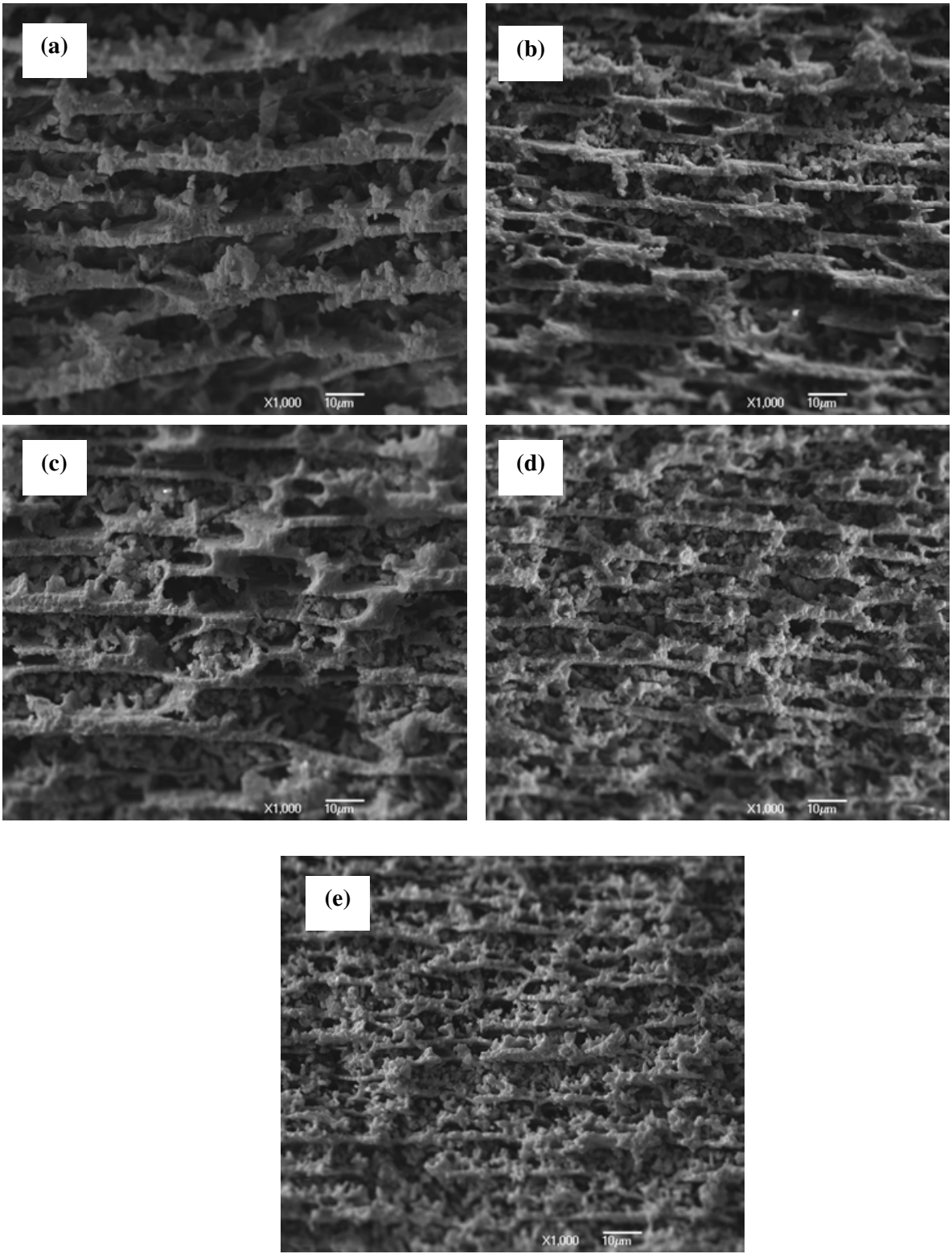

Figure 4.28 SEM photographs of the porous alumina ceramics (1525 ºC, 2h) obtained from the 20 vol.% solids loading slurries with different PVA contents under a cooling rate of 1.1 ºC/sec: (a) 0 wt.% PVA, (b) 3 wt.% PVA, (c) 6 wt.% PVA, (d) 8 wt.% PVA, and (e) 10 wt.% PVA. The ice growth direction is perpendicular to the page.

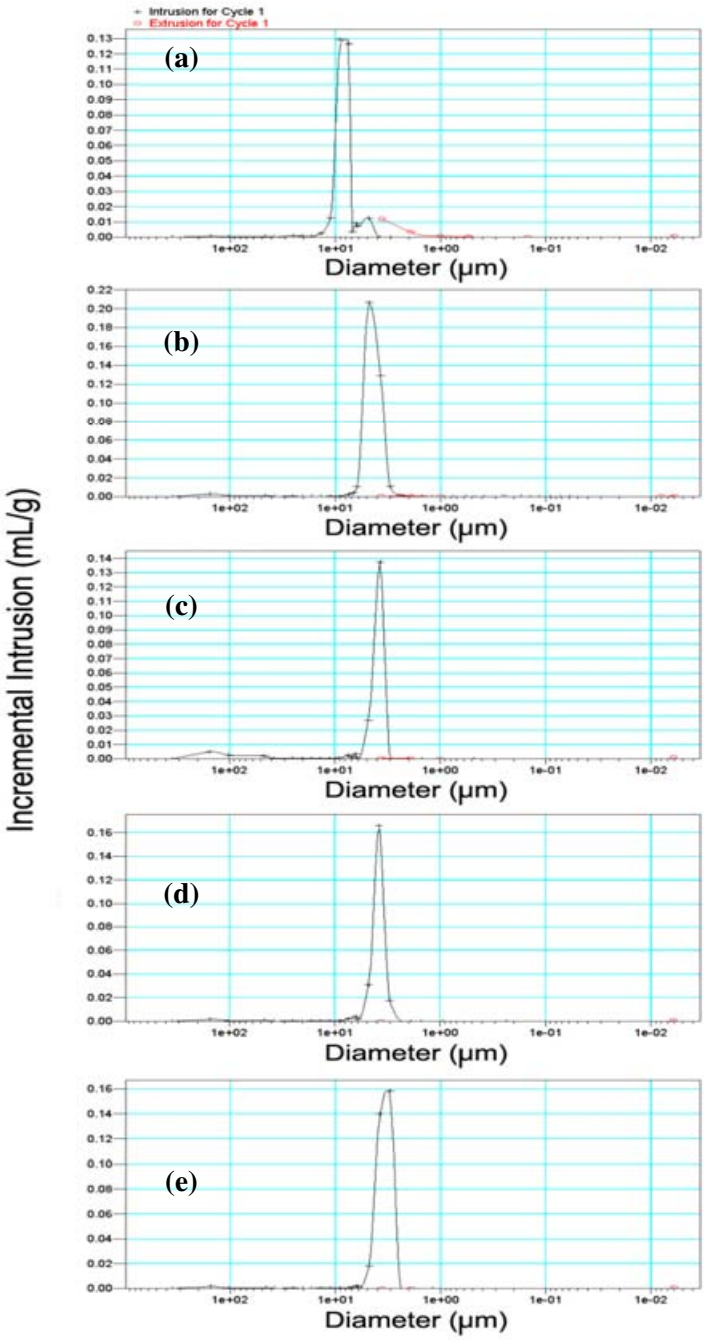

Figure 4.29 Pore size distribution of porous alumina ceramics (1525 ºC, 2h) obtained from the 20 vol.% solids loading slurries with different PVA contents under a cooling rate of 1.1 ºC/sec: (a) 0 wt.% PVA, (b) 3 wt.% PVA, (c) 6 wt.% PVA, (d) 8 wt.% PVA, and (e) 10 wt.% PVA

In summary, the morphologies of the final porous alumina ceramics were significantly affected by the addition of PVA. A theoretical explanation for this particular phenomenon is

shown below.

Thermodynamic arguments[24] show that a particle can only be ejected if the interfacial free energy between the particle and the solid phase, σ_{sp}, is larger than the sum of the surface free energies solid-liqud, σ_{sl} and liquid-particle, σ_{lp}.

$$\Delta\sigma = \sigma_{sp} - (\sigma_{lp} + \sigma_{sl}) > 0 \qquad (4\text{-}3)$$

where σ_{sp}, σ_{lp} and σ_{sl} are the interfacial free energies associated with the solid–particle, liquid–particle and solid–liquid interface, respectively. A schematic diagram illustrating a particle in the interface is shown in Figure 4.30.

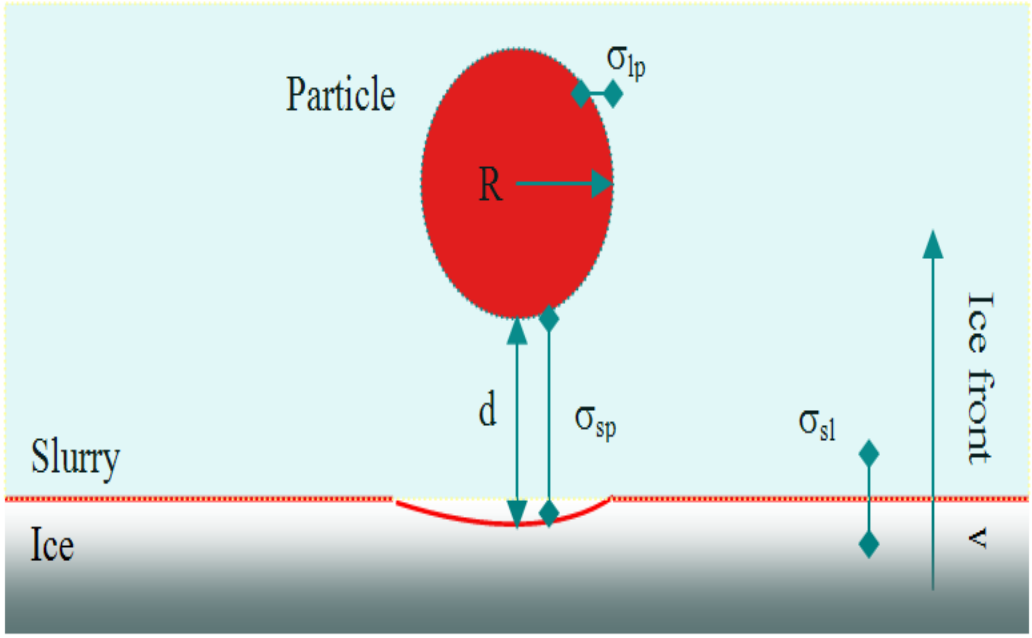

Figure 4.30 Sketch of a spherical particle of radius R in solid-liquid interface during freezing (after Korber[24]).

When the growth rates (cooling rate) is low and external forces are not included, this thermodynamic criterion is usually adequate enough to estimate whether the particle will be ejected or entrapped by the solid[13,24].

However, for the situation of the particles being pushed by the solidification ice front, a liquid film with adequate thickness must exist between the ceramic particles and the ice front

in order to keep continuous transport of molecules for the crystal growth. The thickness of the liquid film will go down when the velocity of the ice front increases. Therefore, a critical velocity, υ_c should exist, for which the thickness of the liquid film is not sufficient enough to let the necessary flow of molecules to maintain the continuous growth of crystal behind the particle, which then becomes engulfed by the solidification front[11].

Some equations have been derived for this critical velocity in the solid-liquid interface, above which a particle will not be ejected. In most expressions[13], the critical velocity, v_c, is defined as a function of the particle size, *R*. A very simple model[13, 21,24], which is based on the force balance in the solid-liquid (particle-ice) interface, yields a critical velocity of the solidification ice front for particle engulfment, which can be expressed as below:.

$$\upsilon_c = \frac{\Delta\sigma d}{3\eta R}\left(\frac{a_0}{d}\right)^z \qquad (4\text{-}4)$$

where $\Delta\sigma$ is the interface free energy, a_0 is the average intermolecular distance in the liquid film between the solidification front and the particle, *d* is the overall thickness, η is the slurry viscosity, *R* is the particle radius and *z* is an exponent

As mentioned in Section 4.9.1, when PVA was added to the dispersed colloidal system (stable alumina suspension), depletion flocculation would be caused and some particles agglomerated forming “large” particles; meanwhile, with the increase of PVA addition in the colloidal system, the amount of “large” particles increased too.

Combining with the equation above, therefore, under the same freezing conditions, with the increase of PVA addition, “large” particles would lead to small critical velocity, and engulfment would happen in the system with higher PVA content; furthermore, with an increase of PVA addition, the engulfment would become worse.

A schematic diagram to illustrate these changes (engulfment or not) during the freezing

process is shown in Figure 4.31.

Figure 4.31 (a) shows that there was no engulfment at all, because there was no PVA addition. Engulfment started to occur (the green particles) in the system with low PVA addition (3 wt.% and 6 wt.% systems), as shown in Figure 4.31 (b). More engulfment occurred in the system with higher PVA addition (8 wt.% and 10 wt.% systems).

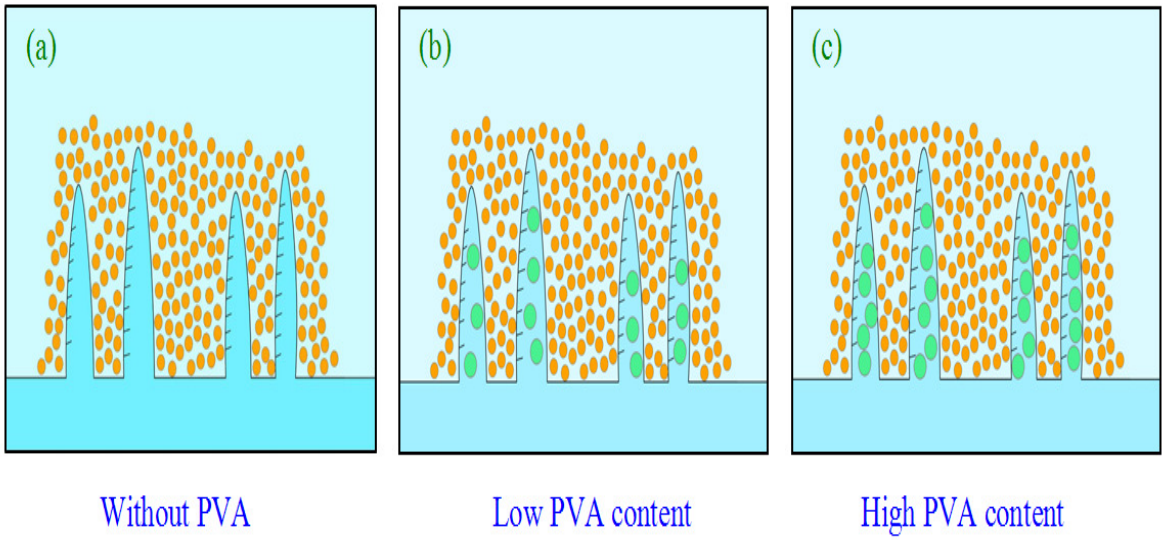

Figure 4.31 Schematic illustrations for the gradual evolution of the microstructure for porous alumina ceramics with the addition of PVA.

The addition of PVA will significantly affect the final morphology of the porous alumina ceramics. Therefore, it also provides a potential way to modify the morphology of the porous ceramics in the freeze casting technique.

4.9.2 Effect of Commercial Binders in the Freeze Casting Technique

As mentioned in Chapter 3, Duramax 3 wt.% B-1000 and 2 wt.% B-1007 were used together as a binder throughout this whole project. Duramax is an acrylic polymer and had been used successfully as a binder in ceramic microfabrication[25,26]. It has been proved that PVA addition (as binder) has a significant effect on the morphology of the porous ceramics, as

shown in Section 4.9.1. As a general mechanism, the emulsion polymer particles such as acrylics are absorbed on the powder surface and act as bridges between the alumina particles, providing interparticle flocculation and a binding action. Therefore, it is necessary to characterize the effect of the commercial binder in the freeze casting technique. In this section, the amount of 3 wt.% B-1000 and 2 wt.% B-1007 was defined as one unit. For example, when 6 wt.% B-1000 and 4 wt.% B-100 are utilized, the amount will be noted as two units. Figure 4.32 shows the typical rheological flow behavior of each binder and their mixture. All of them showed shear-thinning behaviour.

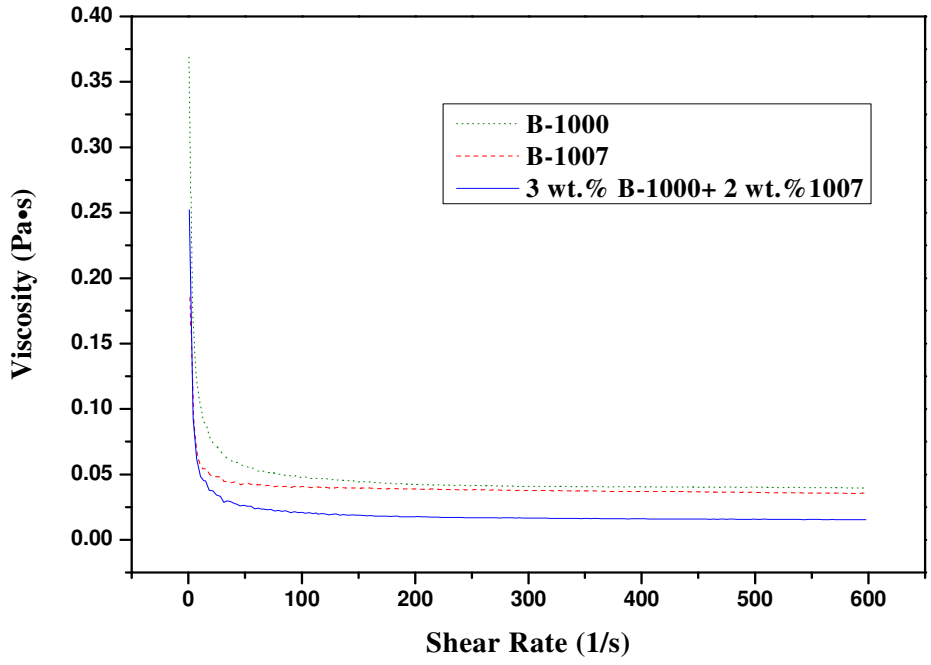

Figure 4.32 Typical rheological flow behaviours of dispersants (B-1000, B-1007, and their mixture).

Alumina slurries with 27 vol.% solid loadings were prepared and used in this section. The cooling rate utilized here was 1.1 ℃/sec. The sintering temperature for all the samples was 1525 ^{o}C, for two hours. Five different amounts of binder (the ratio was fixed) were added into the pre-prepared 27 vol.% alumina slurry, respectively.

Figure 4.33 shows the cross-sectional microstructures that were perpendicular to the ice solidification direction. When there was no binder added, as shown in Figure 4.33 (a), the ceramic walls showed two morphologies: one side remained smooth and the other had dendrites (ceramic arms) just like those shown in Figure 4.8. The pores (the gaps between the alumina ceramic walls) were mostly continuous with one or two terminations in range of the measurements, which could be caused by the overgrowth of the ceramic arms. Figure 4.33 (b) shows that the sample with an addition of half unit of binder had a similar morphology with the one shown in Figure 4.33 (a). It demonstrated continuous pores with several terminations in range of measurement too. It was expected that the further addition of the commercial binder, would depress the liquidus temperature and increase the degree of supercooling, because the overall solute concentration increased. This should cause a morphology change in the growing ice. As expected, Figure 4.33 (c) shows that the pores became smaller and the terminations became more frequent in comparison to those in Figure 4.33 (a) and (b). With further addition of B-1000 and B-1007, the morphologies of porous alumina had been greatly changed, pores became much smaller and the continuous channel had disappeared, and the ceramic walls were connected with adjacent ceramic walls through the ceramic arms, making it more cellular (Figure 4.33 (d) and (e)).

In summary, the addition of commercial binder could greatly change the microstructure of the freeze-cast samples.

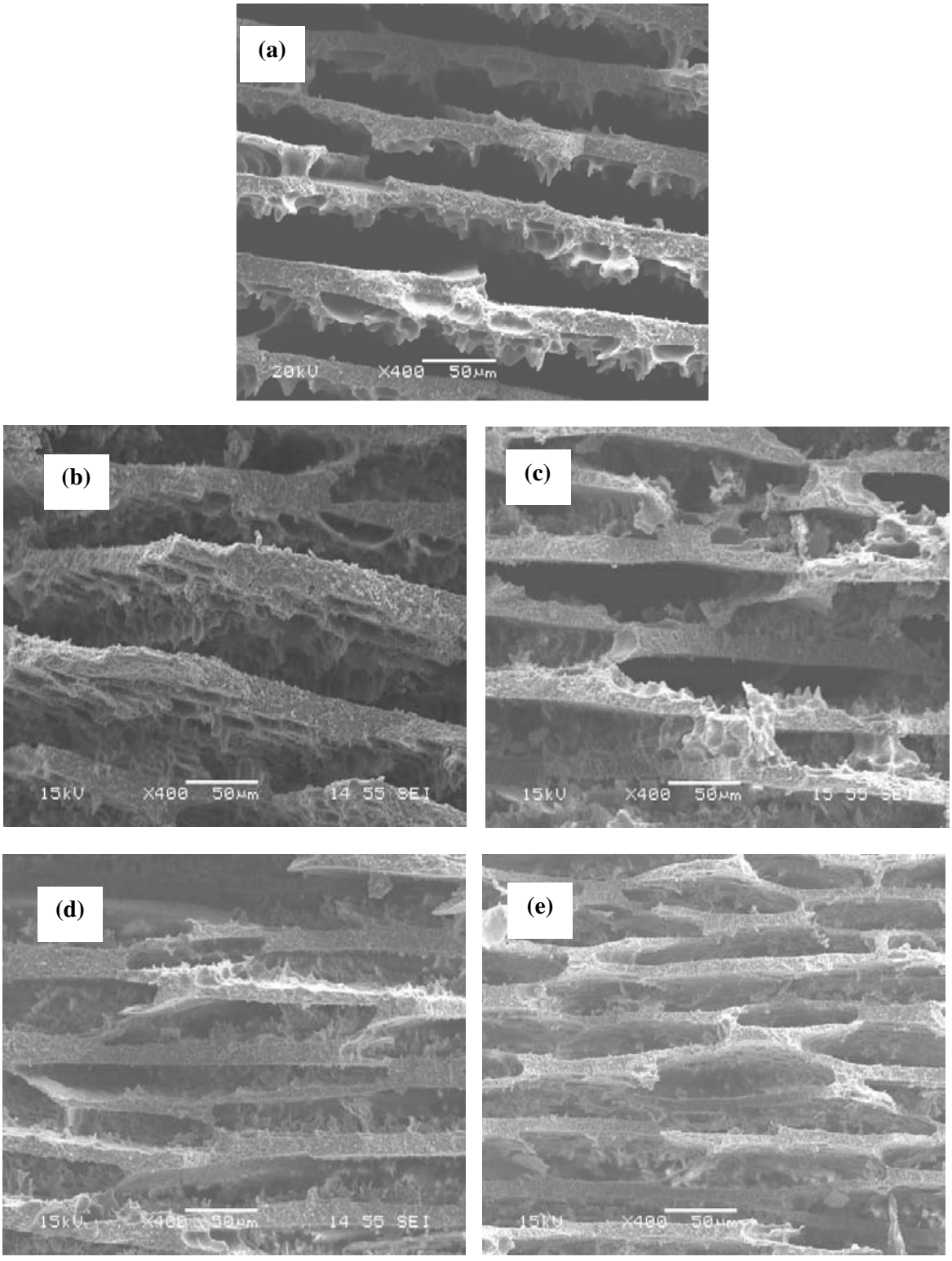

Figure 4.33 SEM micrograph of porous alumina ceramics cross-section with different amounts of commercial binder. Under a cooling rate of 1.1 ºC/sec (solidification direction perpendicular to the page), sintered at 1525 ºC for 2h, (a) 0 unit, (b) 0.5 units (c) 1 unit, (d) 2 units, (e) 4 units. The amount of 3 wt.% B-1000 and 2 wt.% B-1007 was defined as one unit.

4.10 Effects of Glycerol in the Freeze Casting Technique

The freeze casting technique was first employed as a simple approach to fabricate dense ceramic components with complex shapes[27,28]. A lot of effort, such as introducing cryoprotectants to the slurries, has been made to prevent the growth of large ice crystals and freezing defects associated with the crystallization of water. Those cryoprotectants include ethylene glycol, glycol, propylene glycol, methanol, and ethanol. As it is nontoxic, highly pure, highly soluble in water, and inexpensive, glycerol is one of the most frequently used cryoprotectants[28].

Those effects of glycerol described above are involved in the fabrication of dense ceramic components incorporating high solids loading suspensions. In this section, glycerol was employed as well in freeze casting but for a different purpose (for porous ceramic).

In order to characterize the effect of glycerol in the freeze casting of porous ceramics, a solids loading of 20 vol.% alumina suspension was prepared. The cooling rate utilized here was 1.1 ℃/sec and the sintering temperature was 1525 ℃ (for two hours).

For pressureless casting, it is necessary to obtain slurries with low viscosity. The flow behaviour for suspensions was characterized, as shown in Figure 4.34. Slurries with and without glycerol all showed shear thinning behaviour. The viscosities were low and they did not change much as the addition content of glycerol increased (Figure 4.34 (a)). This is in agreement with Sofie's[28] study that although glycerol decreased the viscosity of slurries at high solids loading, the benefit was not significant at low solids loading. Figure 4.34 (b) shows the detail of the viscosities. Though the variation was small, with the increase of glycerol content from 0 wt.% to 5 wt.%, the viscosity increased a slightly, it then decreased when the glycerol content increased from 5 wt.% to 10 wt.%.

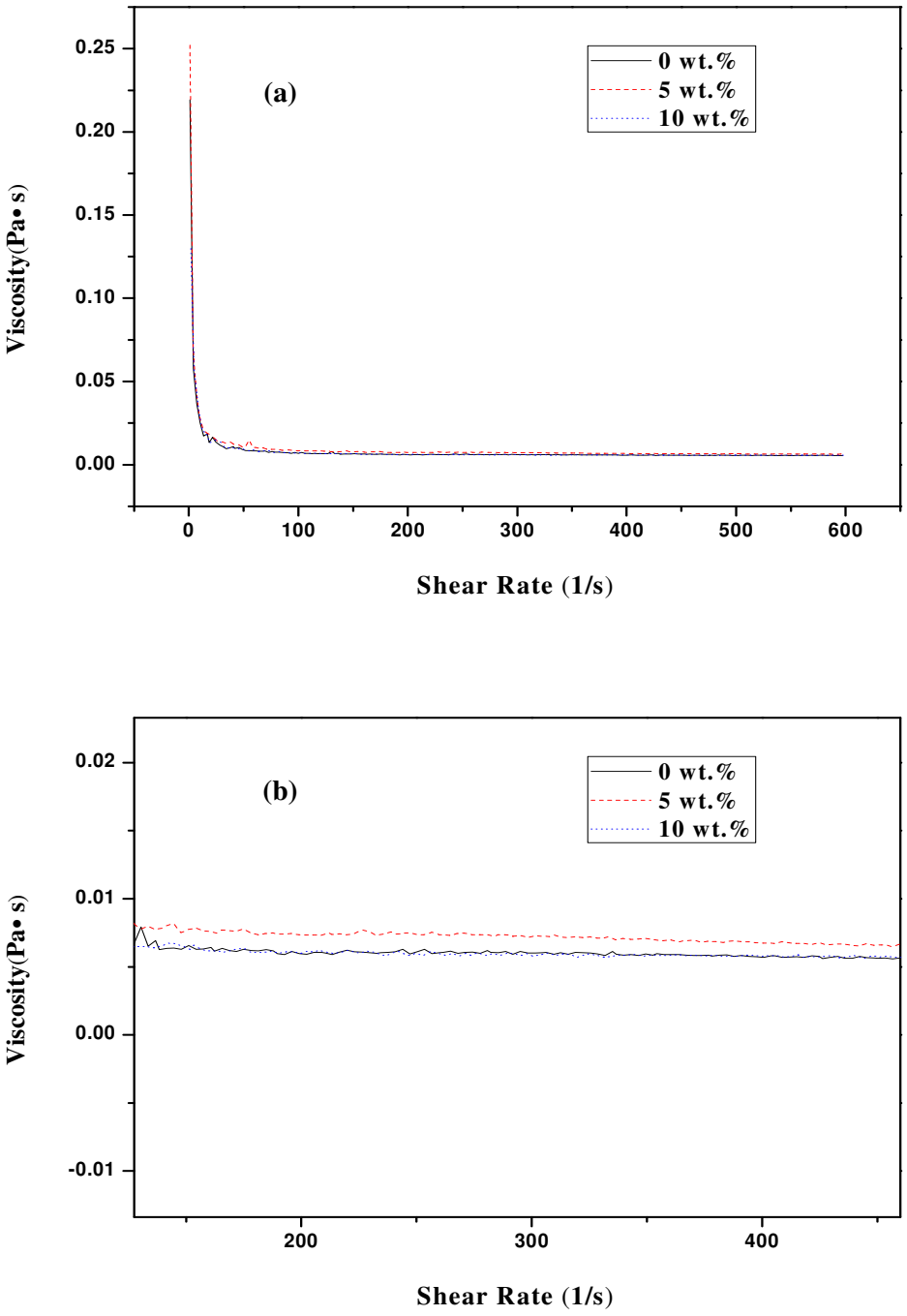

Figure 4.34 (a) Viscosity of 20 vol.% alumina suspension with and without glycerol. The amount of glycerol is expressed as a dry weight of the powder basis (dwb), equivalent to the wt./wt. basis of the ceramic powder. All the suspensions were added with 0.14 wt.% NH_4PAA, without any binder; (b) Detail of picture (a).

The mechanism of the interaction between glycerol and dispersant molecules is not clear and needs further investigation. However, one possible explanation is shown below:

The dispersant used here was ammonium polyacrylate and the mechanism for its effectiveness is eletrosteric stabilization. Glycerol may enhance the steric hindrance of the dispersant to conquer van der Waals attraction or may simply work as a lubricant between particles lowering the viscosity of the slurry[28]. It is known that the hydrophilic ends of the non-ionic surfactant interacting with the hydroxyl groups of glycerol could lead to the hydrophobic ends of glycerol pointing outwards into the solution[29]. Due to their molecular structure, the interaction between dispersant and glycerol probably may lead to the formation of a micelle structure, which is shown in Figure 4.35. When the addition of glycerol was small (from 0 to 5 wt.%), though there was the formation of the micelle structure, the effect of it was weak rather than dominant. However, the viscosity of glycerol (934 mPa·s) is much higher than that of water (1 mPa·s), therefore, the viscosity of the slurry may be increased slightly. With the further addition of glycerol (from 5 to 10 wt.%), the formation of a micelle structure started to affect the viscosity of the slurry, therefore, the viscosity decreased.

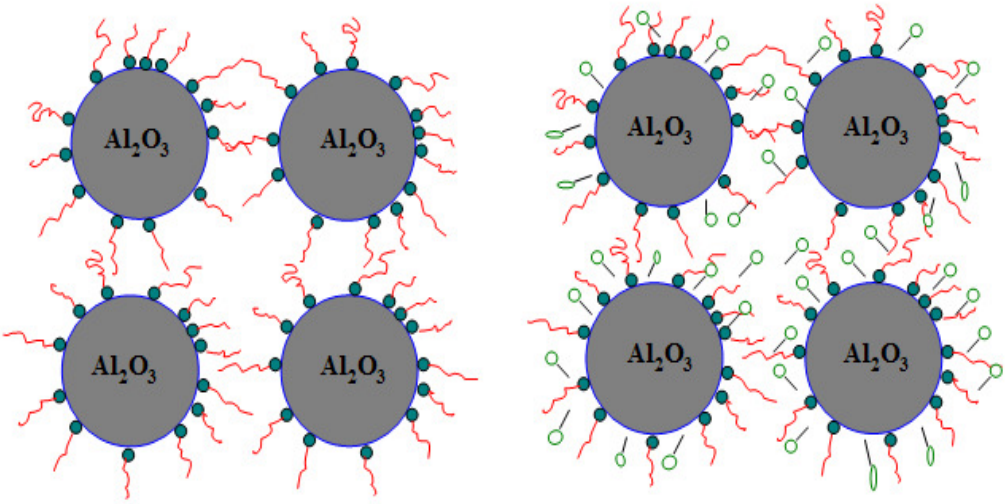

Figure 4.35 Schematic diagram for interaction between the dispersant and glycerol (after Sofie[28])

The typical microstructures of porous alumina ceramics prepared from the slurries

containing glycerol are illustrated in Figure 4.36 and Figure 4.37. Samples without glycerol are shown for comparison.

Figure 4.36 shows the microstructure parallel to the ice growth direction, while figure 4.37 shows the microstructure perpendicular to the ice growth direction. Figure 4.36 (a) and Figure 4.37 (a) were obtained through the sample without glycerol. They showed lamellae microstructures with relatively long range order. The gaps between the ceramic walls were nearly empty, which concretely reflected the complete growth of the ice during freezing. Of course, the ceramic walls showed a normal morphology as shown in the above section of this chapter (Figure 4.37 (a)): one side was smooth, and the other had ceramic arms.

With the addition of glycerol, the microstructures varied significantly. The empty gaps between the ceramic walls disappeared and were instead linked by "ceramic bridges" connecting the adjacent ceramic walls (Figure 4.36 (b) and (c), and Figure 4.37 (b) and (c)), making them more cellular. With the increase of glycerol content, the pore size of the final samples became gradually smaller. Especially, in Figure 4.37 (b) and (c)), the morphologies were much like the herring bone pattern.

In summary, glycerol can effectively bind to the water molecules and disrupts the complete crystallization of ice, leading to a localized cellular architecture, thus reducing the size of growing ice crystals and inhibiting solute ejection. Therefore, introducing glycerol in freeze casting for porous ceramics can greatly change the microstructure, and more importantly offers a very effective way to modify the final pore morphology for some specific application.

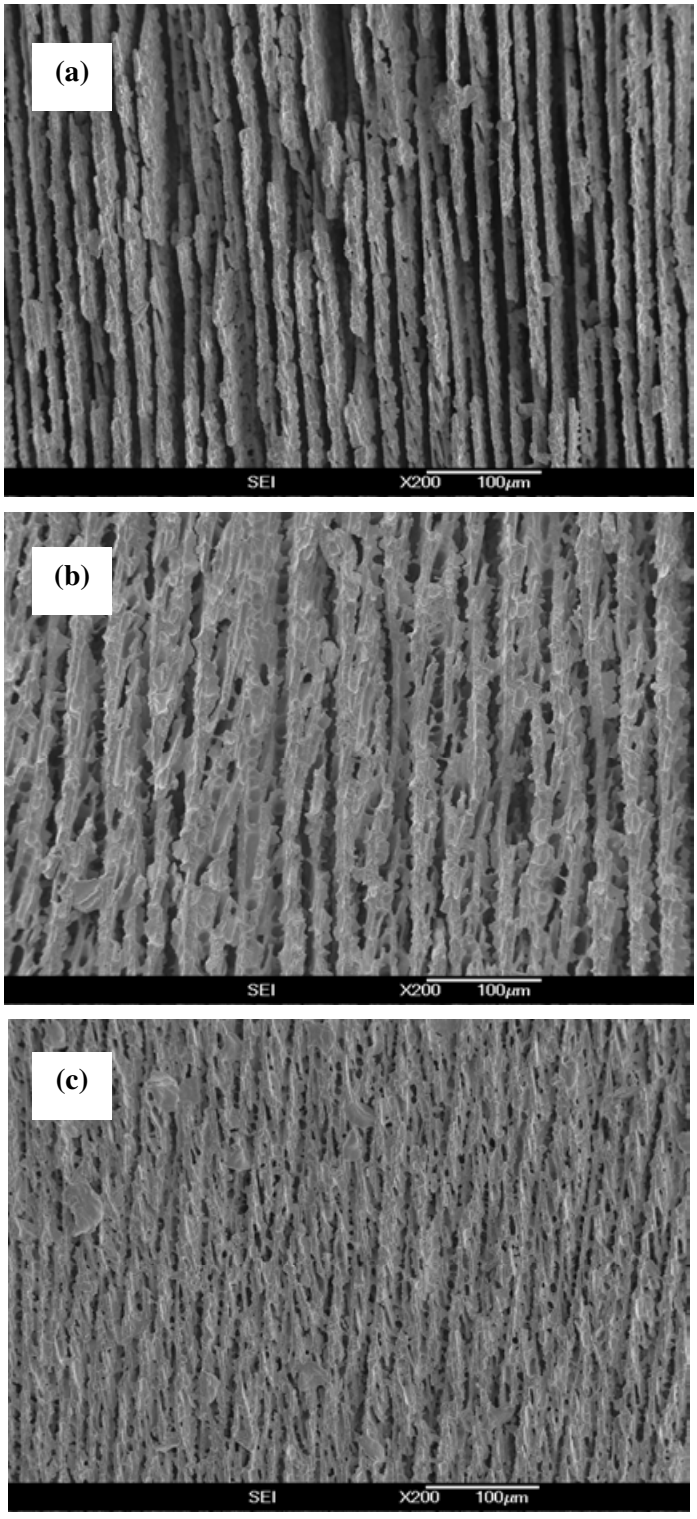

Figure 4.36 Microstructure of sintered alumina samples (1525 ºC, 2h) obtained from 20 vol.% solids loading alumina suspensions (with 0.14 wt.% NH_4PAA) with different amounts of glycerol. Samples were obtained under a cooling rate of 1.1 ºC/sec, parallel to the solidification direction. (a) 0 wt.% glycerol, (b) 5 wt.% glycerol, (c) 10 wt.% glycerol.

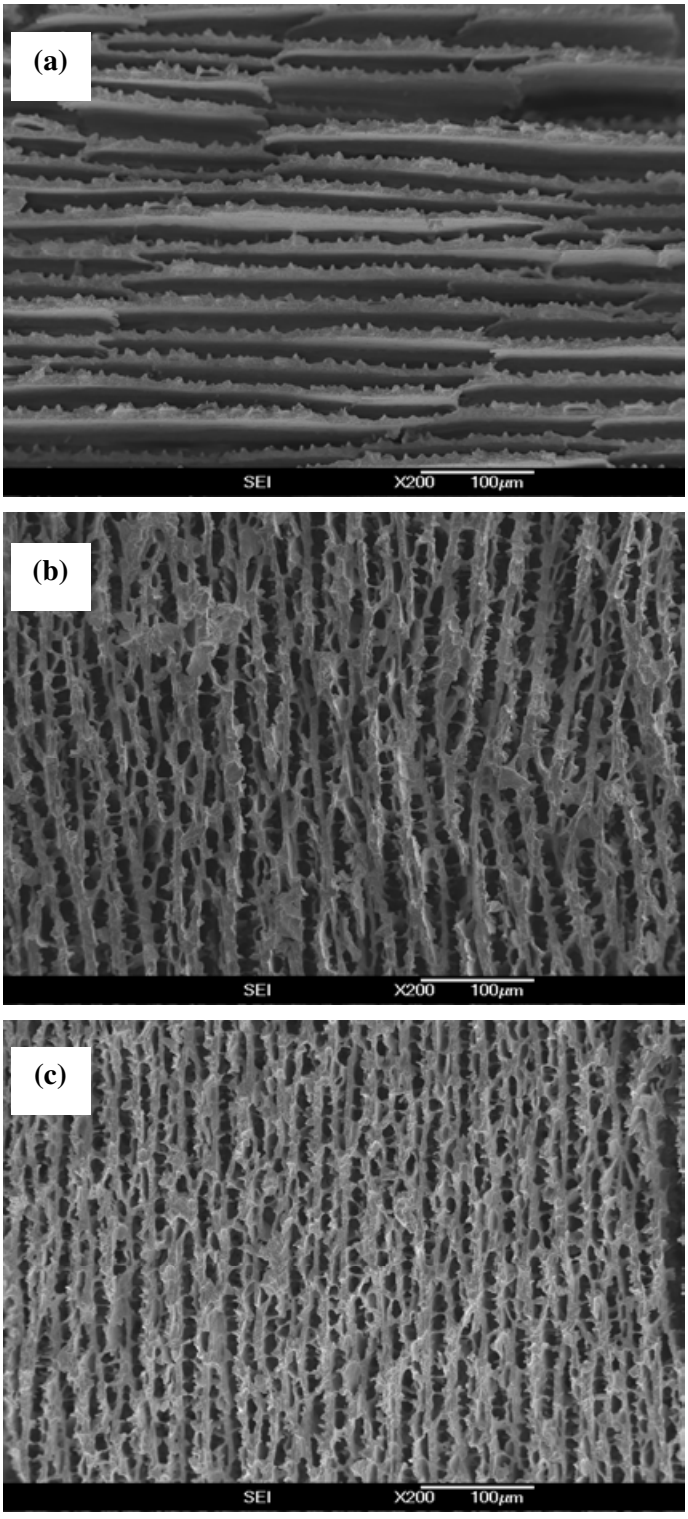

Figure 4.37 Microstructure of sintered alumina samples (1525 ºC, 2h) obtained from 20 vol.% solids loading alumina suspensions (with 0.14 wt.% NH_4PAA) with different amounts of glycerol. Samples were obtained under cooling rate of 1.1 ºC/sec, perpendicular to the solidification direction. (a) 0 wt.% glycerol, (b) 5 wt.% glycerol, (c) 10 wt.% glycerol.

4.11 Double-sided Freeze Casting Technique

The samples demonstrated in the preceding sections were all obtained through a single-sided freezing setup, as shown in Figure 3.3. In order to achieve more homogeneous microstructures in a large area of the final porous ceramic, a double-sided freezing setup was made, which is shown schematically in Figure 4.38. The PDMS moulds used here are hollow ones. Before freeze casting, one side of the hollow PDMS mould was glued on a copper film to prevent the escape of the slurry. The ceramic slurry was then be poured into the mould. After this, the other side of the mould will also be glued on a copper film. Next, the PDMS mould filled with ceramic slurry will be placed between two cold fingers, as presented in Figure 4.38. The two cold fingers (stainless steel) are all cooled by liquid nitrogen, so freezing can start from both sides, making the solidification rate more homogeneous. Therefore, in this section, samples were fabricated via the double-sided freezing setup.

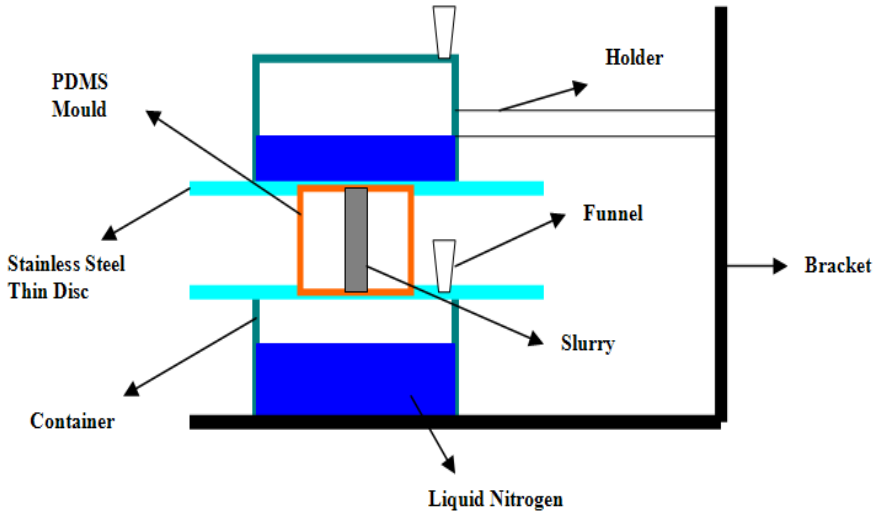

Figure 4.38 Schematic diagram of double-sided freezing setup for the freeze casting technique.

The microstructure of the sample obtained by the double-sided freezing setup is shown in

Figure 4.39 and 4.40. At low magnification (Figure 4.39 (a) and Figure 4.40), it showed a rather homogeneous lamellae architecture in a very large area running through the whole sample (about 5 mm × 4 mm). Figure 4.39 (b) and (c) shows the sample at larger magnifications. They all showed similar features, compared with the samples formed by the single-sided method, for example, the ceramic walls were as dense as the samples in the above sections. Though a homogeneous structure could be obtained as well by using single-sided freeze casting under a high cooling rate, the area with homogeneous pattern was rather small (less than 2 mm × 2 mm). Double-sided freeze casting could change this limitation.

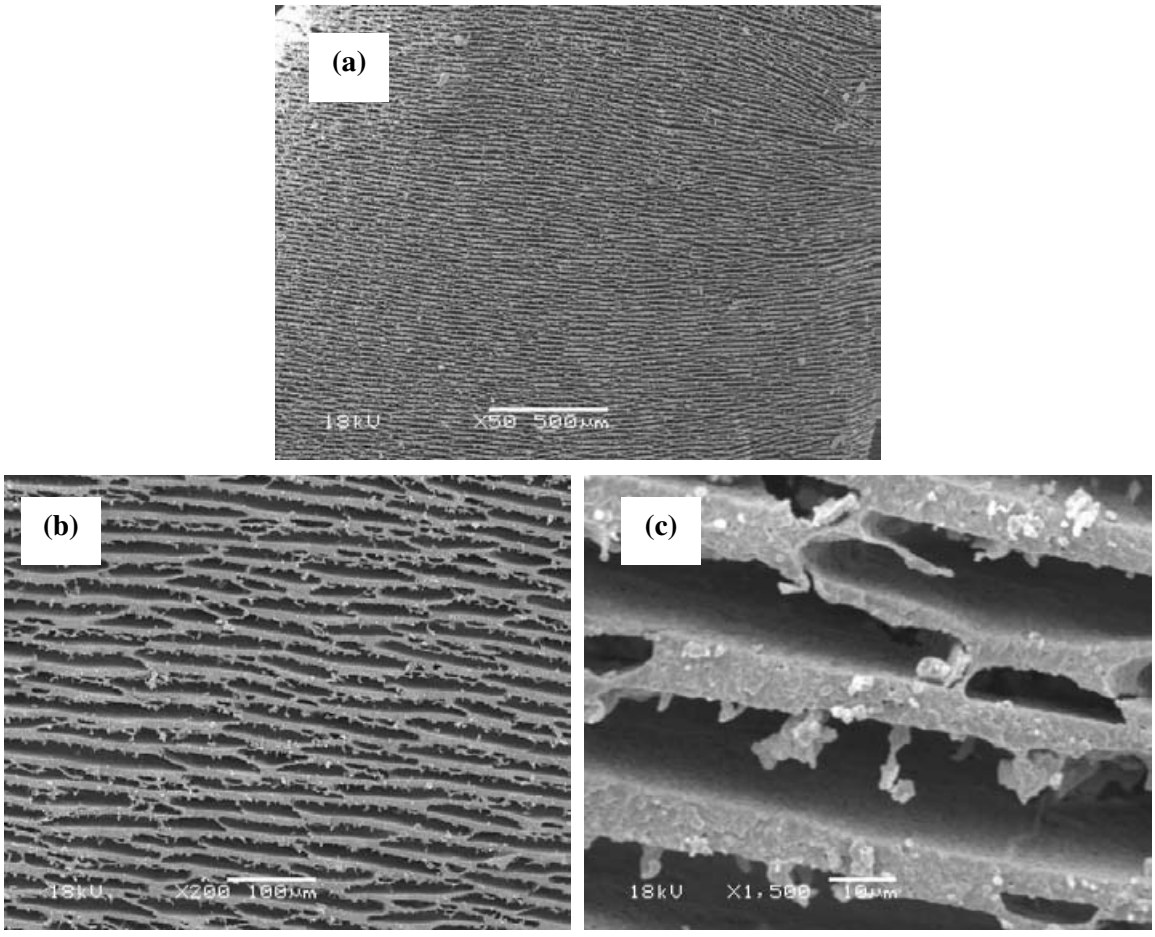

Figure 4.39 SEM microstructure of the sintered (1525 ºC, 2h) porous alumina ceramics (from 20 vol.% slurry with 0.14 wt.% NH_4PAA and 3 wt.% B1000 and 2 wt.% B1007 binders) obtained through double-sided freezing setup, perpendicular to the ice front. Under a cooling rate of 0.5 ºC/sec. (a), (b), and (c) were different magnification rates.

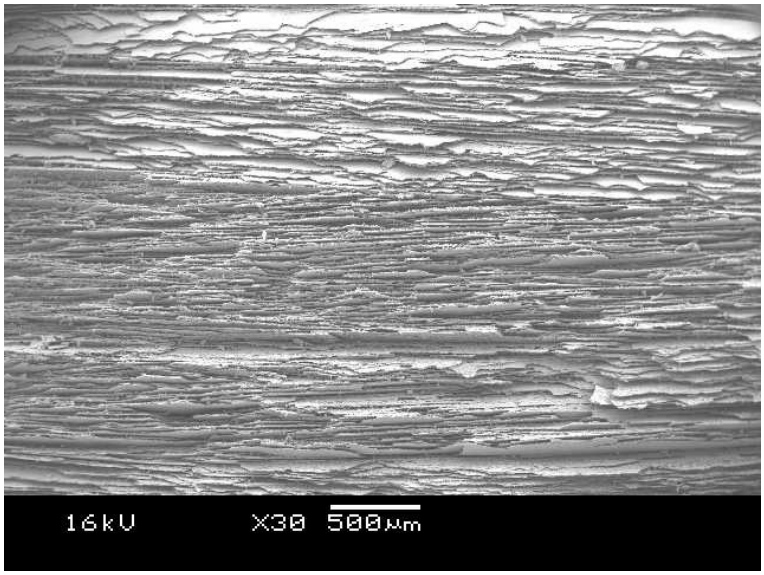

Figure 4.40 SEM microstructure of the sintered (1525 ºC, 2h) porous alumina ceramics (from 20 vol.% slurry with 0.14 wt.% NH_4PAA and 3 wt.% B1000 and 2 wt.% B1007 binders) obtained through double-sided freezing setup, parallel to the ice front, under a cooling rate of 0.5 ºC/sec.

One interesting phenomenon was observed in the middle of one sample obtained by double-sided technique, as shown in Figure 4.41. Above the orange line, the rough sides of the ceramic walls were all toward one side (see the arrows in the picture), while below the orange line, the rough sides were all toward the opposite side.

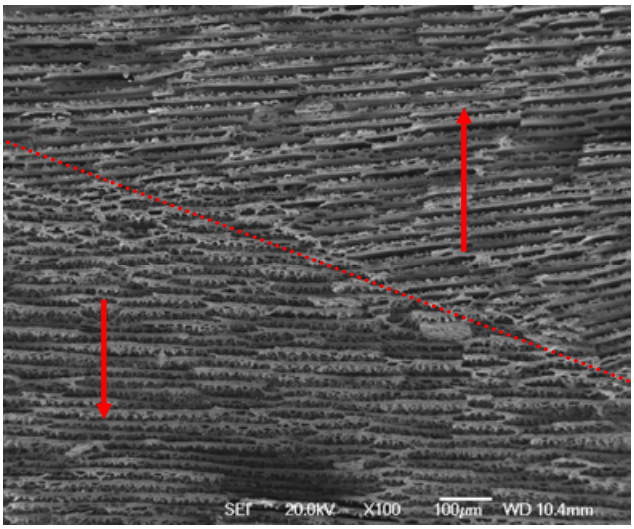

Figure 4.41 SEM microstructure of the sintered (1325 ºC, 2h) samples (24 vol.% slurry with 0.14 wt.% NH_4PAA and 3 wt.% B1000 and 2 wt.% B1007 binders) obtained through double-sided freezing setup, perpendicular to the ice front, under a cooling rate of 0.5 ºC/sec.

One possible explanation for this phenomenon is shown below:

The rough sides of the ceramic walls are caused by the dendrites of ice crystals. So the growth direction of the dendrites of ice crystals determines the direction of the ceramic arms. It is known[13,30] that the ice crystals grow tilted just a few degrees with respect to the direction of the temperature gradient, while in one side of the crystals small dendrites are a few micrometers in height aligned with the direction of the gradient form. In the double-sided freeze casting, the freezing started on both sides of the mould, so the ice crystals began to grow almost simultaneously and joined in the middle part of the sample. Therefore, the phenomenon was probably caused by the opposite temperature gradient.

4.12 Summary

This chapter focuses on the fabrication technique of freeze casting using alumina as a model material. A variety of processing factors in the freeze casting process including the rheological property of the slurries, solids loading of the slurry, the freeze cooling rate, and the sintering temperature, were investigated and discussed in this chapter. Moreover, the influence of additives including PVA binder, commercial binder, and glycerol on the morphology of the porous microstructures was also investigated. An innovative technique of freezing (double-sided freezing) was demonstrated and discussed.

Based on the investigation of fabrication of porous alumina ceramic by freezing casting with various slurry concentrations, different freeze cooling rates, sintering temperatures, additions and freezing technique, the results obtained in this chapter can be summarized as follows:

(1) NH_4PAA is an effective dispersant, and all slurries exhibited typical shear-thinning behaviour making them suitable for freeze casting.

(2) Porous alumina ceramic with total porosity ranging from 33% to 67% were achieved through freezing aqueous alumina slurries, followed by sublimation and sintering. The

resultant pores are open, presenting a lamellar architecture. The size of the pore can be modified by changing the initial slurry concentration and the cooling rate. The wall thickness of the sintered samples increased noticeably from about 10 μm to 60 μm as the solids loading rose from 14 vol.% to 37 vol.%. Furthermore, the ratio (wall thickness/ gap between walls) also increased markedly from about to 0.5 to 6 with increasing initial slurry solids loadings. The thickness of the ceramic wall varied over a wide range, from about 125 μm to 17 μm and it decreased dramatically as the cooling rate increased from 0.25 to 1.1 ºC/sec. The sintering temperature is of significance in obtaining porous ceramics with appropriate porosity and compressive strength for specific applications.

(3) Because of their lamellar microstructures, the samples obtained exhibited compressive strength up to 123 MPa for 33% porosity and 55 MPa for 42% porosity, making them suitable to be considered for potential load-bearing applications.

(4) The addition of PVA (3wt.% to 10 w.%) greatly affects the morphologies and properties of the final porous ceramics through depletion flocculation; commercial binder can affect their morphologies as well through bridge flocculation; glycerol can effectively bind to the water molecules and disrupt the complete crystallization of ice, leading to a cellular architecture.

(5) More homogeneous microstructures in a large area of the final porous ceramic were achieved by a double-sided freezing setup; however, the opposing temperature gradients may lead to different orientations for the ceramic arms limiting its application.

References

1. J.A. Lewis. Colloidal processing of ceramics. Journal of the American Ceramic Society. 2000, 83(10), 2341-2359.

2. M.E. Gomes, A.S. Ribeiro, P.B. Malafaya, et al. A new approach based on injection moulding to produce biodegradable starch-based polymeric scaffolds: morphology, mechanical and degradation behaviour. Biomaterials, 2001, 22(9), 883-889.

3. P.C. Hidber, T.J. Graule, L.J. Gauckler. Citric acid-a dispersant for aqueous alumina suspensions.Journal of the American Ceramic Society. 1996, 79(7), 1857-1867.

4. D. Zhang. Fabrication of microcomponents. PhD thesis. University of Birmingham, UK. 2005.

5. S. Deville, E. Saiz, A. P. Tomsia. Freeze casting of dydroxyapatite scaffolds for bone tissue engineering. Biomaterials. 2006, 27, 5480-5489.

6. J.D. Hunt. Pattern formation in solidification. Materials Research Technology. 1999, 15(9), 9-14.

7. R.W. Rice. Comparison of stress concentration versus minimum solid area based mechanical property-porosity relations. Journal of Materials Science. 1993, 28(8), 2187-2190.

8. D.D. Brown and D.J. Green. Investigation of strut crack formation in open cell alumina ceramics.Journal of the American Ceramic Society. 1994, 77(6), 1467-1472.

9. S. Bose, J. Darsell, H.L. Hosick. Processing and characterization of porous alumina scaffolds. Journal of Materials Science: Materials in Medicine, 2002, 13, 23-28.

10. K. Prabhakaran, Anand Melkeri, N.M. Gokhale. Preparation of macroporous alumina ceramics using wheat particles as gelling and pore forming agent. Ceramic international, 2007, 33, 77-81.

11. H. Schoof, J. Apel, I. Heschel, et al. Control of pore structure and size in freeze-dried collagen sponges. Journal of Biomedical Materials Research. 2001, 58(4), 352-357.

12. V.F. Petrenko and R.W. Whitworth. Physics of ice. Oxford: Oxford University Press, 2002.

13. S. Deville, E. Saiz, A. P. Tomsia. Ice-templated porous alumina structures. Acta Materialia. 2007, 55, 1965-1974.

14. S.W. Sofie. Fabrication of functionally graded and aligned porosity in thin ceramic substrates with the novel freeze-tape-casting process. Journal of the American Ceramic Society. 2007, 90(7), 2024-2031.

15. A.J. Moulson and J. M. Herbert. Electroceramics materials, properties, applications. Chapman and Hall. 1990, 68-76.

16. J. A. Lewis. Binder removal from ceramics. Annual Review of Materials Science. 1997, 27, 147 - 173.

17. F. Chabert, D.E. Dunstan, G. V. Franks. Cross-linked polyvinyl alcohol as a binder for gel casting and green machining. Journal of the American Ceramic Society. 2008, 91(10), 3138-3146.

18. A.U. Khan, B. J. Briscoe, P.F. Luckham. Interaction of binders with dispersant stabilised alumina suspensions. Colloids and Surfaces A: Physicochemical and Engineering Aspects. 2000, 161, 243-257.

19. P. Mikkola, E. Levänen, J.B. Rosenholm. Colloidal processing of aluminum oxide powder for membrane applications. Ceramics International. 2003, 29, 393–401.

20. M.F. Butler. Instability formation and directional dendritic growth of ice studied by optical interferometry. Crystal Growth and Design. 2001, 1(3), 213-223.

21. H.F. Zhang, I. Hussain, M. Brust, et al. Aligned two-and three- dimensional structures by directional freezing of polymers and nanopaticles. Nature Materials, 2005, 4, 787-793.

22. W.W. Mullins and R.F. Sekerka. Stability of planar interface during solidification of dilute binary alloy. Journal of Applied Physics, 1964, 35(2), 444-451.

23. R.F. Sekerka. A stability function for explicit evaluation of the Mullins-Sekerka interface stability criterion. Journal of Applied Physics. 1965, 36(1), 264-267.

24. Ch. Korber, G. Rau, M.D. Cosman, et al. Interaction of particles and a moving ice-liquid interface. Journal of Crystal Growth. 1985, 72, 649-662.

25. D. Zhang, B. Su, T.W. Button. Microfabrication of three-dimensional, free-standing ceramic MEMS components by soft moulding. Advanced Engineering Materials, 2003, 5 (12), 924-927.

26. M. Imbaby, K. Jiang, I. Chang. A soft moulding process for fabrication of micromachine parts from stainless steel powder. Advanced Engineering Materials, 2009, 11(3), 202-205.

27. M.J. Statham, F. Hammett, B. Harris, et al. Net-shape manufacture of low-cost ceramic shapes by freeze-gelation. Journal of Sol-gel Science and Technology. 1998, 13, 171-175

28. S.W. Sofie and F. Dogan. Freeze casting of aqueous alumina slurries with glycerol. Journal of the American Ceramic Society. 2001, 84(7)1459–64.

29. C.S. Miner and N.N. Dalton, Glycerol. Reinhold, New York, 1953.

30. M.G. Worster and J.S. Wettlaufer. Natural convection, solute trapping, and channel formation during solidification of saltwater. The Journal of Physical Chemistry B. 1997, 101 (32), 6132-6136.

CHAPTER 5 POROUS ALUMINA AND ZIRCONIA COMPOSITE CERAMICS

5.1 Introduction

In Chapter 4, a single ceramic phase (alumina) was utilized as the model material to demonstrate several basic factors involved in the freeze casting technique. However, the understanding of this technique is still in the early stage and more research is needed to explore processability and controllability. This chapter reports work on a two-phase (two ceramic phases) system in order to further investigate the freeze casting process.

Al_2O_3 and ZrO_2 ceramic powders (as the model materials) were utilized to fabricate the porous Al_2O_3-ZrO_2 composite ceramics in this chapter. Al_2O_3-ZrO_2 composite ceramics in recent years have received much attention because of their excellent properties such as high mechanical strength, wear resistance, good thermal shock resistance and low thermal conductivity[1,2]. Based on these properties, Al_2O_3-ZrO_2 composite ceramics have been utilized in a variety of fields including dental screws, cutting blades, and insulators[3-5]. Moreover, porous Al_2O_3-ZrO_2 composite ceramics have attracted much attention as well and have been investigated as potential candidates for biomaterials applications[6,7], and been thus chosen for this work.

5.2 Materials

The alumina powder (~ 0.7 μm) used in Chapter 4 (Section 4.2) was also employed here. 3% mol. yttria-stabilized zirconia (Tosoh-zirconia, Japan) power was employed for the composite ceramics. A SEM micrograph of the yttria-stabilized zirconia powder used in this chapter is shown in Figure 5.1. The particle size is 0.1~0.2 μm measured from the SEM

photograph as described in Chapter 3.2.11.

Unless explicitly stated otherwise in this chapter, all slurry samples were prepared using 0.14 wt.% of ammonium polyacrylate (NH_4PAA) solution as the dispersant, and 3 wt.% B-1000 and 2 wt.% B-1007 as binders in aqueous suspensions. The solidification rate in the axial direction of the cylindrical sample was about 110 $\mu m \cdot s^{-1}$(equivalent to a cooling rate of 1.1 ºC/sec, as shown in Chapter 4.7).

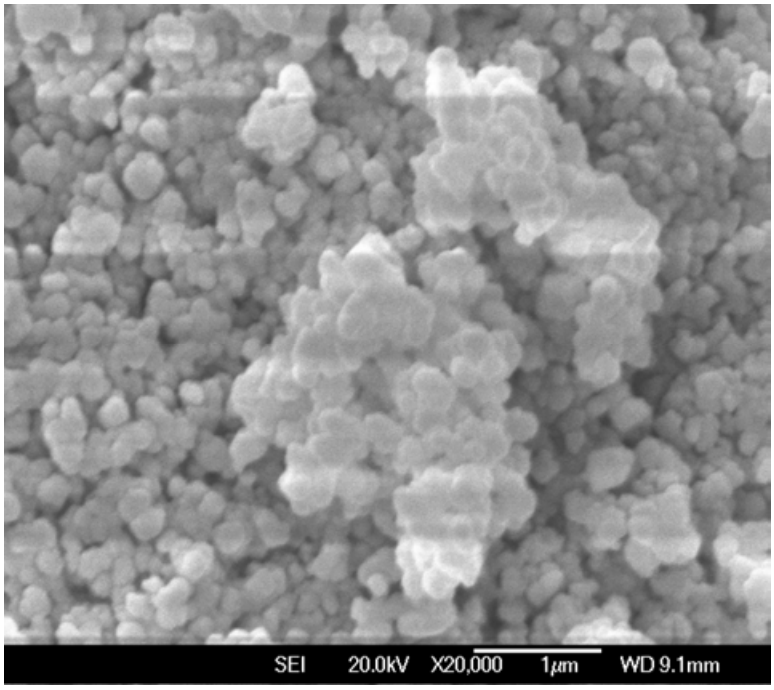

Figure 5.1 SEM photograph of the as received yttria-stabilized zirconia powder used in this study

5.3 General Characteristics of the Composites Obtained through Two-Phase System

The aqueous ceramic suspensions with various solids loadings, ranging from 11 to 42 vol.% were prepared by mixing alumina and zirconia powders with a ratio of 20:80 (Al_2O_3:ZrO_2) by weight according to the way as described in Chapter 3.1.2.1. The Al_2O_3-ZrO_2 composite ceramics were obtained from the resulting suspensions.

Figure 5.2(a) shows a typical sintered Al_2O_3-ZrO_2 composite ceramic (1550 ºC, 2h) produced by directional freeze casting using a suspension of 16 vol.% initial solids loading. The height and diameter of the sample are 11 mm and 10 mm respectively. The samples showed no visible defects such as cracks or distortion, which was very similar to the pure alumina samples shown in Chapter 4 (Figure 4.5).

Figure 5.2 (b) and (c) are the cross sectional SEM micrographs of this composite ceramic at low and high magnifications, showing an aligned lamellae morphology with regular pore features in a long-range order.

This can be explained by using the basic principle (already shown in Chapter 4) that the phase separation occurs during the freezing process of the aqueous suspension[8,9]. The ceramic particles in the slurry are ejected by the advancing ice front and concentrate between the growing ice crystals[10]. Space or porosity will be created after sublimation of the ice. Actually, the final microstructure of the ceramic is a negative replica of the ice. A constant cooling rate will result in a more homogeneous ice nucleation[11], leading to a relatively homogenous morphology in the sample, as shown in Figure 5.2 (b) and (c). Moreover, the surface of the ceramic walls showed a special morphology: one side showed dendritic-like arms and these arms were uniform in size and distribution, about 3~5 μm high; the other side remained smooth, which is consistent with the results shown in Chapter 4 (Figure 4.8). This phenomenon is related to the anisotropic interface kinetics[11]. The dendritic-like arms of the ceramic wall resulted from the formation of the side branches when ceramic particle freeze-concentration around the primary ice cells induced secondary instability which leads to the formation of ice crystals perpendicular to the primary ice growth direction[8,9]. The magnified image of the ceramic wall is shown in Figure 5.2 (d) and the ceramic wall was dense.

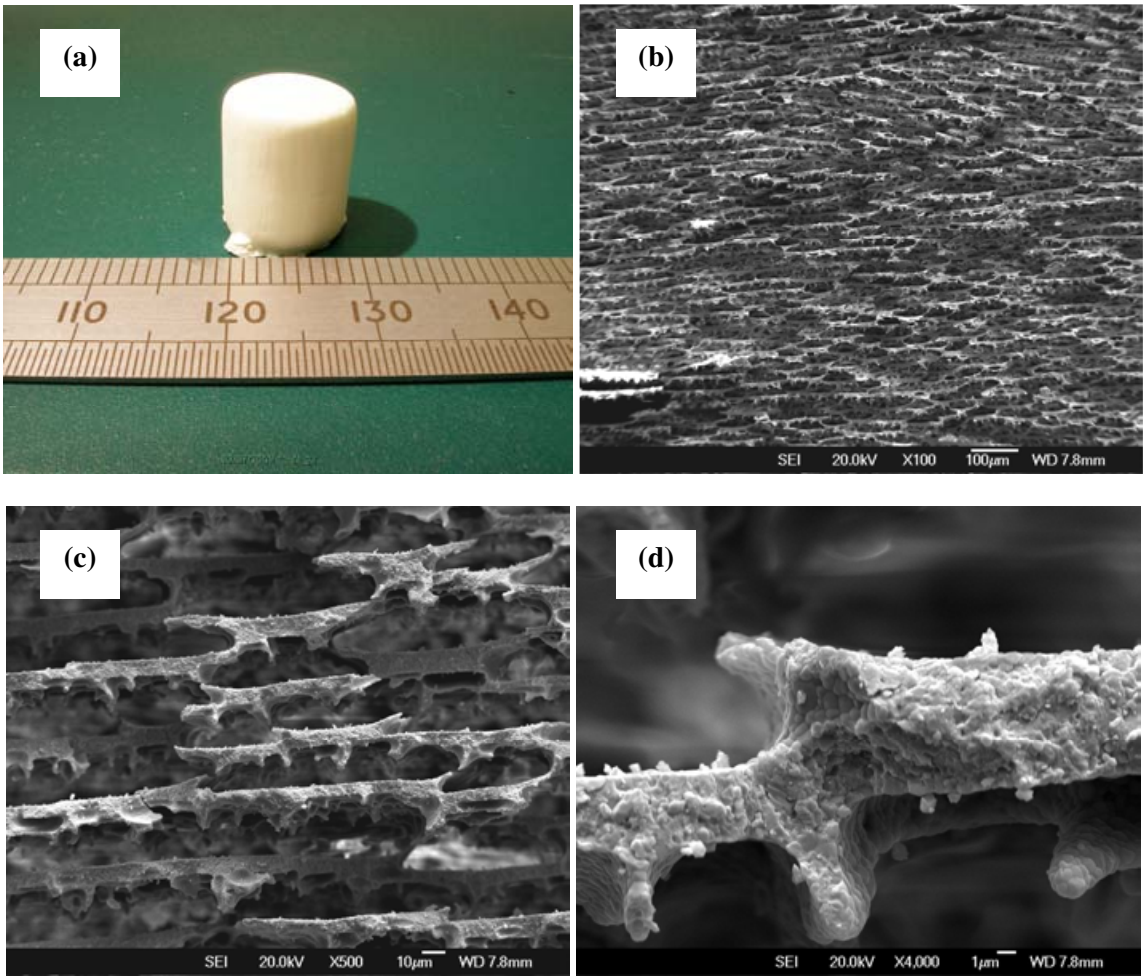

Figure 5.2 Optical and SEM photographs of the porous Al_2O_3-ZrO_2 composite ceramics obtained from 16 vol.% initial solids loading and under a cooling rate of 1.1 ºC/sec and sintered at 1550 ºC for 2 hours: (a) optical image of a typical sintered sample, (b) cross sectional image at low magnification, (c) cross sectional image at high magnification, (d) detail of the ceramic wall. For the micrographs, the solidification direction is perpendicular to the page.

It was further observed that changing the initial solids loading greatly affected the final architecture of the composite ceramics. Figure 5.3 shows SEM micrographs of the sintered composite ceramics obtained from different initial solids loadings at low magnification. The higher magnification SEM micrographs of those porous ceramics (shown in Figure 5.2) are shown in Figure 5.4.

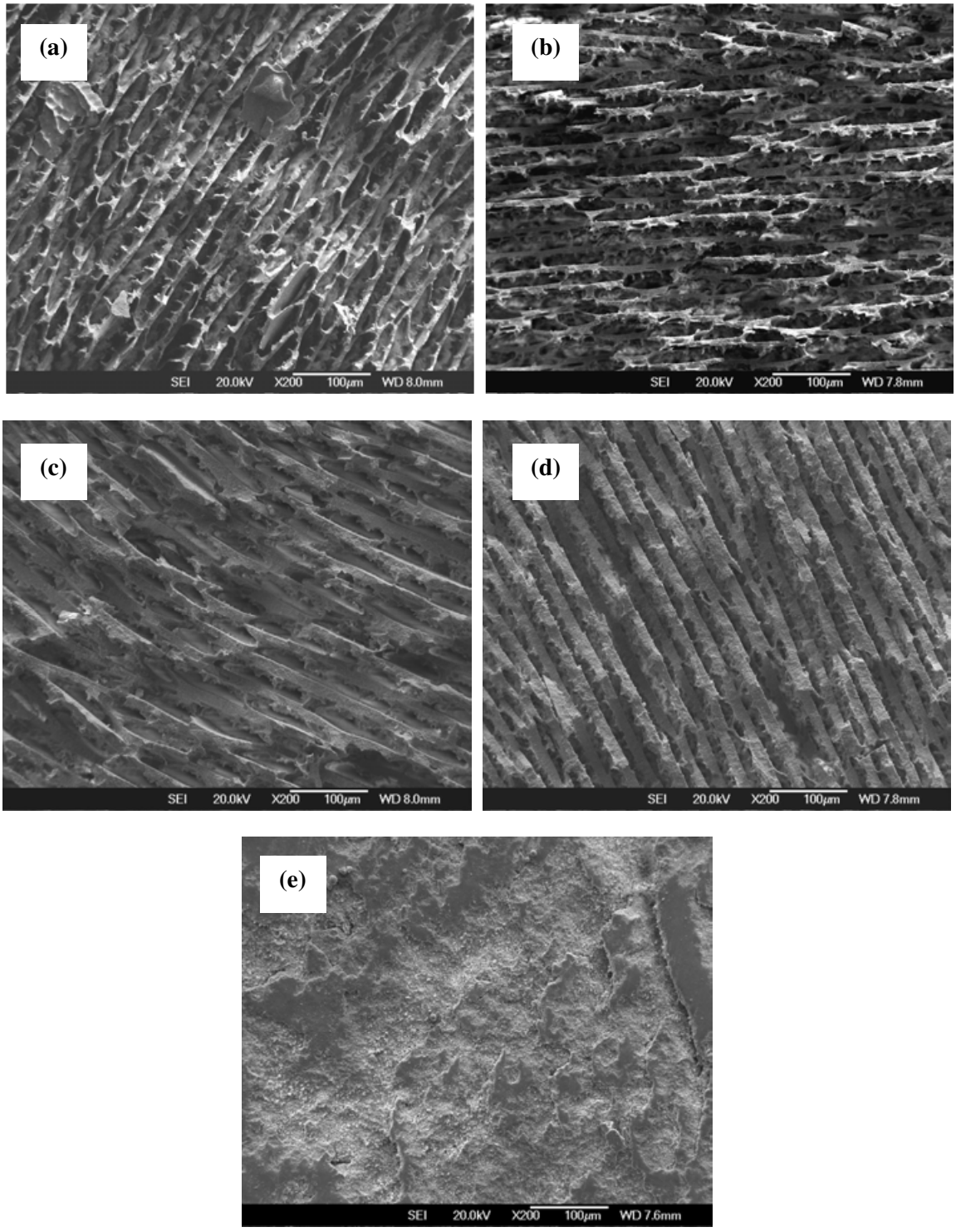

Figure 5.3 Cross-sectional micrographs of the Al_2O_3-ZrO_2 composite ceramics obtained from slurries with different initial solids loadings: (a) 11 vol.% (b) 16 vol.% (c) 22 vol.% (d) 30 vol.% (e) 42 vol.% and under a cooling rate of 1.1 ºC/sec, and sintered at 1550 ºC for 2 hours. The solidification direction is perpendicular to the page.

All the ceramic samples as shown in Figure 5.3 except the one obtained from the 42 vol.% solids loading slurry (Figure 5.3(e)) showed relatively homogeneous and long-range channels but different characteristics. The ceramic walls of these sintered samples were dense as shown in the higher magnification SEM photos (Figure 5.4). The wall thickness of these samples increased from about 4 μm to 17 μm as the solids loading rose from 11 vol.% to 30 vol.%, as shown in Table 5.1.

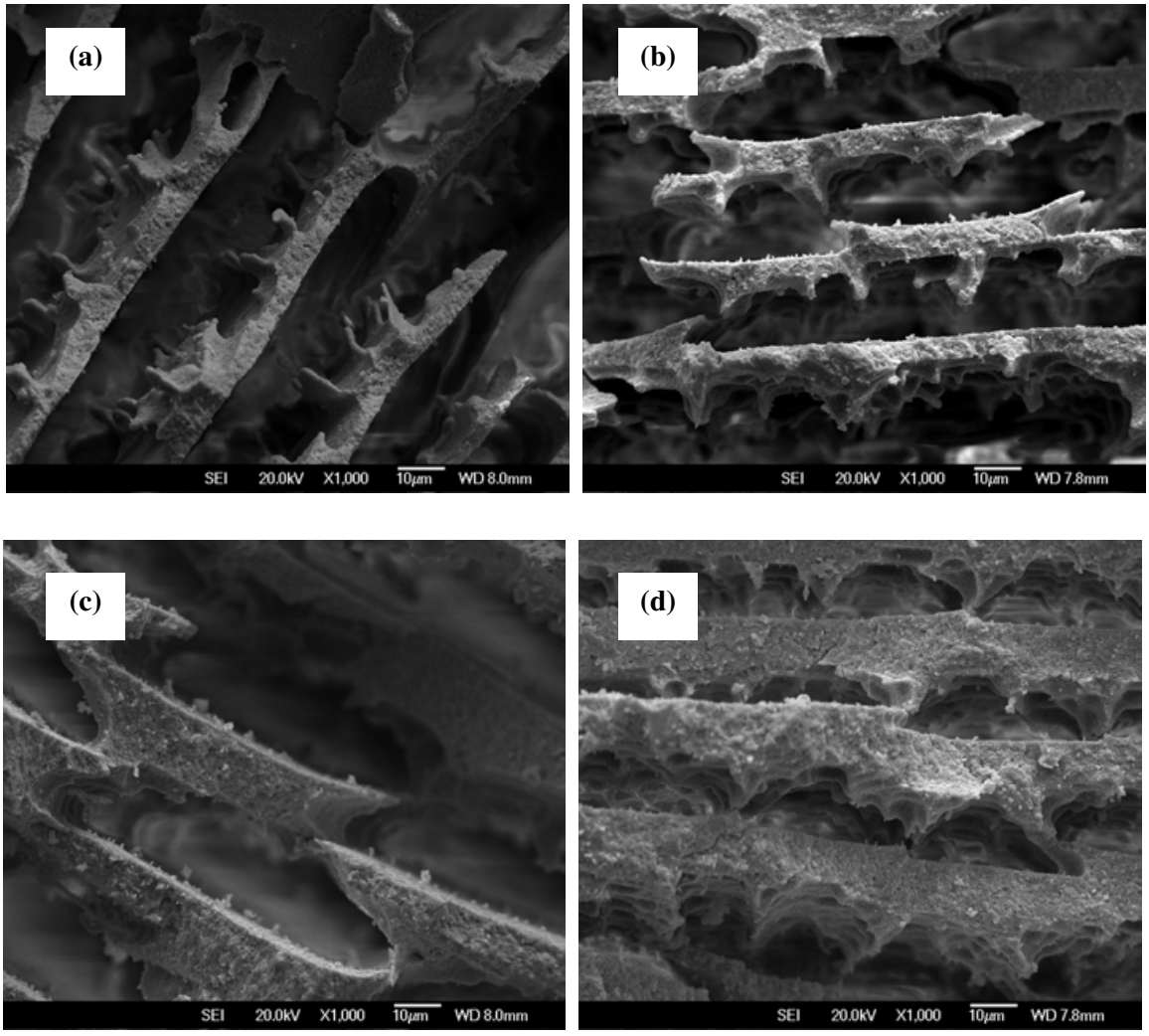

Figure 5.4 Higher magnification of cross-sectional micrographs of the Al_2O_3-ZrO_2 composite ceramics obtained from slurries with different initial solids loading: (a) 11 vol.% (b) 16 vol.% (c) 22 vol.% (d) 30vol.% and under a cooling rate of 1.1 ºC/sec, and sintered at 1550 ºC for 2 hours. Solidification direction is perpendicular to the page.

Table 5.1 Measured average wall thickness of porous Al_2O_3-ZrO_2 composite ceramics obtained from slurries with different initial solids loadings (under a cooling rate of 1.1 ºC/sec, and sintered at 1550 ºC for 2 hours)

Initial solids loading (vol.%)	11	16	22	30	42
Average wall thickness (μm)	4	7	12	17	---

Higher solids loading in the two-phase ceramic system can lead to larger wall thickness similar to the results of the single phase system shown in Chapter 4 (Figure 4.13).

Beside the wall thickness, the porosity of the composite ceramic was also affected by the initial solids loading. Figure 5.5 shows the relationship between the porosity (Chapter 3.2.3.1) of the composite ceramics and the initial slurry solids loading. With the increase of the initial slurry concentration from 11 vol.% to 42 vol.%, the final porosity decreased from 74% to 19%. The linear relationship between the porosity and the initial solid loading can be expressed as follows:

$$P = 93.4 - 1.83X \qquad (5\text{-}1)$$

where P means the porosity, and X means the initial solid loading.

The lower the initial solids loading, the higher the final porosity is. In any freeze casting of an aqueous system (single phase or two-phase), the volume of water contributes much to the final porosity.

In order to evaluate the mechanical properties of the sintered porous Al_2O_3-ZrO_2 composite ceramics, compressive strength tests (Chapter 3.2.5) were conducted and the compressive strength of the sintered composites ceramic is also given in Figure 5.5. Although the compressive strength of the porous composite ceramic was low when the initial solids loading was 11 vol.%, it increased rapidly with the increase of the slurry concentration, reaching 50 MPa for 22 vol.% initial solids lading and 81 MPa for 30 vol.% initial solids loading. The higher solids loading, the higher compressive strength the sample gains. This

shows a potential way to produce porous Al_2O_3-ZrO_2 composite ceramics for loading bearing application. Thus in the aspects of basic characteristics, the porous Al_2O_3-ZrO_2 composite ceramics obtained from two-phase colloidal systems show similar behaviour to those of single phase alumina described in Chapter 4.

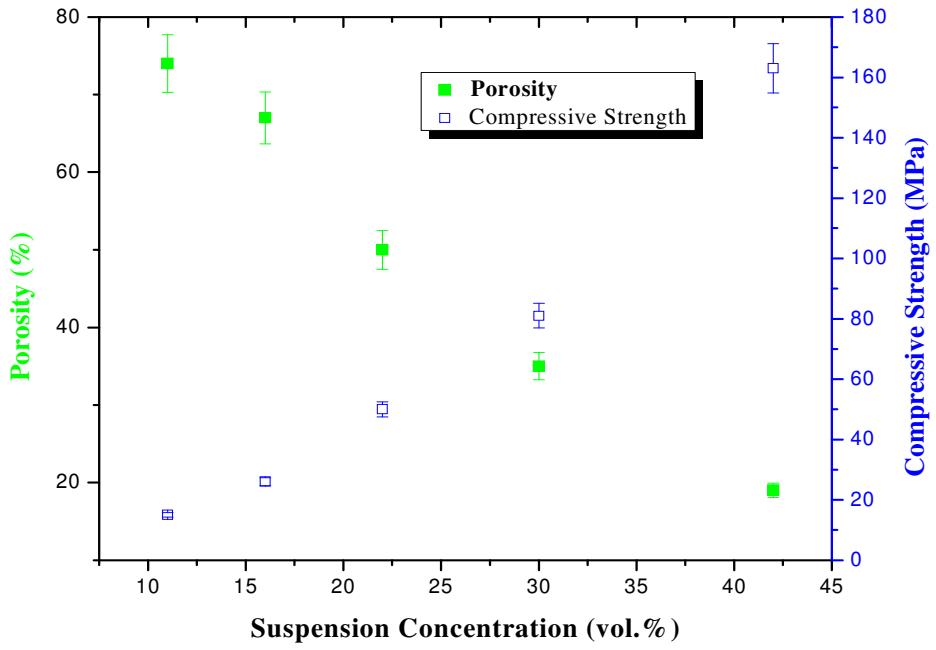

Figure 5.5 Porosity and compressive strength versus slurry concentration. Al_2O_3-ZrO_2 porous ceramics obtained from slurries with different initial solids loadings and under a cooling rate of 1.1 ºC/sec, sintered at 1550 ºC for 2 hours.

5.4 Engulfment and Size Effect

When the initial solids loading reached 42 vol.%, no lamellae structure was observed in the cross section of the sintered samples as shown in Figure 5.6(a). In some parts of this sample, the microstructure was quite dense as shown in Figure 5.6 (b). It has been mentioned in Chapter 4 (section 4.9.1) that in the freeze casting process a critical velocity v_c for a certain particle size exists, above which the particle can not be ejected by the advancing solidification front and engulfment will happen. A simple model has been given in Chapter

4.9.1 (Equation 4-4).

For the 42 vol.% solids loading system, compared with slurries with lower solids loading, a large change of R (the particle radius) and η (the slurry viscosity) may occur. As shown in Figure 5.6(c), the green body indicated that the dispersion of particles in the 42 vol.% slurry was good, so the large change of R caused by flocculation is unlikely. Moreover, Figure 5.6 (d) shows the rheological property of the suspensions. The viscosity of 42 vol.% suspension was nearly 10 to 20 times higher than those of 30 vol.% and 22 vol.% at low shear rates, which is consistent with our former study[12,13] that the ceramic suspension viscosity normally increases with increasing the solids loading. One possible explanation for this phenomenon is that higher solids loading caused much higher viscosity, leading to a marked decrease of the critical velocity (v_c). Therefore, under the same cooling rate as being used for the slurries of lower initial solids loading, the particles in the 42 vol.% solids loading suspension could not be ejected by the advancing ice front and engulfment formed, finally resulting in the loss of the porous architecture.

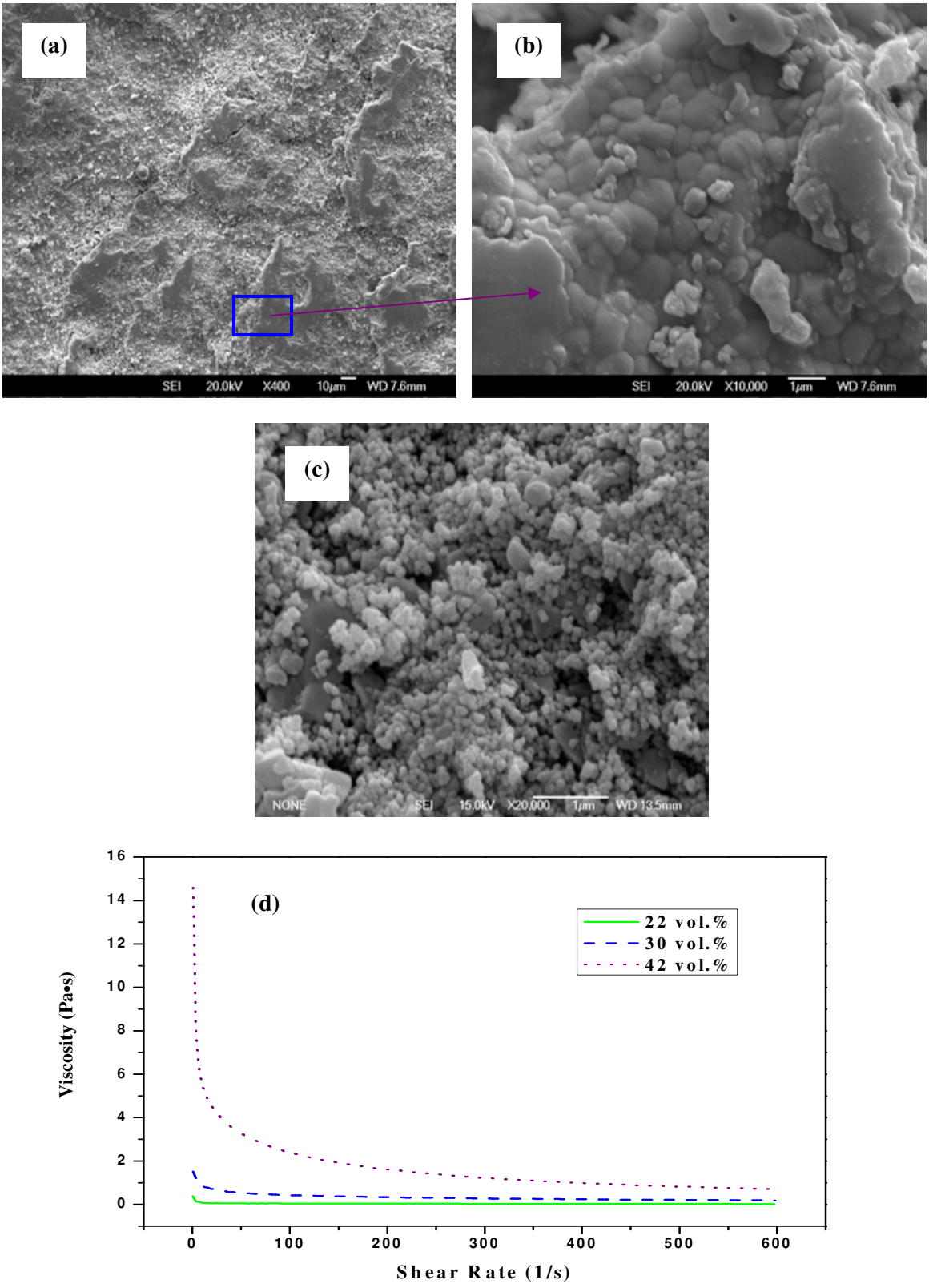

Figure 5.6 (a) cross-sectional micrographs of the Al_2O_3-ZrO_2 composites obtained from 42 vol.% slurries; (b) Detail of the zone in (a); (c) SEM micrograph of green body obtained by centrifugal casting from the 42 vol.% slurry; (d) viscosity of the suspensions versus shear rates.

One interesting phenomenon was observed when the ratio (Al_2O_3:ZrO_2) was changed. Figure 5.7 (a), (b), and (c) show the cross-sectional micrographs of porous single phase ceramic or two-phase ceramics obtained from 42 vol.% initial solids loading but with different Al_2O_3/ZrO_2 ratios. The sample shown in Figure 5.7 (a) was 100% alumina, and engulfment occurred and the lamellae architecture was lost. The sample shown in Figure 5.7 (b) is the Al_2O_3-ZrO_2 composite ceramic with a ratio of 30/70 (Al_2O_3:ZrO_2). Engulfment also happened in this sample. The sample shown in Figure 5.7 (c) is 100% zirconia. Engulfment did not happen in this sample and the lamellae structures were still there.

It is known that engulfment depends mainly on the critical velocity as described above. For these three samples, they were obtained under the same cooling rate and from the same solids loading (42 vol.%). The only difference is the alumina content. As mentioned in section 5.2, the alumina powder has a larger particle size (about 0.7 μm) compared with that of the zirconia powder (0.1~0.2 μm). Moreover, the slurries of the three samples showed very similar rheological behaviours as shown in Figure 5.7 (d). Therefore, incorporating the simple model (4-4), the v_c was mainly dominated by the particle size. It is probably that under a same solidification rate, the samples with alumina powder reached their critical velocities and engulfment happened in these samples, while the 100% zirconia sample did not reach its v_c due to a smaller size. In a two-phase system, therefore the critical velocity is mainly determined by the phase with the larger particle size.

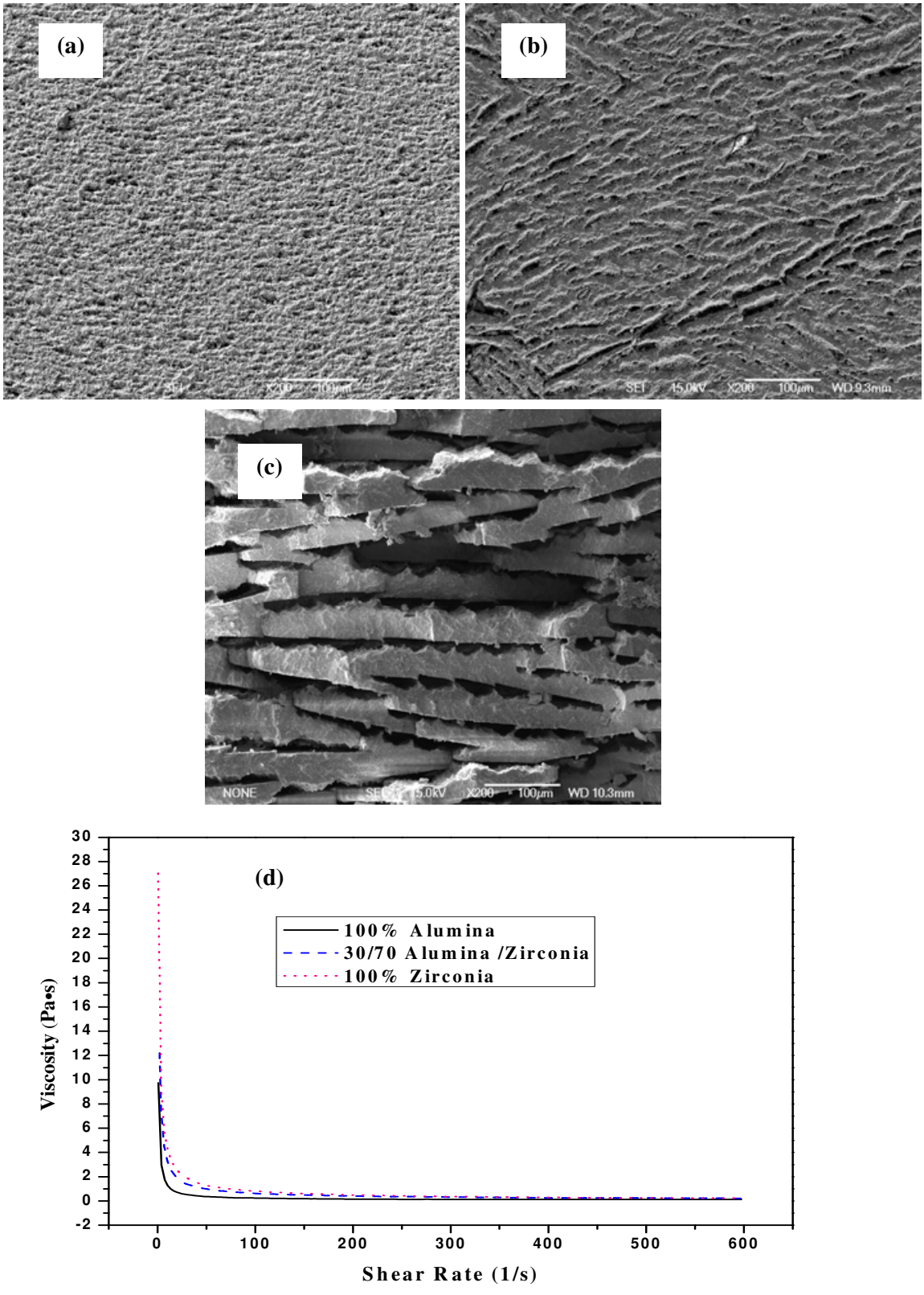

Figure 5.7 Cross-sectional micrographs of porous ceramic or composite ceramics obtained from 42 vol.% initial solids loading, same solidification rate (110 μm/s), but with different Al_2O_3/ZrO_2 ratio: (a) 100/0 (b) 30/70 (c) 0/100; (d) viscosity of the suspensions versus shear rates.

5.5 Phase Segregation in Two-Phase System

Another interesting phenomenon was observed in the Al_2O_3-ZrO_2 composite ceramics obtained from the two-phase colloidal suspension system.

The chemical compositions of the ceramic wall and arm have been analysed by EDX. As shown in Figure 5.8 and Figure 5.9, both the results showed that the element ratio (Al/Zr) of the ceramic wall was slightly smaller than the initial one (17.88% (weight), and 60.29% (atomic)) and the element ratio of the ceramic arm was much higher than the initial one. Therefore, it appears said "phase segregation" has occurred in these samples.

Because of the lack of experimental data about submicron particles in the interface, it is very difficult to make a quantitative explanation. Actually, the forces involved in the interface during freezing are rather complicated. One qualitative and possible explanation is that during freezing (under a cooling rate of 1.1μm/sec, below the v_c), under the effects of interface forces, zirconia particles (with higher density) were much more difficult to be pushed and mostly concentrate in the field of ceramic walls; while, alumina powders (with lower density) were much easier to be ejected and mostly settle down in the field of the ceramic arms.

However, it can be concluded that in freeze casting, especially in a two-phase system, the choice of particle size of the ceramic powder becomes very critical.

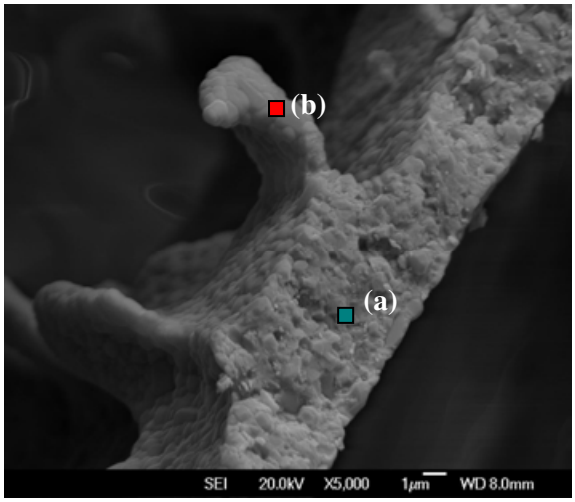

(a)

Element	Weight%	Atomic%
Al K	14.33	36.12
Zr L	85.67	63.88
Totals	100.00	

(b)

Element	Weight%	Atomic%
Al K	48.56	76.14
Zr L	51.44	23.86
Totals	100.00	

Figure 5.8 EDX analysis for the Al_2O_3-ZrO_2 composite ceramic obtained from 11 vol.% slurry (Al_2O_3/ZrO_2 : 20/80), sintered at 1550 ºC for 2 hours, (a) ceramic wall, (b) ceramic arm.

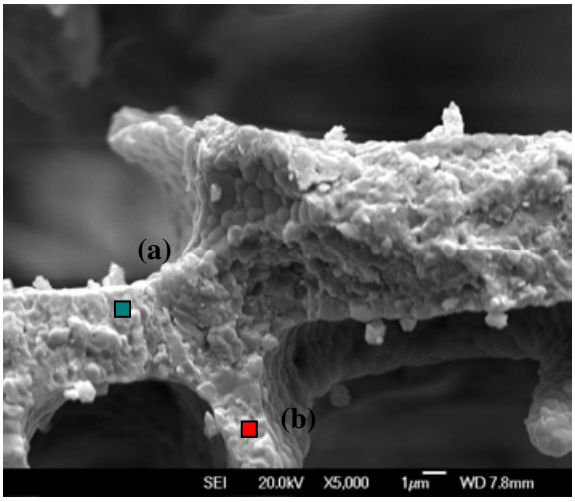

(a)

Element	Weight%	Atomic%
Al K	14.60	36.62
Zr L	85.40	63.38
Totals	100.00	

(b)

Element	Weight%	Atomic%
Al K	65.34	86.44
Zr L	34.66	13.56
Totals	100.00	

Figure 5.9 EDX analysis for the Al_2O_3-ZrO_2 composite ceramic obtained from 16 vol.% slurry (Al_2O_3/ZrO_2 : 20/80, sintered at 1550 ºC for 2 hours (a) ceramic wall, (b) ceramic arm.

5.5 Summary

In summary, porous Al_2O_3-ZrO_2 composites with relatively homogenous and long-range order channels have been produced through a two-phase colloidal system. The pore characteristics, porosity and the compressive strength of the sintered composites ceramic can be modified through change of the initial solids loading. As the initial solids loading

increased from 11 vol.% to 30 vol.%, the porosity of the sintered composite ceramics decreased from 74% to 35%, conversely. Therefore, in the aspects of basic characteristics, the porous ceramics obtained from two-phase colloidal systems show a similar behaviour to the one obtained for a single phase suspension.

The initial solids loading demonstrated a significant role in the formation of the final architecture and high solids loading, i.e. $\geq$ 42 vol.%, may lead to engulfment and result in the loss of porous and lamellae architecture.

Furthermore, in the freeze casting technique, especially in a two-phase system, the choice of particle size of the ceramic powder is of great significance, because it may lead to engulfment and phase segregation.

References

1. N. Claussen. Fracture toughness of Al_2O_3 with an unstabilized ZrO_2 dispersed phase. Journal of the American Ceramic Society, 1976, 59 (1-2), 49-51.

2. S.M. Olhero, I. Ganesh, and P.M.C. Torres. Aqueous colloidal processing of ZTA composites. Journal of the American Ceramic Society, 2009, 92(1), 9-16.

3. Y.S. Shin, Y.W. Rhee, and S.J. Kang. Experimental evaluation of toughening mechanisms in alumina-zirconia composites. Journal of the American Ceramic Society, 1999, 82(5), 1229-1232.

4. R.H.J. Hannink, P.M. Kelly, and B.C. Muddle. Transformation toughening in zirconia-containing ceramics. Journal of the American Ceramic Society, 2000, 83(3), 461-487.

5. W.H. Tuan, R.Z. Chen, T.C. Wang, et al. Mechanical properties of Al_2O_3/ZrO_2 composites. Journal of the European Ceramic Society, 2002, 22(16), 2827-2833.

6. J.Y. Yu, X.D. Sun, Q. Li, et al. Preparation of Al_2O_3 and Al_2O_3–ZrO_2 ceramic foams with adjustable cell structure by centrifugal slip casting. Materials Science and Engineering: A. 2008, 476 (1-2), 274-280.

7. X. He, Y.Z. Zhang, B. Su, et al. Zirconia toughened alumina ceramic foams for potential bone graft applications: fabrication, bioactivation, and cellular responses. Journal of Materials Science. Materials in Medicine, 2008, 19(7), 2743-2749.

8. H.F. Zhang, I. Hussain, M. Brust, et al. Aligned two-and three- dimensional structures by directional freezing of polymers and nanopaticles. Nature Materials, 2005, 4, 787-793.

9. M.F. Butler. Instability formation and directional dendritic growth of ice studied by optical interferometry. Crystal Growth and Design, 2001, 1(3), 213-223.

10. S. Deville, E. Saiz, and R.K. Nalla, et al. Freezing as a path to build complex composites. Science, 2006, 311, 515-518.

11. S. Deville, E. Saiz, and A.P. Tomsia. Ice-templated porous alumina structures. Acta Materialia. 2007, 55, 1965-1974.

12. G. Liu, D. Zhang, and T.W. Button. Preparation of concentrated barium titanate suspensions incorporating nano-sized powders. Journal of the European Ceramic Society, 2010, 30, 171-176.

13. D. Zhang, B. Su, and T.W. Button. Preparation of concentrated aqueous alumina suspensions for soft-moulding microfabrication. Journal of the European Ceramic Society, 2004, 24, 231-237.

CHAPTER 6 DISPERSION OF NANO-SIZED BT POWDERS AND PREPARATION OF BT-BASED EPOXY COMPOSITES

6.1 Introduction

The preceding two chapters (Chapter 4 and 5) focused on an investigation of the preparation techniques of freeze casting, including the basic influencing factors, the effect of additives and several other interesting phenomena. This chapter and also Chapter 7 concentrate on the application of the freeze casting technique incorporating functional materials, especially the functional properties.

It is known that $BaTiO_3$ is an important ceramic material in the electronics industry. It has been widely used to fabricate high-value capacitors[1,2], thermistors[3,4], and piezoelectric sensors[5,6]. Meanwhile, there is an ever-growing interest in electrically charged and piezoelectric materials, because they could be helpful in the field of bone grafting based on the electrical activity of bone itself[7-10]. $BaTiO_3$, therefore, has been investigated and reported to be a potential bioactive material. It could induce apatite formation in simulated body fluid[11,12], and it could improve bone formation in the biological environment due to its piezoelectric properties. Moreover, nano-sized powders have recently attracted much attention in order to gain significant improvement in key properties. In the case of $BaTiO_3$, improved performance such as the potential for device miniaturization, and improved dielectric and piezoelectric properties, can be achieved by incorporating nano-sized BT powders[13-15] and aqueous colloidal environmental friendly processing[16-19]. However, accurate microstructural control is essential when specific electrical requirements have to be fulfilled. Therefore, there is a need to investigate the incorporation of nano-sized BT powders in the freeze casting technique.

This chapter reports on experiments where nano-sized BT powders were employed to obtain BT and alumina doped BT epoxy composites for potential applications. The first section of this chapter focuses on the dispersion and sintering of nano-sized BT powders in order to obtain a well-dispersed BT suspension for freeze casting and optimization of the electrical properties. The second part of this chapter focuses on the BT and alumina-doped BT epoxy composites fabricated by freeze casting. Meanwhile, in order to improve the mechanical properties of the BT ceramics, nano-sized α–alumina was doped into BT through both a traditional electroceramics fabrication method and the freeze casting technique.

6.2 Dispersion and Sintering of Nano-sized BT Powder

6.2.1 Powder Characterization

A SEM micrograph of the BT powder (HPB-1000,TPL Inc., USA) utilized in this chapter is shown in Figure 6.1. The BT powder had a near-spherical morphology with a primary particle size around 50 nm, which was consistent with the data provided by the supplier.

Figure 6.2 shows the results of XRD analysis of the nano-sized BT powder. Through comparing XRD pattern with the JCPDS standards, the diffraction peaks from the nanoparticles could be mainly indexed as cubic BT, as no peak splitting was observed at the (200) peak. However, an impurity was found in the nano-sized BT powder. The peak in the XRD pattern around $2\theta=24°$ indicated the presence of $BaCO_3$ in the BT powder, which could significantly affect the final electrical properties as will be shown later in this section. The tetragonality (c/a ratio) of this nanosized BT powder is 1.0 which was caculated according to the XRD crystal lattice parameters. The Ba/Ti molar ratio is 0.995~1.010, which was provided by the BT powder manufacturer.

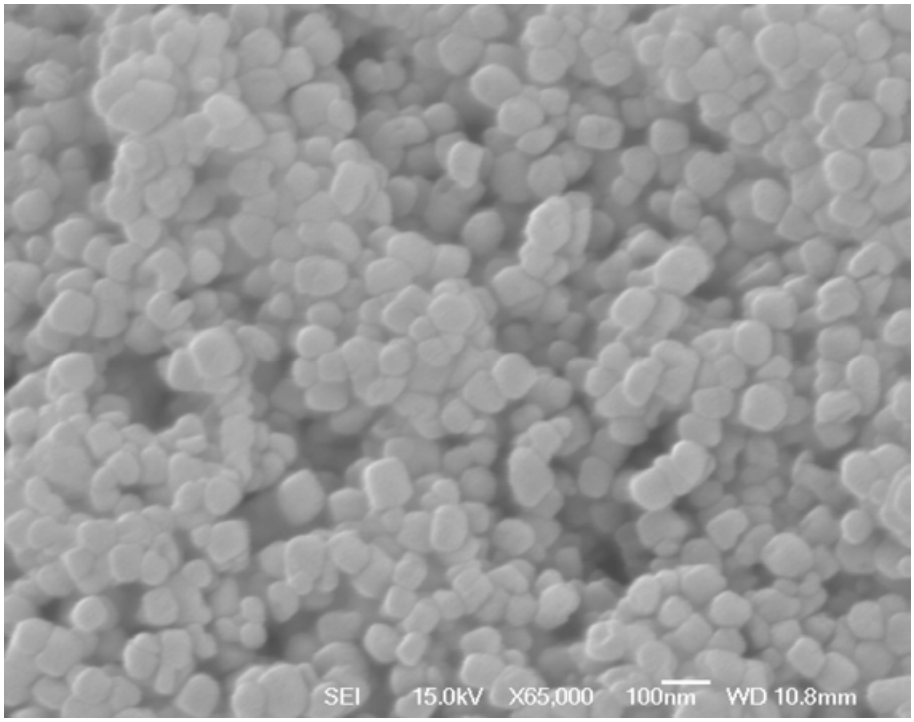

Figure 6.1 SEM photo of the commercial nano-sized BT powder utilized in this chapter with a primary particle size around 50 nm.

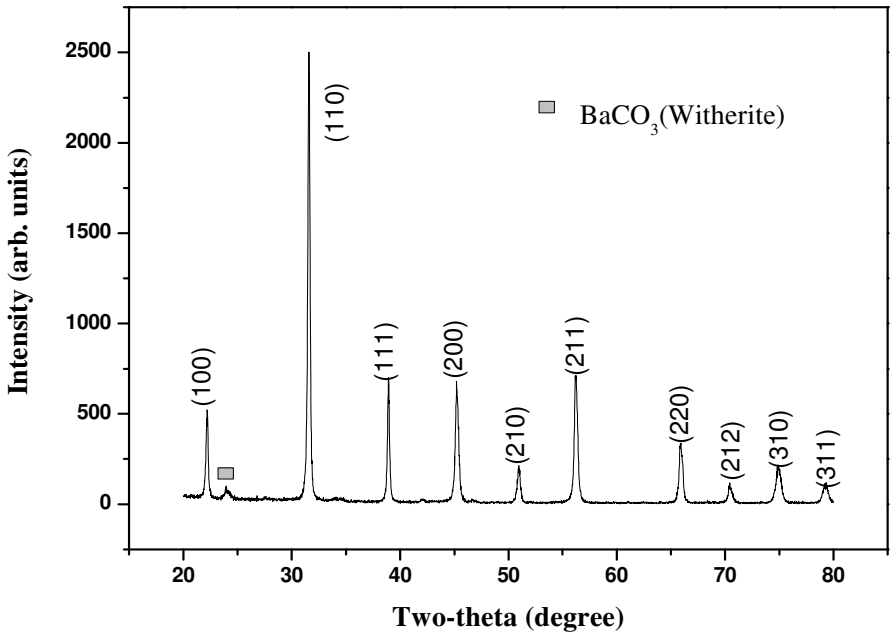

Figure 6.2 XRD patterns for the commercial nano-sized BT powder utilized in this chapter.

6.2.2 Rheological Property of $BaTiO_3$ Suspensions

The suspensions used in this chapter were prepared according to the method described in Chapter 3. Because of the particle size of BT powder, the process of adding the powder into the bottle was done very slowly, compared with the alumina powder, in order to avoid agglomeration.

6.2.2.1 Effect of Dispersant Content on the Viscosity of the BT Slurry

NH_4PAA is widely used in the preparation of stable colloidal suspensions, the mechanism for NH_4PAA being by eletrosteric stabilization. The amount of NH_4PAA used in a suspension can significantly affect the final property of the slurries. In order to obtain stable and well-dispersed BT suspension, different amounts of NH_4PAA were tried. The variation of the viscosity of a 30 vol.% BT suspension with dispersant (NH_4PAA) concentration is displayed in Figure 6.3.

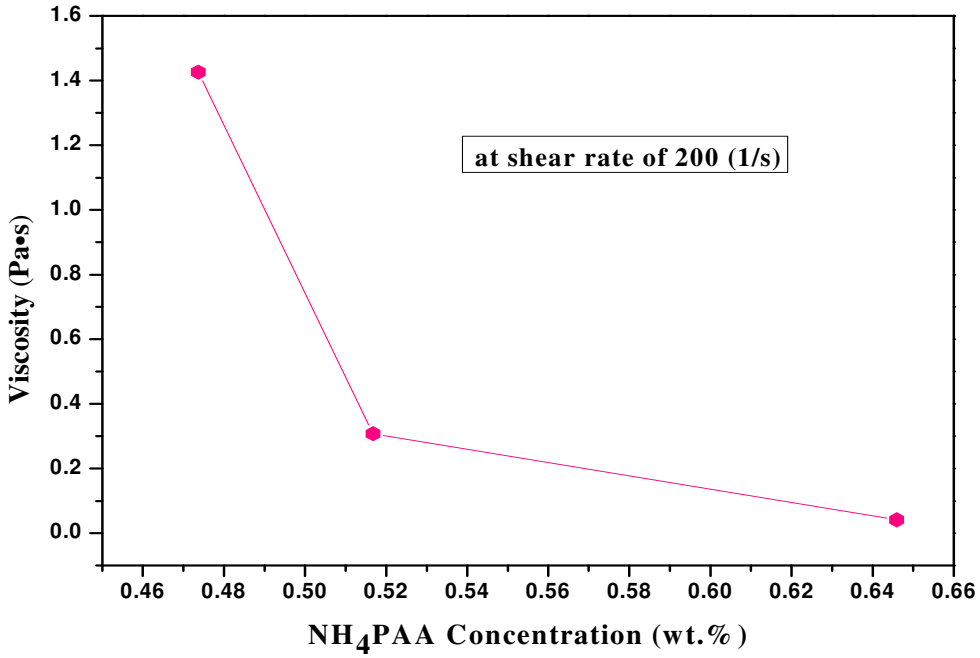

Figure 6.3 Viscosity versus dispersant (NH_4PAA) concentration for 30 vol.% BT suspension at share rate of 200 s^{-1}.

All the measurements of the viscosity were obtained under a shear rate of 200 s^{-1}. In the range of this experiment, the viscosity of the suspensions decreased dramatically as the NH_4PAA concentration increased. Therefore, NH_4PAA was found to be an effective dispersant of nano-sized BT powder. Furthermore, the viscosity of the suspension containing 0.646 wt.% NH_4PAA was low enough for freeze casting, so slurries with greater levels of dispersant were not investigated.

6.2.2.2 Effect of pH Value on the Viscosity of the BT Slurry

The variation of the viscosity of a 30 vol.% BT suspension with 0.646 wt.% NH_4PAA by adjusting the pH value (Chapter 3.1.2.1) of the suspension is shown in Figure 6.4. The natural pH of the suspension was around 10. NH_4PAA, a polyelectrolyte, was used to provide the electrosteric stabilization energy to the ceramic powders in suspension.

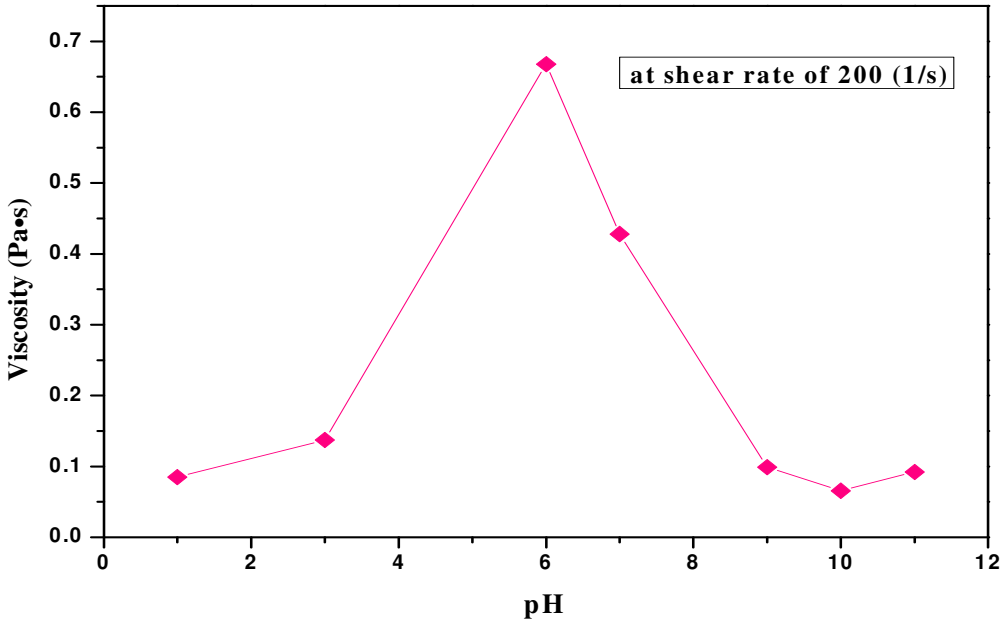

Figure 6.4 Viscosity versus pH for the 30 vol.% solids loading BT suspension with 0.646 wt.% NH_4PAA.

When changing the pH value of the suspension, both the ionisation of NH_4PAA absorbed on

the surface of the particles and the structure of the double-electrical layer would be affected. Therefore, the electrostatic repulsion energy would be changed. Meanwhile, the steric stabilization could also be influenced by the pH value. As shown in Figure 6.4, with decreasing the pH from the intrinsic pH value, the viscosity of the suspension first increased, and then decreased. The maximum viscosity occurred at a pH value around 6, which is consistent with the isoelectric point (IEP) of $BaTiO_3$ in López's work [20]. When the pH value was increased from the intrinsic value, the viscosity also increased. Therefore, for the rest of this study, it was decided there was no need to modify the pH value of the suspension to obtain good liquidity since the viscosity of the suspension at the natural pH is suitable for processing.

6.2.2.3 Effect of Solids Loading on the Viscosity of the Slurry

Figure 6.5 shows the typical relationship between the shear rate and shear stress, as well as the relationship between the viscosity and the shear rate of 30 vol.% BT suspension with 0.646 wt.% NH_4PAA.

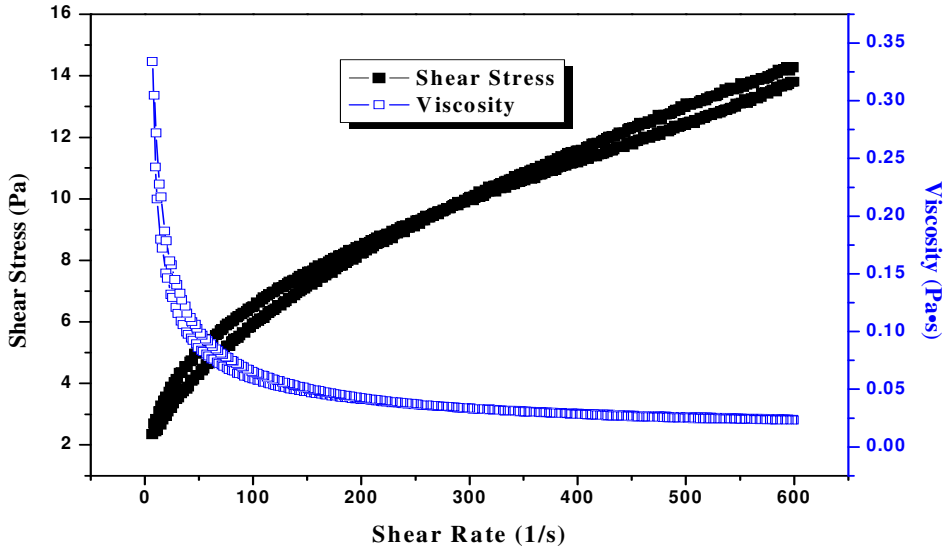

Figure 6.5 Typical rheological flow behaviour of 30 vol.% BT suspension with 0.646 wt.% NH_4PAA.

The viscosity decreased with the increase of the shear rate, meanwhile, the shear stress increased as the shear rate increased, which represented a typical shear thinning behaviour. The relatively steady decrease of the viscosity with increasing the shear rate (Figure 6.5) indicated a well-dispersed suspension.

The viscosities of BT suspensions with different solids contents are shown in Figure 6.6.

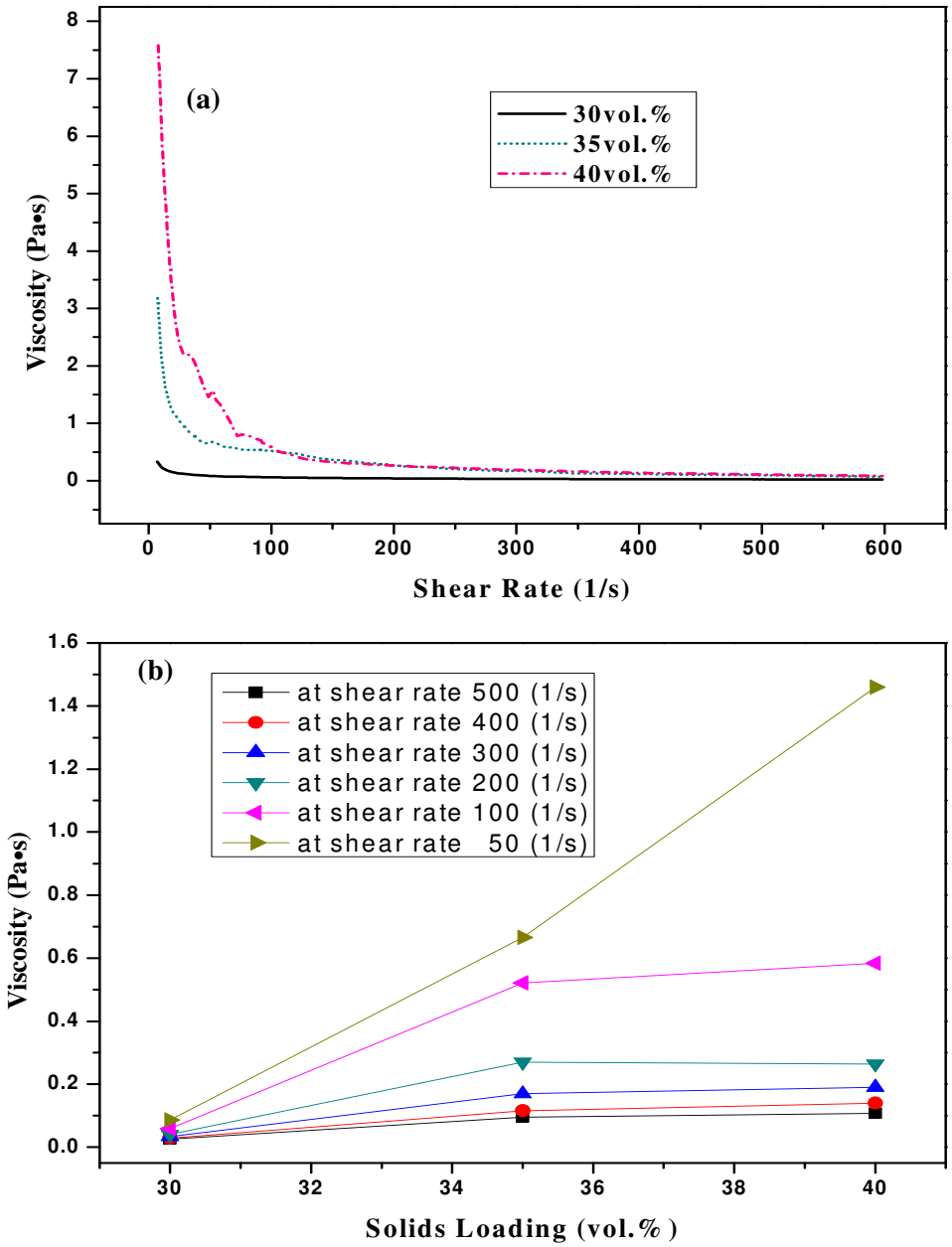

Figure 6.6 (a) Flow behaviour of BT suspensions with 0.646 wt.% NH_4PAA for different solids loadings; (b) Viscosity of BT suspensions containing 0.646 wt.% NH_4PAA for different solids loadings at different shear rates.

As shown in Figure 6.6(a), all of these suspensions showed typical shear thinning characteristics. When the solids loading was more than 40 vol.%, the viscosity increased dramatically, and the suspension with a solids loading of 45 vol.% could not be tested due to a very high viscosity. As shown in Figure 6.6 (b), the higher the solids content was, the more viscous the suspension became at all shear rates.

6.2.3 Characteristic of Centrifugally Cast Bulk $BaTiO_3$ Ceramics

Centrifuging aided slip casting (Chapter 3.1.3) is an easy forming technique. Therefore, in this section, centrifuging aided slip casting was employed to obtain bulk BT ceramics to characterize the dispersion of nano-sized BT powder.

6.2.3.1 General Properties and Microstructrue of the Sintered Samples

To optimize the sintering conditions, four different sintering temperatures (1300, 1325, 1350, and 1400 ^{o}C, for 1.5 h) were tested and their effects on the density and dielectric constant of the bulk BT ceramics from a 30 vol.% suspension with 0.646 wt.% NH_4PAA are shown in Figure 6.7.

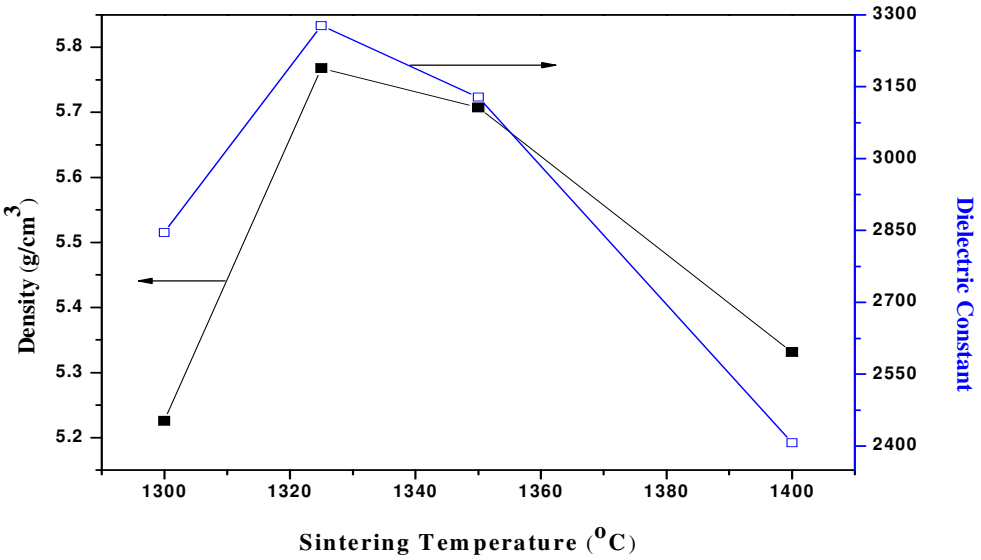

Figure 6.7 Density and room temperature dielectric constant of the bulk BT ceramics as a function of sintering temperature, obtained from 30 vol.% BT suspension with 0.646 wt.% NH_4PAA.

As the sintering temperature increased, the bulk density first increased, and then decreased. The dielectric constant showed a similar behaviour as would be expected. Sintered at 1325 ^{o}C, the specimens gained the highest bulk density 5.77 (g/cm^{3}), nearly 95.8 theoretical density and dielectric constant 3277. The cross-sectional SEM micrographs of the BT ceramics sintered at different temperatures are shown in Figure 6.8.

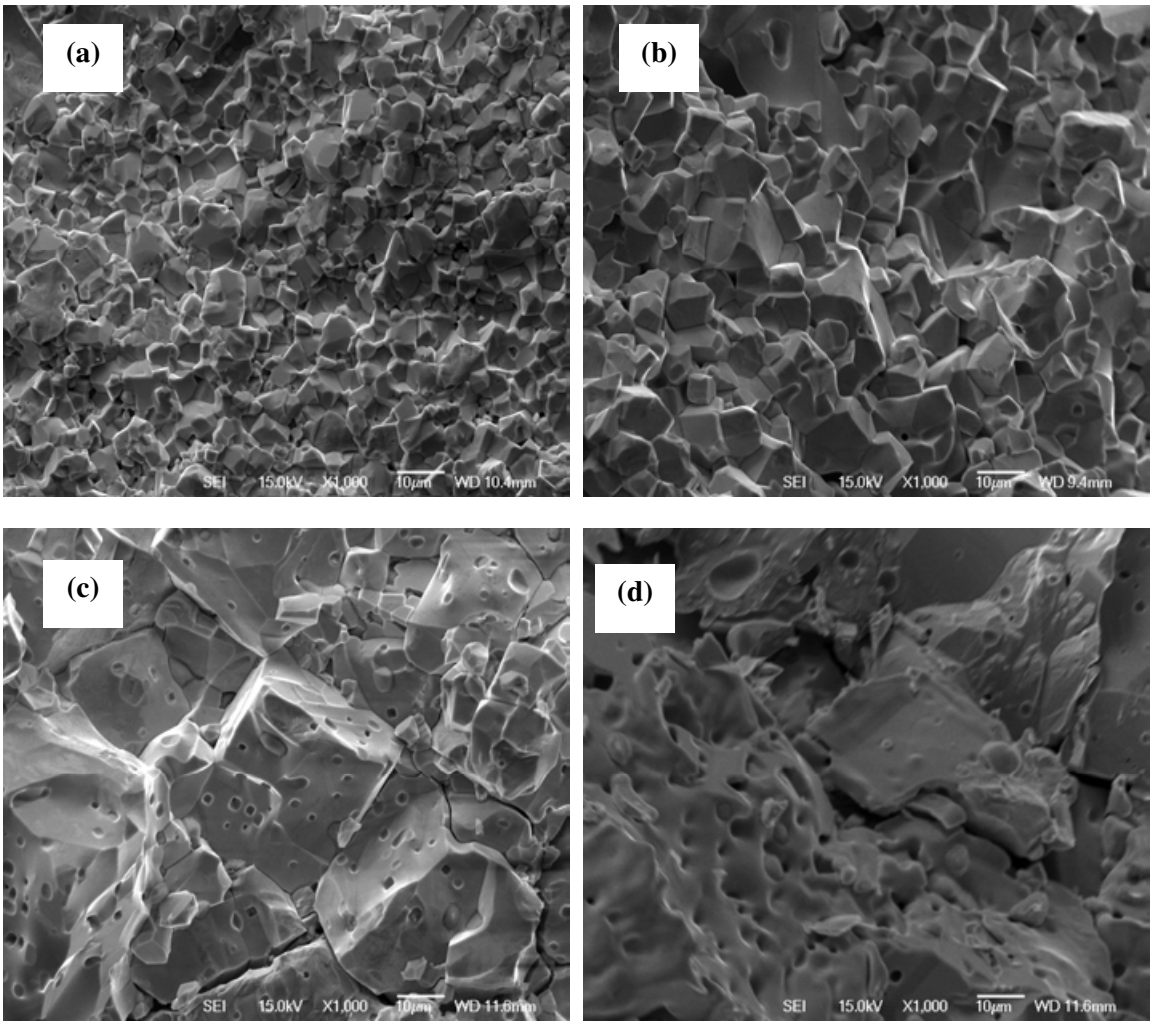

Figure 6.8 SEM micrographs of a cross-section of the sintered bulk BT ceramics obtained from 30 vol.% slurries with 0.646 wt.% NH_4PAA and sintered at: (a) 1300, (b) 1325, (c) 1350, (d) 1400 ^{o}C, 1.5 h.

Samples sintered at 1300 ^{o}C and 1325 ^{o}C presented a relatively uniform distribution of the grain sizes and their grain size increased from about 6 μm to 15 μm as the sintering temperature increased. Abnormal coarse grains were found in the specimen sintered at 1350

^{o}C. The grain structure was not apparent in the sample sintered at 1400 ^{o}C, indicating an even stronger overgrowth of the grains at this sintering temperature. Moreover, all the samples sintered at 1350 ^{o}C and 1400 ^{o}C show more porosity compared with the sample sintered at 1325 ^{o}C, which could be one of the factors leading to the reduction in sintered density at these temperatures.

Figure 6.9 shows the micrographs of the cross-section of sintered samples obtained from different solids loadings slurries.

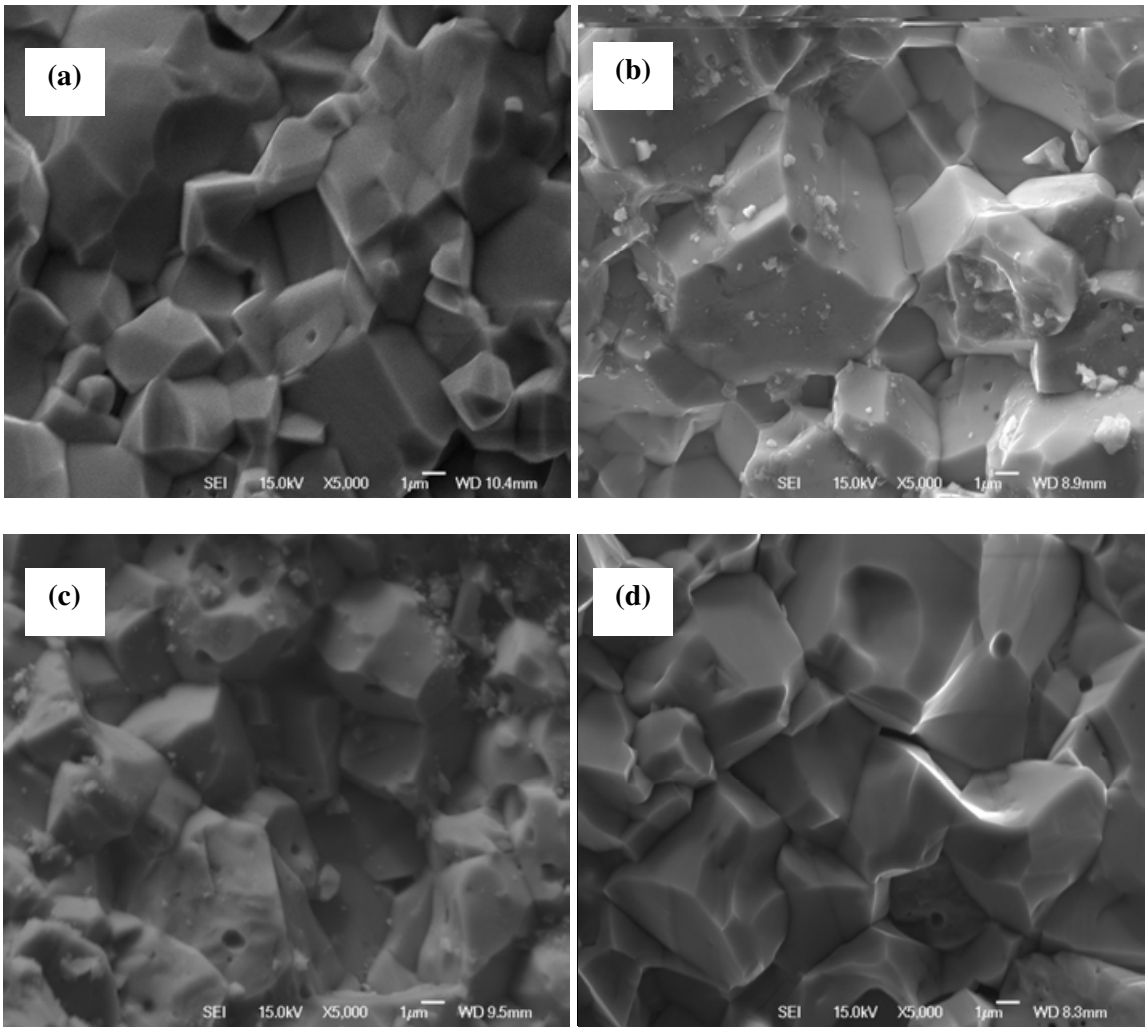

Figure 6.9 SEM micrographs of the cross-section of sintered samples obtained from slurries with different solids loadings : (a) 30 vol.%, (b) 35 vol.% , (c) 40 vol.%, (d) 45 vol.%. (sintered at 1325 ^{o}C, for 1.5 hours).

All the samples were sintered at 1325 ^{o}C. They all showed a relatively homogeneous, dense

microstructure and similar grain sizes (around 6 μm), indicating 1325 °C was a good sintering temperature for this BT powder without any sintering additives.

6.2.3.2 Phase Evolution of the Sintered Samples

The phase evolution of the sintered bulk BT samples is shown in Figure 6.10. Comparing the XRD pattern with the JCPDS standards, the main phase found in the samples sintered at 1300 and 1325 °C was the tetragonal $BaTiO_3$ phase indicated by its strong peak splitting around $2\theta=45^{\circ}$. The tetragonal phase was still the main phase in the sample sintered at 1350 °C (Figure 6.10(c)), however, evidence for the barium-rich titanate phase of Ba_2TiO_4 (monoclinic) was also found in this sample.

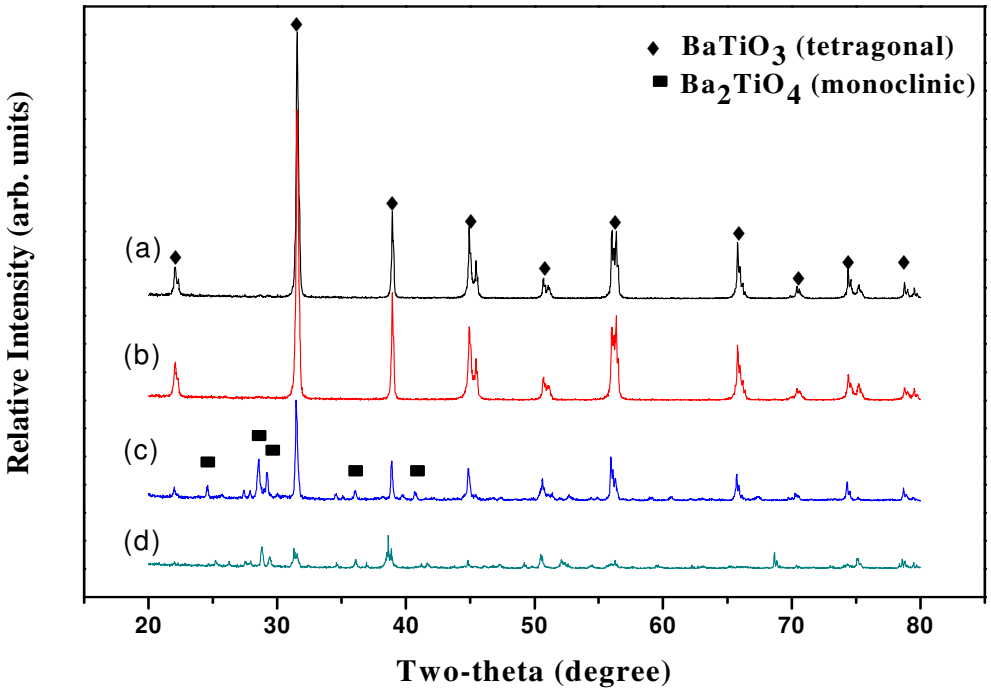

Figure 6.10 X-ray diffraction patterns of BT sintered at different temperatures: (a) 1300 °C, (b) 1325 °C, (c) 1350 °C, (d) 1400 °C. Samples were obtained from 30 vol.% solids loading slurries with 0.646 wt.% NH_4PAA.

In some work[21], acid cleaning has been used to decrease the $BaCO_3$ content in commercial powders in order to limit the abnormal grain growth but this has not been done here. As mentioned in the powder characterization (Section 6.2.1), impurity of $BaCO_3$ was found in

this starting nano BT powder, therefore, the barium-rich titanate phase of Ba_2TiO_4 could be formed through the reaction of BT with $BaCO_3$ in the powder at elevated temperature (1350 ^oC), which is also consistent with W. Lu's work[15]. Furthermore, the theoretical density of monoclinic Ba_2TiO_4 is 5.20 g/cm^3 and less than that of tetragonal BT (6.02 g/cm^3), so the existence of Ba_2TiO_4 in this sample is another contributing factor to the decrease of sintered density. It can also be seen from Figure 6.10 (d), that the diffraction intensity of the sample sintered at 1400 ^oC weakened markedly compared with the samples sintered at lower temperatures (Figure 6.10 (a),(b),(c)), indicating poorer crystalline quality. Figure 6.11 presents detailed patterns of this sample, which has been mainly indexed using hexagonal BT, orthorhombic Ba_2TiO_4 and tetragonal BT phases. This is consistent with Ritter[22] who described that the orthorhombic phase was the high-temperature form of orthotitanate and the monoclinic one was stable at room temperature.

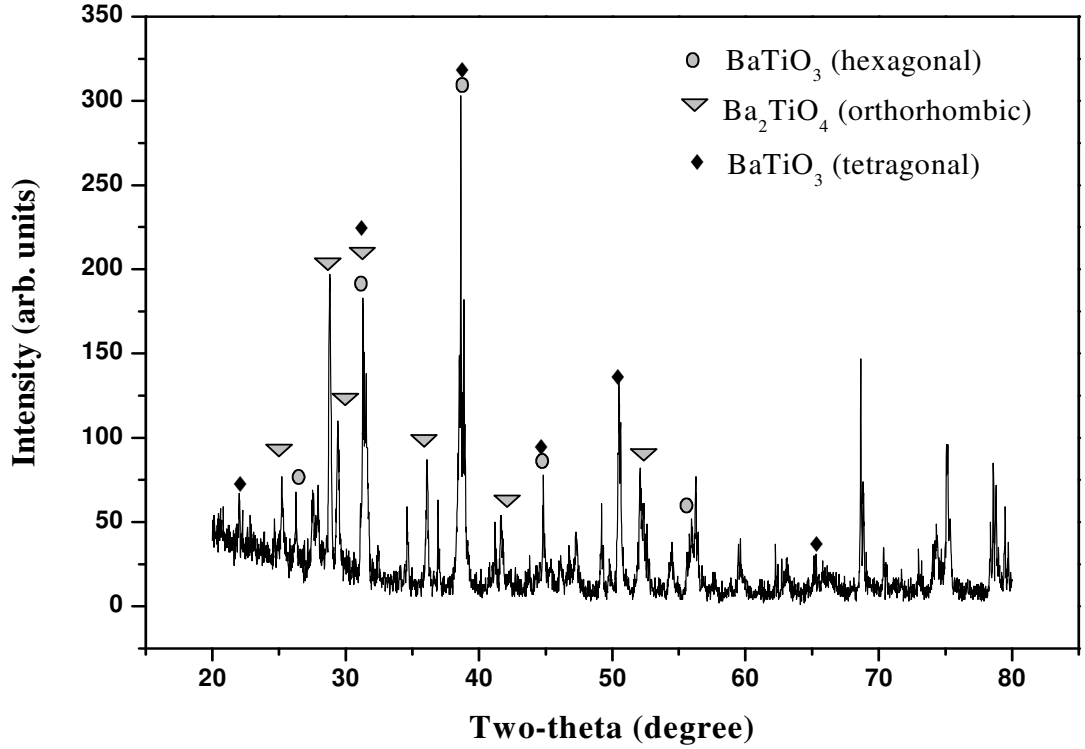

Figure 6.11 Detailed information of XRD spectrum of Figure 6.10 (d). Sample was obtained from 30 vol.% solids loading slurry with 0.646 wt.% NH_4PAA and sintered at 1400 ^oC.

Therefore, in order to avoid excessive grain growth and these additional phases, it can be concluded that 1325 ^{o}C was a suitable sintering temperature for this BT powder, which is consistent with the microstructural characterization shown in Section 6.2.3.1.

Figure 6.12 shows the initial solids loading and room temperature dielectric constant (measured at 1 kHz) versus sintered density of samples sintered at 1325 ^{o}C for 1.5h. When the initial solids loading varied from 30 vol.% to 45 vol.%, the final sintered density changed from about 5.77 g/cm^3 (95.8% of the theoretical density) to 5.85 g/cm^3 (97.0% of the theoretical density). Actually this variation of the sintered density was only 1.2% of the theoretical density, which indicated that a good dispersion of this nano BT powder had been achieved. Moreover, when the sintered density increased, the dielectric constant of the bulk ceramic increased. Thus, higher bulk density is helpful in improving electrical properties.

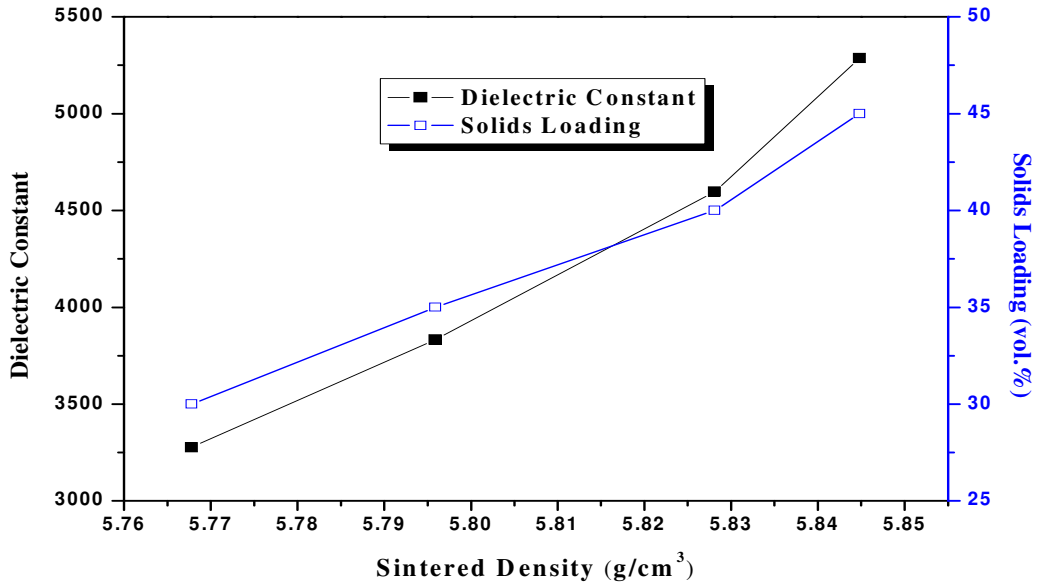

Figure 6.12 Initial solids loading and room temperature dielectric constant (1 kHz) versus sintered density. Samples were obtained from different solids loading (30 vol.%, 35 vol.% , 40 vol.%, and 45 vol.%) and sintered at optimal temperature 1325 ^{o}C for 1.5h.

6.2.4 Summary

Rheological properties of suspensions with nano-sized BT powders have been characterized

with regard to pH, solids loading and dispersant concentration. It was found that NH_4PAA is very effective as a dispersant for this BT colloidal system. With this dispersant, stable and well-dispersed suspensions have been obtained. The pH value has a strong effect on the stability of BT suspension, and moreover, the intrinsic pH is suitable for techniques such as centrifugal aided slip casting or other casting techniques.

1325 ^{o}C is the optimal sintering temperature for this nano-sized BT powder without any sintering additives. BT ceramic sintered at this temperature shows a bulk density of 5.85 g/cm^3, nearly 97.0% of the theoretical density, and room temperature dielectric constant of 5270 (measured at 1 kHz).

6.3 Porous BT Ceramic and BT-Epoxy Composites by Freeze Casting

Utilizing the stable and well-dispersed $BaTiO_3$ suspensions described in the above section, porous BT ceramics fabricated by the freeze casting technique and BT ceramic-epoxy composites were prepared and characterized.

6.3.1 Porous BT Ceramics

All the samples shown here were the sintered porous BT ceramics obtained from slurries with initial solids loadings of 20 vol.%, 25 vol.%, 30 vol.%, and 45 vol.%. All the samples were prepared according to the method described in Chapter 3.1.2. The cooling rate used in this chapter was 0.5 ºC/sec.

The total porosity (Chapter 3.2.3.2) of porous BT ceramics as a function of the initial solids loading is shown in Figure 6.13. Very similar behaviour had been exhibited by the porous alumina and Al_2O_3-ZrO_2 systems. With the increase of initial solids loading from 20 vol.% to 45 vol.%, the final total porosity decreased from 42% to 18%, due to the influence of the water content of the slurry on the final porosity as discussed in the preceding two chapters.

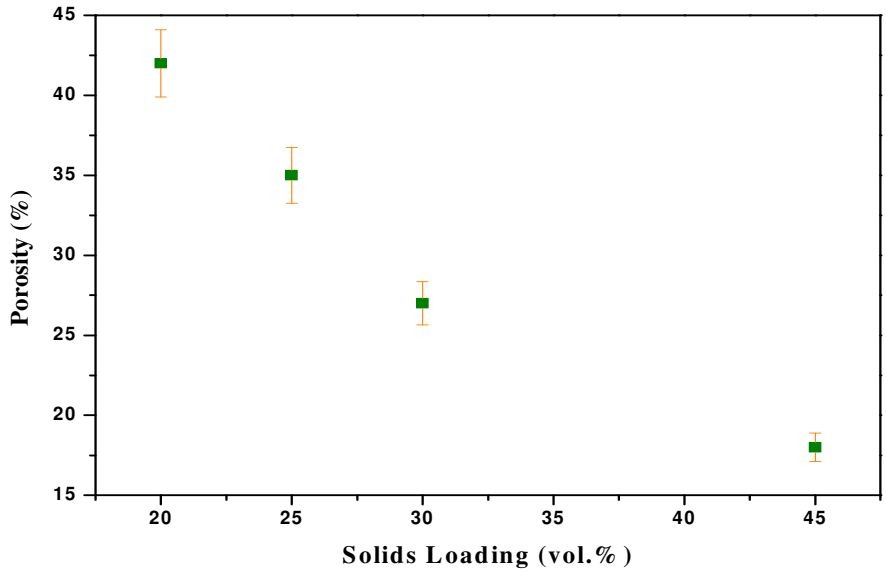

Figure 6.13 Porosity of BT porous ceramics as a function of the initial solids loading. Samples were obtained from different solids loadings (30 vol.%, 35 vol.%, 40 vol.%, and 45 vol.%) and sintered at optimal temperature 1325 ^{o}C for 1.5h.

The cross-sectional microstructures of the porous BT ceramics are shown in Figure 6.14. All the samples except for the one shown in Figure 6.14 (d) exhibited lamellae microstructure, which were formed during the directional freezing. The ceramic wall thickness of these samples increased with the increase of the initial solids loading, showing a similar tendency to the previous chapters on alumina and Al_2O_3-ZrO_2 systems. It can be seen in Figure 6.14 (d), that although it still had a lamellae appearance, the gaps between the ceramic walls in these samples were filled, indicating that engulfment had taken place. Incorporating the simple model (4-4), it can be seen that higher viscosity leads to smaller critical velocity. Although BT suspensions showed a good dispersing ability of this nano-sized BT powder, the viscosity of a 45 vol.% BT slurry became too high to be measured. In comparison the viscosities of other slurries with lower initial solids loadings were less than 0.1 Pa·s at a shear rate of 50 (1/s). The very high viscosity of 45 vol.% BT slurry lowered its critical velocity markedly and finally led to the engulfment and the loss of the lamellar architecture.

Moreover, the small debris between the lamellae that can be seen in Figure 6.14 (a) and (b) were the remnants from the cutting process. The compressive strength of porous BT was really so low that it could not be recorded, which will be a limitation.

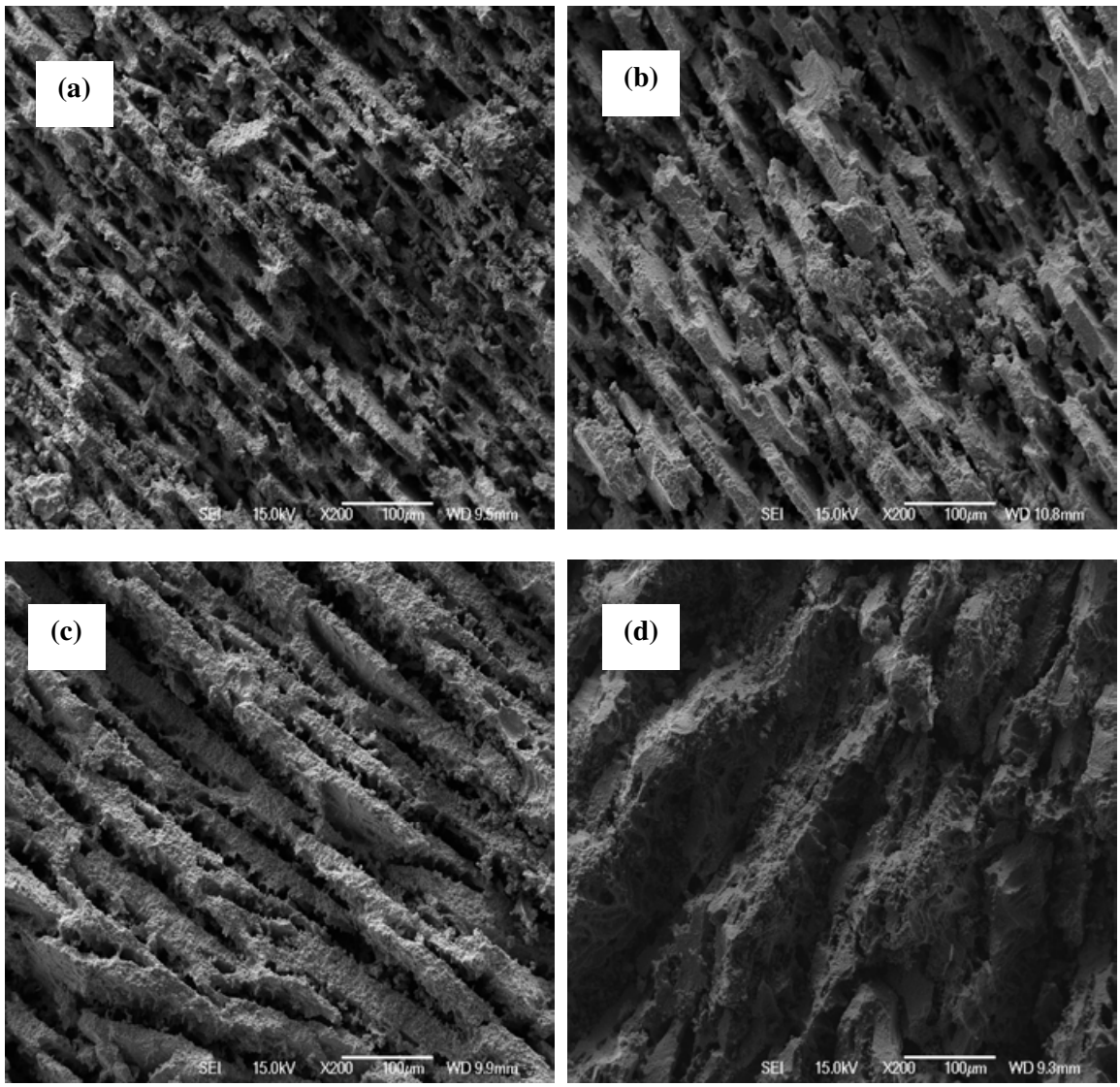

Figure 6.14 SEM photographs of the porous BT ceramics obtained from slurries with initial solids loadings of: (a) 20 vol.%, (b) 25 vol.%, (c) 30 vol.%, (d) 45 vol.%. and sintered at an optimal temperature of 1325 ^{o}C for 1.5h

6.3.2 BT-Epoxy Composites

The resultant porous BT ceramics were filled with epoxy in vacuum, made into composites and then cut into discs for further electrical measurement as described in Chapter 3.1.5 and

Chapter 3.2.6.

Figure 6.15 shows the correlation between the volume fraction of the BT ceramic in the BT-epoxy composites and the initial solids loading of BT slurry. With the increase of initial solids loading from 20 vol.% to 45 vol.%, the volume fraction of BT ceramic phase in the BT-epoxy composite increased accordingly from about 40 vol.% to 78 vol.% (values obtained by the method described in Chapter 3.2.3.2). The space in the composite occupied by the epoxy resin is the place where the ice originally was. Higher solids loading means less water, therefore, the volume of resin required decreased when the initial solids loading increased.

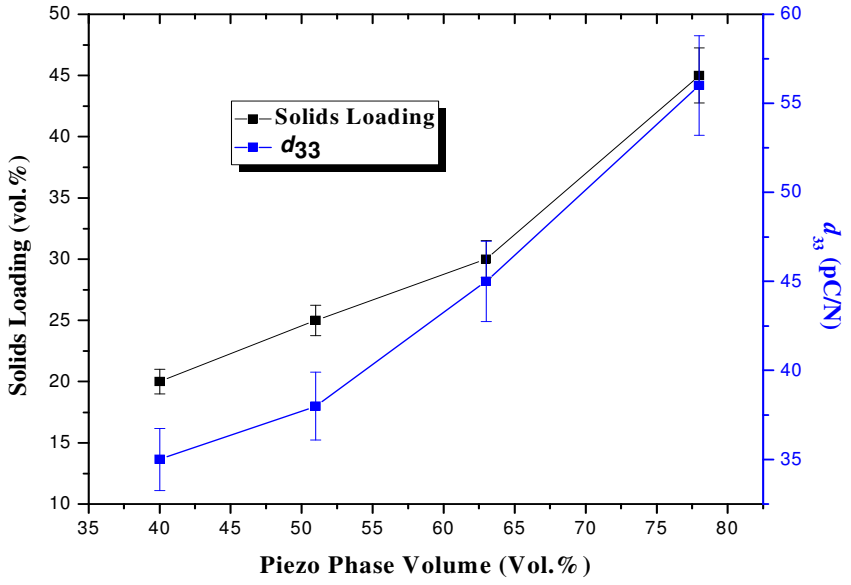

Figure 6.15 Initial solids loading and piezoelectric constant d_{33} as a function of piezoelectric phase volume. BT-epoxy piezocomposites were prepared from the porous BT ceramics which were obtained from slurries with initial solids loadings of: 20 vol.%, 25 vol.%, 30 vol.%, 45 vol.%, and sintered at optimal temperature of 1325 ^{o}C for 1.5h.

The piezoelectric constant d_{33} of the BT-epoxy composites is also shown in Figure 6.15. It increased from about 35 pC/N to 56 pC/N as the volume of the BT ceramic phase in the composite increased from about 40 vol.% to 78 vol.%. In the composite, BT ceramic is the piezoelectric phase and thus responsible for the piezoelectric response. The d_{33} values of

these BT-epoxy composites were relatively low compared with 100% BT ceramics (190 pC/N[23], 315 pC/N[24]) which may be due to the lack of a good process to pole such a BT-epoxy composite. The dielectric properties of the BT-epoxy composites versus frequency are illustrated in Figure 6.16.

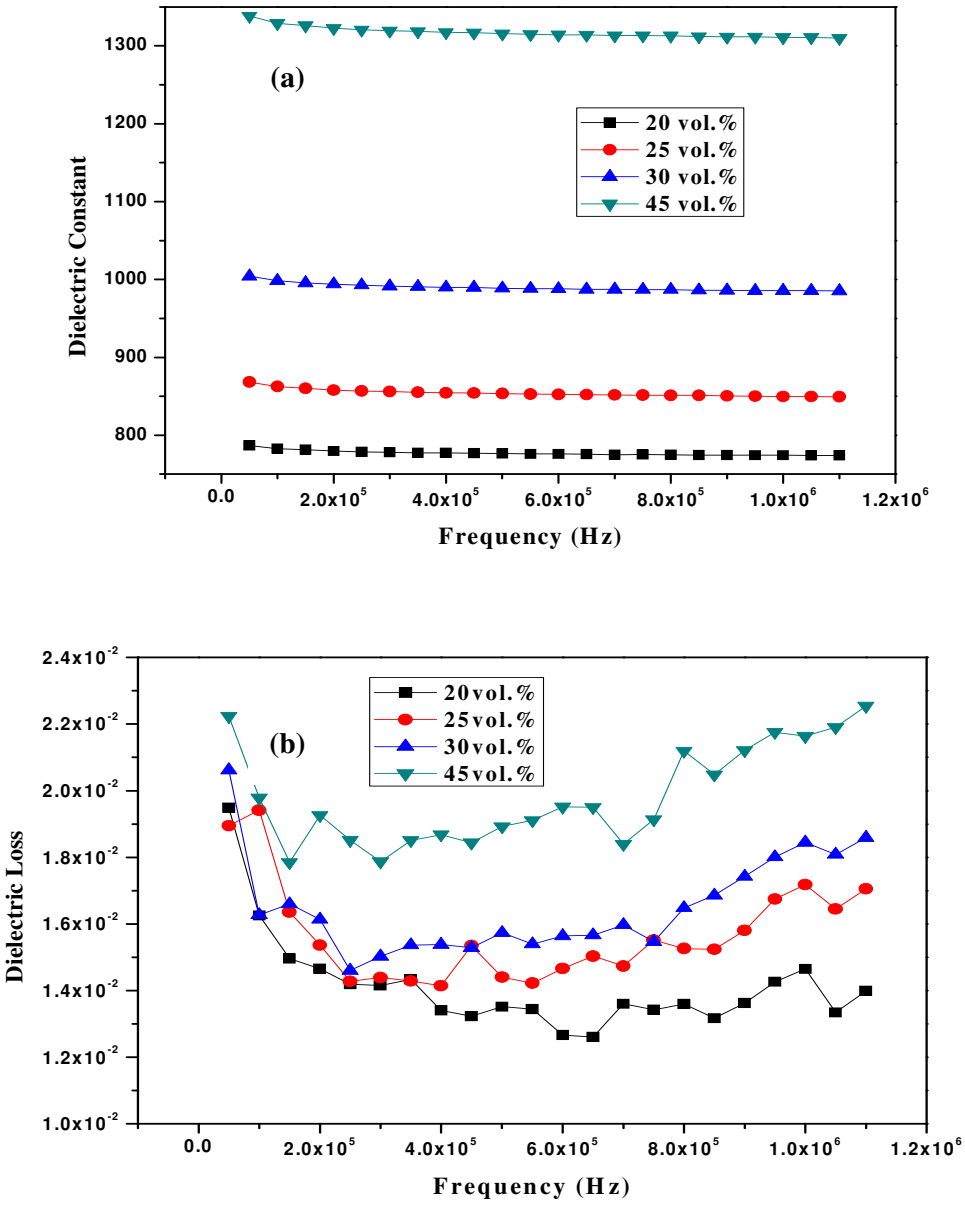

Figure 6.16 Dielectric properties of BT-epoxy composites (a) dielectric constant, (b) dielectric loss as a function of frequency. BT-epoxy composites were prepared from the porous BT ceramics which were obtained from slurries with initial solids loadings of: 20 vol.%, 25 vol.%, 30 vol.%, and 45 vol.%, and sintered at optimal temperature of 1325 ^{o}C for 1.5h.

With the increase of initial solids loading from 20 vol.% to 45 vol.%, the dielectric constant increased from about 770 to 1290 at 1 MHz (Figure 6.16 (a)), which is at least 1 order of magnitude higher than that of traditional composites with randomly distributed BT ceramic particles at a similar volume fraction[25-27]. The lamellae structure of BT ceramic phase in the composites contributed much to this. Normally the capacitors in parallel show the additive nature[28], and the dielectric constant of such BT-epoxy composites was significantly increased. Furthermore, the dielectric constant of the composites increased as the initial solids loading increased. Usually the dielectric constant of the ceramic-epoxy composite can be calculated by the following equation[12]:

$$\varepsilon_{com} = \nu_r \bullet \varepsilon_r + \nu_c \bullet \varepsilon_c \qquad (6\text{-}1)$$

where ε_x and ν_x are the dielectric constant and the volume fraction of constituent x, respectively; com, r, and c stand for composite, resin and ceramic, respectively.

The dielectric constant of epoxy (the pure resin phase) is 4, while that of the pure BT ceramic used in this study is more than 3200. The expected dielectric constant of the composites according to the equation (6-1) and dielectric constant of pure epoxy and BT ceramic is shown in Table 6.1. It increased with the increase of the initial solids loading. The measured dielectric constant as shown in Figure 6.16 (a) exhibited a similar behaviour with the calculated value, though it was smaller than that of the calculated value.

Table 6.1 Calculated dielectric constant of the composite according to the equation (6-1)

Initial solids loading (vol.%)	20	25	30	45
Calculated dielectric constant	1282	1634	2017	2497

Higher initial solids loading in the slurry results in a higher volume fraction of ceramic phase in the composites, therefore resulting in the increase of the final dielectric constant of the composite. Though the dielectric constant showed a clear change with the initial solids

loading, the loss tangent, as shown in Figure 6.16 (b), showed relatively little change especially below 10^5 Hz. However, at higher frequency (>10^5 Hz), the dielectric loss increased as the initial solids loading increased. This may be because BT has a higher loss tangent (0.01 at 1 kHz) than the epoxy (loss tangent <0.001 at 100 kHz, provided by the supplier), therefore, the dielectric loss increased with the increasing the BT volume fraction.

In summary, the BT-epoxy composites obtained in this section exhibited a high dielectric constant, at least 1 order of magnitude higher than the traditional composites. Therefore, the freeze casting technique offers a viable method for creating high-quality dielectric composites. However, the very poor mechanical property of the porous BT ceramic makes it difficult to process, therefore, efforts were made to improve this limit and these are described in the following section.

6.4 Nano-sized α–Al_2O_3 Doped BT Ceramics

As shown in Section 6.2, porous BT ceramics have very poor mechanical properties, which were too low to be recorded. Many papers [29-33] have reported that the PZT and BT matrix could be reinforced with the addition of mechanically hard particles to provide improved strength, hardness and fracture behaviour. In this work, the same principle was (probably for the first time) applied to the nano-sized BT matrix. Here, the nano-sized particles of Al_2O_3 were introduced into the BT ceramics in order to achieve improved mechanical properties. Moreover, in order to simplify the investigation, a traditional electroceramic fabrication process was employed to obtain the bulk BT ceramic and alumina-doped BT ceramics, which has already been described in detail in Chapter 3.1.4.

6.4.1 Powder Characterization

X-ray diffraction pattern of the as received nano-sized alumina powder (α–phase, 99%, Alfa

Aesar) used in this study is shown in Figure 6.17. By comparing the XRD pattern with JCPDS standards, the diffraction peaks from the sintered sample can be indexed as α-Al_2O_3, the only phase found present, which is consistent with the data provided by the manufacturer. No secondary phases were found.

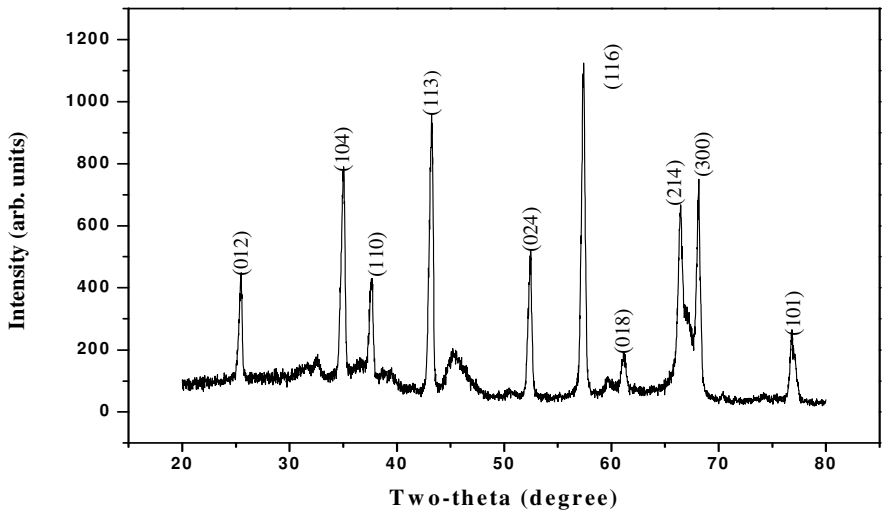

Figure 6.17 XRD spectrum of the as received nano-sized α–Al_2O_3 powder utilized to reinforce the BT ceramics.

6.4.2 Effect of Doping Concentration on Properties

A range of nano-sized alumina compositions from 0 vol.% to 5 vol.% were doped into the BT powders. Pellets samples were made for further characterization. (Chapter 3.1.4)

6.4.2.1 Phase Evolution of the Sintered Samples

BT monolithic and the alumina-doped BT ceramics were sintered at 1275 ºC. This was because higher sintering temperature, e.g. 1325 ºC and 1300 ºC, led to distortion especially in the samples with higher content of nano-sized alumina. The XRD diffraction patterns of monolithic BT ceramic and the alumina-doped BT ceramics are shown in Figure 6.18. Comparing the XRD pattern with the JCPDS standards, the only phase found in BT ceramic

and the alumina-doped BT with 0.5 vol.% Al_2O_3 ceramics was tetragonal $BaTiO_3$ phase indicated by strong peak splitting around $2\theta=45^{o}$. Moreover, the diffraction density of BT ceramic was higher than that of the alumina-doped BT ceramic.

With the increase of the Al_2O_3 addition from 1 vol.% to 5 vol.%, though the main phase found in alumina-doped BT ceramics was still the tetragonal $BaTiO_3$ phase, $Ba_3TiAl_{10}O_{20}$ (Orthorhombic) was detected in all of the three samples, which is the small peak marked by the rectangle shown in Figure 6.18.

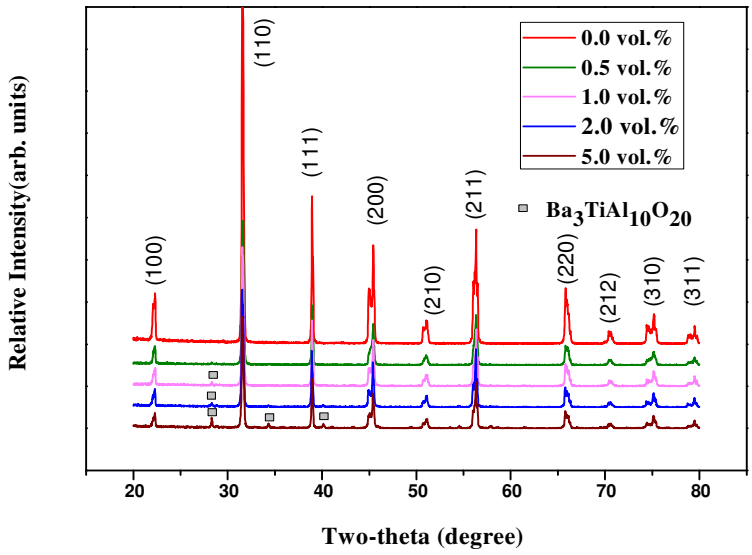

Figure 6.18 XRD spectra of bulk BT ceramic and alumina-doped BT ceramics sintered at 1275 ^{o}C.

6.4.2.2 Effect of Doping Concentration on Several Properties

The densities and relative densities of the BT ceramics and alumina-doped BT ceramics are shown in Figure 6.19 as a function of the volume percent addition of alumina. The theoretical densities of the alumina-doped BT ceramics were calculated based on the both theoretical densities of $BaTiO_3$ (density: 6.02 g/cm^3) and Al_2O_3 (density: 3.96 g/cm^3). As shown in Figure 6.19, the density and relative densities showed a similar changing tendency.

They all decreased with the increase of the addition of nano-sized alumina. That is because with the increase of alumina addition, the $Ba_3TiAl_{10}O_{20}$ (density: 4.13 g/cm^3, from JCPDS standard) content increased, which contributed much to the observed decrease of density.

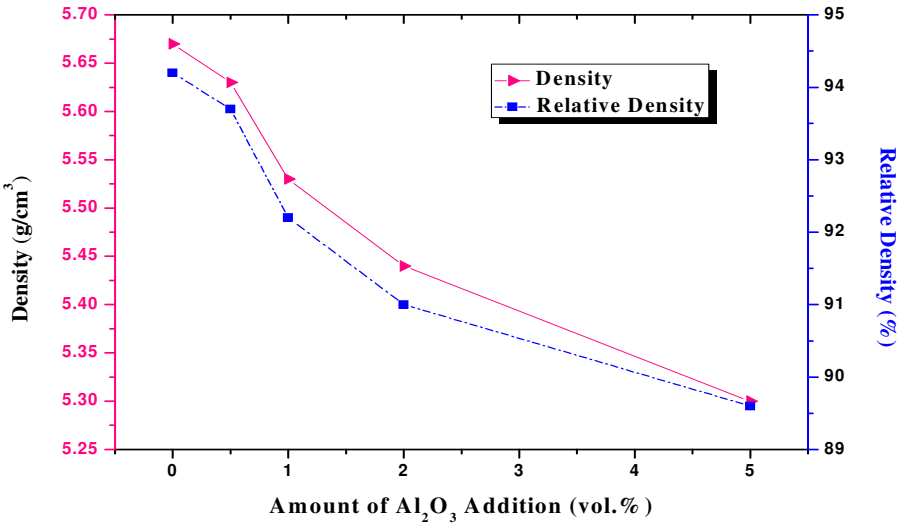

Figure 6.19 Densities of BT ceramic and alumina-doped BT ceramics as a function of the addition amount of Al_2O_3.

The hardness of BT ceramic and alumina-doped BT ceramics are shown in Table 6.2. With the increase of alumina addition, the hardness increased from 6.5 GPa to 10.7 GPa approximately. The addition of nano-sized alumina into BT could clearly enhance the mechanical property.

Table 6.2 Hardness of BT and Alumina-doped BT ceramics

Al_2O_3 content (vol.%)	0.0	0.5	1.0	2.0	5.0
Hardness (GPa)	6.5	3.4	7.9	8.7	10.7

The DSC curves of the pure BT ceramic and the doped BT sintered ceramics with various amounts of alumina are shown in Figure 6.20(a). For the sample of pure BT ceramic without alumina addition, its Curie point was around 125.4 ºC. The Curie point shifted towards a

lower temperature of 123.5 ºC when doping 0.5 vol.% alumina. With the further increase in alumina addition from 1 vol.% to 5 vol.% as shown in Figure 6.20 (b), the Curie point shifted towards the higher temperature from 123.8 to 126.5 ºC. Moreover, the peak widths of doped BT were markedly broadened compared with the non-doped BT ceramic, indicating that the tetragonal to cubic phase transition became dispersive.

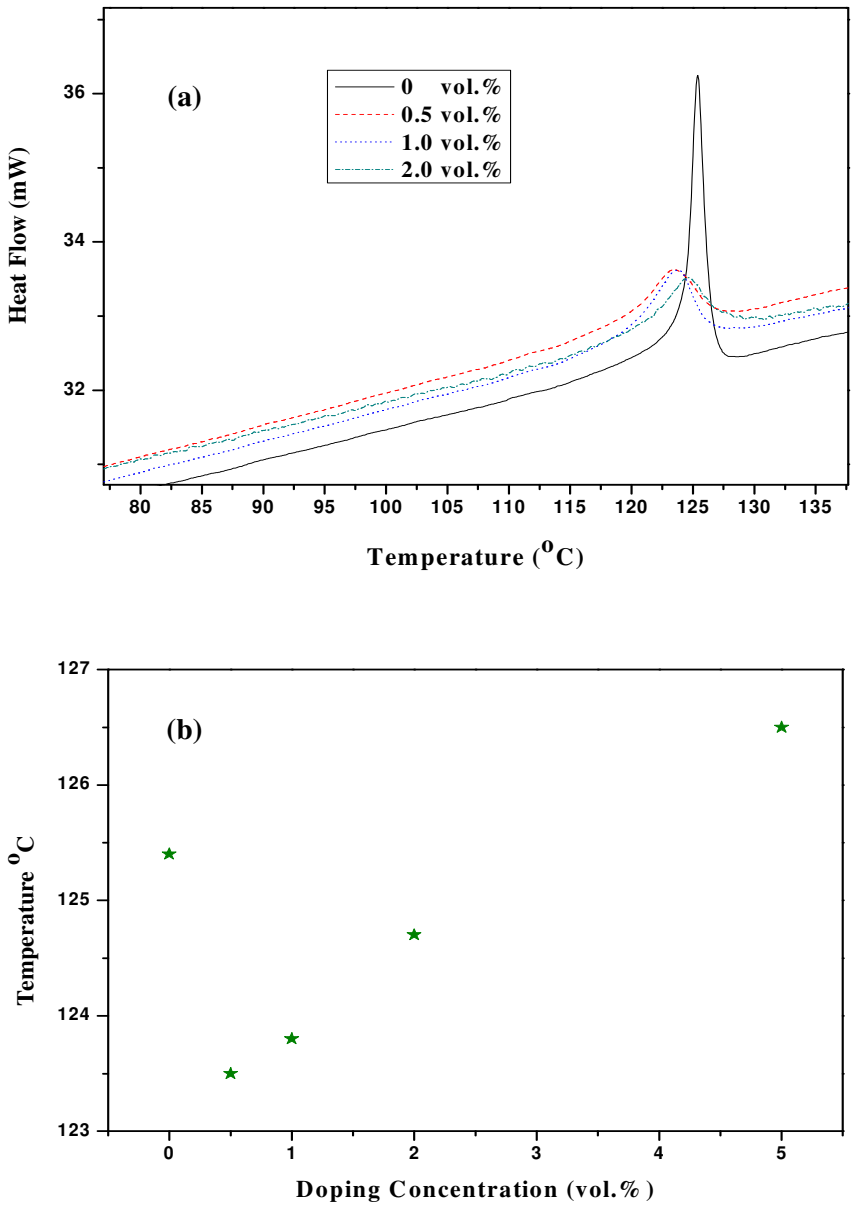

Figure 6.20 DSC curve and Curie point for the BT and the doped BT sintered ceramics: (a) DSC curve; (b) Curie point versus doping concentration.

6.4.2.3 Effect of Doping Concentration on the Electrical Properties of BT Ceramics

The effect of Al_2O_3 doping concentration on the dielectric properties characteristics of BT and alumina doped BT ceramics is shown in Figure 6.21.

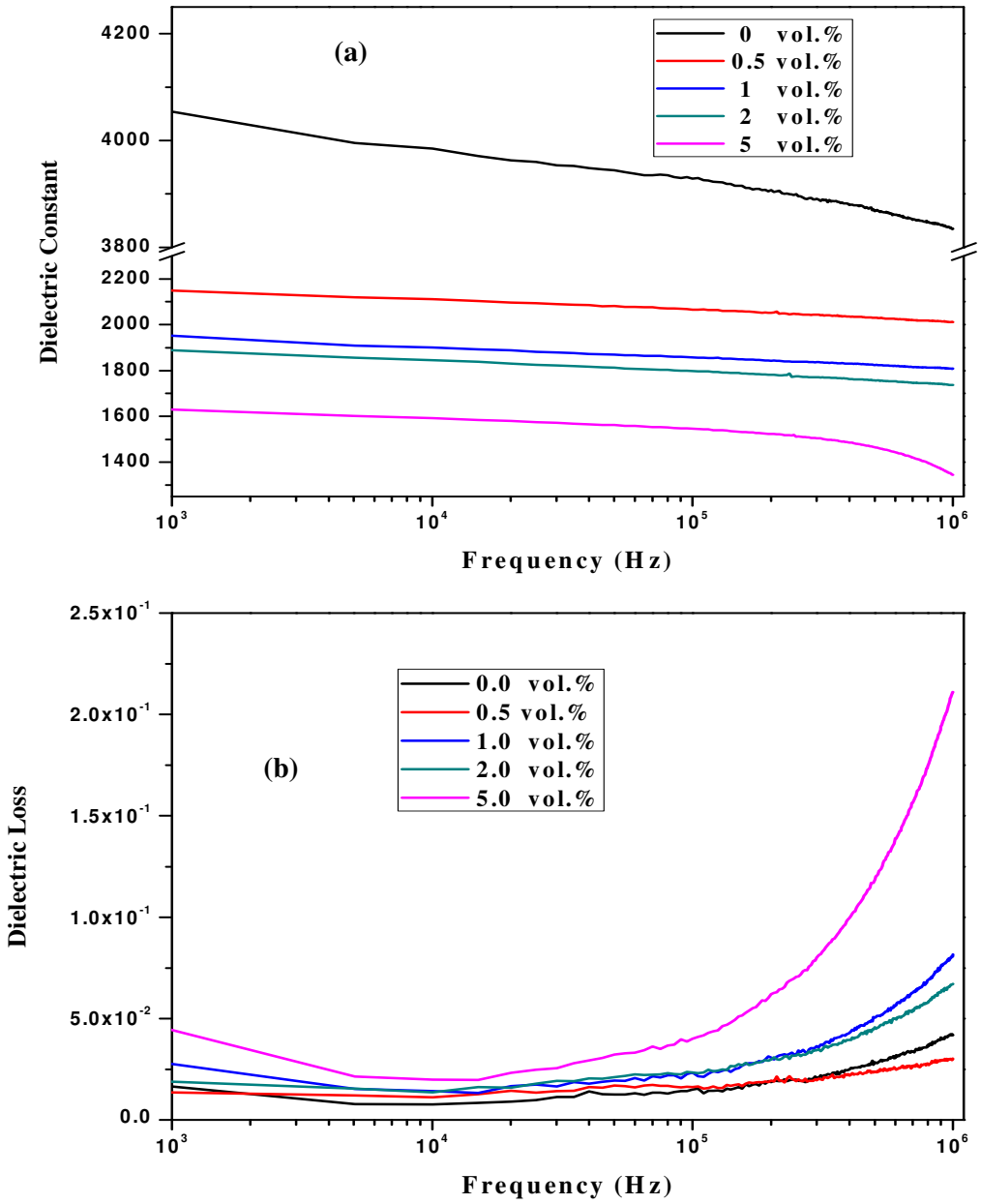

Figure 6.21 Plots of (a) dielectric constant and (b) dielectric loss of BT ceramic and alumina-doped BT ceramics as a function of frequency at room temperature.

The measurements were taken at room temperature (20 ºC). With the increase of alumina addition from 0 to 5 vol.% (Figure 6.21 (a)), the dielectric constant (ε_r) decreased markedly from 3836 to 1350 (at 1 MHz). Meanwhile, the addition of alumina would lead to the increase in dielectric loss (tan δ), as illustrated in Figure 6.21 (b). The reduction in dielectric constant and increase in dielectric loss with the increase of alumina addition is thought to be caused by the presence of an Al-rich phase, the $Ba_3TiAl_{10}O_{20}$ (Orthorhombic) detected by the XRD.

The piezoelectric properties of the pure BT ceramic and alumina doped BT ceramics are shown in Figure 6.22. The piezoelectric constant d_{33} decreased from ~ 210 pC/N to ~145 pC/N as the addition of alumina increased, which is also because of the increase of the Al-rich phase. Compared with the d_{33} values of the BT-epoxy composites shown in Chapter 6.3.2, these d_{33} values are much higher. That is probably because bulk BT ceramics are much easier to pole than the porous BT ceramics.

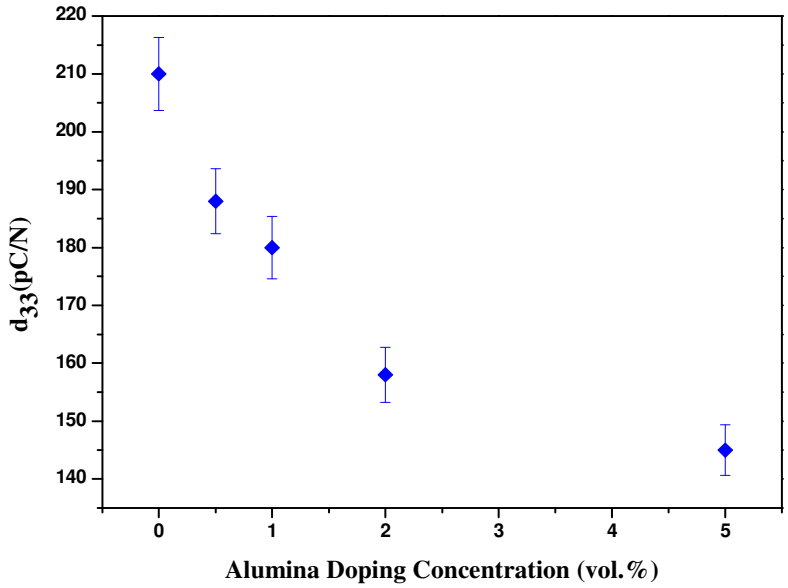

Figure 6.22 Piezoelectric constant d_{33} values of the BT ceramic and the alumina-doped ceramics as a function of the alumina concentration

6.4.3 Microstructure of the Sintered Samples

The microstructures of the BT and alumina-doped BT ceramics are shown in Figure 6.23.

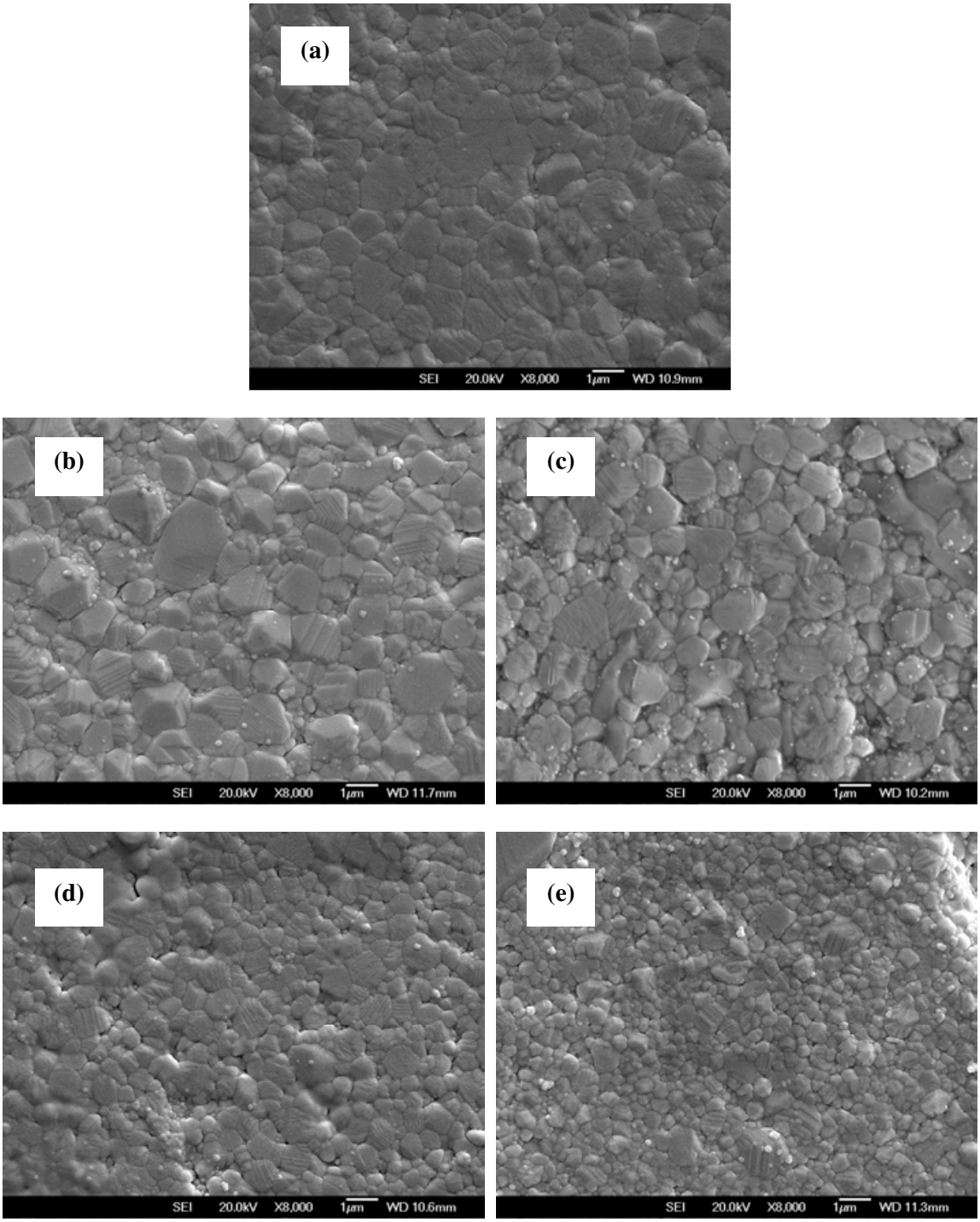

Figure 6.23 SEM micrographs of the BT and alumina-doped BT ceramic samples sintered at 1275 ºC: (a) 0 vol.%, (b) 0.5 vol.%, (c) 1 vol.%, (d) 2 vol.%, (e) 5 vol.%.

For the BT sample (Figure 6.23 (a)), it showed dense and relatively homogenous

microstructure. When the alumina concentration was less than 1 vol.%, the samples (Figure 6.23 (b) and (c)) also showed a relatively dense microstructure. Some pores were found in the samples with higher concentrations (Figure 6.23 (d) and (e)), which could be one factor contributing to the lower densities. Furthermore, one noticeable phenomenon was that with the increase of alumina concentration, the grain size of the BT and BAT ceramics became smaller (from ~1 μm to ~0.6 μm), especially for samples with the 2 vol.% and 5 vol.% alumina concentration. This phenomenon is thought to be induced by the grain-boundary pinning force of nano-sized alumina, which could depress the grain boundary migration of BT during sintering[34].

As the second phase had been detected by XRD (Figure 6.18) in some samples, some Al^{3+} (r_{Al}^{3+} = 0.054 nm)[33] had incorporated into the ABO_3-type perovskite structure of $BaTiO_3$. According to some ionic radius (r_{Ti}^{4+} = 0.061 nm, r_{Ba}^{2+} = 0.135 nm, r_{O}^{2-} =0.140 nm)[33] the Goldschmidt tolerance factor *t* (as shown in equation (2-6)) of alumina doped BT can be calculated, as shown in Table 6.3.

Table 6.3 Tolerance factor *t* and Δ*r*/*r* values of alumina doped $BaTiO_3$

Lattice site	*t*	Δr/r%
A	0.68	60
B	~1	11

The tolerance factor *t* of B-site substitution is very close to 1, therefore, an estimate that Al^{3+} (as accepter) will probably substitute the B-site occupied by Ti^{4+} can be made. This would lead to the generation of oxygen vacancies and make the material more electrically hard. This phenomenon has already been reported in PZT/Al_2O_3 composites[33,35,36]. In this work, however, the Al-rich second phase, $Ba_3TiAl_{10}O_{20}$ (Orthorhombic), has also been detected. Meanwhile, the reduction of the grain size caused by the addition of nano-sized alumina contributed much to the improved hardness of the alumina doped BT ceramics. It is known

that free energy of gain boundaries is higher than that of grains, which can act as obstacles to dislocation slip and thus enhance the material. The reduction of grain size means more grain boundaries exist in the ceramics; therefore, the mechanical property of the ceramics has been improved.

6.4.4 Summary

In summary, doping nano-sized alumina (from 0.5 vol.% to 5 vol.%) into this nano BT matrix could effectively suppress the growth of the grain and improve the mechanical property of $BaTiO_3$ ceramics. Meanwhile, the Al-rich phase in the samples with higher alumina doping concentration could worsen the dielectric and piezoelectric properties.

6.5 Porous Alumina-Doped BT Ceramics and Their Epoxy Composites

The freeze casting technique will also be applied with alumina-doped BT materials. Therefore, based on the study of alumina-doped BT bulk ceramics shown in section 6.4, this section reports the work on the preparation of (1) porous alumina-doped BT ceramics by the freeze casting technique and (2) their epoxy composites.

6.5.1 Porous Alumina-doped BT Ceramics

All the samples shown here are the sintered porous alumina-doped BT ceramics (1275 ^{o}C, 2h), obtained from slurries with the same initial solids loading of 20 vol.%. All samples were also prepared under the same cooling rate of 0.5 ºC/sec.

The total porosity of porous alumina-doped BT ceramics is shown in Figure 6.24. Though all of the samples were obtained from the slurries with the same concentration and under the same cooling rate, the porosities of the samples with different alumina additions are not the same. They generally decreased from 41% to 38% as the additive amount increased. The

different porosities were caused by the different shrinkages during sintering, which are shown in Table 6.4. With the increase of alumina concentration, the shrinkage increased slightly from 22.3% to 26.4%. As it is known that larger shrinkage will lead to smaller porosity, therefore, the observation that the porosities decreased with the increase of alumina concentration can be explained.

The compressive strengths of the porous alumina doped BT ceramics are also shown in Figure 6.24 as a function of the alumina concentration. Compared with the porous BT ceramic, the compressive strength of the porous alumina doped BT ceramics has been improved. With the increase of the alumina concentration from 0.5 vol.% to 5.0 vol.%, the compressive strength increased from 0.99 MPa to 1.75 MPa.

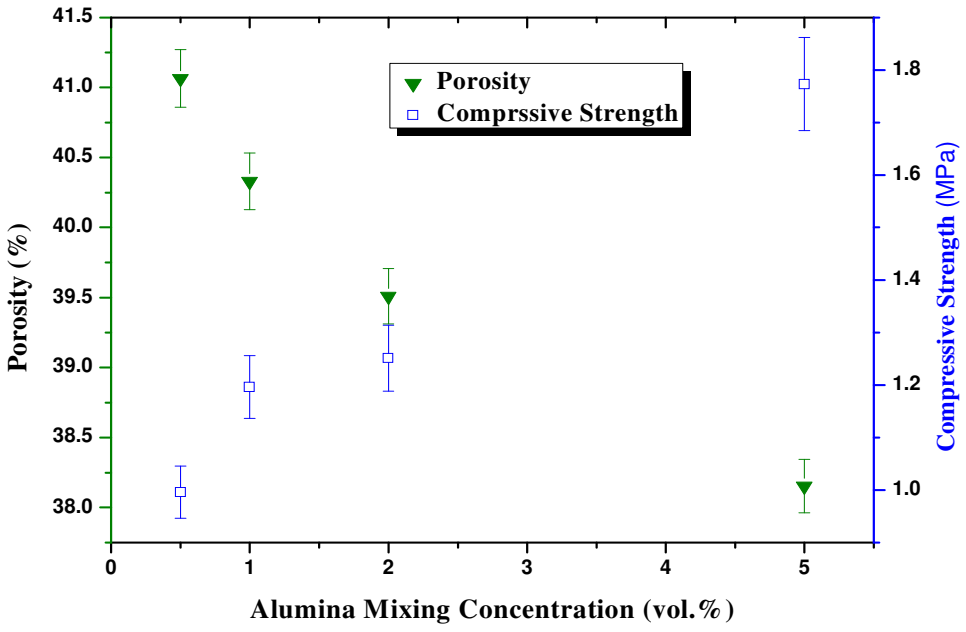

Figure 6.24 Porosities and compressive strength of porous alumina-doped BT ceramics obtained from slurries (20 vol.% solids loading) with various alumina concentrations by freeze casting.

Table 6.4 Shrinkage of porous alumina-doped BT ceramics sintered at 1275 ºC, in the direction perpendicular to the ice front

Al_2O_3 concentration (vol.%)	0.5	1.0	2.0	5.0
Shrinkage (%)	22.3	23.8	24.6	26.4

The cross-sectional microstructures of the porous alumina doped BT ceramics are shown in Figure 6.25. All samples exhibited clear lamellae architecture. The ceramic walls exhibited the distinct morphology in that one side was smooth and the other side was rough with ceramic arms, similar to the results shown in Chapter 4 and 5.

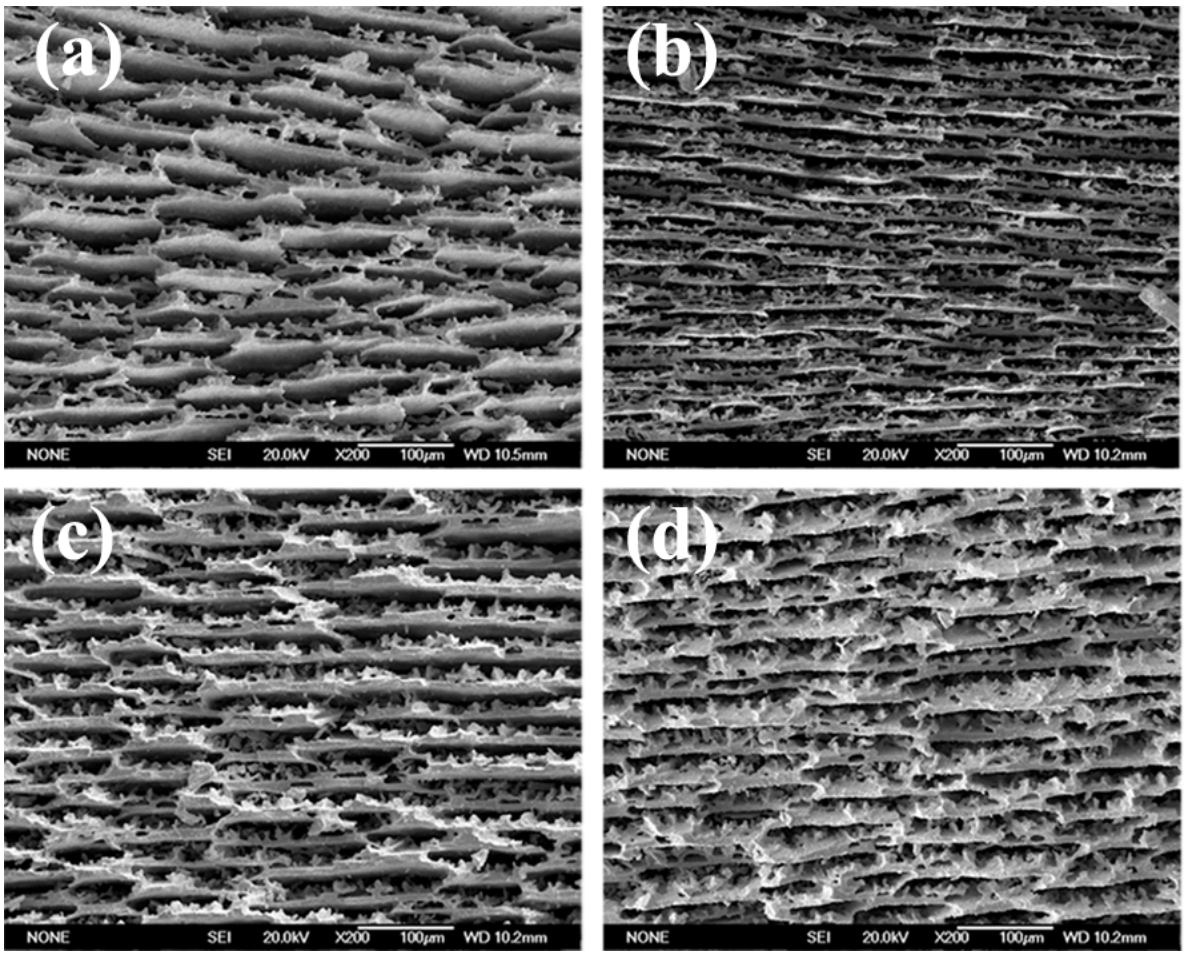

Figure 6.25 SEM photos of sintered (1275 ºC, 2h) porous alumina-doped BT ceramics with various alumina concentration: (a) 0.5 vol.%, (b) 1.0 vol.%, (c) 2.0 vol.%, (d) 5.0 vol.%. Samples were obtained from slurries with 20 vol.% initial solids loading by freeze casting.

Moreover, this is no debris from cutting compared with those samples shown in Figure 6.14

(a). The handling of the samples became much easier, indicating the improvement of the mechanical strength after the addition of nano-sized alumina in BT ceramics.

6.5.2 BAT-Epoxy Composites

Using the same technique as for the porous BT ceramics, the resultant porous alumina-doped BT ceramics were also backfilled with epoxy, made into composites and then cut into pellets for further electrical measurement (Chapter 3.1.5).

With increasing the amount of alumina concentration in the BT from 0.5 vol.% to 5.0 vol.%, the piezoelectric constant d_{33} decreased from about 45 pC/N to 33 pC/N, as shown in Table 6.5. Some of the d_{33} values were a little higher compared with the value of BT-epoxy (from 20 vol.% slurry), probably due to the difficulty in poling pure BT.

Table 6.5 Piezoelectric constant d_{33} of alumina-doped BT-epoxy composites

Al_2O_3 concentration (vol.%)	0.5	1.0	2.0	5.0
Piezoelectric constant d_{33} (pC/N)	45	44	39	33

The dielectric properties of the alumina-doped BT epoxy composite versus frequency are shown in Figure 6.26. Though the dielectric constant of the composites decreased compared with that of the BT-epoxy composites shown in Figure 6.16, it was still much higher than the traditional composites with randomly distributed ceramic particles. An increasing of alumina concentration led to lower dielectric constant.

As shown in Figure 6.26 (b), the loss tangent increased slightly with the increase of frequency. When the alumina concentration was increased from 0.5 vol.% to 2 vol.%, the loss tangent did not change much. However, when the addition of alumina reached 5 vol.%, the loss tangent increased markedly, which is in agreement with the results of bulk alumina-doped BT ceramics (Chapter 6.4.2.3).

In summary, the porous alumina-doped BT ceramics showed improved mechanical

properties compared with the porous BT ceramics, which could make later process easier. The dielectric constant of alumina-doped BT epoxy composites reported here also showed improved values, though lower than those of BT-epoxy composites, but still nearly 1 order of magnitude higher than the traditional composites. Thus, the properties of the composites can be optimized by adjustment of the amount of alumina added.

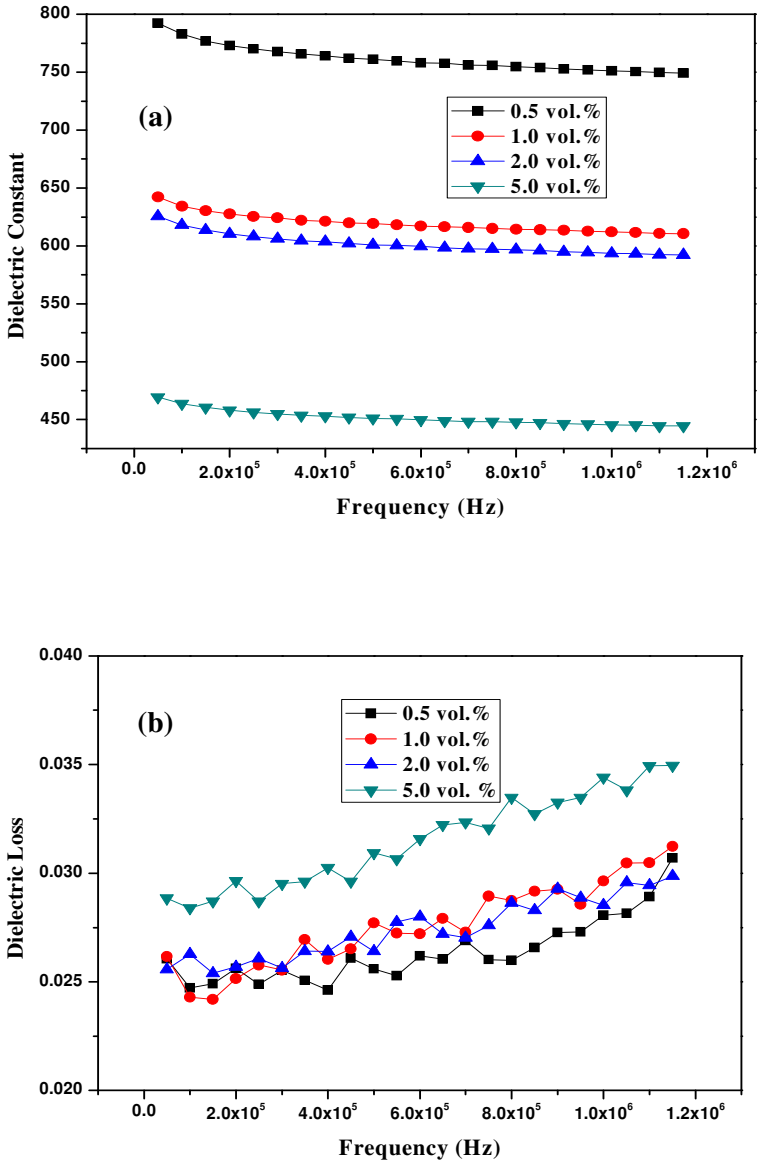

Figure 6.26 Dielectric properties of alumina-doped BT-epoxy composites: (a) dielectric constant, (b) dielectric loss as a function of frequency measured at room temperature.

6.6 Summary

In summary, NH_4PAA is very effective as a dispersant for this BT colloidal system. Stable and well-dispersed suspensions incorporating nano-sized BT powder have been obtained. The pH value had strong effect on the stability of the BT suspensions, and moreover, the intrinsic pH is suitable for centrifugal aided slip casting or other casting techniques. A temperature of 1325 ºC was found to be the optimal sintering temperature for this nano-sized BT powder without any sintering additives. BT ceramic sintered at this temperature shows a bulk density of 5.85 g/cm^3, nearly 97.0% of the theoretical density, and room temperature dielectric constant and loss tangent of 5270 and 0.01 (measured at 1 kHz), respectively.

Porous BT ceramic exhibited lamellae architectures, and BT-epoxy composites made from this possessed only a modest piezoelectric constant, but the dielectric constant was 1 order of magnitude higher than conventional BT composites with randomly distributed ceramic particles. However, the poor mechanical properties limit its applications especially for biomedical application.

The mechanical properties of $BaTiO_3$ bulk ceramics were improved by doping nano-sized alumina (from 0.5 vol.% to 5 vol.%) into this BT matrix, which effectively suppresses the growth of the grains. An Al-rich phase ($Ba_3TiAl_{10}O_{20}$) observed in the samples with higher alumina concentration could be responsible for deteriorating the dielectric and piezoelectric properties. If the amount of nano-sized alumina addition is less than 2 vol.%, the mechanical and electrical properties can be optimized.

The porous alumina-doped BT ceramics showed improved mechanical properties compared with that of porous BT ceramic, which could facilitate the later processing. Though the dielectric constant values of alumina-doped BT-epoxy composites obtained in this work were lower than those of BT-epoxy composites, they were still nearly 1 order of magnitude higher

than the traditional composites. Thus, the properties of the composites can be optimized by adjustment of the amount of alumina added.

References

1. H. Kamiya, K. Gomi, and Y. Iida, Preparation of highly dispersed ultrafine Barium Titanate powder by using microbial-derived surfactant. Journal of American Ceramic Society, 2003, 86 (12), 2011-2018.

2. C.S. His, Y.C. Chen, and H. Jantunen. Barium titanate based dielectric sintered with a two-stage process. Journal of European Ceramic Society, 2008, 28, 2581-2588.

3. J.D. Russell and C. Leach. β–Conductivity contrast at Barium Titanate thermistor grain boundaries. Journal of European Ceramic Society, 1996, 16, 1035-1039.

4. X.Y. Liu, Y. Luo, and X.Q. Li. Electrical properties of $BaTiO_3$-based NTC ceramics doped by $BaBiO_3$ and Y_2O_3. Journal of Alloys and Compounds, 2008, 459, 45-50.

5. H.T. Langhammer, D. Makovec, and Y.P. Pu. Grain boundary reoxidation of donor-doped barium titanate ceramics. . Journal of European Ceramic Society, 2006, 26, 2899-2907.

6. X.S. Wang, L.L. Zhang, and H. Liu. Dielectric nonlinear properties of $BaTiO_3$–$CaTiO_3$–$SrTiO_3$ ceramics near the solubility limit. Materials Chemistry and Physics, 2008, 112,675-678.

7. J.Q. Feng, H.P. Yuan, and X.D. Zhang. Promotion of oteogenesis by a piezoelectric biological ceramic. Biomaterials, 1997, 18, 1531-1534.

8 F.R. Baxter, C.R. Bowen, I.G. Turner, et al. Electrically active bioceramics: A review of interfacial response. Annals of Biomedical Engineering, 2010, 38(6), 2079-2092.

9. D. Kumar, J.P. Gittings, I.G. Turner, et al. Poalrization of hydroxyapatite: influence on osteoblast cell proliferation. Acta Biomaterialia, 2010, 6(4), 1549-1554.

10. J.P. Gittings, C.R. Bowen, A.C.E. Dent, et al. Electrical characterization of hydroxyapatite-based bioceramics. Acta Biomaterialia, 2009, 5(2), 743-754.

11. J.P. Gittings, C.R. Bowen, I.G. Turner, et al. Characterization of ferroelectric-calcium phosphate composites and ceramics. Journal of European Ceramic Society, 2007, 27, 4187-4190.

12. C.R. Bowen, J.P. Gittings, and I.G. Turner. Dielectric and piezoelectric properties of hydroxyapatite-$BaTiO_3$ composites. Applied Physics Letters, 2006, 89, 132906.

13.Y.J. Hotta , K. Tsunekawa, T. Isobe. Synthesis of $BaTiO_3$ powders by a ball milling-assisted hydrothermal reaction. Materials Science and Engineering A, 20084, 75, 12-16.

14. D.S. Jung, S.K. Hong, and J.S. Cho. Nano-sized barium titanate powders with tetragonal crystal structure prepared by flame spray pyrolysis. Journal of the European Ceramic Society 2008,28, 109-115.

15. W. Lu, M. Quilitz, and H. Schmidt. Nanoscaled $BaTiO_3$ powders with a large surface area synthesized by precipitation from aqueous solutions: Preparation,characterization and sintering. Journal of the European Ceramic Society, 2007, 27, 3149-3159.

16. C.C. Li and J.H. Jean. Interaction between dissolved Ba^{2+} and $PAANH_4$ dispersant in aqueous barium titanate suspensions. Journal of the American Ceramic Society, 2002, 85(6), 1449-1455.

17. C.C. Li and J.H. Jean. Interaction of organic additives with boric oxide in aqueous barium titanate suspensions. Journal of the American Ceramic Society, 2002, 85(6), 1441-1448.

18. M.C.B. López, B. Rand, and F.L. Riley. The properties of aqueous phase suspensions of barium titanate. Journal of the European Ceramic Society, 1997, 17, 281-287.

19 J. Zhao, X. Wang, and L. Li. Electrophoretic deposition of $BaTiO_3$ films from aqueous suspensions. Materials Chemistry and Physics, 2006, 99, 350-353.

20. M.C.B. López, B. Rand, and F.L. Riley. The isoelectric point of $BaTiO_3$. Journal of the European Ceramic Society, 2000, 20, 107-118.

21. C. Hérard, A. Faivre, and J. Lemiatre. Surface decontamination treatments of undoped $BaTiO_3$—Part: powder and green body properties. Journal of the European Ceramic Society, 1995, 15, 135-143.

22. J.J. Ritter, R.S. Roth, and J. E. Blendell. Alkoxide Precursor Synthesis and Characterization of Phases in the Barium-Titanium Oxide System. Journal of the American Ceramic Society, 1986, 69 (2), 155-162.

23. H. Jaffe. Piezoelectric ceramics. Journal of the American Ceramic Society, 1958, 41(11), 494-498.

24. S.F. Shao, J.L. Zhang, Z. Zhang, P. Zheng, et al. High piezoelectric properties and domain configuration in $BaTiO_3$ ceramics obtained through the solid-state reaction route. Journal of Physics D: Applied Physics, 2008, 41, 125408.

25. D.H. Kuo, C.C. Chang, and T.Y. Su. Dielectric behaviours of multi-doped $BaTiO_3$/epoxy composites. Journal of the European Ceramic Society, 2001, 21, 1171-1177.

26. D.H. Kuo, C.C. Chang, and T.Y. Su. Dielectric properties of three ceramic/epoxy composites. Materials Chemistry and Physics, 2004, 85, 201-206.

27. Z.M. Dang, Y.F. Yu, and H.P. Xu. Study on microstructure and dielectric property of the $BaTiO_3$/epoxy resin composites. Composites Science and Technology, 2008, 68, 171-177.

28. E.P. Gorzkowski, M.J. Pan. Barium titanate-polymer composites produced via directional freezing. IEEE Transactions on Ultrosonics, Ferroelectrics and Frequency Control, 2009, 56(8), 1613-1616.

29. H.J. Hwang, K. Watari, M. Sando, et al. Low-temperature sintering and high-strength $Pb(Zr,Ti)O_3$-matrix composites incorporating silver particles. Journal of the American Ceramic Society, 1997, 80(3), 791-793.

30. H.J. Hwang and K. Niihara. Perovskite-type $BaTiO_3$ ceramics containing particulate SiC. Journal of Materials Science, 1998, 33, 548-558.

31. K. Tajima, H.J. Hwang, M. Sando, et al. PZT nanocomposites reinfored by small amount of oxides. Journal of the European Ceramic Society, 1999, 19, 1179-1182.

32. S.R. Panteny, R. Stevens, and C.R. Bowen. Piezoelectric particulate reinforced nanocomposites. The Alden group, Oxford, 2000.

33. S. Jiansirisomboon, A. Watcharapasorn. Effects of alumina nano-particulates addition on

mechanical and electrical properties of barium titanate ceramics. Current Applied Physics, 2008, 8, 48-52.

34. M. Hillert. Inhibition of grain growth by second-phase particles. Acta Metallurgica, 1988, 36(12), 3177-3181.

35. K. Tajima, H.J. Hwang, M. Sando, et al. 28GHz microwave sintering for high performance PZT-based nanocomposites. Key Engineering Materials, 1999, 161-163, 505- 508.

36. K. Tajima, H.J. Hwang, and M. Sando. Electric-field-induced crack growth behaviour in PZT/Al_2O_3 composites. Journal of American Ceramic Society, 2000, 83(3), 651-653.

CHAPTER 7 PZT-EPOXY PIEZOCOMPOSITES

7.1 Introduction

Lead zirconate titanate is one of the most widely utilized piezoelectric ceramics for actuator and transducer applications due to its excellent electromechanical properties[1,2].

In the field of ultrasonic transducer applications, PZT-epoxy composites have attracted much attention due to their superior properties compared with monolithic PZT thin plates[3]. One of the key features of piezoelectric composites is the stress transfer capability between the hard ceramic and soft polymer, which offers the composite a high level of piezoelectric capability and at the same time, reduces the effective acoustic impedance of the composite and also minimizes the propagation of lateral modes to make it more suitable for underwater and medical applications[4-6].

The most common composite connectivity used for the transducers are of the form 2-2 and 1-3[7]. The design and fabrication technique are very critical, because the piezoelectric response of these composites can be significantly affected.

There are several manufacturing techniques which can be utilized to fabricate piezoelectric ceramic-polymer composites, including dice and fill and injection moulding. The conventional dice and fill method is limited by the thickness of the dicing saw blades[7] especially for the fabrication of composites for high frequency applications. More recently, solid freeform fabrication techniques were introduced to produce ceramic-polymer composites with 2-2 connectivity. These techniques produce a green ceramic body in a layer-by-layer build sequence through the deposition of a feedstock material, in the form of a ceramic powder-loaded filament or a concentrated colloidal gel-based ink[8,9]. Other available techniques include the computer numeric-controlled (CNC) machining of green ceramics

and the co-extrusion process[10,11]. However, the employment of polymeric binders and lubricating agents in the ceramic system are potential disadvantages for those methods mentioned above (solid freeform, co-extrusion process), which could cause problems during sintering and pose potential environmental issues. Freeze casting as a cost effective and environmental friendly process, and has attracted a lot of attention. In particular, the lamellar structure of the samples fabricated by freeze casting may provide a potential way to produce piezocomposites with 2-2 connectivity. Therefore, an investigation of the applicability of the freeze casting technique for the fabrication of 2-2 PZT piezocomposites is reported here in order to demonstrate the versatility of this technique. Later in this chapter, the relationship between the structure and properties is also discussed.

7.2 Powder Characterization

A SEM micrograph of the PZT powder (TRS610, TRS Ceramics, USA) utilized in this chapter is shown in Figure 7.1.

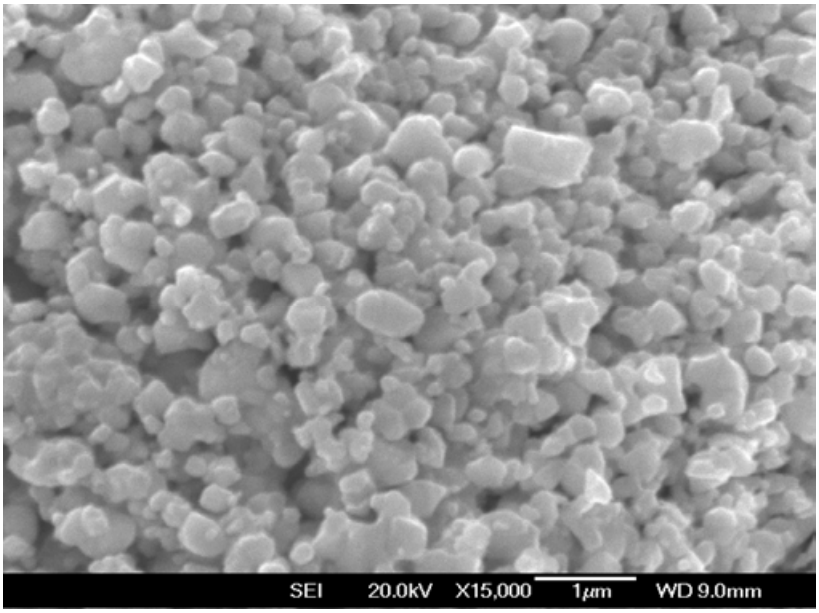

Figure 7.1 SEM photograph of the commercial PZT powder utilized in this work with a primary particle size around 0.7 μm

The PZT powder has an irregular morphology with an average particle size around 0.7 μm. Figure 7.2 shows the result of XRD analysis of the PZT powder. By comparing the XRD pattern with JCPDS standards, the diffraction peaks from the powder can be indexed as cubic $PbZr_{0.58}Ti_{0.42}O_3$. No other phase can be found.

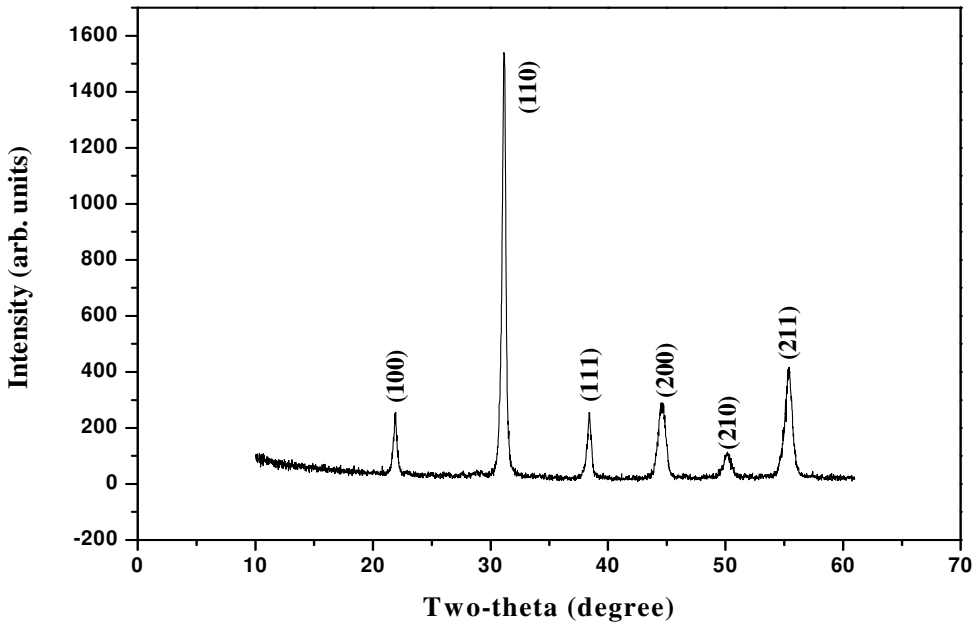

Figure 7.2 XRD patterns for the commercial PZT powder utilized in this work

7.3 Phase Segregation (Polymer and Ceramic) of PZT Sample during Freeze Casting

The suspensions utilized in this work were obtained according to the method described in Chapter 3.1.2.1. Various initial solids loadings of PZT suspensions were prepared (11 vol.%, 16 vol.%, 23 vol.% and 25 vol.%).

Figure 7.3 shows the viscosities of 11 vol.% solids loading PZT suspensions with different amounts of dispersant (NH_4PAA), i.e. 0.12 wt.%, 0.25wt.% and 0.38 wt.%. All the slurries showed relatively low viscosity at high shear rate and relatively high viscosity at low shear rate, indicating a typical shear-thinning behaviour. With the increase of the dispersant

amount from 0.12 wt.% to 0.25 wt.%, the viscosity decreased dramatically, however, the viscosity changed little when the dispersant amount increased from 0.25 wt.% to 0.38 wt.%.

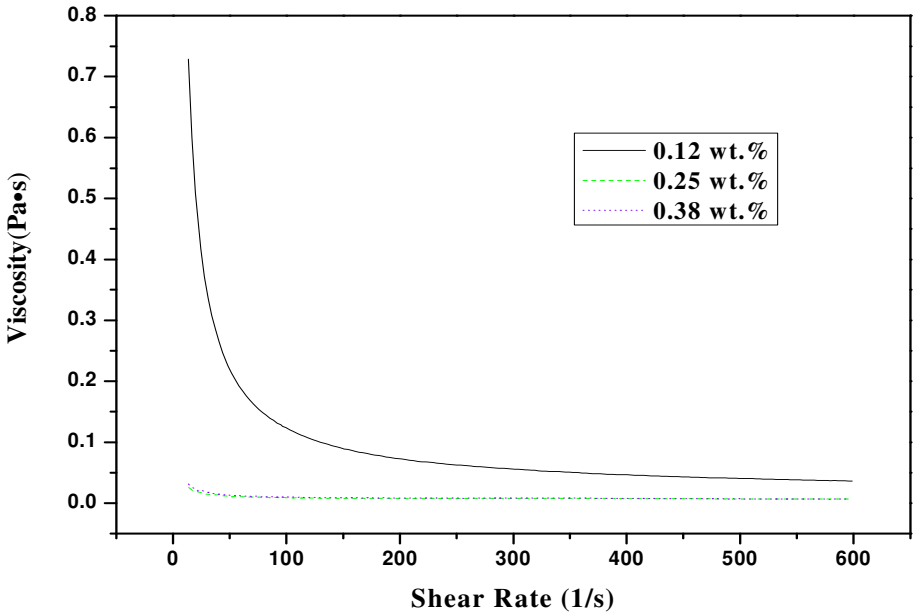

Figure 7.3 Rheological properties of the PZT slurries (11 vol.% solids loading) with different amounts of dispersant (0.12 wt.%, 0.25 wt.% and 0.38 wt.%), but with the same amount of binders (3 wt.% B-1000 and 2 wt.% B-1007).

One interesting phenomenon was observed in the PZT green samples after sublimation, which was only found in the process of freezing the PZT suspensions. As shown in Figure 7.4 (a), phase segregation (polymer and ceramic phases) occurred in this sample. Along the solidification direction (the red arrow), two distinct parts could be found. One part is composed of polymer (the white part), and the other is composed of PZT ceramic powder (the yellow part). The sample shown in Figure 7.4 (b) is also a PZT sample, but no phase segregation occurred in this sample.

The two samples shown in Figure 7.4 were all obtained from the slurries with the same initial solids loading (11 vol.%) and also under the same cooling rate of 0.5 ºC/sec. Moreover, the binder contents in the two samples were also the same (3 wt.% B-1000 and 2 wt.% B-

1007). The only difference was the dispersant amount. In the case of the abnormal sample (Figure 7.4 (a) where phase segregation were observed), the amount of the dispersant was 0.38 wt.%, while for the normal sample it was 0.12 wt.%.

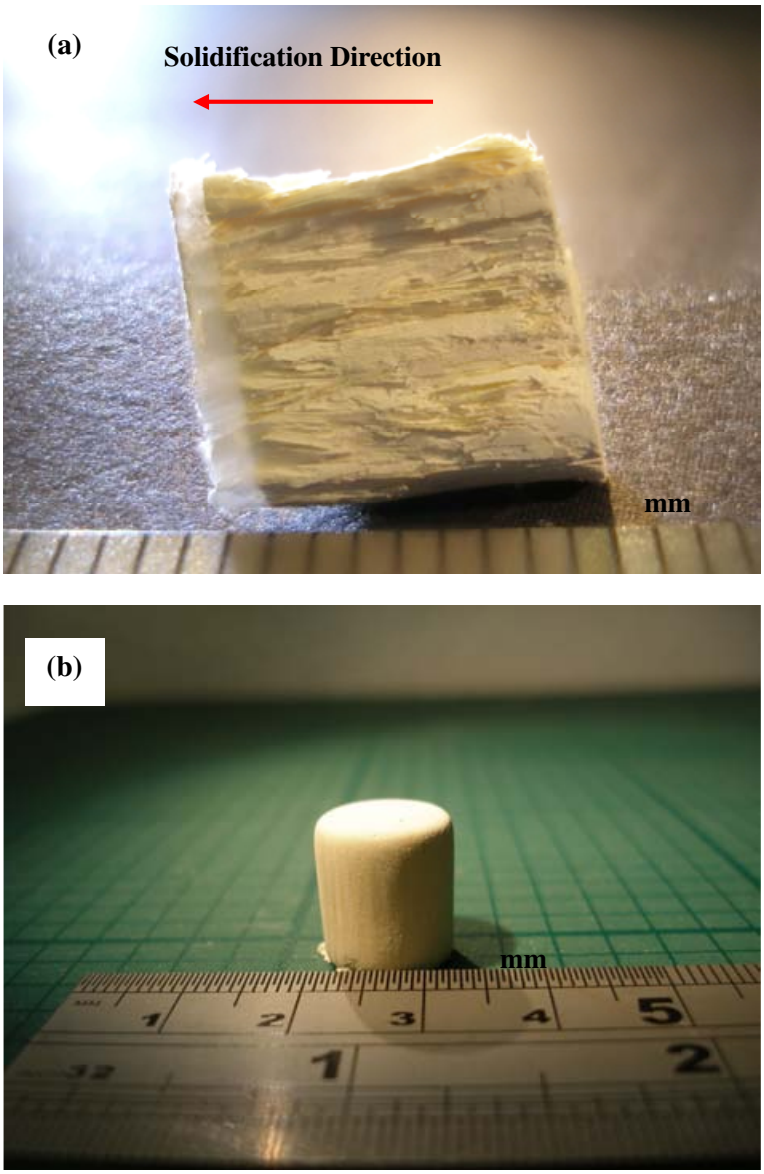

Figure 7.4 Photos of green PZT samples obtained from 11 vol.% solids loading slurries with different amounts of dispersant ((a) 0.38 wt.% and (b) 0.12 wt.%), but with the same binders (3 wt.% B-1000 and 2 wt.% B-1007). Samples had the same cooling rate of 0.5 ºC/sec

The phase segregation phenomenon is related to the stabilization of PZT suspension. As it is known, the stabilization mechanism for NH_4PAA is electrosteric stabilization. Compared

with other materials used in the whole study, e.g. Al_2O_3, Al_2O_3-ZrO_2, $BaTiO_3$, the PZT powder possesses the largest density (8.02 g/cm^3). When the amount of dispersant in the PZT suspension was lower, i.e. 0.12 wt.%, the viscosity was relatively high compared with those with more dispersant, so the forces in the interface, especially van der Waals attraction, was large enough to conquer the sedimentation caused by the gravity. Thus, the stabilization for this suspension was good. However, when more dispersant was added, i.e. 0.38 wt.%, the relative force equilibrium in the colloidal system was broken, therefore, the forces in the interface were not enough to overcome the gravity to keep the force equilibrium. As a result, the suspension was no longer stable as the one with 0.12 wt.% dispersant, finally leading to sedimentation. A color change of the suspension (from yellow to light yellow) has been observed when freezing the slurry with 0.38 wt.% dispersant, indicating sedimentation has occurred. Two distinct parts appeared after freeze casting as shown in Figure 7.4 (a). Therefore, in order to avoid the phase segregation during freezing, the amount of dispersant was fixed at 0.12 wt.%.

7.4 Effect of Solids Loading on Pizeoelectric and Electrical Impedance Properties

Porous PZT samples were obtained through the method described in Chapter 3.1.2.2. After sintering (1200 ºC, 2 hours), the resultant porous PZT ceramics were then backfilled with epoxy and made into composites according to the method described in Chapter 3.1.5. The relationship between the ceramic (piezoelectric phase) volume fraction in the composite and the initial solids loading is shown in Figure 7.5. With the increase of initial solids loading from 11 vol.% to 25 vol.%, the volume of ceramic phase (piezoelectric phase) gradually increased from about 30 vol.% to 50 vol.%. As mentioned in Chapter 6, the space in the

composite occupied by the epoxy is the place where the ice originally was. Therefore, the volume of epoxy required decreased when the initial solids loading increased, resulting in the increase of the piezo phase volume fraction. The piezoelectric constant d_{33} is also shown in Figure 7.5. The piezoelectric constant d_{33} increased from about 103 pC/N to 203 pC/N with the increase of piezo phase volume fraction. In the composite, PZT ceramic is the piezoelectric phase, and thus responsible for the piezoelectric response. Therefore, it can be explained that the piezoelectric constant d_{33} increased with a rise in the piezo phase volume fraction.

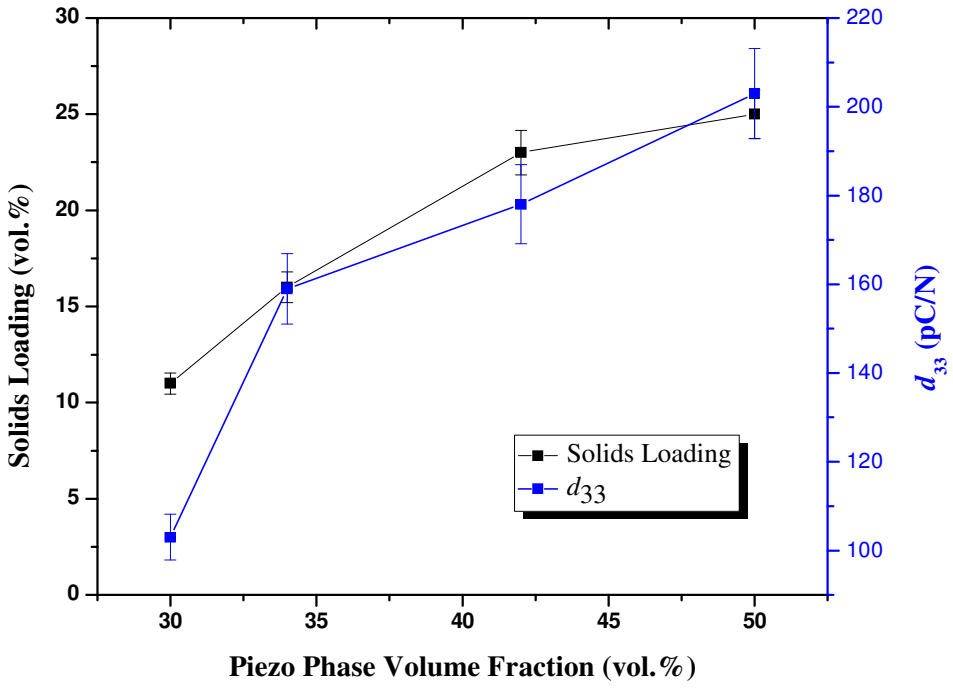

Figure 7.5 The initial solids loading and piezoelectric constant d_{33} as a function of piezoelectric phase volume fraction.

Typical SEM photos of porous PZT and PZT-epoxy composites are shown in Figure 7.6. As shown in Figure 7.6 (a) and (c), the wall thickness of the porous PZT ceramics increased from about 16 μm to 25 μm with an increase of initial solids loading from 16 vol.% to 23

vol.%, which shows a similar behaviour as shown in Chapter 4.6. Figure 7.6 (b) and (d) shows the microstructure of the PZT-epoxy composites obtained from the porous PZT ceramics shown in Figure 7.6 (a) and (c), respectively. Homogeneous architectures were observed in the range of the photos. However, they are not homogeneous in the whole sample, especially with regards to the orientation, which will be discussed later in this chapter.

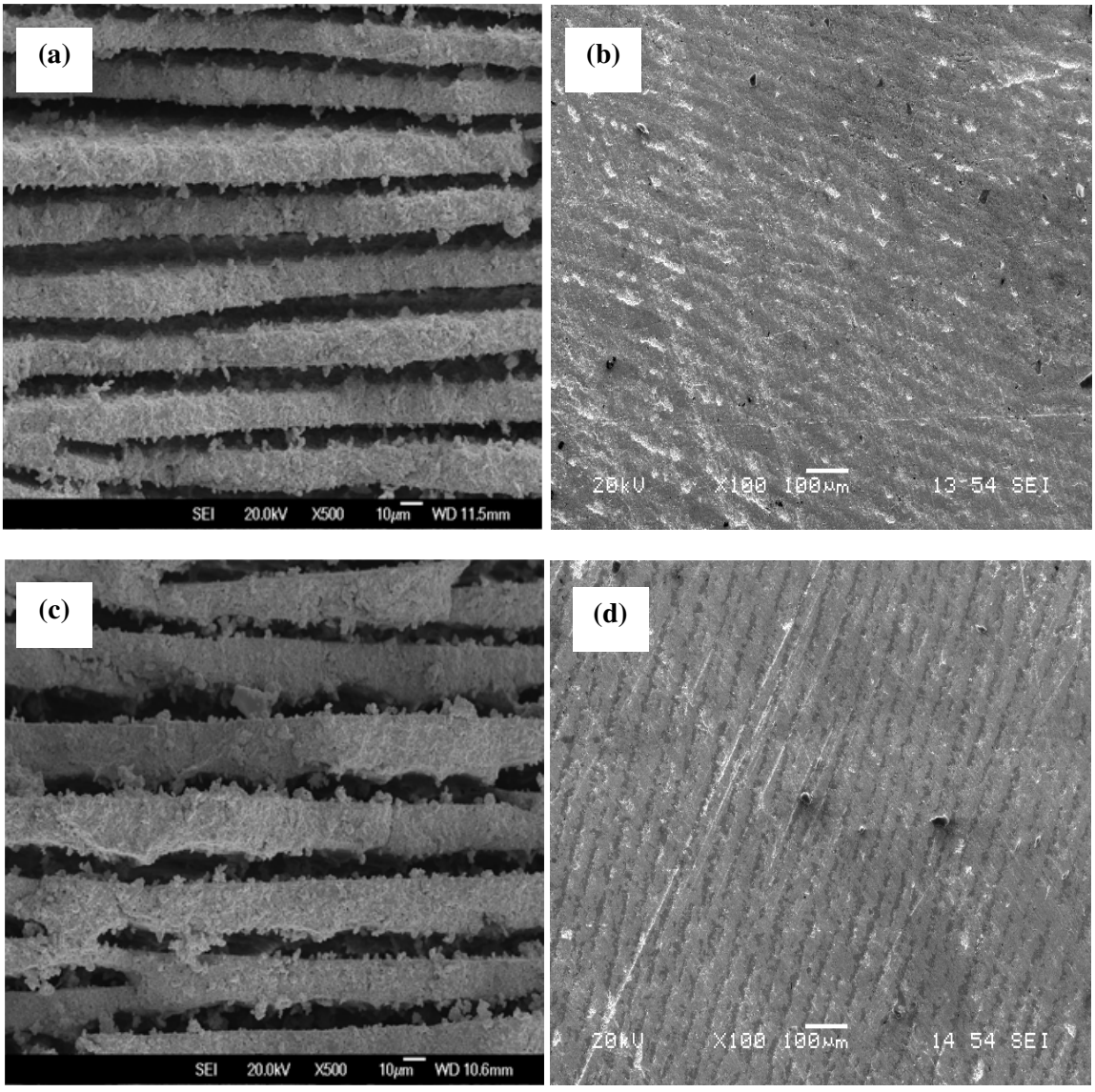

Figure 7.6 Typical SEM photographs of sintered (1200 ºC, 2h) porous PZT ceramics and their epoxy composites. Samples were obtained from different initial solids loadings ((a)&(c) 16 vol.%, and (b)&(d), 23 vol.%.) under a cooling rate of 0.5 ºC/sec.

The impedance spectra for the resultant composites are shown in Figure 7.7. The series resonance frequency of the piezocomposites changed from about 122 Hz to 164 Hz with increasing the volume fraction of active phase. However, the frequency was low. Two factors contribute to this low frequency: one is the non-homogenous structure throughout the whole sample, and the other is the thickness of the measured sample (1.5 mm).

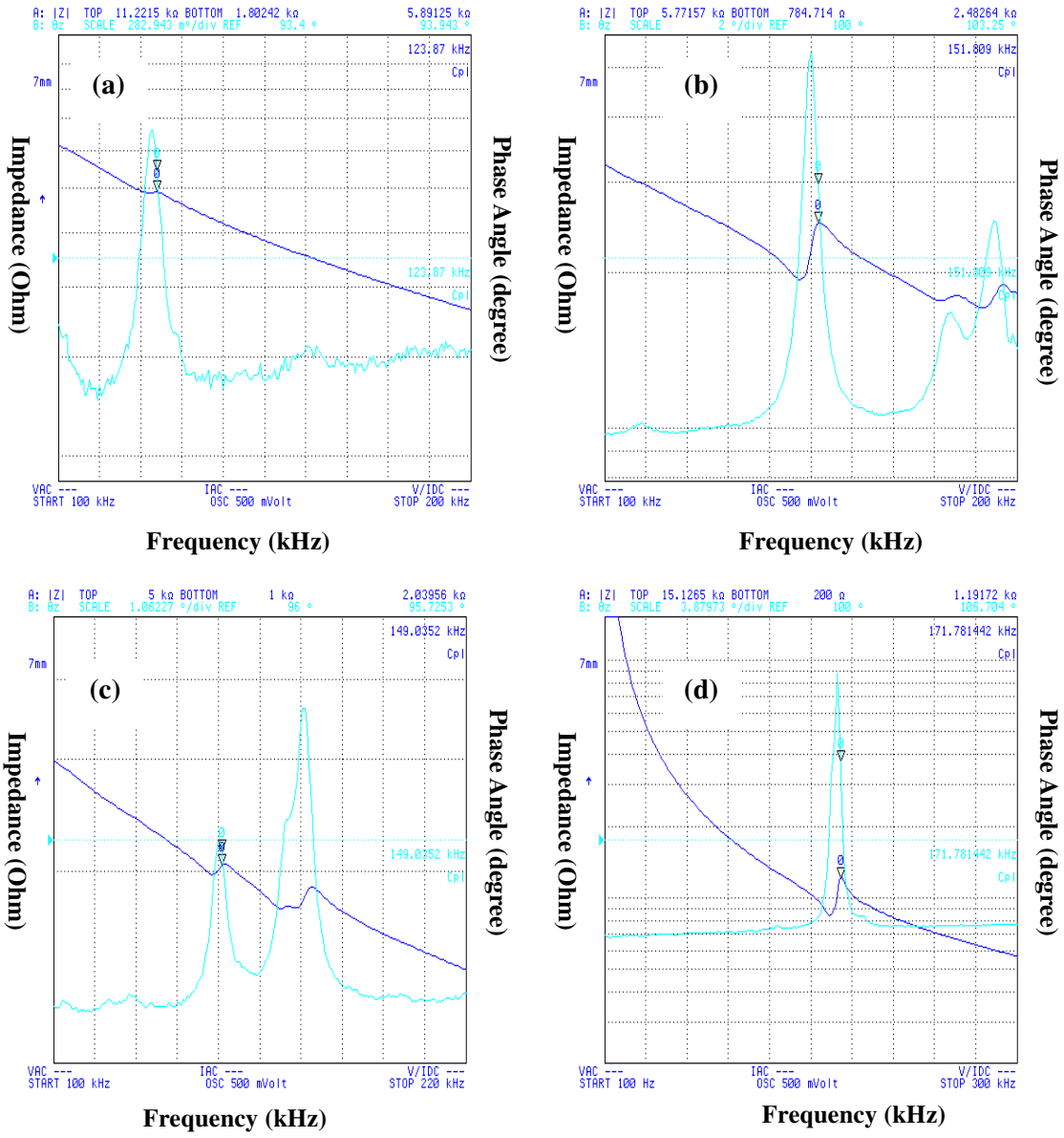

Figure 7.7 Impedance spectra for the PZT-epoxy composites originated from different initial solids loadings under a cooling rate of 0.5 ºC/sec: (a) 11 vol.% (b) 16 vol.% (c) 23 vol.% (d) 25 vol.%. The thickness of the sample disc was 1.5 mm.

The planar coupling factor k_p of the resultant PZT-epoxy composites was obtained from the series (f_s) and parallel (f_p) resonance frequencies as described in Chapter 3.2.8. As shown in Table 7.1, the planar coupling factor k_p showed a similar trend with the series resonance frequency. It increased roughly from about 0.21 to 0.36 as the increased initial solids loading increased from 11 vol.% to 25 vol.%.

Table 7.1 Planar coupling coefficient k_t of the PZT-epoxy composites obtained from different initial solids loadings.

Solids Loading (vol.%)	11	16	23	25
k_p	0.21	0.27	0.25	0.36

7.5 Effect of Sintering Temperature on Property of Composites

Just as shown in Chapter 4.8, sintering conditions can affect the final properties of the porous alumina. Thus the sintering conditions were also changed here in order to investigate their effect on the functional property of the PZT-epoxy composites. Figure 7.8 shows the XRD results of the porous PZT ceramics sintered at various sintering temperatures (2 hours).

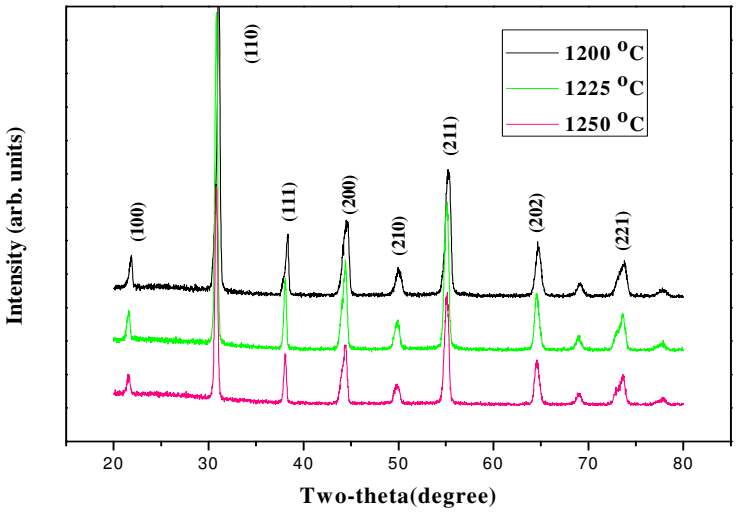

Figure 7.8 XRD spectrum of porous PZT ceramics sintered at different temperatures for 2 hours. Samples were obtained from the same PZT suspensions with a solids loading of 23 vol.% and under a cooling rate of 0.5 °C/sec.

All the porous PZT ceramics were obtained from the same PZT suspension with a solids loading of 23 vol.%. There was no difference between the peaks of the sample sintered at different temperatures. By comparing the XRD patterns with JCPDS standards, the diffraction peaks from all the sintered samples can be mainly indexed as cubic PZT. Therefore, in the range of the sintering temperatures, there was no new phase formed. No evidence for the tetragonal or rhombohedral phase was seen, although, as shown below, the samples are clearly piezoelectric.

The porous PZT ceramics sintered at different temperatures were also made into composites according to the methods described in Chapter 3.1.5. The ceramic (piezoelectric phase) volume fraction in the composite is shown in Table 7.2. Higher sintering temperature led to less total porosity, therefore, with the increase of sintering temperature from 1200 ºC to 1250 ºC , the volume fraction of the ceramic phase (piezoelectric phase) in the composites gradually increased from about 42 vol.% to 46 vol.%. The piezoelectric constant d_{33} of the resultant composites increased from about 178 pC/N to 286 pC/N as the sintering temperature increased from 1200 ºC to 1250 ºC, as shown in Table 7.2.

Table 7.2 Volume fraction and piezoelectric constant d_{33} of the PZT-epoxy composites

Sintering temperature (^{o}C)	1200	1225	1250
Volume Fraction (%)	42	43	46
d_{33} (pC/N)	178	275	286
k_p	0.25	0.26	0.30

The SEM photographs of PZT-epoxy composites originated from the porous PZT with various sintering temperatures are shown in Figure 7.9. With the increase of sintering temperature, the gaps between the ceramic walls did not change significantly. The microstructures of the ceramic walls of the porous PZT are shown in Figure 7.10. With the increase of sintering temperature, the grain size of the ceramic wall did not change much but

the ceramic walls became slightly denser, which probably contributed to the increase of d_{33}.

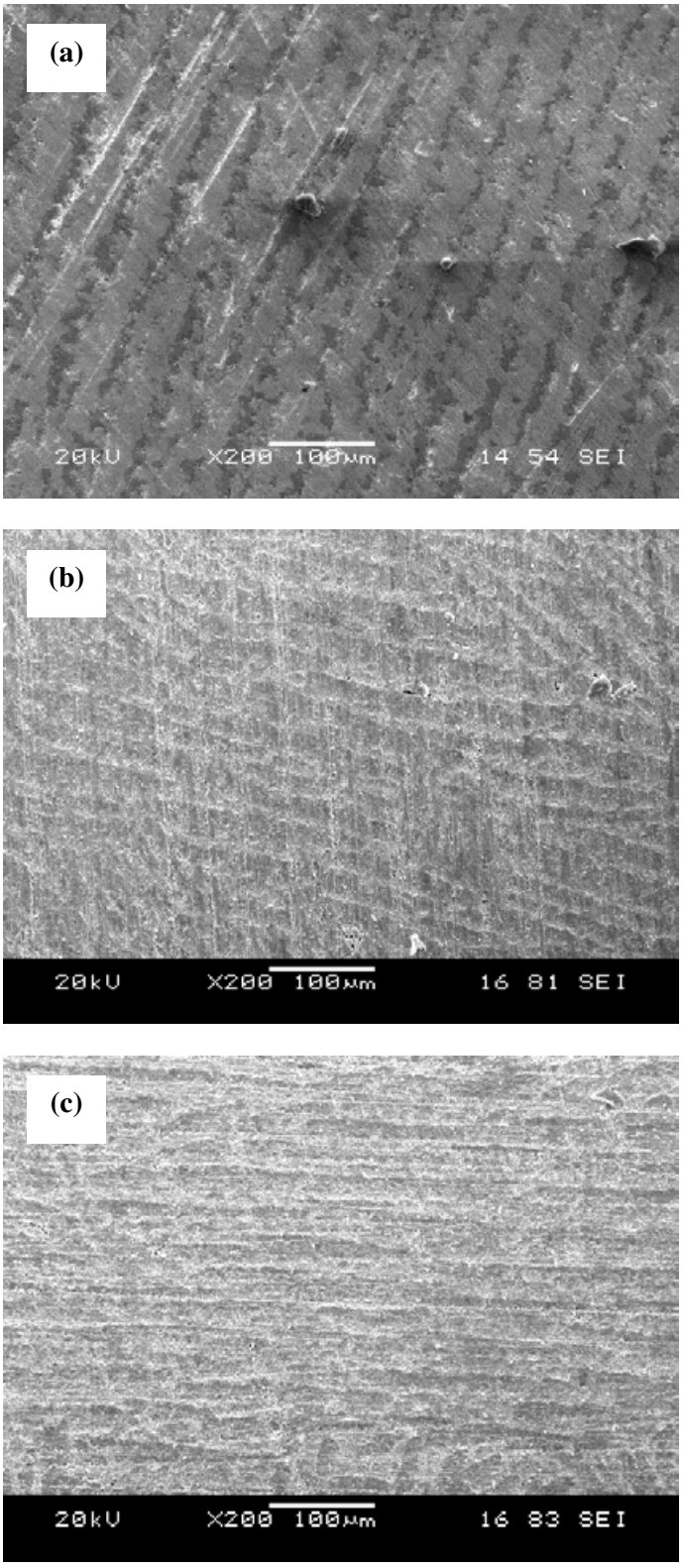

Figure 7.9 SEM photographs of PZT-epoxy composites obtained from a 23 vol.% solids loading suspension. The PZT ceramic phase were sintered at different temperatures: (a) 1200 ºC, (b) 1225 ºC, and (c) 1250 ºC.

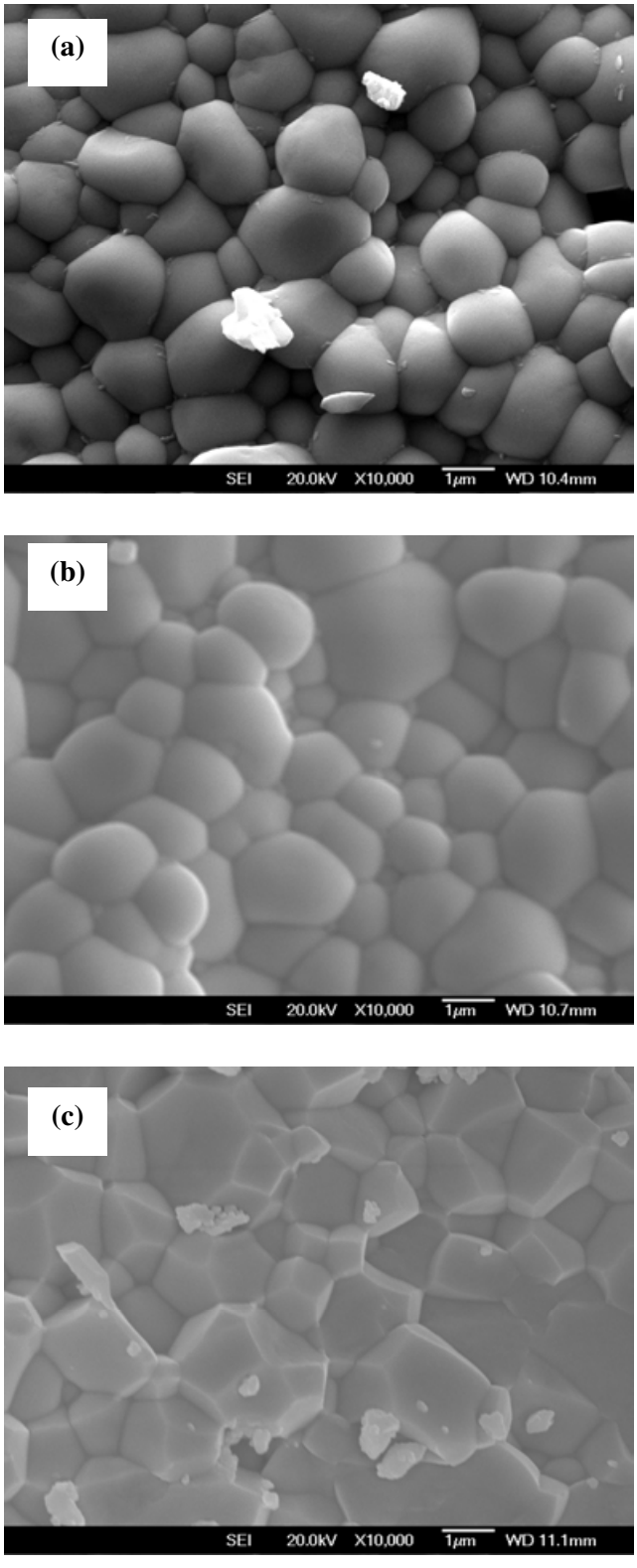

Figure 7.10 SEM photos of ceramic walls of the porous PZT sintered at different temperatures. (a) 1200 ºC, (b) 1225 ºC, and (c) 1250 ºC. (a) and (b) are natural surfaces, and (c) is fracture surface.

With the increase of the sintering temperature, the series resonance frequency of the composite did not change significantly, as shown in Figure 7.6 (c) (146 kHz) and Figure 7.11 (139 kHz, 144 kHz). The planar coupling factor k_p did increase from about 0.25 to 0.30 as shown in Table 7.2.

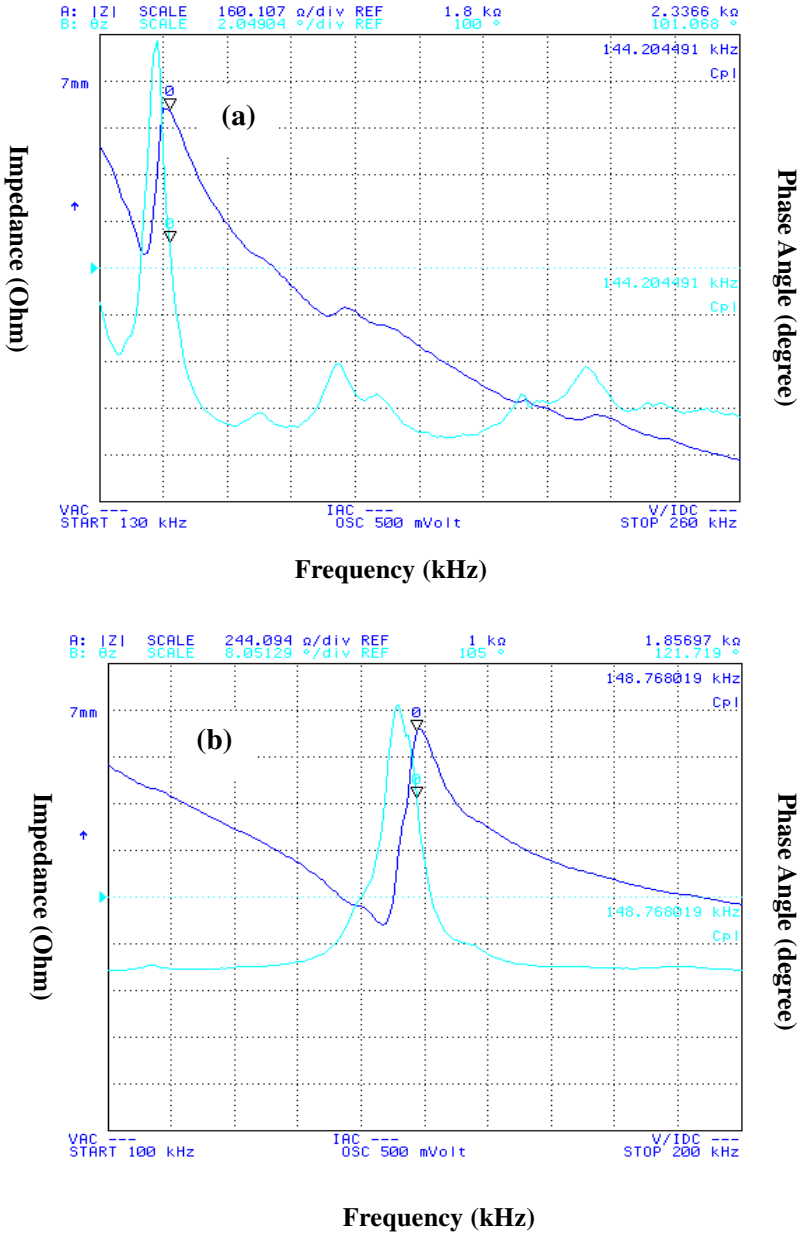

Figure 7.11 Impedance spectrums for the PZT-epoxy composites originated from 23 vol.% solids loading suspension but sintered at different temperatures: (a) 1225 ºC, and (b) 1250 ºC.

Therefore, higher sintering temperature can improve the d_{33} value of the composite and also

the planar coupling factor k_p.

7.6 Orientation Effects

Figure 7.12 shows the architecture of the PZT-epoxy composite obtained from the 23 vol.% suspension at low magnification. We can see that in a small zone, e.g. the circled zone of this sample, the orientation of the ceramic walls is uniform; however, in some parts especially near the edge of the sample (the rectangular zone), the orientation is rather inhomogeneous. This effect was also observed in samples of other materials discussed in previous chapters. However, for a 2-2 composite application, it is of much more significance.

As mentioned in section 7.4, the inhomogeneous architecture will limit its application. The uniformity of the initial freezing and the cooling rate are the major factors affecting the orientation of the ceramic walls. The inhomogeneity of orientation of ceramic wall was caused by the limit of homemade freezing setup, because any slight disturbance during freezing could affect it.

Therefore, future work should preferentially focus on improving the design and implementation of the freezing setup in order to avoid such limits.

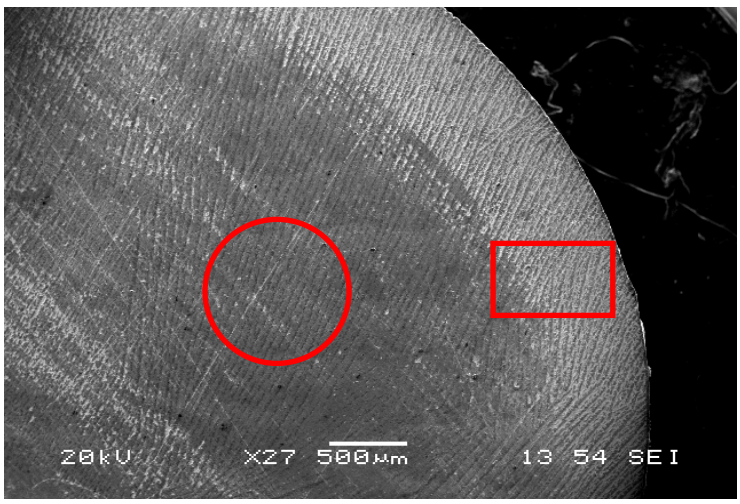

Figure 7.12 SEM photographs with small magnification of PZT-epoxy composites obtained from 23 vol.% suspension. The PZT ceramic phase was sintered at 1200 ºC.

7.6 Summary

This chapter has focused on the application of the freeze casting technique incorporating PZT, and the results obtained can be summarized as follows:

Stable PZT suspensions with good fluidity can be produced by adding 0.12 wt.% NH_4PAA. Further addition of NH_4PAA would lead to phase segregation.

With the increase of initial solids loading from 11 vol.% to 25 vol.%, the volume of ceramic phase in the composite gradually increased from about 30 vol.% to 50 vol.%, the piezoelectric constant d_{33} increased from about 103 pC/N to 203 pC/N.

The piezoelectric constant d_{33} of the resultant composites increased from 178 pC/N to 286 pC/N when the sintering temperature increased from 1200 ºC to 1250 ºC. The elevated temperature could effectively improve the piezoelectric constant d_{33} of the composites and the planar coupling factor k_p.

The limitation of the homemade freezing setup caused the inhomogeneity of the ceramic wall orientation, which would limit its application.

References

1. Y.H. Xu. Ferroelectric materials and their applications. North-Holland: Amsterdam, 1991.

2. T.R. Gururaja. Piezoelectrics transducers for medical ultrasonic imaging. American ceramic Society Bulletin, 1994, 73, 50-54.

3. C.B. Yoon, S.H. Lee, S.M. Lee, et al. Piezoelectric mutilayer ceramic/polymer composite transducer with 2-2 connectivity. Journal of the American Ceramic Society, 2006, 89(8), 2509-2513.

4. R.E. Newnham, D.P. Skinner, and L.E. Cross. Connectivity and piezoelectric-pyroelectric composite. Materials Research Bulletin, 1978, 13, 525-536.

5. Q.M. Zhang, W.W. Cao, J. Cao, et al. Piezoelectric performance of piezoceramic-polymer composites with 2-2 connectivity− A combined theoretical and experimental study. IEEE Transactions and Ultrasonic, Ferroelectrics and Frequency Control, 1994, 41(4).

6. J.Y. Chapelon, D. Cathignol, C. Cain, et al. New piezoelectric transducers for therapeutic ultrasound. Ultrasound in Medicine and Biology, 2000, 26(1), 153-159.

7. R.B. Liu, K.A. Harasiewicz, et al. 2-2 piezoelectric composites with high density and fine scale fabricated by interdigital pair bonding. Applied Physics Letters, 1999, 75(21), 3390-3392.

8. G.M. Lous, I.A. Cornejo, T.F. McNulty, et al. Fabrication of piezoelectric ceramic/polymer composite transducer using fused deposition of ceramics. Journal of the American Ceramic Society, 2000, 83(1), 124-128.

9. J.E. Smay, J. Cesarano, B.A. Tuttle, et al. Directed colloidal assembly of linear and ammular lead zirconate titanate arrays. Journal of the American Ceramic Society, 2004, 87(2), 293-295.

10. C.B. Yoon, S.M. Lee, G.T. Par, et al. Mutilayer actuator composed of PZN-PZT/Ag fabricated by co-extrusion process. Journal of the American Ceramic Society, 2005, 88(6), 1625-1627.

11. C.V. Hoy, A. Barda, M. Griffith, et al. Microfabrication of ceramics by co-extrusion. Journal of the American Ceramic Society, 1998, 81 (1), 152-158.

12. IEEE Standard on Piezoelectricity, ANSI/IEEE Standard 176-1987, New York: IEEE, Inc., 1988.

CHAPTER 8 CONCLUSIONS AND FUTURE WORK

This chapter presents the major conclusions drawn from the research work reported in this thesis. There are also several issues addressed in this study which need further investigation, therefore, some recommendations for future work are also proposed.

8.1 Conclusions

Based on the fabrication of porous alumina ceramics, porous alumina-zirconia ceramics, BT-epoxy composites, and PZT-epoxy piezocomposites using the freeze casting technique, several conclusions can be made as shown below:

NH_4PAA is an effective dispersant for the ceramic materials investigated, and all slurries exhibited typical shear-thinning behaviour making them suitable for freeze casting.

Porous alumina ceramics with total porosity ranging from 33% to 68% were achieved through freezing aqueous alumina slurries, followed by sublimation and sintering. The resultant pores were open, presenting a lamellar architecture. The size of the porosity could be modified by changing the initial solids loading and the cooling rate. The wall thickness of the sintered samples increased noticeably from about 10 μm to 60 μm as the solids loading increased from 14 vol.% to 37 vol.%. Furthermore, the ratio (wall thickness/ gap between walls) also increased markedly from about 0.5 to 6 with an increase of the initial slurry solids loadings. The thickness of the ceramic wall varied over a wide range, from about 125 μm to 17 μm and it decreased dramatically as the cooling rate increased from 0.25 to 1.1 ºC/sec. The sintering temperature was of significance in obtaining porous ceramics with appropriate porosity and compressive strength for specific applications. Due to their lamellar

microstructures, the samples obtained exhibited high compressive strength for such material, for instance, up to 123 MPa for 33% porosity and 55 MPa for 42% porosity in porous aluminas, making them suitable to be considered for potential load-bearing applications. The addition of PVA (from 3 wt.% to 10 wt.%) greatly affects the morphologies and properties of the final porous ceramics through depletion flocculation; a commercial binder can also affect their morphologies through bridge flocculation; glycerol can effectively bind to the water molecules and disrupt the complete crystallization of ice, leading to a cellular architecture. More homogeneous microstructures in a large area of the final porous ceramic were achieved by a double-sided freezing setup; however, the opposing temperature gradients may lead to differing orientations for the ceramic arms.

Porous Al_2O_3-ZrO_2 ceramics with homogenous and relatively long-range order channels have been produced through a two-phase colloidal system. The pore characteristics, porosity and the compressive strength of the sintered composites ceramic could be modified through the change of the initial solids loading. As the initial solids loading increased from 11 vol.% to 30 vol.%, the porosity decreased from 74% to 35%. Therefore, the porous ceramics obtained from a two-phase colloidal system showed the same trends as the relevant ones obtained from suspensions with a single ceramic phase. The initial solids loading demonstrated a significant role in the formation of the final architecture and high solids loading, i.e. $\geq$ 42 vol.%, could lead to engulfment and result in the loss of the porous architecture. Furthermore, in the freeze casting technique, especially in a two-phase system, the choice of particle size of the ceramic powder is of great significance, because it may lead to engulfment and phase segregation.

Stable and well-dispersed aqueous suspensions incorporating nano-sized BT powder have been obtained. The pH value had a strong effect on the stability of the BT suspensions, and moreover, the intrinsic pH was found to be suitable for centrifugally aided slip casting or other casting. A temperature of 1325 ºC was found to be the optimal sintering temperature for this nano-sized BT powder without any sintering additives. BT ceramic sintered at this temperature shows a bulk density of 5.85 g/cm^3, nearly 97.0% of the theoretical density, and a room temperature dielectric constant and loss tangent of 5270 and 0.01 (measured at 1 kHz), respectively.

Porous BT ceramic exhibited lamellae architectures, and BT-epoxy composites made from this possessed only a modest piezoelectric constant, but the dielectric constant was 1 order of magnitude higher than for a conventional composite with randomly distributed ceramic particles. However, the very poor mechanical properties may limit its applications especially for biomedical application. The mechanical properties of bulk $BaTiO_3$ ceramics could be improved by doping nano-sized alumina (from 0.5 vol.% to 5 vol.%) into this BT matrix, which effectively suppresses the growth of the grains. An Al-rich phase ($Ba_3TiAl_{10}O_{20}$) observed in the samples with higher alumina doping concentration could be responsible for deteriorating the dielectric and piezoelectric properties. The porous alumina-doped BT ceramics showed improved mechanical properties compared with that of porous BT ceramic, which could facilitate the later processing. Though the dielectric constant values of alumina-doped BT-epoxy composites obtained in this work were lower than those of BT-epoxy composites, they were still nearly 1 order of magnitude higher than the traditional composites. Thus, the properties of the composites can be optimized by adjustment of the amount of alumina added.

Stable PZT suspensions with good fluidity can be produced by adding 0.12 wt.% NH_4PAA. Further addition of NH_4PAA would lead to phase segregation. With the increase of initial solids loading from 11 vol.% to 25 vol.%, the volume of ceramic phase in the composite gradually increased from about 30 vol.% to 50 vol.%, and the piezoelectric constant d_{33} increased from about 103 pC/N to 203 pC/N. The piezoelectric constant d_{33} of the resultant composites increased from 178 pC/N to 286 pC/N when the sintering temperature increased from 1200 ºC to 1250 ºC. The elevated temperature could effectively improve the piezoelectric constant d_{33} of the composites and the planar coupling factor k_p. The limitations of the homemade freezing setup caused the inhomogeneity of the ceramic wall orientation, which would limit its application.

8.2 Future Work

Due to the time and funding restrains of this project, there were several very interesting points that could not be investigated, and which could prove very valuable and worthy of further investigation.

The data presented in this study have already shown strong trends, particularly in terms of critical velocity, which needs to be more fully analyzed and understood. The development of a predictive capacity through modeling should be very helpful to help realize this. Of course, for the modeling work, the knowledge of the thermal conductivities and the thermal boundary conditions like the heat transfer coefficients are required, which depends much on an accurate setup and sufficient accurate data. The lack of enough relevant data in ceramic colloidal systems, especially in term of systems with nano-sized particles, may become a hurdle for the development of this modeling work.

This study has shown that the freezing setup plays a very significant role in this fabrication

technique, especially for the preparation of 2-2 piezocomposites. The current setups shown in this study have the disadvantage that the temperature gradient during freezing is not homogenous especially when the cooling rate is low, so improvement of the setup should be made. Sylvain Deville[1] has shown a more elaborate setup (as shown in Figure 8.1) for freeze casting, to which we should pay more attention. In Sylvain's design, liquid nitrogen and ring heater were employed simultaneously to control the freezing kinetics and freezing can start from both bottom and top. Therefore, a more homogenous cooling rate can be obtained.

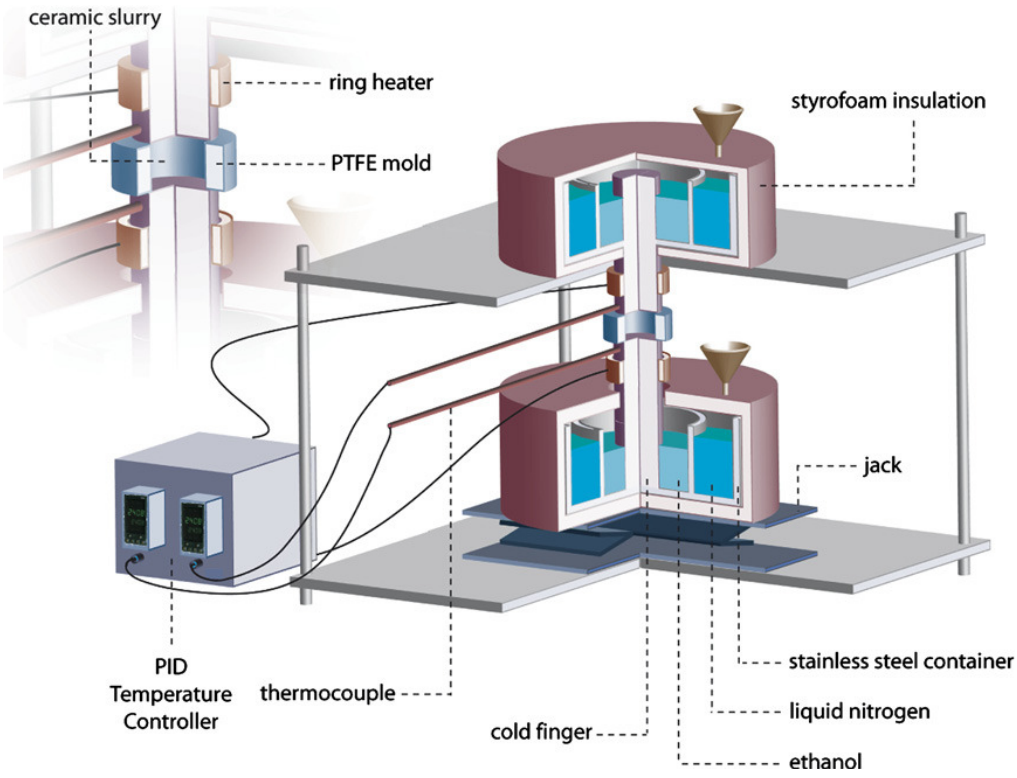

Figure 8.1 Sylvain Deville's setup for freeze casting[1].

Moreover, in order to analyze the activities in the interface during freezing, the mould should be also improved. A proposed mould is shown in Figure 8.2. The mould is transparent, which is good for observation of the freezing process. Many thermocouples are added inside the mould at different levels so that the temperature changes during freezing can be obtained, which will also be quite useful for the modelling work.

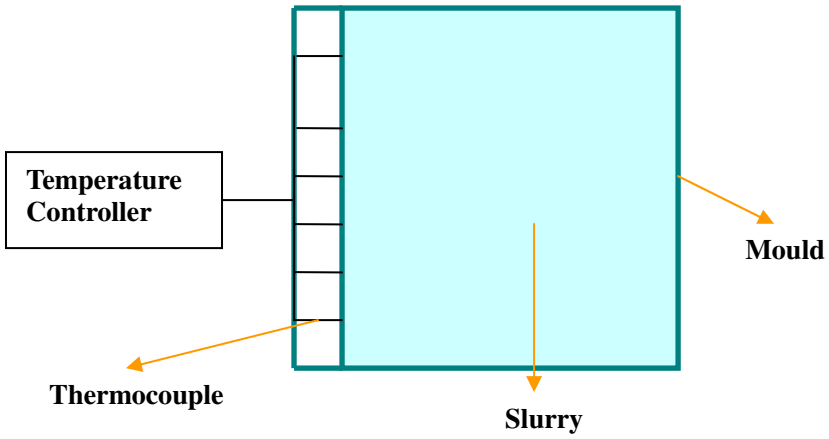

Figure 8.2 Proposed mould for freeze casting

The effect of particle size in freeze casting was shown in Chapter 5 and demonstrated that the critical velocity of solidification is greatly affected by the ceramic particle size, which is in agreement with early experimental and theoretical work. If the velocity of the advancing ice front is above the critical value, particles will be engulfed by the interface, and then the interconnected and open porous architecture will be lost. However, the quantitative relationship between the critical velocity of solidification and the particle size is still unknown and there is a lack of relevant reports, especially with relevance to nano-sized particles. Therefore, it would be very meaningful to carry out further research on this aspect.

Moreover, though nano-sized BT powders were utilized in the study in this work (Chapter 6), the high sintering temperatures used made it impossible to obtain BT ceramics with nano-sized grains. Introducing a sintering aid or different sintering method (e.g. two step sintering method) into this BT system may be helpful in obtaining nano-sized grains and therefore achieve better electrical and mechanical properties. Thus, this would also be an aspect of future work.

It has been shown in this study that lower suspension concentrations and high cooling rates lead to fine architecture. However, the architecture obtained from ceramic suspension using

freeze casting is normally a micro-sized structure, because the samples obtained from slurries of less than e.g. 14 vol.% (alumina slurry) will collapse during sublimation even after the incorporation of binders, which has been proved by our experiments. In order to obtain porous ceramics with nano-sized lamellar architecture, one route could be to utilize ceramic precursors in the freeze casting technique.

References

1. S. Deville, E. Saiz, and A.P. Tomsia. Ice-templated porous alumina structures. Acta materialia, 2007, 55, 1965-1974.

APPENDICIES: PAPERS

Published Papers:

Gang Liu, Dou Zhang, Tim W Button. Preparation of concentrated barium titanate suspensions incorporating nano-sized powders. Journal of the European ceramic society, 2010, 30, 171–176.

Gang Liu, Dou Zhang, Tim W Button. Porous Al_2O_3–ZrO_2 composites fabricated by an ice template method. Scripta Materialia, 2010, 62, 466–468.

Kechao Zhou, Yan Zhang, Dou Zhang, **Gang Liu**, Tim Button. Porous hydroxyapatite ceramics fabricated by an ice-templating method. Scripta Materialia, 2011, 64, 426-429.

Submitted Papers:

Gang Liu, Yun Jiang, Tim W Button. Low temperature sintering and dielectric properties of $BaTiO_3$ ceramics incorporating nano-sized powders. (Submitted to **Ferroelectrics**)

Gang Liu, Dou Zhang, Tim W Button. Porous $BaTiO_3$ ceramics and its composites fabricated by freeze casting process. (Submitted to **Scripta Materialia**)

Will Submit:

Gang Liu, Dou Zhang, Tim W Button. Morphology control in freeze casting. (will submit to **Journal of European ceramic society**)

Gang Liu, Dou Zhang, Tim W Button. Size effect and phase segregation in freeze casting. (will submit to **Scripta Materialia**).

Gang Liu, Dou Zhang, Tim W Button. PZT-epoxy piezoelectric composite fabricated by freeze casting. (will submit to **Applied Physics Letters**)

Gang Liu, Dou Zhang, Tim W Button. Electrical properties of nano-sized alumina doped $BaTiO_3$-based ceramics. (will submit to **Journal of European ceramic society**)